Exploration of Co^{II}-Based (Co^{II} and Co^{II}-*4f*) Single Molecule Magnets

Zur Erlangung des akademischen Grades eines

DOKTORS DER NATURWISSENSCHAFTEN

(Dr. rer. nat.)

der Fakultät für Chemie und Biowissenschaften der

Karlsruher Institut für Technologie (KIT)-Universitätsbereich

Genehmigte

DISSERTATION

Von

YAN PENG

M.S

aus JIANGXI, CHINA

Dekan: Prof. Dr. Peter Roesky

Referent: Prof. Dr. Annie K. Powell

Korreferent: PD. Dr. Karin Fink

Tag der mündlichen Prüfung: 16.07.2015

Die vorliegende Arbeit wurde in der Zeit von May. 2012 bis July. 2015 am Institut für Anorganische Chemie des Karlsruher Instituts für Technologie (KIT) unter Anleitung von Prof. Dr. Annie K. Powell angefertigt.

Contents

Zusammenfassung

Die Entdeckung der Einzelmolekül Magneten (SMMs) liefert nicht nur einzigartige Möglichkeiten zur Beobachtung von Quanteneffekten, sondern bietet auch einen neuen Weg zur Entwicklung von molekularen Geräten zur Informationsspeicherung und Quantenrechnung. Man weiß, dass die Schlüsselvoraussetzung für SMM Verhalten eine Kombination aus ungepaartem Spin und uniaxialer Anisotropie im Molekül ist. Verbindungen aus *3d* und *4f* Metallionen in einem heterometallischen Komplex stellen eine ideale Syntheseroute für SMMs dar. Um solche Komplexe zu konstruieren wurden polydentate Schiffbasen-Liganden eingesetzt. Die magneto-strukturellen Beziehungen der erhaltenen Verbindungen wurden mit Hilfe einer Kombination aus Einkristall XRD, magnetischen Suszeptibilität und micro-SQUID Messungen untersucht

In Kapitel 3, wird die Synthese von 15 verschiedenen heterometallischen *3d-4f* und homometallischen 4f Koordinationsverbindungen (**1-15**) mit den Aminopolyalkohol Liganden H_2**dea**, H_3**L1,** H_2**L2 and** H_3**L3** beschrieben. Variation der Reaktionsbedingungen führte zu sieben unterschiedlichen Strukturtypen. Die magnetischen Messungen deuten darauf hin, dass die Verbindungen **3**, **4**, **5**, **10**, **11**, **14** und **15** langsame Relaxation der Magnetisierung ohne angelegtes dc Magnetfeld zeigen. Allerdings zeigt nur Verbindung **15** ein Maximum mit U_{eff} = 27.3 K. Verbindung **5** und **14** zeigen feldinduziertes SMM Verhalten mit einer Energiebarriere von 16.13 K beziehungsweise 72.48 K. Verbindungen **5** und **6** sind isostrukturell und unterscheiden sich nur in der Wahl des 3d Metalls (Fe^{III}, **5** and Cr^{III}, **6**). Verbindung **5** ist ein feldinduzierter SMM, während bei Verbindung **6** kein AC Signal, selbst bei angelegtem Feld gefunden werden konnte, was die Vermutung nahe legt, dass die unterschiedliche elektronische Struktur der 3d Metallionen für das unterschiedliche Verhalten verantwortlich sein muss.

In Kapitel 4 wurden zwanzig *3d-4f* und *4f* Koordinationsverbindungen (**16-35**) erfolgreich synthetisiert, basierend auf dem Schiffbasen Liganden H_3**L4**, H_2**L5**, H_3**L6**, H_2**L7**, H_2**L8** und H_4**L9**. Die magnetischen Messungen zeigen, dass die Verbindungen **16**, **17**, **18** und **19** zeigen feldinduziertes SMM Verhalten mit Energiebarrieren von 7.30 K, 10.18 K, 14.10 K beziehungsweise 35.36 K. Verbindungen **20, 21, 22, 23** und **24** zeigen langsame Relaxation ohne angelegtes dc Feld. Verbindung **20** zeigt typisches SMM Verhalten mit einer Energiebarriere von 38. 46 K.

In Verbidnung **21**, bedingt die trigonal prismatische Koordinationsgeometrie um das Co^{II} Ion eine Energiebarriere von 98 K. Die Verbidnungen **22** und **23** zeigen zwei langsame

Relaxationsprozesse mit Energiebarrieren von 17.85 K (bei niedriger Temperatur) und 104,78 K (bei hoher Temperatur) fur **22** und mit Energiebarrieren von 17.45 K (bei niedriger Temperatur) und 94.53 K (bei hoher Temperatur) für **23**, wobei Verbindung **24** einen einzelnen Prozess mit einer Barriere von 140 K. In Verbidnungen **22**-**24** konnte zum ersten Mal beobachtet werden, dass die Anisotropie eines einzelnen Dy^{III} Ions durch Veränderungen in der Koordinationsgeometrie des 3d Metalls in den $Co_2^{II}Ln^{III}$ gesteuert werden kann. Dies liefert den experimentellen Beweis, für Ergebnisse aus *ab* inito Rechnungen an $Co_2^{II}Dy_2^{III}$ Verbindungen, die zuvor von unserer Gruppe berichtet wurde, dass zwei oder mehr Relaxationspfade wichtig für die Bestimmung des Gesamt-magnetischen Verhalten des Co^{II}-4f Systems sein kann.

Chapter 1

Introduction

1.1 Introduction to Molecular Magnetism

Historically, the intriguing phenomenon of magnetism was first noticed (900 B.C.) when the naturally occurring magnet lodestone, found in Magnesia (Greece) was observed to attract iron. The phenomenon was used by the Chinese to create the floating compass.[1] With the development of science over the centuries applications of magnets have seen a huge expansion, including magnetomechanical applications, acoustic devices, information/telecommunications devices, electrical motors and generators, and magnetic shielding.[2]

Recently, worldwide interest in molecule-based magnets has arisen for both fundamental scientific and technological reasons. Molecules are produced by chemical reactions that can be controlled and thus provide the opportunity for new phenomena, and combinations of properties not observed for classical magnets.[3] One of the milestones was the first organic-based ferromagnet, i.e. ionic, 'zero-dimensional' (0-D), organic-solvent soluble $[Fe(C_5Me_5)_2]^+[TCNE]^-$ (TCNE = tetracyanoethylene) compound. This would not have been predicted to magnetically order based on the conventional understanding of magnetism, which was only expected to arise in 3-dimensional (3D) solid-state materials. The $[Fe(C_5Me_5)_2]^+[TCNE]^-$ system is characterised by magnetic hysteresis and has a saturation magnetisation characteristic of a ferromagnet with a critical (Curie) temperature T_c of 4.8 K.[4] Since then, a large number of molecule-based magnets including organic, organometallic and inorganic coordination compounds have been synthesized and characterized.[5] In early 1990, another breakthrough was the identification of the 1st SMM (single molecule magnet), $[Mn_{12}O_{12}(O_2CMe)_{16}(H_2O)_4]$, showing magnetic hysteresis below a certain blocking temperature T_B,[6] which could be potentially used for high-density information storage and quantum computing. Moreover, the size of the clusters is positioned at the frontier between molecular and bulk materials, allowing study of new physical phenomena such as quantum tunnelling of the magnetisation.[7] Over the past two decades of research into SMMs, fine details of the properties of these tiny magnets have become better understood and the synthesis of diverse compounds has been developed. However, there is a continuous quest for new SMMs, in order to understand better both the structural aspects that favour SMM behaviour, and also the synthetic methodologies needed to achieve this, with the long-term goal of developing such systems.[8]

1.2 Single Molecule Magnets (SMMs)

A single molecule magnet (SMM) is a molecule that shows slow relaxation of the magnetisation of purely molecular origin, which is a property of the molecule itself. It is a molecule that can be magnetised in a magnetic field and that will remain magnetised even after switching off the magnetic field. SMMs are discrete molecular clusters which act as nanomagnets below a certain blocking temperature (T_B). SMM behaviour was first discovered in Mn_{12}-Ac (**Fig 1.1**) which showed an S = 10 ground state and slow relaxation of the magnetisation.[6, 9]

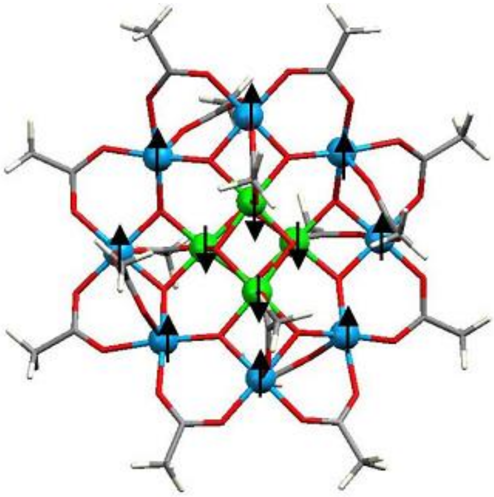

Fig 1.1 First discovered SMM Mn_{12}-Ac

Thus, the field of single molecule magnets was born and Mn_{12}-acetate became a classical SMM material. The prerequisites for such a system are (a) a high spin ground state (S), (b) a uniaxial anisotropy characterised by the high zero-field splitting parameter D and (c) negligible magnetic interaction between molecules. The uniaxial anisotropy removes the degeneracy of the ground spin state splitting it into microstates ranging from M_S= -S to +S (**Fig 1.2**). The S and D parameters combine to give rise to a significant energy barrier towards the reversal of spin reorientation with the result that the relaxation of magnetisation becomes slower. The energy barrier is given by $|D|S^2$ or $|D| (S^2-1/4)$ for integer and half-integer spins, respectively.

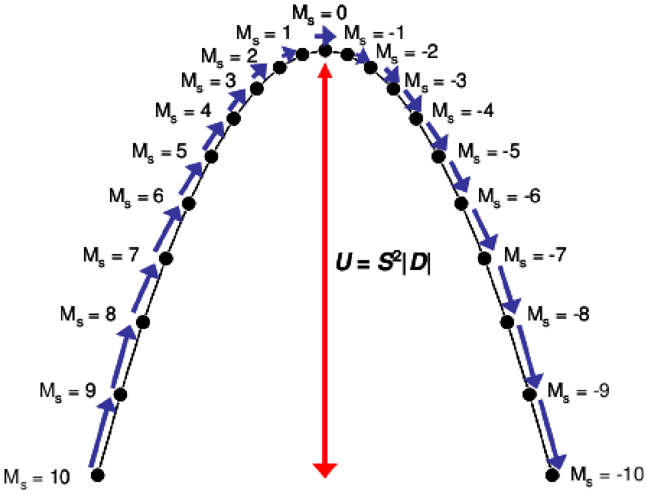

Fig 1.2 Energy diagram showing the zero-field splitting of the MS levels for a hypothetical S = 10 ground state and the energy barrier (*U*) between the $+M_S$ and $-M_S$ levels.

Below the blocking temperature, the magnetisation of SMMs shows hysteresis as shown in **Fig 1.3** for the case of Mn_{12}-Ac. The clear hysteresis loops are directly associated with the slow relaxation dynamics of the system. The steps which are seen have been shown to arise from quantum effects within the magnetic molecules. This phenomenon is termed quantum tunnelling of the magnetisation (QTM).

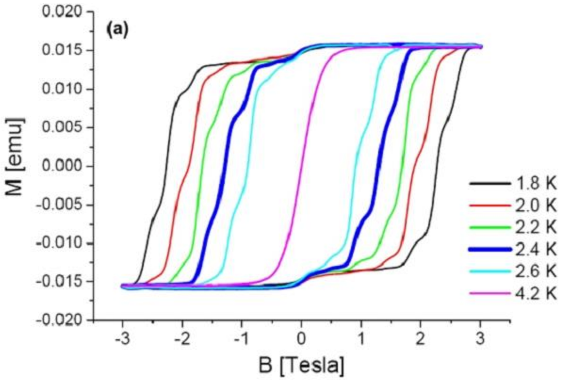

Fig 1.3 Hysteresis curves of a Mn12-Ac single crystal at different temperatures with an axially applied magnetic field. The steps indicate the relative change in magnetisation upon tunnelling

1.3 Co^{II} SMMs

Cobalt, translated from its German name ‘Kobold ’ chosen by its discoverer Georg Brandt, meaning goblin or evil spirit, is an intriguing element in its dipositive oxidation state for scientists interested in structural chemistry and magnetism. There are two interesting aspects to working with the Co^{II} ions in contrast to other 3d metal ions. One is the structural aspect, with a range of possible coordination geometries, such as linear, trigonal, octahedral, tetrahedral, square-pyramidal, trigonal prismatic, trigonal-bipyramidal and square-planar.[10] The other concerns the magnetic aspects with high anisotropy arising from spin-orbit coupling. These make Co^{II} ions good candidates for single molecule magnets and by implication for potential applications in data storage and quantum computing.[11]

The promise of Co^{II} for use in polymetallic SMMs has been previously highlighted, with a particular emphasis placed on the effects of the molecular shape, size and symmetry,[12] however, difficulties are encountered in analysing the magnetic data of the high-spin Co^{II} ions. For example, in octahedral coordination there are significant challenges resulting from the presence of unquenched orbital angular momentum.[13] Generally, the effects of spin-orbit coupling occur in conjunction with the effects of a symmetry-lowering structural distortion, e.g. away from O_h symmetry.[13a] The contributions from the orbital angular momentum are taken into account in terms of the zero field splitting (ZFS) tensor and anisotropic g-factor. In many cases the spin-only Hamiltonian is also used for octahedrally coordinated Co^{II}, assuming that the distortion from the octahedral environment is strong enough to remove the orbital degeneracy. In other words, the spin-only Hamiltonian can be used only when a strong distortion splits the orbital triplet leading to stabilisation of the orbital singlet. If the distortion is not strong enough the ZFS approach cannot be used and the orbital angular momentum must be included into consideration.[11]

The weak exchange limit presents a different situation to most SMMs based on ions with only second order spin-orbit coupling {e.g. Mn^{III}}, where generally the exchange interactions are larger than the effects of the magnetic anisotropy. For Co^{II} systems, the anisotropy could easily be of the same order of magnitude or even larger than the exchange coupling. A further consequence of using Co^{II} is that the equation relating the height of the energy barrier to S^2 and D is no longer valid, as S is not a good quantum number for polynuclear Co^{II} clusters.[14] However; it is possible to see how slow magnetic relaxation in Co^{II} SMMs can occur. It requires two levels ($Ms = \pm X$) separated by an energy barrier, well separated from excited states. Additionally, just as for strong-exchange limit SMMs, quantum tunnelling can shortcut the energy barrier for Co^{II} SMMs. In fact, those Co^{II} SMMs that have been shown to display quantum tunnelling show that the process is much more efficient than in SMMs based on the other 3d ions. What makes a good Co^{II} SMM is therefore a fascinating scientific question, especially given the tantalizing potential for the production of very large magnetic anisotropies and by extension, higher blocking temperatures.[12a]

1.4 Ln^{III} SMMs

In 2003, with the discovery of unprecedented relaxation behaviour in Ln-phthalocyanine complexes,[15] Ln ions gained gradual acceptance in the field of molecular magnetism. The distinguishing feature of *4f* elements as spin carriers for SMMs is their single-ion anisotropy. Among the lanthanide family, the dysprosium (Dy^{III}) ion has become a favourite ingredient in making magnetic materials mainly because of its high magnetic moment and the high anisotropy of the spin-orbit coupled Kramers doublet ground state ($S = 5/2$, $L = 5$, $J = 15/2$). Consequently, homometallic polynuclear Dy^{III} SMMs have become of increasing interest since the observation of the unusual slow relaxation behaviour in a triangular Dy_3 cluster in spite of its almost nonmagnetic ground state.[16] Although recent research in this area has yielded many interesting SMMs incorporating Dy^{III} ions, the science of making 4f-based SMMs is still in its infancy and hence there is need to explore this rich area of coordination chemistry.

Lanthanides have very complicated spin properties owing to relativistic spin-orbit coupling, which makes analysis difficult when dealing with large complexes. In 2011, Rinehart and Long proposed an approach for exploiting the single-ion anisotropy of lanthanides in SMMs.[17] Relevant to the current work is the conclusion that the properties of lanthanides can be optimised by providing the correct coordination environment. Based on a consideration of the occupancy of the *f*-orbitals of the free-ions, the shape of the anisotropy ellipsoid can be proposed.

These shapes can be axially elongated (prolate), equatorially elongated (oblate), or spherical (isotropic) and are given in **Fig 1.4**.

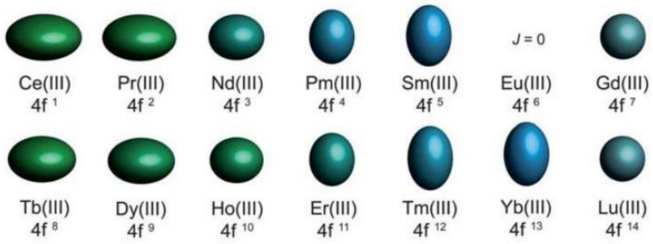

Fig 1.4 The shapes of the lanthanides range from oblate to prolate to spherical based on which f orbitals are occupied[17]

This allows one to predict what coordination geometry will best maximise anisotropy. For oblate ions, Rinehart and Long propose that the ligand electron density should be above or below the lanthanide, while for prolate ions the ligand field should be maximum in the plane of the lanthanide.[17] These models also suggests a less explored method of generating strong single-ion anisotropy for single-molecule magnet synthesis involving strongly prolate ions like Tm^{III} and Yb^{III}. In general the Ln^{III} ions can provide remarkable examples of SMMs and SIMs showing very high energy barriers.[18] However, very fast relaxation rates and QTM effectively remove any possibility of using these high barriers to trap information in one magnetic sublevel state.

1.5 Co^{II}-4f SMMs

As the search for new SMMs expanded, several groups explored mixed metal compounds, and particularly Co^{II}-Ln ones, as an attractive area. These efforts were greatly stimulated by the Cu_2Tb_2 SMM reported by Matsumoto and co-workers.[19] The strategy is obviously to take advantage of the lanthanide ion's significant spin and its large anisotropy, as reflected in a large D value, to generate SMMs distinctly different from the homometallic ones. Additionally, unlike the other 3d ions, Co^{II} has first order spin-orbit coupling and is frequently found have an effective spin S = 1/2 at low temperature. The anisotropy can therefore easily be of the same order of magnitude or even larger than the exchange coupling. Indeed, there are now several Co^{II}-Ln polynuclear SMMs, including CoY,[20] Co_2Ln,[21] Co_3Ln,[22] Co_4Ln_2,[23] Co_2Dy_{10}[24] and Co_2Dy_2.[25] Given the relatively low number of Co^{II} containing SMMs, it is clear that many more examples are needed in order to understand how to increase the energy barrier.

1.6 Ligand Selection and Synthetic Strategy

The main goal of this research was to construct *3d-4f* coordination clusters, especially Co^{II}-*4f* coordination clusters and to study their magnetic properties. To obtain such clusters, the choice of the ligands is always a key issue. Many researchers have employed polydentate chelating ligands containing N and O donors. Following the soft-hard concept, the *4f* ions as hard acids prefer hard oxygen donors, while *3d* ions are borderline acids, having the tendency to coordinate to N-donors as well as O-donors. Thus the ligands will coordinate to the *4f* ion through oxygen atoms and bind the transition metal ions with both nitrogen and oxygen atoms. Such polydentate ligands have led to the discovery of many interesting 3d-4f clusters showing interesting magnetic behaviour.[26]

In this work the amino-polyalcohol ligands (**Scheme 1.1**):

2-[(2-hydroxy-ethyl)-pyridin-2-ylmethyl-amino]-ethanol (H_2**L1**),

2-(bis-pyridin-2-ylmethyl-amino)-ethanol (H_1**L2**),

2-(bis-pyridin-2-ylmethyl-amino)-propane-1,3-diol (H_2**L3**)

As well as the Schiff-base ligands (**Scheme 1.1**):

3-hydroxy-naphthalene-2-carboxylic acid

(6-hydroxymethyl-pyridin-2-ylmethylene)-hydrazide (H_3**L4**),

(6-hydroxymethyl-pyridin-2-ylmethylene)-hydrazide (H_2**L5**),

2-hydroxy-benzoic acid (6-hydroxymethyl-pyridin-2-ylmethylene)-hydrazide (H_3**L6**),

6,6'-((1Z)-((piperazine-1,4-diylbis(propane-3,1-diyl))bis(azanylylidene))bis(methanylylidene))

bis(2-methoxyphenol) (H_2**L7**)

2-[(2-hydroxy-phenylimino)-methyl]-6-methoxy-phenol (H_2**L8**)

(N',N'''E,N',N'''E)-N',N'''-(pyridine-2,6-diylbis(methanylylidene))bis(2-hydroxybenzohydrazide)

(H_4**L9)** were selected.

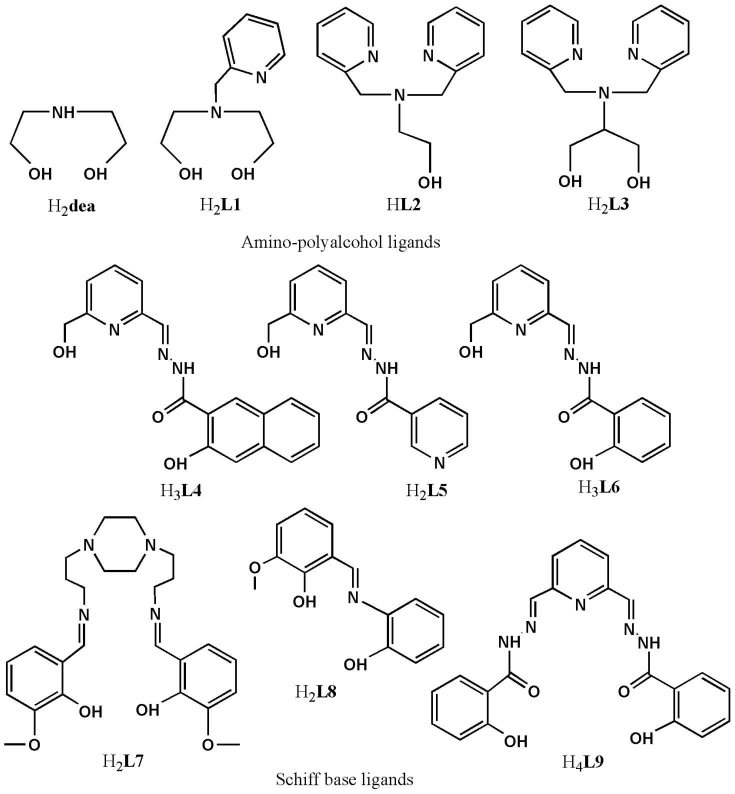

Scheme 1.1 The selected ligands

At the beginning, amino-polyalcohol ligands were used. These would seem an ideal continuation of previous efforts as they possess an affinity to 4f ions due to their O donors, but also incorporate N functionalities which can take part in bonding, though to date there are significantly fewer *3d-4f* and *4f* compounds with this type of ligand than there are with 3d metals alone.

Recently, several Co^{II}-*4f* clusters coordinated by Schiff base ligands were reported and showed interesting magnetic properties, so three ligands (H_3**L4**, H_2**L5** and H_2**L6**) based on 6-hydroxymethyl-pyridine-2-carbaldehyde were selected to explore the coordination chemistry of Co^{II}-*4f* systems. All three ligands have two separated NNOO and OO or ON coordination pockets, the first of which is expected to have a good affinity for divalent *3d* ions, while the second donor set can coordinate *4f* ions. They can all occur in the enol form and, in the presence of metal ion, can transform into different tautomers (**Schemes 1.2** and **1.3**). It was therefore considered that these ligands were highly suitable for the synthesis of complexes containing both divalent 3d ions and lanthanides. In fact, it was found that H_3**L4**, H_2**L5** and H_3**L6** only chelate Co^{II} ions, and formed mononuclear complexes, which maybe because of the rich N coordination sites and steric constraints. Although these three ligands are not favourable for the assembly of Co^{II}-4f systems, they provide further proof that these kinds of Schiff base ligands can stabilise Co^{II} ions. Thus, ligand H_2**L7** was selected which has NNNOO and OOOO coordination pockets. Again, mononuclear Co^{II} complexes were obtained which is probably because of the flexible nature of this ligand.

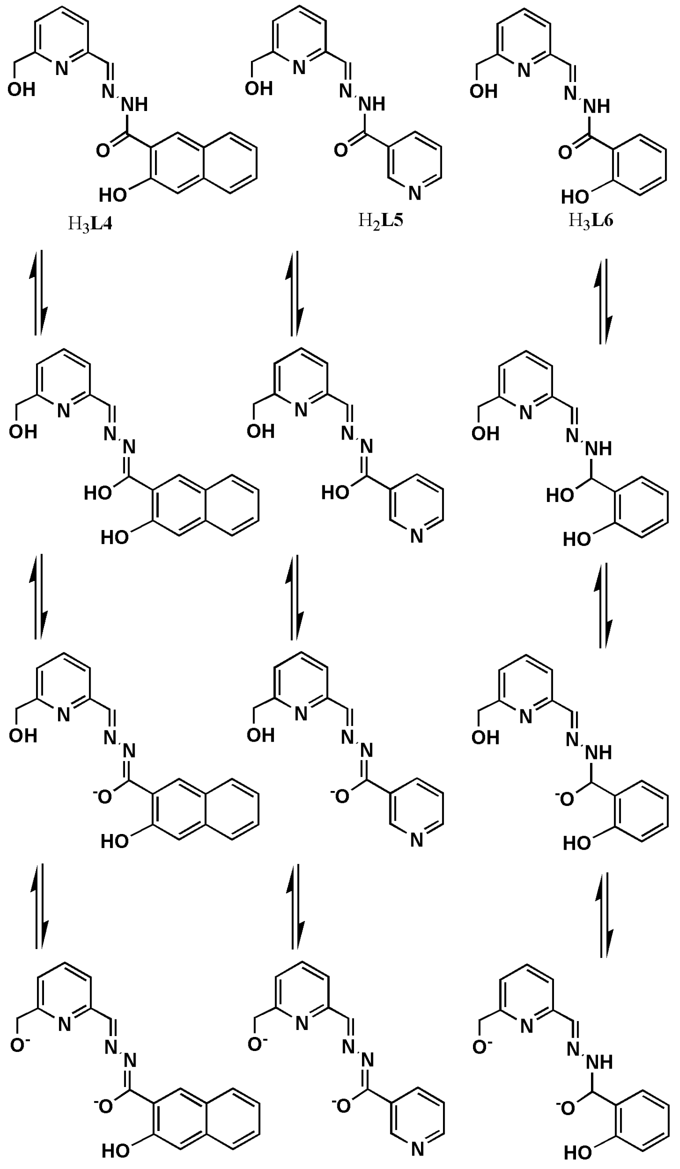

Scheme 1.2 The tautomers of ligands H_3**L4**, H_2**L5** and H_3**L6**

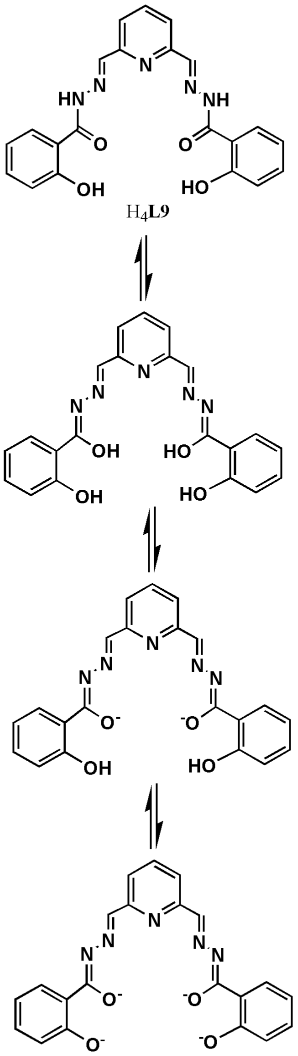

Scheme 1.3 The tautomers of ligand H_4**L9**

When ligand H_2**L8** and H_4**L9** were used, the former one was successfully used to assemble the $Co^{II}_2Dy^{III}_2$ compound previously reported by our group,[25] while the latter one, based on pyridine-2,6-dicarbaldehyde with the more rigid NNNOO and OOOO coordination pockets led to Co^{II}_2Dy and $Co^{II}_2Dy^{III}_2$ linear complexes as well as a two-dimensional coordination polymer. Thus these two ligands are suitable for the assembly of Co^{II}-*4f* clusters.

It is now well established that co-ligands are a useful addition in assembling 3d-4f clusters with carboxylates providing the most studied multi-bridging groups in coordination chemistry. They can undergo self-assembly complexation reactions with metal ions to produce polynuclear metal compounds in which they can assume various coordination modes and can bridge many metal centres. Therefore the carboxylic acids shown in **Scheme 1.4** were used as co-ligands to obtain further examples of *3d-4f* metal aggregates.

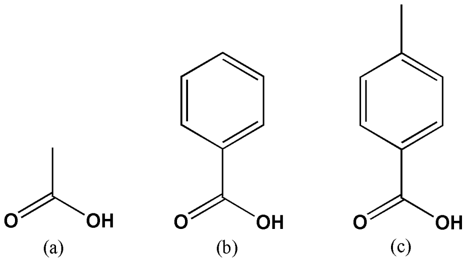

Scheme 1.4 The selected carboxylic acid co-ligands

1.7 Thesis Overview

This thesis describes the synthesis of homo- and hetero-metallic complexes which have been crystallographically characterised and magnetically investigated. The research results are divided into two chapters (3 and 4).

Chapter 3 is concerned with the synthesis and characterisation of *3d-4f* and *4f* complexes using aminopolyalcohol ligands (H_2**dea**, H_2**L1**, H_1**L2**, and H_2**L3**) along with co-ligands such as benzoic acid. All of the compounds were full magnetically investigated and presented.

Chapter 4 describes the synthesis and characterisation of mononuclear Co^{II}, *4f* and heterometallic *3d-4f* complexes using Schiff-base ligands (H_3**L4**, H_2**L5**, H_3**L6**, H_2**L7**, H_2**L8** and H_4**L9**) along as well as with carboxylate co-ligands. All of the compounds were full magnetically investigated and presented.

Chapter 2

Research Objectives

Single molecule magnets (SMMs)[6,27] present an interesting class of compounds with multiple possible applications in fields of modern technology, e.g. highly efficient data storage systems, molecular freezers,[28] quantum computers[29] or contrast agents.[30]

The key requirement for SMM behaviour is a combination of sufficient spin and uniaxial anisotropy within the molecule. Some metal ions, such as Fe^{III}, Mn^{II}, Cr^{III} and Gd^{III}, can contribute high spin but minimal anisotropy, whereas others, such as Mn^{III}, Co^{II} and most of the trivalent lanthanide ions, can contribute high single ion anisotropy. Furthermore, some of these ions can contribute both spin and anisotropy and previous work has shown that it can be advantageous to introduce both spin and anisotropy into a coordination cluster using a combination of *3d* and *4f* metal ions in a heterometallic complex.

Although some progress has been made in optimizing the magnetic properties of existing SMMs, it is still not easy to control the key parameters in a cluster. It is difficult to control the arrangement of the metal ions with respect to each other as well as the magnetic coupling between them and the relative orientations of the single-ion anisotropy axes. These factors all have profound effects on the height of the energy barrier to spin reorientation, the splitting of the magnetic states and the possibilities of Quantum Tunnelling of the Magnetisation (QTM).

In order to construct such polynuclear complexes, the concept of self-assembly of the paramagnetic metal ions using suitable ligands like amino-polyalcohol ligands and Schiff base ligands was applied. Amino-polyalcohol ligands were previously used in reaction systems with *3d*, *4f* and *3d*-*4f* mixtures, but so far little attention being devoted to the synthesis of Co^{II}-*4f* and *4f* clusters. In terms of the Schiff base ligands, a first objective was to investigate the coordination chemistry of these ligands with either a single *3d* ion or a single 4f ion. Drawing on these results, it was then possible to utilize the ligands to design the synthesis of heterometallic *3d*-*4f* Co^{II}-*4f* complexes. These studies were supported by full structural determinations using X-ray diffraction, single-crystal X-ray diffraction and detailed magnetic susceptibility measurements.

Chapter 3

3d-4f and *4f* Coordination Clusters with Amino-Polyalcohol Ligands

3.1 Introduction

3d-4f coordination complexes are very interesting from both a theoretical and a practical point of view. To obtain such clusters, the choice of the ligands is always a key issue. Many researchers have employed polydentate chelating ligands containing N and O donors with the idea that the soft-hard acid-base concept will lead to the *4f* ions acting as hard acids and thus preferring hard oxygen donors, while the *3d* ions acting as borderline acids will tend to prefer the softer N-donors, but can also accept O-donors. In other words, the expectation is that the ligands will coordinate to the *4f* ion through its oxygen atoms and bind the transition metal ions with both nitrogen and oxygen atoms. Such polydentate ligands have led to the discovery of many interesting *3d-4f* clusters which show exciting magnetic behavior.[26] Amino-polyalcohol ligands are an ideal extension of such previous efforts since they possess the required O and N donors. To date there is a limited number of *3d-4f* and *4f* compounds with this type of ligand compared with those for pure *3d* metals. The lack of examples of *3d-4f* coordination cluster compounds was the motivation for the research presented here. The amino-polyalcohol ligands used to obtain the *3d-4f* and *4f* clusters reported here are shown in **Scheme 3.1**

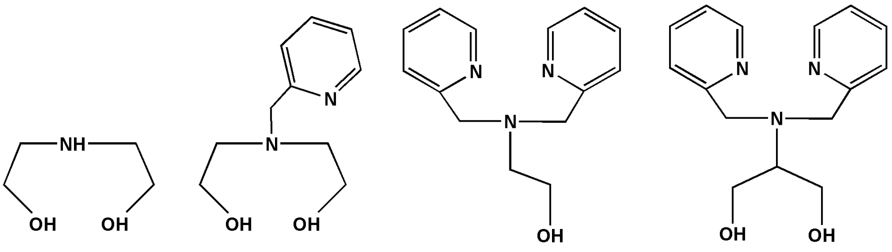

H_2**dea** H_2**L1** H**L2** H_2**L3**

Amino-polyalcohol ligands

Scheme 3.1 The selected ligands

3.2 Synthesis

It is now well-known that the choice of ligand and starting metal salt, the relative ratios of reactants, temperature, solvent, reaction time can affect the nature of the final product. Selected conditions have been investigated, leading to different products as shown in **Table 3.1**.

Table 3.1 The relationship of reaction conditions and final products for compounds discussed in Chapter 3

Molar ratio	Solvent	Volume (mL)	Base	Temperature	products
$H_2\mathbf{dea}$:$Co(NO_3)_2$:$LnCl_3$:$PhCO_2Na$ 4:4:1:4	MeOH	12	Et_3N	rt	$Co^{III}_3Co^{II}_2Ln^{III}_2$ (**1** and **2**)
$H_2\mathbf{L1}$:$CoCl_2$:$DyCl_3$:$PhCO_2H$ 2:1:1:4	MeOH/MeCN	25	Et_3N	rt	$Co^{III}_3Dy^{III}_3$ (**3**)
$H_2\mathbf{L1}$:$CoCl_2$:$DyCl_3$:*Me*-$PhCO_2H$ 2:1:1:4	MeOH/MeCN	25	Et_3N	rt	$Co^{III}_3Dy^{III}_3$ (**4**)
$H_2\mathbf{L1}$:$FeCl_2$:$DyCl_3$:$PhCO_2H$ 2:1:1:4	MeOH/MeCN	25	Et_3N	rt	$Fe^{III}_2Dy^{III}_2$ (**5**)
$H_2\mathbf{L1}$:$CrCl_3$:$DyCl_3$:$PhCO_2H$ 2:1:1:4	MeOH/MeCN	25	Et_3N	rt	$Cr^{III}_2Dy^{III}_2$ (**6** and **7**)
$H_2\mathbf{L1}$:$[Fe_3O(O_2CPh)_6(H_2O)_3](O_2CPh)$: $Ln(NO_3)_3$ 8:1:1	MeCN	25		rt	$Fe^{III}Ln^{III}$ (**8** and **9**)
$H_2\mathbf{L1}$: $FeCl_3$:$Ln(NO_3)_3$:$PhCO_2Na$ 1:1:1:8	MeOH	20	Et_3N	rt	$Fe^{III}Ln^{III}$ (**9-12**)
$H_2\mathbf{L1}$:$Dy(NO_3)_3$ 2:3	MeOH/MeCN	45	Et_3N	rt	Dy^{III}_2 (**13**)
$H\mathbf{L2}$:$Dy(NO_3)_3$ 2:3	MeOH/MeCN	45	Et_3N	rt	Dy^{III}_2 (**14**)
$H_2\mathbf{L3}$:$Dy(NO_3)_3$ 2:3	MeOH/MeCN	45	Et_3N	rt	Dy^{III}_2 (**15**)

The ligand $H_2\mathbf{dea}$ was chosen as a starting point. The reaction of $H_2\mathbf{dea}$, $Co(NO_3)_2\cdot 6H_2O$, $LnCl_3\cdot 6H_2O$ and $PhCO_2Na$ in MeOH in a molar ratio of 4:4:1:4 in presence of Et_3N produced crystals of $Co^{III}_3Co^{II}_2Ln^{III}_2(OH)_2(PhCO_2)_6(\mathbf{dea})_4(H\mathbf{dea})(NO_3)](NO_3)\cdot 3MeOH\cdot H_2O$ [Ln = Dy, (**1**) and Gd (**2**)]. Subsequently, the three ligands: $H_2\mathbf{L1}$, $H\mathbf{L2}$ and $H_2\mathbf{L3}$ were investigated. The reaction of $H_2\mathbf{L1}$, $CoCl_2\cdot 6H_2O$, $DyCl_3\cdot 6H_2O$ and $PhCO_2H$ or para-*Me*-$PhCO_2H$ in MeOH and MeCN in a molar ratio of 2:1:1:4 in presence of Et_3N produced $[Co^{III}_3Dy_3(\mathbf{L1})_3(\mu_3\text{-}OH)_4(O_2CPh)_6(H_2O)_3]\cdot(O_2CPh)\cdot Cl\cdot 4MeOH\cdot 10H_2O$ **(3)** and

$[Co^{III}_3Dy_3(\mathbf{L1})_3(\mu_3\text{-}OH)_4(O_2CPh\text{-}\mathit{Me})_6(H_2O)_3]\cdot 2Cl\cdot 10MeOH$ (**4**), respectively. With the same reaction conditions, using $FeCl_2\cdot 3H_2O$ or $CrCl_3\cdot 6H_2O$ in place of $CoCl_2\cdot 6H_2O$, three isomorphous compounds: $[Fe^{III}_2Dy^{III}_2(\mathbf{L1})_2(\mathit{Me}\text{-}PhCO_2)_6(OH)_2]\cdot 2MeCN\cdot MeOH\cdot 3.35H_2O$ (**5**) and two $[Cr_2Ln_2(\mathbf{L1})_2(\mathit{Me}\text{-}PhCO_2)_6(OH)_2]\cdot 2MeCN$ [Ln = Dy (**6**) and Y (**7**)] have been obtained. Attempts to synthesize Fe^{III}-4f compounds using other iron salts were also made. The reaction of $H_2\mathbf{L1}$, $[Fe_3O(O_2CPh)_6(H_2O)_3](O_2CPh)$ and $Ln(NO_3)_3\cdot 6H_2O$ in MeCN in a molar ratio of 8:1:1 produced $[Fe^{III}Ln^{III}(H\mathbf{L1})_2(O_2CPh)_3(NO_3)]$ [Ln = Dy (**8**) and Y (**9**)] and the reaction of $H_2\mathbf{L1}$, $FeCl_3\cdot 6H_2O$, $Dy(NO_3)_3\cdot 6H_2O$ and $PhCO_2Na$ in MeOH in a molar ratio of 1:1:1:8 in presence of Et_3N produced a series of compounds: $[Fe^{III}_4Ln^{III}_4(\mathbf{L1})_2(PhCO_2)_{10}(O)_3(OH)_2(MeOH)_2(MeO)_2]\cdot 3MeOH\cdot xH_2O$ [Ln = Dy (**10**), x = 0; Tb (**11**), x = 1 and Y (**12**), x = 1].

All attempts to obtain 3d-4f clusters with H**L2** and H_2**L3** ligands were unsuccessful, but it was possible to synthesise homometallic *4f* clusters. The reaction of H_2**L1** or H**L2** or H_2**L3**, $Dy(NO_3)_3\cdot 6H_2O$ in MeCN and MeOH in a ratio of 2:3 in the presence of Et_3N produced related $[Dy_2(H\mathbf{L1})(NO_3)_4]$ (**13**), $[Dy_2(\mathbf{L2})(NO_3)_4]$ (**14**) and $[Dy_2(H\mathbf{L3})_2(NO_3)_4]$ (**15**), respectively.

In this chapter the synthesis, crystal structures and magnetic properties of the novel compounds (**1-15**) are presented.

3.2.1 Structures of $[Co^{III}_3Co^{II}_2Ln^{III}_2(OH)_2(PhCO_2)_6(dea)_4(Hdea)(NO_3)](NO_3)\cdot 3MeOH\cdot H_2O$ [Ln = Dy (1) and Gd (2)]

A full structure determination was performed for compound **1** using single crystal X-ray diffraction data. Compound **2** was found to be isomorphous with **1** which was confirmed by powder XRD (**Fig 3.2**). Therefore, only compound **1** is discussed here in detail. The compound **1** crystallizes in the $P2_1/c$ space group and the asymmetric unit contains two Dy^{III} ions, two Co^{II} ions, three Co^{III} ions, two OH^- groups, four doubly deprotonated $\mathbf{dea}^{2-}$, one mono-depronated $H\mathbf{dea}^-$, six benzoate ions, one coordinated NO_3^-, one free NO_3^-, three MeOH molecules and one water molecule (**Fig 3.1**).

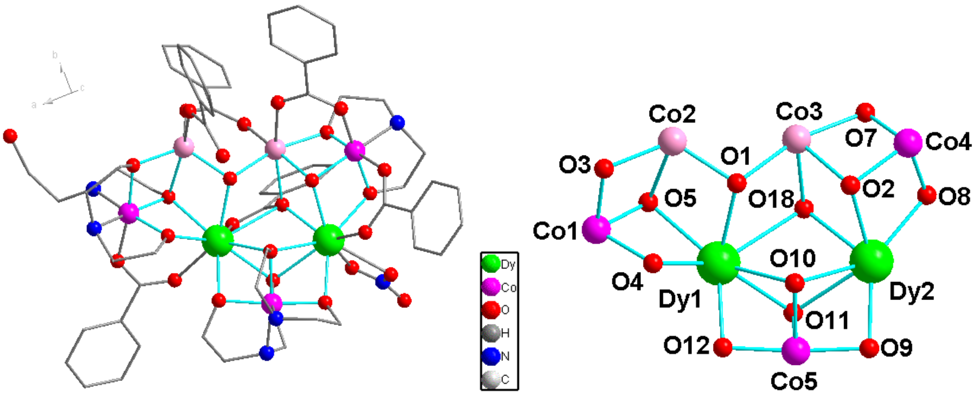

Fig 3.1 Molecular structure (left) and core (right) of compound **1**: pink, Co^{II}; purple, Co^{III}

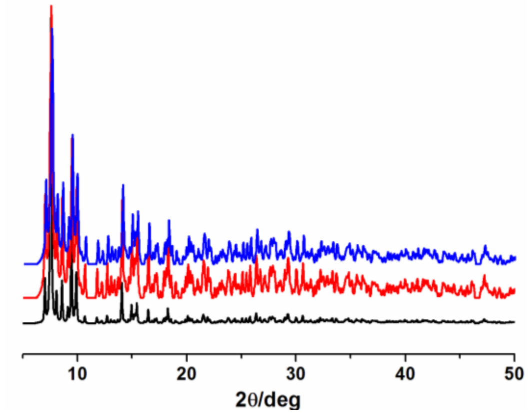

Fig 3.2 The XRD of **1** (red) and **2** (blue), simulated (black, based on Co_5Dy_2)

Both Dy^{III} ions (Dy1 and Dy2) adopt a nine coordinated distorted mono-capped square anti-prism geometry with an O9 donor set. The three Co^{III} ions adopt distorted octahedral geometry (N2O4 for Co1 and Co5, NO5 for Co3). One of the Co^{II} (Co3) ions also adopts distorted octahedral geometry with an O6 donor set, the other Co^{II} (Co2) has distorted square pyramidal geometry with an O5 donor set. The core of the structure can be illustrated as a combination of one small "boat" $\{Co^{III}Dy^{III}{}_2O4\}$ carried by four Co ions. Each Dy^{III} ion fixes one Co^{II} ion and one Co^{III} ion to give a defect cubane $\{Co^{III}Co^{II}Dy^{III}O4\}$ unit. The five ligands and five benzoate co-ligands adopt three different coordination modes (**Fig 3.1** and **Scheme 3.2**). Two ligands chelate Co5 and bridge Dy1 with Dy2 by a $\eta^3:\eta^1:\eta^2:\mu_3$ coordination mode (**Scheme 3.2**, a). One ligand chelates Co4 and bridges Co3 and Dy2 by two alkoxide O atoms with $\eta^2:\eta^1:\eta^2:\mu_3$ coordination mode (**Scheme 3.2**, b). One ligand with $\eta^2:\eta^1:\eta^2:\mu_3$ coordination mode (**Scheme 3.2**, b) and other one with $\eta^3:\eta^1:\eta^0:\mu_3$ (**Scheme 3.2**, c) chelate Co1 and bridge Co2 and Dy1. The benzoates adopt three different coordination modes in bridging and/or chelating metal ions (**Scheme 3.2**: d, e and f). The two OH^- ligands are μ_3 bridging and the two remaining coordinate sites of Dy2 are occupied by a chelating NO_3^-. The Co^{III}-O/N, Co^{II}-O and Dy-O bond distances vary from 1.865 (5) to 1.959 (7)Å, 1.960 (5) to 2.314 (4)Å and 2.291(4) to 2.556(4)Å, respectively.

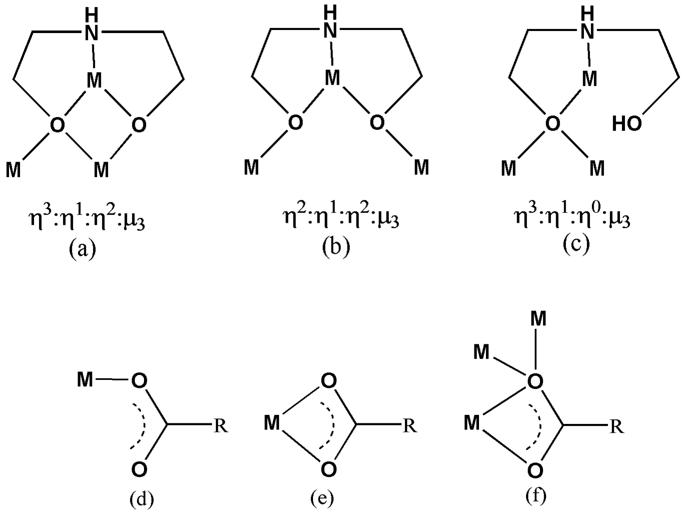

$\eta^3:\eta^1:\eta^2:\mu_3$ (a)

$\eta^2:\eta^1:\eta^2:\mu_3$ (b)

$\eta^3:\eta^1:\eta^0:\mu_3$ (c)

(d) (e) (f)

Scheme 3.1 The coordination modes of the H_2**dea** and benzoate ligands found in compound **1**

3.2.2 Magnetic properties of compounds 1 and 2

The temperature dependence of the magnetic susceptibilities of complexes **1** and **2**, were measured on powder samples in the temperature range 1.8-300 K under an applied dc magnetic field of 1000 Oe (**Fig 3.3**). The magnetic data of **1** and **2** are summarized in **Table 3.2**. The experimental χT values at 300 K, are a little larger than the expected theoretical ones for two non-interacting Co^{II} ions and two non-interacting Ln^{III} ions.[13] The χT products of compounds **1** and **2** follow a similar trend, remaining almost constant down to about 100 K and then decrease reaching 24.65 cm^3 K mol^{-1} (**1**) and 13.89 cm^3 K mol^{-1} (**2**) at 1.8 K. The initial slow decrease of the χT value at low temperature (100-25 K) is likely to result from gradual depopulation of the Stark sublevels, and the sharp fall below 25 K is due to intramolecular antiferromagnetic interactions and/or ZFS of Ln^{III} ions.

At 2 K, the field dependence of magnetization of **1** and **2** rapidly increases below 1 T and at higher fields, increases almost linearly and reaches the maximum value of 14.17 (**1**) and 15.39 μ_B (**2**) at 7 T without a true saturation (**Fig 3.4**), which indicates the presence of low lying energy states and/or anisotropy in the systems.[31]

Table 3.2 Magnetic data of compounds **1** and **2** summarized from the dc measurements

Compound	Ground state of Ln^{III} ion	χT expected for non-interacting ions per complex (cm^3 K mol^{-1})	χT measured at 300 K per complex (cm^3 K mol^{-1})	χT measured at 1.8 K per complex (cm^3Kmol^{-1})	Magnetization at 2 K and 7 T (Nβ)
$Co^{III}_3Co^{II}_2Dy^{III}_2$ (**1**)	$^6H_{15/2}$	32.09	39.25	24.65	14.17
$Co^{III}_3Co^{II}_2Gd^{III}_2$ (**2**)	$^8S_{7/2}$	19.51	21.53	13.89	15.39

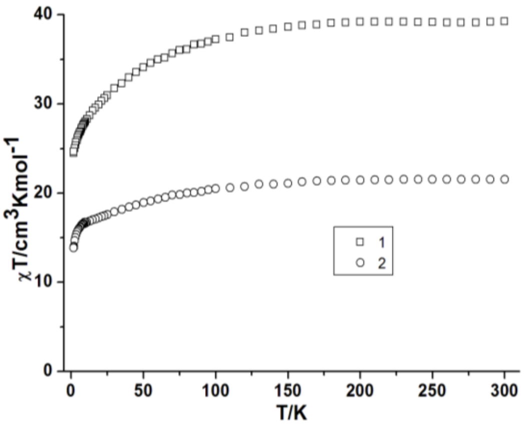

Fig 3.3 Plots of χT vs T of compounds **1** and **2** under applied 1000 Oe dc magnetic field

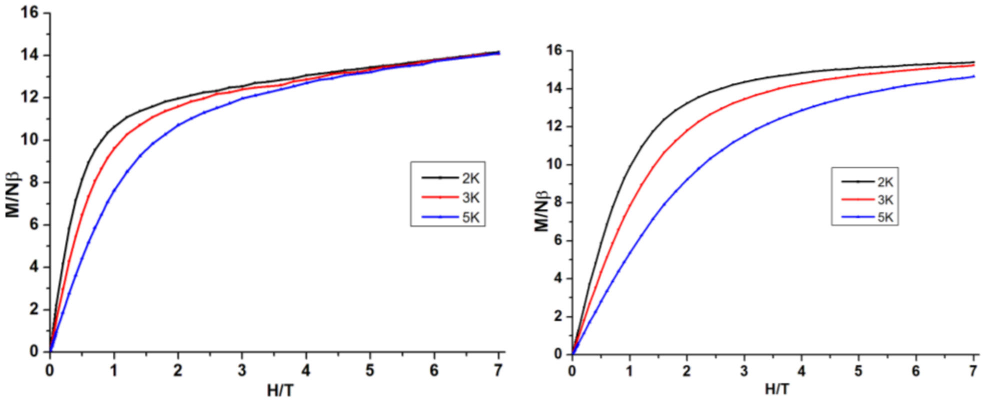

Fig 3.4 Plots of M vs H of compounds **1** (left) and **2** (right)

In order to explore their potential SMM behaviour, alternating current (ac) magnetic susceptibility studies were carried out on freshly filtered samples of compounds **1** and **2** (**Fig 3.5** and **3.6**). No out-of-phase signal (χ'') was observed even when a static dc field was applied, which indicates the absence of SMM behaviour within the measurement parameters of the SQUID.

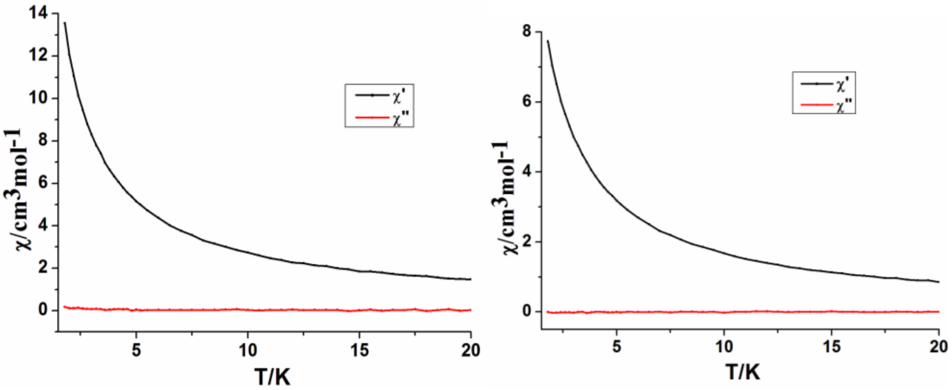

Fig 3.5 Plots of χ’ vs T and χ’’ vs T of compounds **1** (left) and **2** (right) (1000Hz)

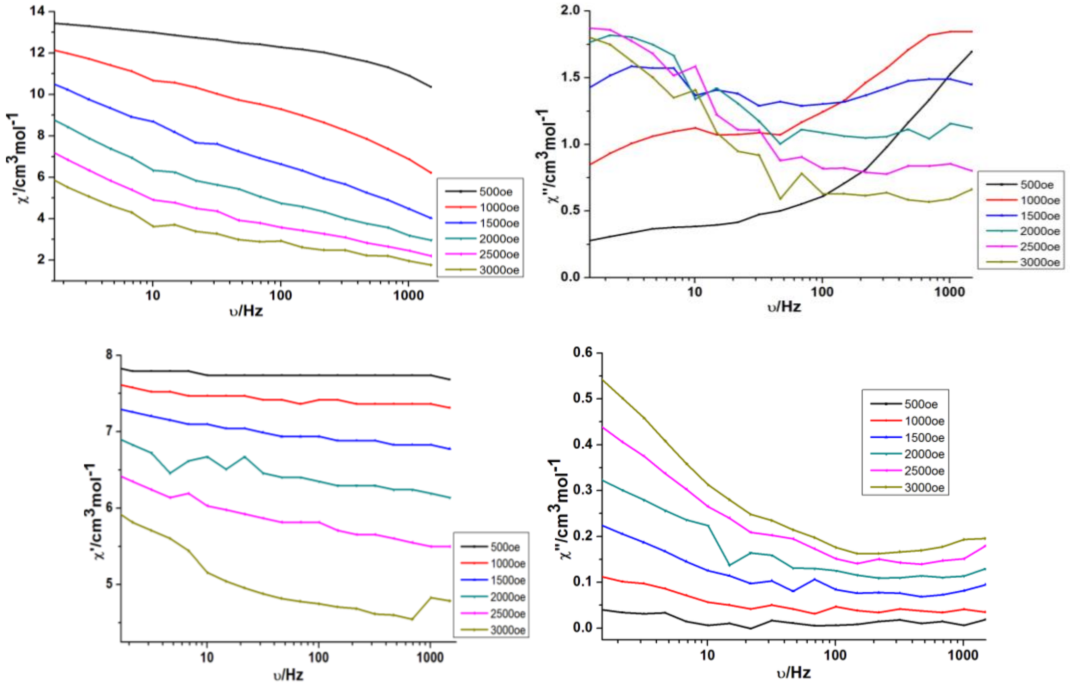

Fig 3.6 Plots of χ’ (left) and χ’’ (right) vs frequecy of compounds **1** (top) and **2** (bottom) at 1.8 K at indicated applied magnetic fields

3.2.3 Structures of $[\mathrm{Co^{III}}_3\mathrm{Dy}_3(\mathbf{L1})_3(\mu_3\text{-OH})_4(\mathrm{O_2CPh})_6(\mathrm{H_2O})_3]\cdot(\mathrm{O_2CPh})\cdot\mathrm{Cl}\cdot4\mathrm{MeOH}\cdot10\mathrm{H_2O}$ (3) and $[\mathrm{Co^{III}}_3\mathrm{Dy}_3(\mathbf{L1})_3(\mu_3\text{-OH})_4(\mathrm{O_2CPh}\text{-}Me)_6(\mathrm{H_2O})_3]\cdot2\mathrm{Cl}\cdot10\mathrm{MeOH}$ (4)

The compounds **3** and **4** are isostructural and differ from each other only in terms of counter anions and lattice solvent molecules. The powder XRD patterns are shown in **Fig 3.8**. Both compounds crystallize in triclinic space group (P-1). The asymmetric unit contains $\{\mathrm{Co^{III}}_3\mathrm{Dy^{III}}_3(\mu_3\text{-OH})_4\}$ units. Only the structure of **3** will be described here. The crystal structure of **3** consists of cationic entities $[\mathrm{Co^{III}}_3\mathrm{Dy^{III}}_3(\mathbf{L1})_3(\mu_3\text{-OH})_4(\mathrm{PhCOO})_6(\mathrm{H_2O})_3]^{2+}$ (**Fig 3.7**), chloride and benzoate anions for charge balance, and lattice solvent molecules. Each $\mathrm{Co^{III}}$ adopts distorted octahedral coordinate geometry with N2O4 donor sets. Each $\mathrm{Dy^{III}}$ adopts square-antiprism coordination geometry with O8 donor sets. The cationic cluster $[\mathrm{Co^{III}}_3\mathrm{Dy^{III}}_3(\mathbf{L1})_3(\mu_3\text{-OH})_4(\mathrm{PhCOO})_6(\mathrm{H_2O})_3]^{2+}$ is built from three $\mathrm{Dy^{III}}$ ions arranged in a triangular fashion with $\{\mathrm{Co^{III}}\mathbf{L1}^{2-}\}$ units on each edge of the triangle (**Fig 3.7**). Each mono-deprotonated ligand ($\mathbf{L1}^{2-}$) displays a $\eta^2:\eta^1:\eta^1:\eta^2:\mu_3$ coordination mode chelating one $\mathrm{Co^{III}}$ and bridging to two $\mathrm{Dy^{III}}$ ions (**Scheme 3.3**, a). One of the four μ_3-OH groups bridges the three $\mathrm{Dy^{III}}$ ions giving a central $\{\mathrm{Dy^{III}}_3(\mathrm{OH})\}$ unit. Each of the other three μ_3-OH groups connects a $\{\mathrm{Co^{III}}\mathbf{L1}^{2-}\}$ to this triangular $\{\mathrm{Dy^{III}}_3(\mathrm{OH})\}$ unit. Three of the benzoates display *syn syn* coordination modes bridging one $\mathrm{Co^{III}}$ and one $\mathrm{Dy^{III}}$ (**Scheme 3.3**, c). The other three benzoates are coordinating each $\mathrm{Dy^{III}}$ ion by one oxygen atom, and along with three water ligands complete the square anti-prism coordination geometry of the $\mathrm{Dy^{III}}$ ions (**Scheme 3.3**, b). The Co-N/O and Dy-O distances are in the range 1.859(4)-1.937(4)Å and 2.273(3)-2.470(3)Å, respectively.

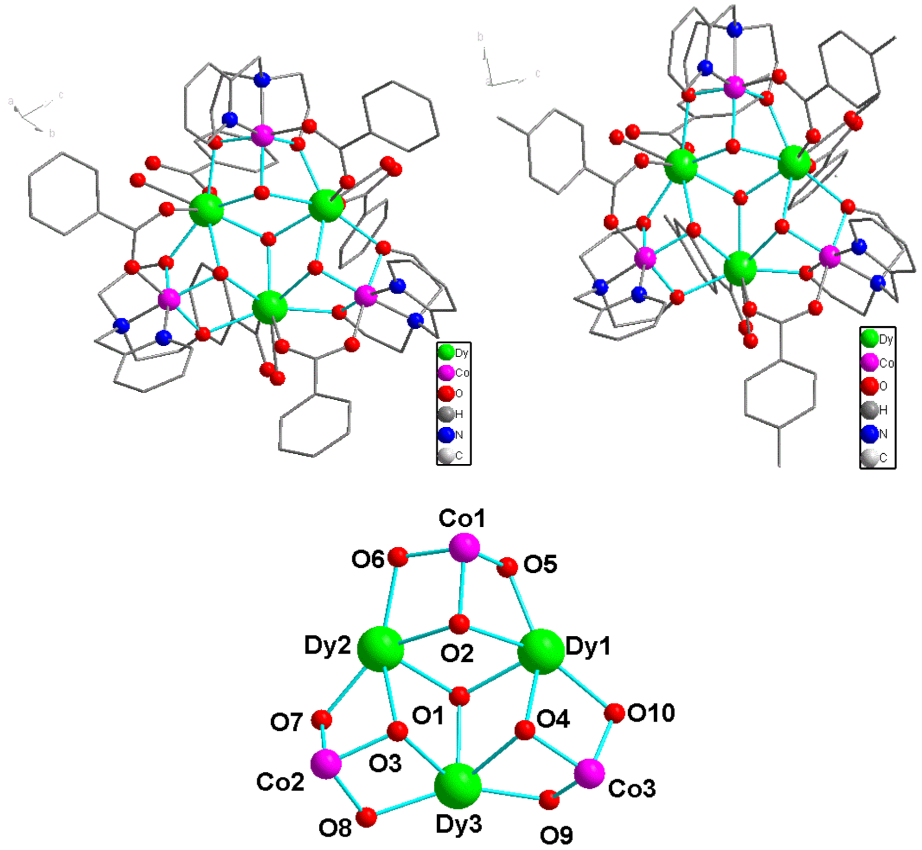

Fig 3.7 Molecular structure of **3** (up left), **4** (up right), and core (down) of compounds **3** and **4**

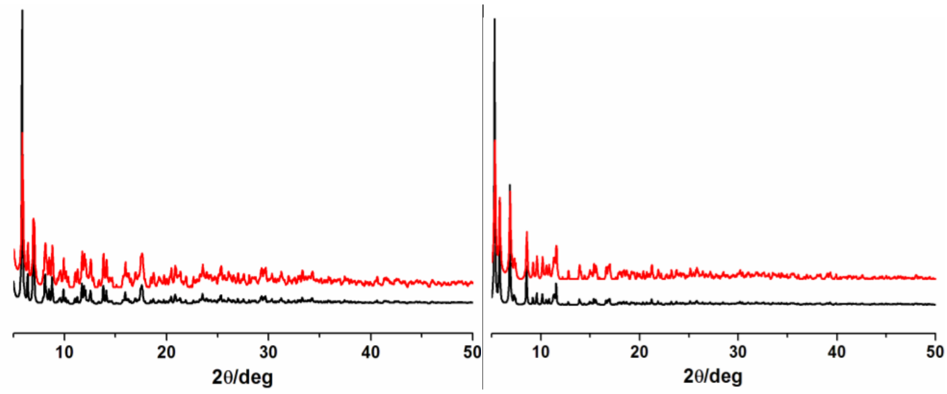

Fig 3.8 The XRD of compounds **3** (left) and **4** (right): simulated (black), experimental (red)

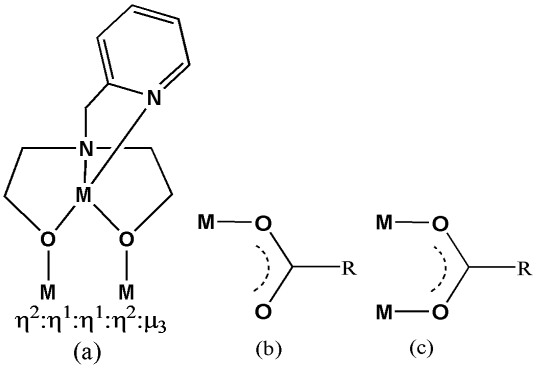

Scheme 3.3 The coordination mode of the H_2**L1** and benzoate ligands found in compound **3** and **4**

3.2.4 Magnetic properties of compounds 3 and 4

The direct-current (dc) magnetic susceptibilities of **3** and **4** were measured in the 1.8-300 K temperature range under an applied magnetic field of 1000 Oe. The obtained data for all studied compounds are summarized in **Table 3.3** and shown as χT vs T plots in **Fig 3.9**. The χT values for **3** and **4** of 40.56 and 40.99 cm^3 K mol^{-1} at 300 K are compatible with the calculated values of 42.51 cm^3 K mol^{-1} for three non-coupled Dy^{III} ions, respectively, in the free-ion approximation. On cooling, the χT product remains essentially constant from 300 K to ~100 K and then drops sharply to reach a value of 11.40 and 13.66 cm^3 K mol^{-1} at 2 K for **3** and **4**, respectively. Such a decrease of the χT product at low temperature is mainly due to depopulation of the excited M_J states of the Dy^{III} ions and/or weak antiferromagnetic interactions between the metal cores.

For the compounds **3** and **4**, the magnetisation at 2 K reaches values of 15.07, and 16.41 Nβ, respectively, under an applied field of 7 T but does not show any sign of saturation (**Fig 3.10**), suggesting the existence of significant magnetic anisotropy and/or low lying excited states in **3** and **4**.[32]

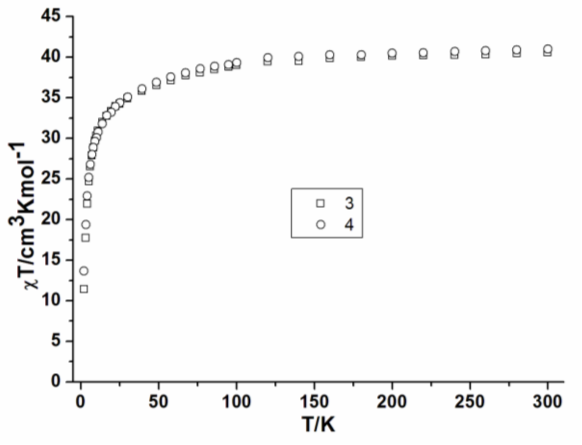

Fig 3.9 Plots of χT vs T of compounds **3** and **4**

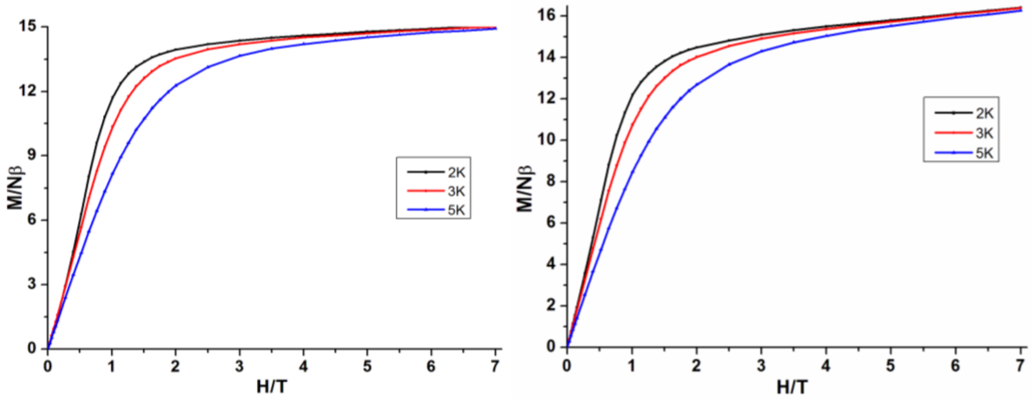

Fig 3.10 Plots of M vs H of compounds **3** (left) and **4** (right)

Table 3.3 Magnetic data of compounds **3** and **4** summarized from the dc measurements

Compound	Ground state of Ln^{III} ion	χT expected for non-interacting ions per complex (cm^3Kmol^{-1})	χT measured at 300 K per complex (cm^3Kmol^{-1})	χT measured at 1.8 K per complex (cm^3Kmol^{-1})	Magnetization at 2 K and 7 T (Nβ)
$Co^{III}_3Dy^{III}_3$ (**3**)	$^6H_{15/2}$	42.51	40.56	11.40	15.07
$Co^{III}_3Dy^{III}_3$ (**4**)	$^6H_{15/2}$	42.51	40.99	13.66	16.41

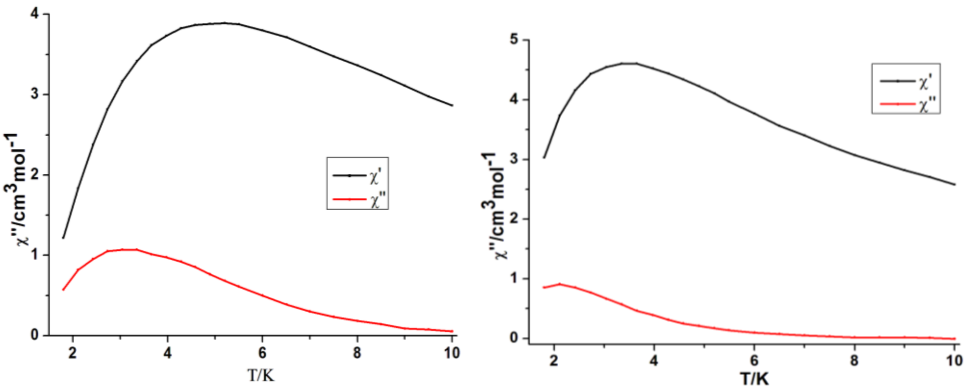

Fig 3.11 Plots of χ' vs T and χ'' vs T of compounds **3** (left) and **4** (right) (1000Hz)

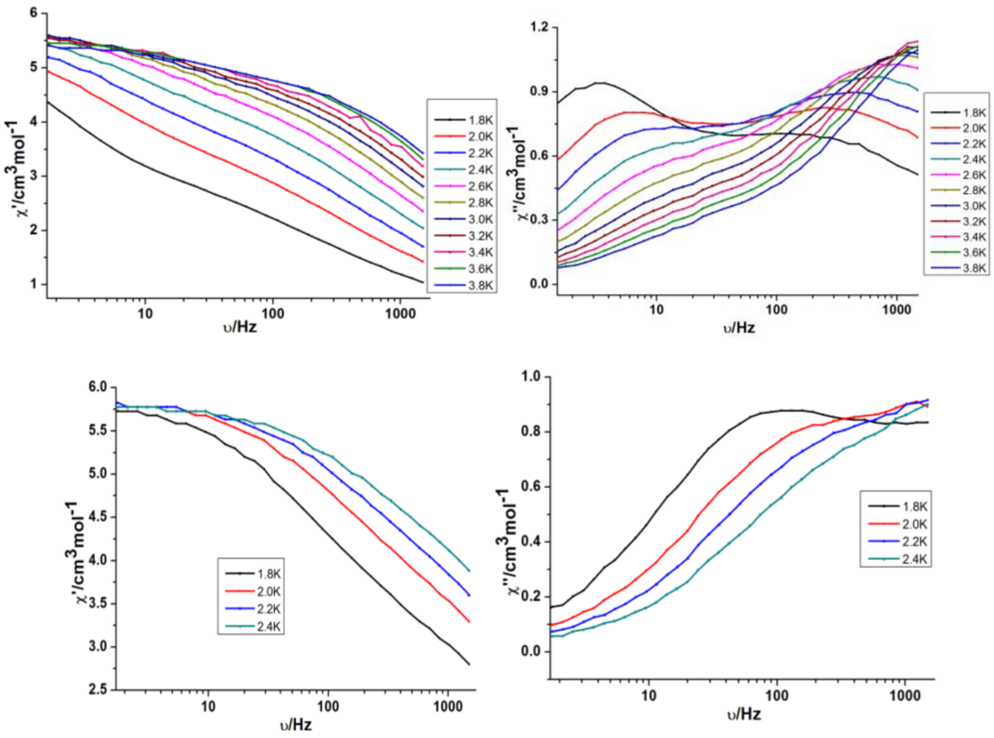

Fig 3.12 Plots of χ' (left) and χ'' (right) vs frequency of compounds **3** (up) and **4** (down)

In order to explore potential SMM behaviour alternating current (ac) magnetic susceptibility studies were carried out on freshly filtered samples of compounds **3** and **4**. Under zero dc field, as shown in **Fig 3.11**, an obvious temperature-dependent ac signal is detected for compounds **3** and **4**, indicating slow relaxation of magnetization expected for a single-molecule magnet. The χ'' (T) plots show broad peaks (2-8 K for **3**, and 2-4 K for **4)** which mean there maybe multiple relaxation pathways in these complexes. The non-vanishing of ac susceptibility at low temperatures indicate there maybe quantum tunnelling of the magnetization often observed in lanthanide SMMs.[33] Furthermore, the χ'' (ν) plot of compound **3** clearly shows the occurrence of two distinct peaks in the out-of-phase ac signals, which demonstrates the possible occurrence of two relaxation processes. For instance, the χ'' versus frequency plot at 2.0 K clearly shows two peaks, which are centred at 10 and 570 Hz, respectively (**Fig 3.12**). However, it is not possible to extract the energy barrier of compound **3** from these data as the peaks are very broad. For compound **4**, slow relaxation of magnetization was observed only over a short range of temperature, and no maximum of χ'' is observed in the frequency window technically available. Thus we cannot determine the energy barrier and corresponding relaxation time. A small dc field was applied to see whether relaxation would slow down due to the possible presence of a quantum relaxation pathway for compounds **3** and **4**. The relaxation mode is indeed almost unchanged under a small dc field (**Fig 3.13**). This observation shows that the relaxation mechanism of this SMM, at least above 1.8 K, is not influenced much by quantum effects.

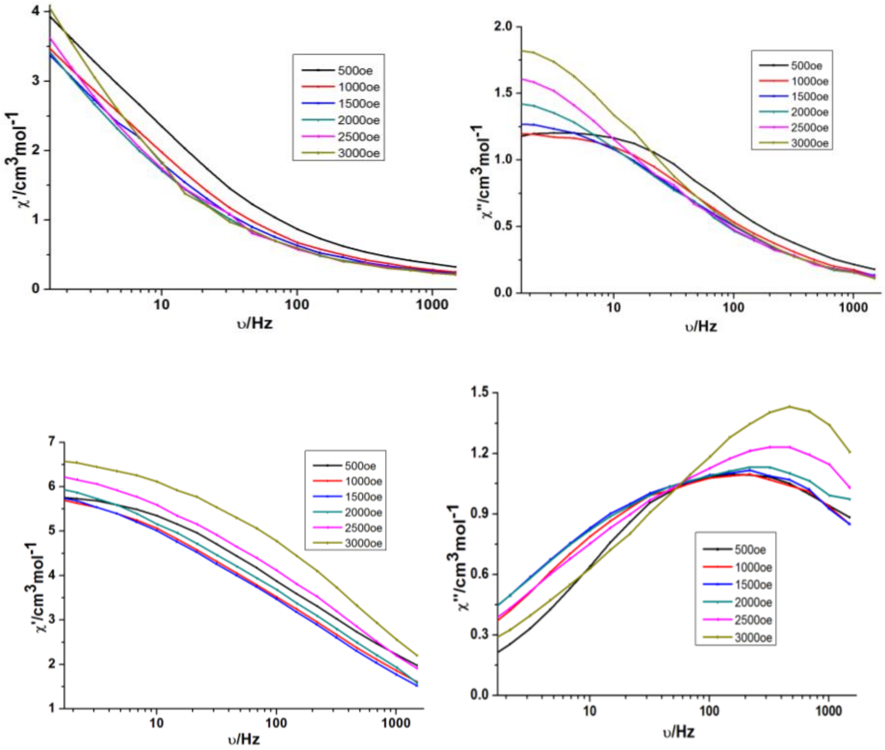

Fig 3.13 Plots of χ' (left) and χ'' (right) vs frequency of compounds **3** (up) and **4** (bottom) at 1.8 K at indicated applied magnetic fields (1000 Hz)

3.2.5 Structure of $[Fe_2Dy_2(L1)_2(\mathit{Me}\text{-}PhCO_2)_6(OH)_2]\cdot 2MeCN\cdot MeOH\cdot 3.35H_2O$ (5)

Compound **5** crystallizes in the monoclinic space group $P2_1/n$ with the asymmetric unit consisting of two Dy^{III} and Fe^{III} ions (**Fig 3.14**) and phase purity was confirmed from powder diffraction patterns (**Fig 3.15**). The compound is neutral and could be best described as a planar butterfly motif with the two Fe^{III} ions occupying the body positions and the Dy^{III} ions the outer wing-tips. The core is stabilized by two μ_3-OH^- ligands, both bridging to two Fe^{III} ions and one Dy^{III} ion. Around the periphery of the cluster are six benzoate ligands. Four of them display *syn syn* coordination modes, bridging an Fe^{III} to a Dy^{III} ion (**Scheme 3.4**, b), the other two display a chelating coordination mode and are coordinated to the two Dy^{III} ions (**Scheme 3.4**, c). There are also two doubly deprotonated **L1**$^-$ ligands, both displaying the η^2:η^2:η^1:η^1:μ_3 (**Scheme 3.4**, a) coordination mode with the pyridine N and imine N atoms coordinating to a wing-tip Dy^{III} ion and the O-atoms bridging from the Dy^{III} to the body Fe^{III} ions. The two Fe^{III} ions are six coordinate with octahedral geometries with an average Fe-O bond length of 2.007Å. The two Dy^{III} ions are nine coordinate with mono-caped square antiprismatic geometries with an average Dy-O/N bond length of 2.435Å. The 3d···3d distance is 3.232(4)Å, while the intramolecular Dy···Dy distance is 6.014(8)Å. The closest intermolecular Dy···Dy distance is 7.772(14)Å.

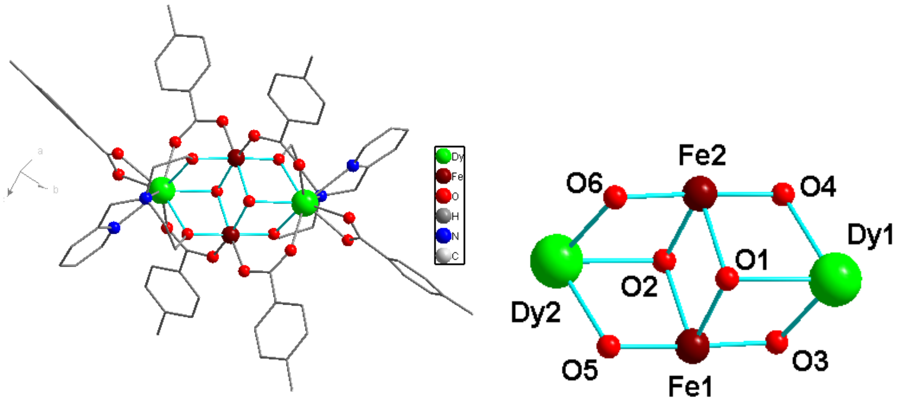

Fig 3.14 The molecular structure (left) and core (right) of compound **5**

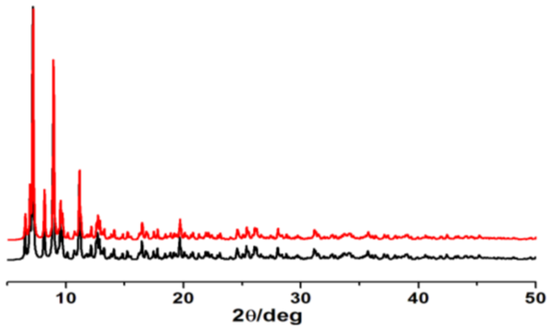

Fig 3.15 The XRD of compound **5**: Simulated (black), experimental (red)

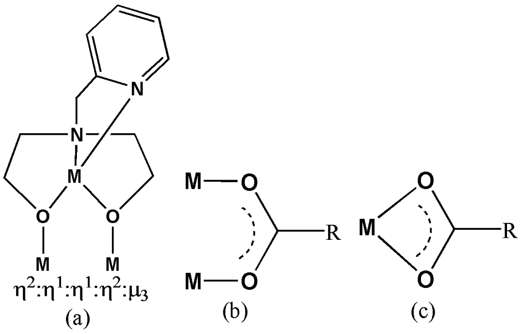

Scheme 3.4 The coordination modes of the H_2**L1** and benzoate ligands found in compound **5**

3.2.6 Magnetic properties of compound 5

Direct-current (dc) magnetic susceptibility studies on **5** were carried out under an applied magnetic field of 1000 Oe in the 300-1.8 K temperature range (**Fig 3.15**). The room temperature χT values of 35.96 cm^3 K mol^{-1} are in good agreement with the expected value (36.84 cm^3 K mol^{-1}) for two high-spin Fe^{III} ions with S = 5/2, g = 2, and C = 4.37 cm^3 K mol^{-1} and two Dy^{III} ions with S = 5/2, L =5, $^6H_{15/2}$, g = 4/3 and C = 14.17 cm^3 K mol^{-1}. The compound shows a steady decrease of its χT product on decreasing the temperature from 300 to 100 K, and then a more rapid decrease from 100 to 1.8 K, reaching a value for χT of 25.0 cm^3 K mol^{-1}, suggesting that antiferromagnetic interactions between paramagnetic centres are present in this molecule. The thermal depopulation of the Dy^{III} excited states, the sublevels of the $^6H_{15/2}$ state, is also partially responsible for the continuous decrease of χT below 100 K.[34] The field dependence of the magnetization of **5** was performed at fields ranging from 0 to 7 T at 2, 4 and 5 K (**Fig 3.16**). At higher fields, the magnetization increases linearly without clear saturation to ultimately reach 11.90 μ_B (H = 7 T, at 2K). The lack of saturation of the magnetization for complex **5** suggests the presence of magnetic anisotropy and/or low-lying excite states.

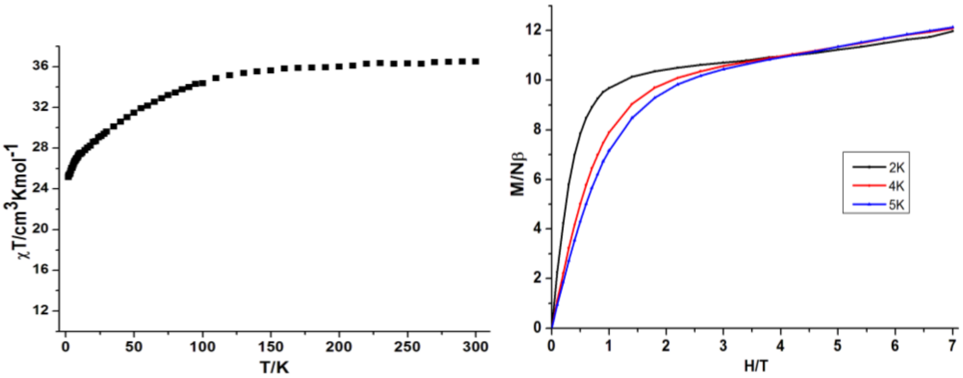

Fig 3.16 Plot of χT vs T (left) and M vs H (right) of compound **5**

To probe slow magnetization relaxation, ac magnetic measurements were carried out. Under zero applied dc field, significant quantum tunnelling of the magnetization (QTM) was observed for **5**, preventing the occurrence of full peaks. However, by applying a dc field, the QTM was minimized, revealing full peaks in the out-of-phase (χ'') signals as shown in **Fig 3.17**. The optimum applied dc field, where the minimum of the characteristic frequency was observed, was determined to be H_{dc} = 1000 Oe. The presence of peaks that shift to lower frequency as the temperature decreases is indicative of slow magnetization relaxation (**Fig 3.18**). The anisotropic energy barrier was obtained from a fitting using the Arrhenius equation ($\iota = \iota_0 \exp(U_{eff}/k_BT)$), which resulted in U_{eff} = 16.2 K ($\iota_0 = 2.76 \times 10^{-6}$ s) (**Fig 3.19**). This value is very close to the value obtained for the previously reported compound $[\mathrm{DyFe_2Dy(\mu_3\text{-}OH)_2(H\mathbf{tea})_2(\mathit{p}\text{-}\mathit{Me}\text{-}PhCO_2)_6}]$ (U_{eff} = 24.0K, 1.71×10^{-7} s),[35] which has a small modification in the ligand system. From these results we have reasoned that the difference in magnetic behaviour observed between compound **5** and the reported one is a result of contribution from the ligand donor atoms. Such behaviour is similar to that observed in the literature, where a reduced electron density along the hard axis leads to a more anisotropic $\mathrm{Dy^{III}}$ ion and higher energy barrier for the relaxation of magnetization.[36] However, what we observe here is an opposite effect. Introducing an electron withdrawing substituent in para position of the benzoic ring leads to smaller energy barriers. The reason for such different behaviour in compounds **5** and the previously reported one could be that in these compounds the position of N and O atoms is not along a hard axis. On the other hand, in the reported Fe_2Dy_2 series,[37] not only is a position of an atom changed, but about fifty percent of the $\mathrm{Dy^{III}}$ ion surface area is coordinated by carboxylate ligands and thus affected by the electronic density alteration on the carboxylate oxygens. Therefore, such studies and observations are not safe to be taken as a rule for the generation of improved SMMs.

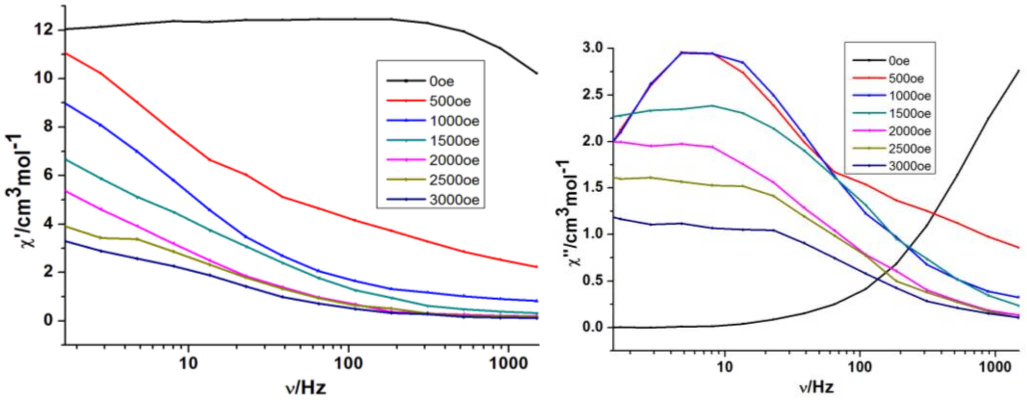

Fig 3.17 Plots of χ' (left) and χ'' (right) vs frequency of compound **5** at 1.8 K at indicated applied magnetic fields

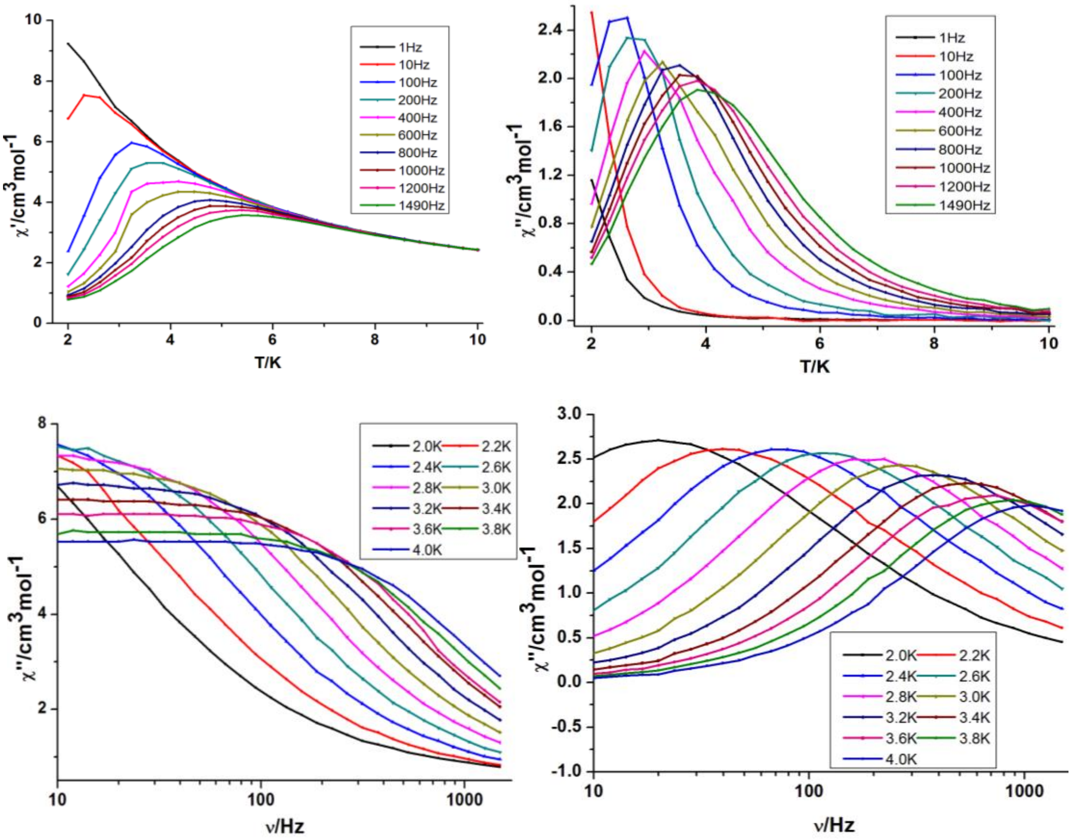

Fig 3.18 Plots of χ' (left) and χ'' (right) vs T (up) at indicated frequencies; plots of χ' (left) and χ'' (right) vs frequency (down) of compound **5** at 1.8 K at different temperatures in 1000 Oe dc field

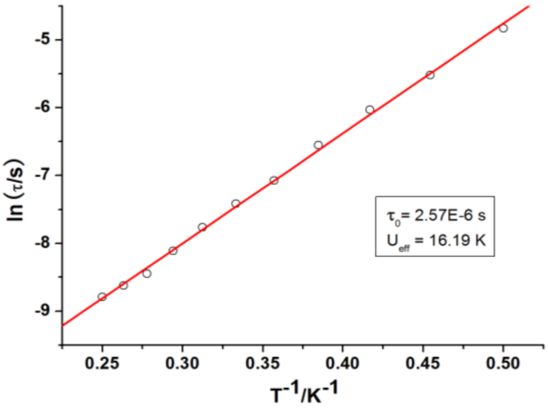

Fig 3.19 τ vs T^{-1} plot of compound **5** in 1000 Oe dc field

3.2.7 Structures of $[Cr_2Ln_2(L1)_2($*Me*-$PhCO_2)_6(OH)_2]\cdot 2MeCN$ [Ln = Dy (6) and Y (7)]

The tetranuclear Cr_2Ln_2 compounds **6** and **7** are isostructural, crystallizing in the space group C2/c. The compound **6** is fully crystallographically characterized while for the **7** the unit cell and powder XRD were checked (**Fig 3.21**). The structures of **6** and **7** are isostructural with **5** which have been described above, and their structures will not be described in detail here.

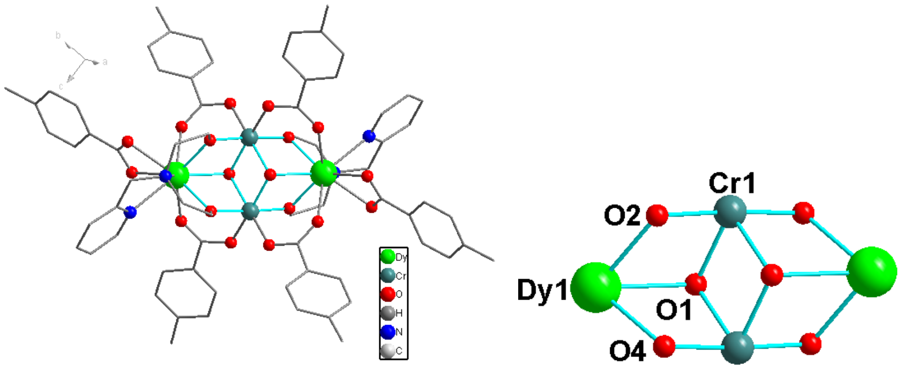

Fig 3.20 The molecular structure (left) and core (right) of compound **6**

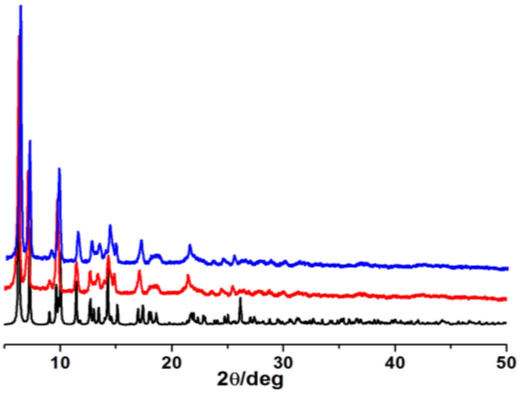

Fig 3.21 The XRD of compounds **6** (red) and **7** (blue)**:** simulated (black, based on Cr_2Dy_2)

3.2.8 Magnetic properties of compounds 6 and 7

Direct-current (dc) magnetic susceptibility measurements of compounds **6** and **7** have been carried out in an applied magnetic field of 1000 Oe in the 300-1.8 K temperature range. The obtained dc data for both compounds are summarized in **Table 3.4**. The χT versus T data, where χ is the molar magnetic susceptibility, are shown in **Fig 3.22**. At 300 K, the experimental χT value of **6** (27.19 cm^3 K mol^{-1}) is smaller than the expected value (32.09 cm^3 K mol^{-1}) for two spin-only Cr^{III} ions and two Dy^{III} ions, suggesting the presence of dominant antiferromagnetic exchange, which was reported in similar Fe-4f clusters.[38] The χT product remains essentially constant over the whole temperature range, reaching a minimum value of 23.00 cm^3 K mol^{-1} at 1.8 K. This behaviour is typically observed when antiferromagnetic interactions between magnetic ions are dominant. Nevertheless, the thermal depopulation of the Dy^{III} excited states, the Stark sublevels of the $^6H_{15/2}$ state,[34] may be partially responsible for the decrease of χT below 100 K. The theoretical and experimental χT values for compound **7** at room temperature are very close, which means that the interaction between Cr^{III}-Cr^{III} is very weak antiferromagnetic or very weak ferromagnetic coupling.

The field dependence of the magnetization of **6** and **7** was performed at fields ranging from 0 to 7 T at 2 and 5 K. At higher fields, M increases linearly without clear saturation to ultimately reach 16.64 μ_B and 6.96 μ_B (H = 7 T, at 2 K) for **6** and **7**, respectively. The lack of saturation of the magnetization for **6** and **7** suggests the presence of magnetic anisotropy within both compounds (**Fig 3.23**).

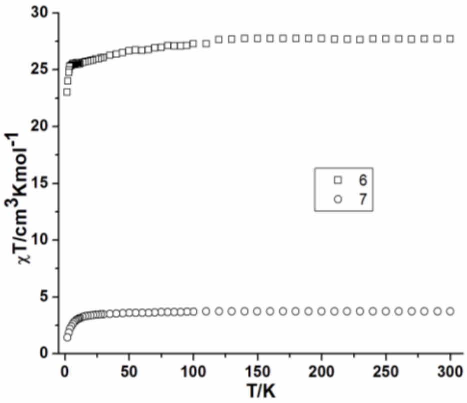

Fig 3.22 Plots of χT vs T of compounds **6** and **7**

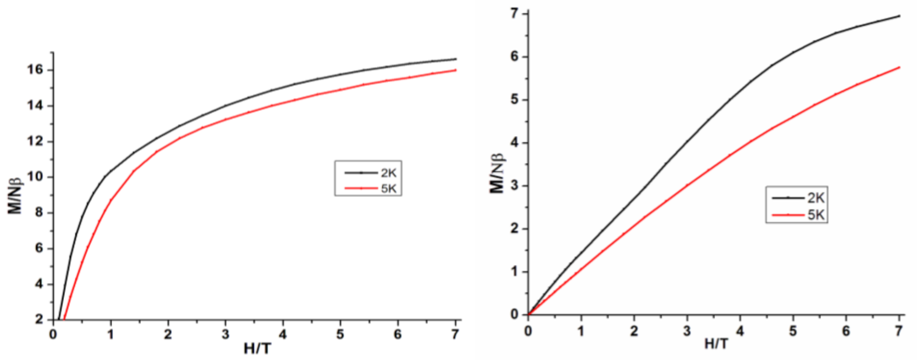

Fig 3.23 Plots of M vs H of compounds **6** (left) and **7** (right) at indicated temperatures

Table 3.4 Magnetic data of compounds **6** and **7** summarized from the dc measurements

Compound	Ground state of Ln^{III} ion	χT expected for non-interacting ions per complex (cm^3 K mol^{-1})	χT measured at 300 K per complex (cm^3 K mol^{-1})	χT measured at 1.8 K per complex (cm^3 K mol^{-1})	Magnetization at 2 K and 7 T (Nβ)
$Cr^{III}_2Dy^{III}_2$ (**6**)	$^6H_{15/2}$	32.09	27.69	23.00	16.64
$Cr^{III}_2Y^{III}_2$ (**7**)		3.75	3.73	1.44	6.96

To probe potential slow magnetization relaxation, ac magnetic measurements were carried out for **6**, no out-of-phase signal (χ'') was observed even after a static dc field (**Fig 3.24** and **3.25**) was applied, indicating the absence of SMM behaviour within the measurement parameters of the

SQUID.

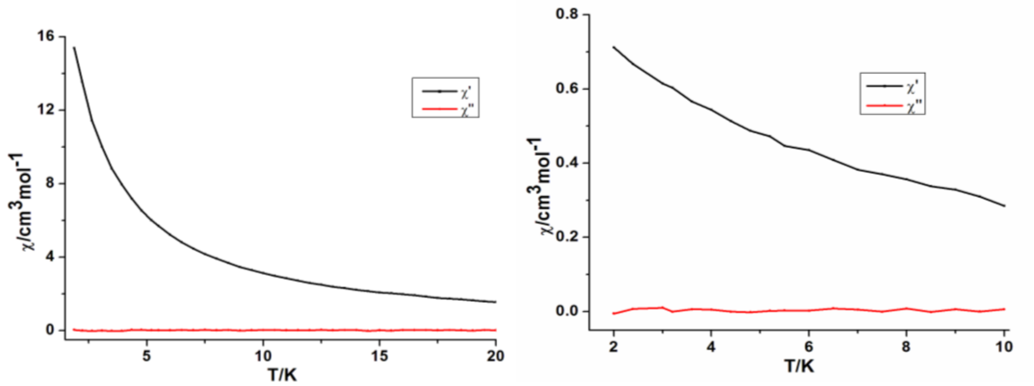

Fig 3.24 Plots of χ’ and χ’’ vs T of compounds **6** (left) and **7** (rignt) at 1000 Hz and zero-applied dc field

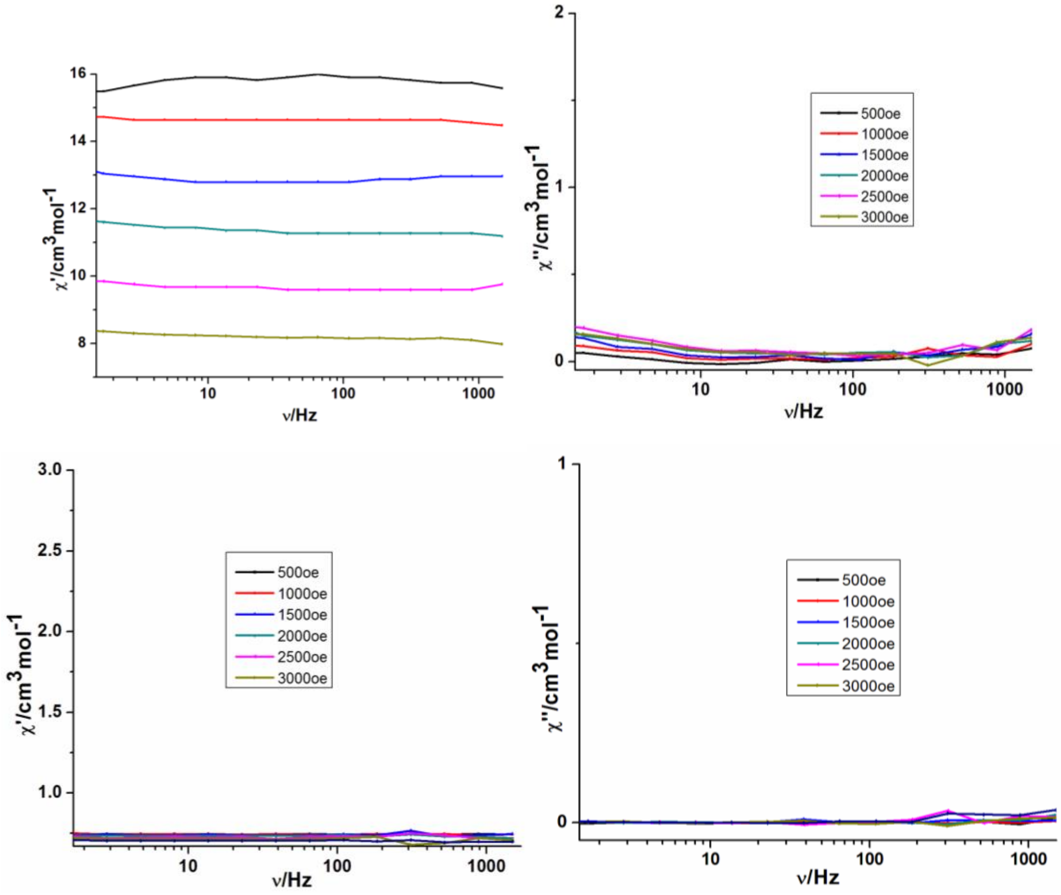

Fig 3.25 Plots of χ’ (left) and χ’’ (right) vs frequency of compounds **6** (up) and **7** (down) at 1.8 K at different dc fields

3.2.9 Structures of [FeLn(HL1)$_2$(O$_2$CPh)$_3$(NO$_3$)] [Ln = Dy (8) and Y (9)]

Full structure determination was performed for compound **9** using single crystal X-ray diffraction (**Fig 3.26**). Compound **8** was found to be isomorphous with **9** which confirmed by powder XRD analysis (**Fig 3.27**). Therefore, only compound **9** will be presented here in detail.

Compound **9** crystallizes in the monoclinic space group $P2_1/c$. The asymmetric unit contains one Fe^{III} ion, one Y^{III} ion, two mono-protonated ligands (**L1**$^{2-}$), three benzoates and one chelating nitrate (NO_3^-) (**Fig 3.26**). The Fe^{III} ion displays distorted octahedral geometry with an N2O4 donor set while the Y^{III} ion displays a nine coordinate distorted mono capped square antiprism geometry with an N2O7 donor set. Both Fe^{III} and Y^{III} ions are chelated by one mono-protonated ligand (**L1**$^-$) which displays a $\eta^2:\eta^1:\eta^1:\eta^0:\mu_2$ coordination mode (**Scheme 3.5**, a), One deprotonated alkoxy O from each ligand acts as a bridge between the Y and Fe ions (**Scheme 3.5**, b). The fifth coordination site of the Fe^{III} ion is taken by an oxygen atom of a bridging benzoate between the Fe^{III} and Dy^{III} ions (**Fig 3.26**). The final coordination site of the Fe^{III} is from one monodentate O of a benzoate. The coordination sphere of the Y^{III} ion is completed by two O-atoms of a chelating nitrate and a monodentate O from a benzoate. The Y-O/N bond distances vary from 2.281(2) to 2.654(3)Å, while the Fe-O/N bond distances vary from 1.911(2) to 2.270(3)Å. The Fe···Y distance is 3.3960(7)Å, and Fe1-O-Y1 bridging angles are 105.33(11) and 104.27(11)°. There are no π-π stacking interactions between the aromatic parts of the ligands.

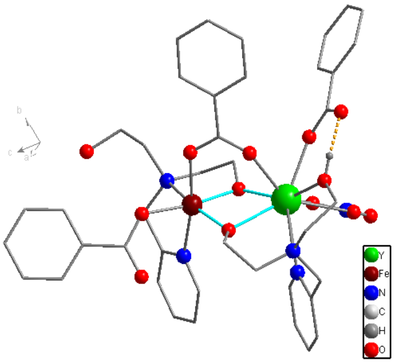

Fig 3.26 The structure of compound **9**

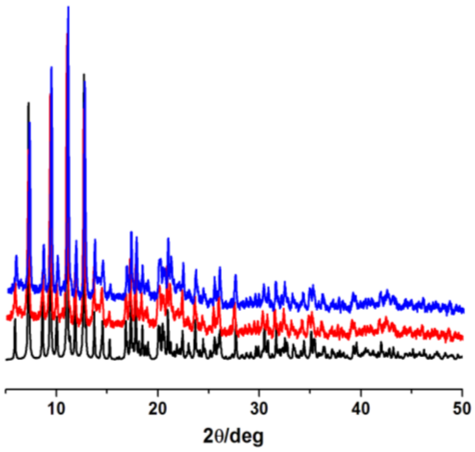

Fig 3.27 The XRD of compounds **8** (red) and **9** (blue): simulated (black)

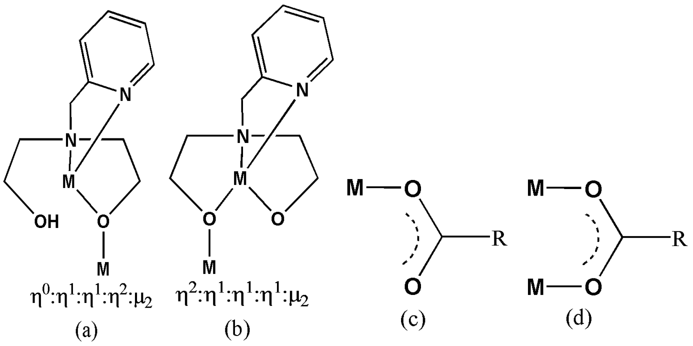

Scheme 3.5 The coordination modes of the H_2**L1** and benzoate ligands found in compound **9**

3.2.10 Magnetic properties of 8 and 9

The temperature dependence of the magnetic susceptibility was measured on powdered samples of **8** and **9** in the temperature range 1.8-300 K under an applied dc magnetic field of 1000 Oe (**Fig 3.28**). The obtained dc data for all studied compounds are summarized in **Table 3.5**. The experimental χT value (17.62 cm^3 K mol^{-1}) at 300 K, is slightly lower than the theoretical value (18.54 cm^3 K mol^{-1}) for one Dy^{III} and one Fe^{III} as non-interacting ions. The χT product of **8** slowly decreases on decreasing temperature to reach a value of 16.82 cm^3 K mol^{-1} at 25 K, after which it rapidly increases to 20.24 cm^3 K mol^{-1} at 1.8 K. This type of behaviour (increase below 25 K) suggests the presence of intramolecular weak ferromagnetic couplings between the Fe^{III} and Dy^{III} ions. The decrease of the χT product in the high temperature range is more likely due to the depopulation of Stark sublevels of the Dy^{III} ion. The field dependence of the magnetization at low temperatures (**Fig 3.29**) reveals that the magnetization has a relatively rapid increase below 1 T and then follows a steady increase up to 7 T. The M value at 7 T is 11.69 μ_B, lower than the expected value of 15.4 μ_B, indicating a lack of saturation. Such behaviour indicates the presence of magnetic anisotropy and/or low-lying excited states.

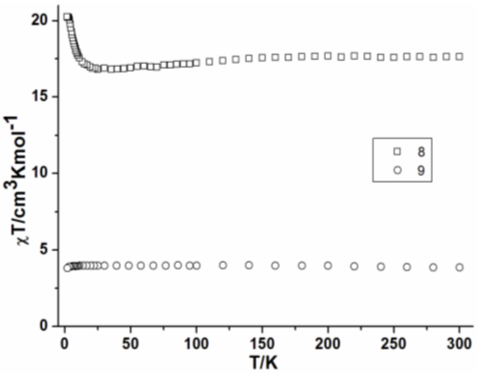

Fig 3.28 Plots of χT vs T of compounds **8** and **9** at 1000 Oe

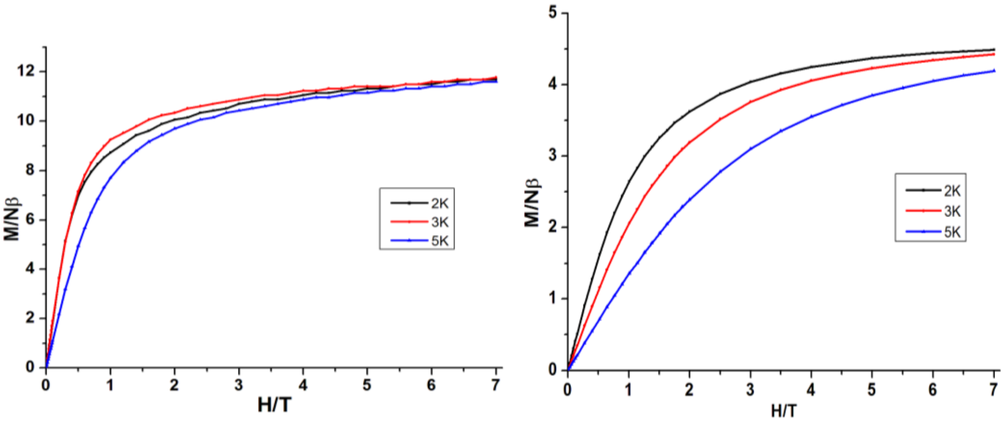

Fig 3.29 Plots of M vs H of compounds **8** (left) and **9** (right) at indicated temperatures

Table 3.5 Magnetic data of compounds **8** and **9** summarized from the dc measurements

Compound	Ground state of Ln^{III} ion	χT expected for non-interacting ions per complex (cm^3Kmol^{-1})	χT measured at 300 K per complex (cm^3Kmol^{-1})	χT measured at 1.8 K per complex (cm^3Kmol^{-1})	Magnetization at 2 K and 7 T (Nβ)
$Fe^{III}Dy^{III}$ (**8**)	$^6H_{15/2}$	18.545	17.62	20.24	11.69
$Fe^{III}Y^{III}$ (**9**)		4.375	3.85	3.81	4.49

Ac measurements did not show any out-of-phase signals indicating the absence of SMM behaviour in these two compounds even at applied dc fields (**Fig 3.30** and **3.31**)

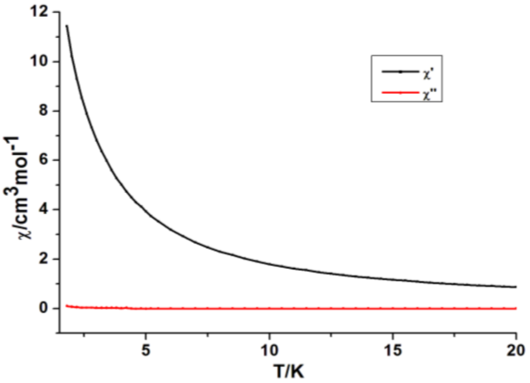

Fig 3.30 Plots of χ' vs T and χ'' vs T of compound **8** at 1000 Hz

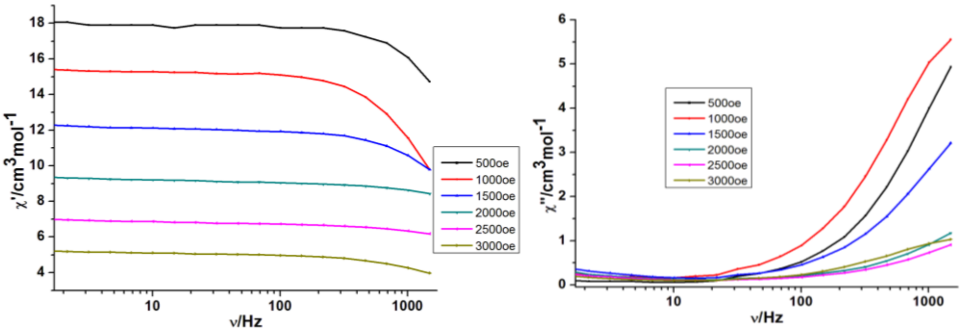

Fig 3.31 Plots of χ' (left) and χ'' (right) vs frequency of compound **8** at 1.8 K at indicated applied magnetic fields

3.2.11 Structures of $[Fe_4Ln_4(L1)_2(PhCOO)_{10}(\mu_4\text{-}O)_3(\mu_3\text{-}OH)_2(MeOH)_2(MeO)_2]\cdot 3MeOH\cdot xH_2O$ [Ln = Dy (10), x = 0; Tb (11), x = 1 and Y (12), x = 1]

Compounds **10-12** are isomorphous (confirmed by the unit cell constants and powder XRD patterns) **(Fig 3.33)**, hence only the structure of **10** is described here. Compound **10** crystallizes in the monoclinic space group $P2_1/n$. The asymmetric crystallographic unit contains four Fe^{III} ions, four Dy^{III} ions, two doubly deprotonated ligands (**L2**$^{2-}$), ten benzoates, three μ_4-O^{2-}, two μ_3-OH^-, two μ_3-MeO^- and two MeOH molecules (**Fig 3.32**). Two of the Fe^{III} ions (Fe1 and Fe2) adopt a distorted octahedral geometry with an N2O4 donor set. The atoms Fe3 and Fe4 have an environment of six oxygen atoms. All Dy^{III} ions adopt an O9 coordination environment which can be best described as a capped square anti-prism. The internal part of the metal core is supported by three μ_4-O^{2-}, two μ_3-OH^-, two μ_3-MeO^- and four deprotonated alkoxy O atoms from two ligands. The external periphery of the cluster consists of two doubly deprotonated ligands, ten benzoates and two MeOH molecules. Each of the ligands, **L1**, adopts the $\eta^2:\eta^2:\eta^1:\eta^1:\mu_3$ coordination mode chelating one external Fe^{III} and bridging two Dy^{III} ions with two deprotonated alkoxy groups (**Scheme 3.6**, a). Eight of the ten benzoates display the *syn*, *syn*-bridging mode (**Scheme 3.6**, c) between two metal ions. Two benzoates are mono-coordinated to the peripheral Dy ions, the square anti-prism geometry of every Dy ion being completed by one MeOH molecule (**Scheme 3.6**, b). The Fe-N/O distances range from 1.860(6) to 2.248(9)Å and the Dy-N/O from 2.284(7) to 2.608(6)Å. There are intramolecular hydrogen bonds in compound **10** (**Fig 3.32**). No close intermolecular interactions were found.

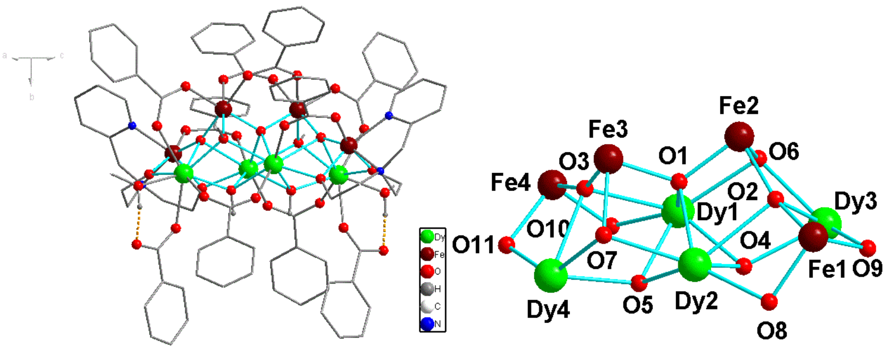

Fig 3.32 The molecular structure (left) and core (right) of compound **10**

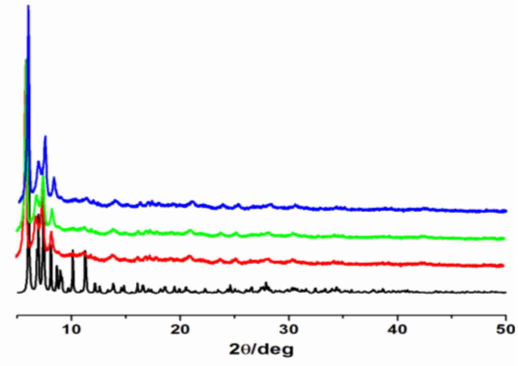

Fig 3.33 The powder XRD of compounds **10** (red), **11** (green) and **12** (blue): simulated (black, based on Fe_4Dy_4)

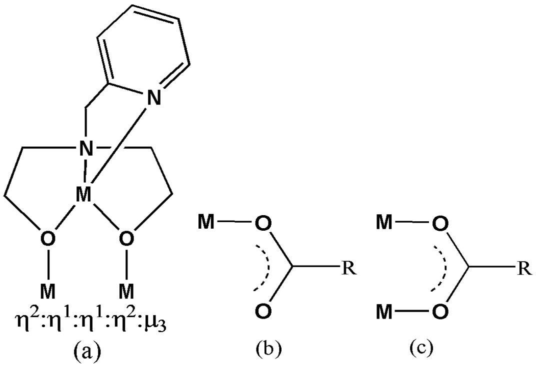

Scheme 3.6 The coordination modes of the H_2**L1** and benzoate ligands found in compound **10**

3.2.12 Magnetic properties of compounds 10-12

Dc magnetization measurements were carried out on polycrystalline samples of compounds **10-12** in the temperature range 1.8-300 K under an applied field of 1000 Oe. The dc magnetic data of **10-12** are summarized in **Table 3.6**. As shown in **Fig 3.34**, at 300 K, the product χT is 57.21 and 53.76 cm^3 K mol^{-1} for **10** and **11**, respectively. On lowering the temperature (300-15 K), a similar steady decrease of χT is observed for both compounds. At lower temperatures, χT decreases further and in a more abrupt manner, down to 32.30 and 14.17 cm^3 K mol^{-1} at 1.8 K, respectively. The

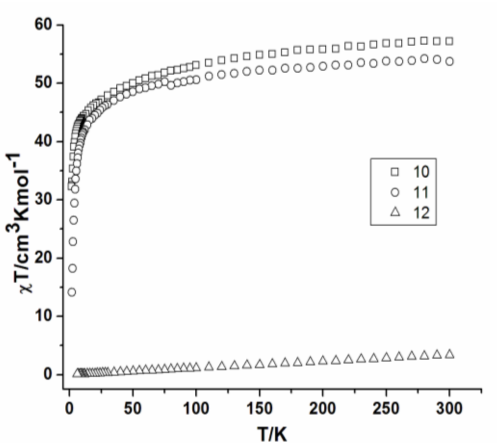

Fig 3.34 Plots of χT vs T of compounds **10-12** at 1000 Oe field

Table 3.6 Magnetic data of compounds **10-12** summarized from the dc measurements

Compound	Ground state of Ln^{III} ion	χT expected for non-interacting ions per complex (cm^3 K mol^{-1})	χT measured at 300 K per complex (cm^3 K mol^{-1})	χT measured at 1.8 K per complex (cm^3 K mol^{-1})	Magnetization at 2 K and 7 T (Nβ)
$Fe^{III}_4Dy^{III}_4$ (**10**)	$^6H_{15/2}$	74.18	57.21	32.30	20.90
$Fe^{III}_4Tb^{III}_4$ (**11**)	$^7H_6$	69.48	53.76	14.17	26.65
$Fe^{III}_4Y^{III}_4$ (**12**)		17.5	3.41	0	

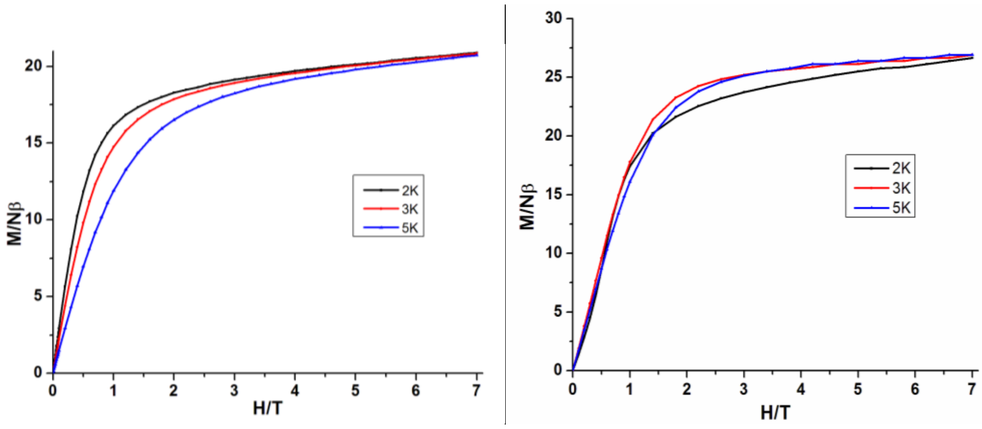

Fig 3.35 Plots of M vs H of compounds **10** (left) and **11** (right)

Ac susceptibility measurements were carried out in the frequency range 1-1500 Hz and at temperatures between 2 and 10 K. At zero dc applied field, ac susceptibility for **10** and **11** displayed a strong frequency-dependent out-of-phase signal, but no maxima were observed even with applied dc fields between 500 and 3000 Oe (**Fig 3.36** and **3.37**)

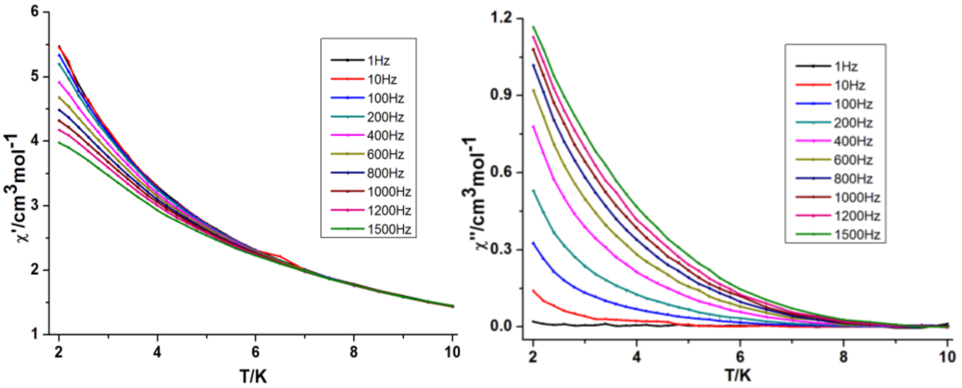

Fig 3.36 Plots of χ’ (left) and χ’’ (right) vs T at indicated frequencies of **10**

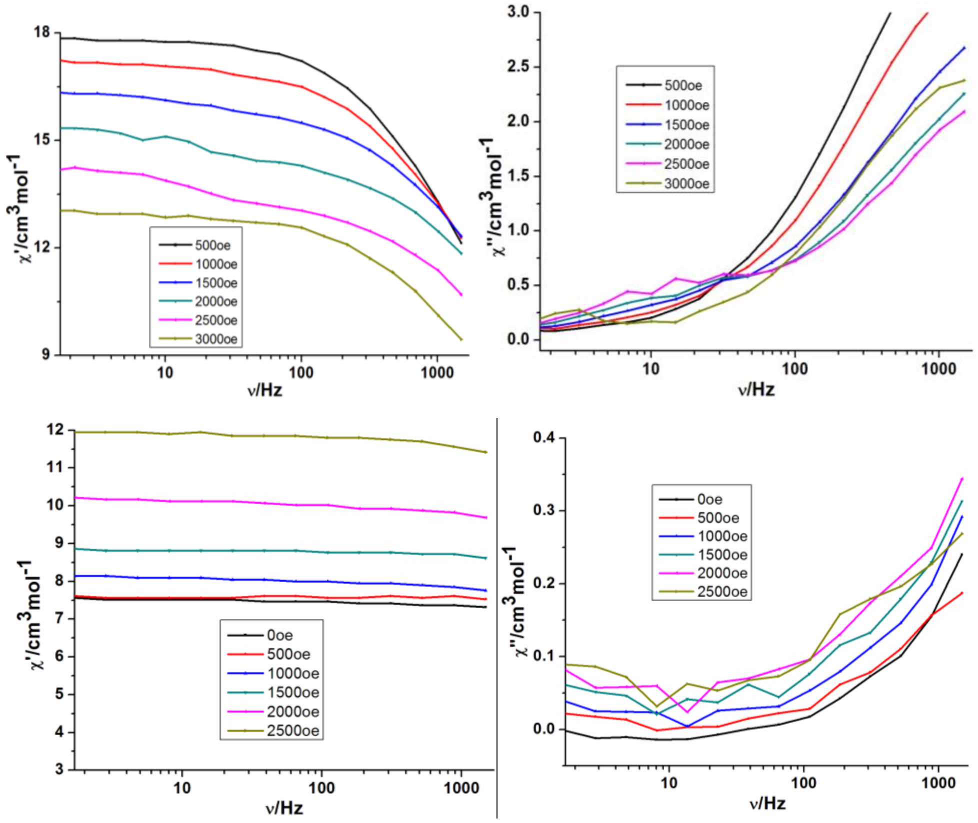

Fig 3.37 Plots of χ’ vs (left) and χ’’ (right) vs frequency of compounds **10** (top) and **11** (bottom) at 1.8 K at indicated applied magnetic fields

observed lowering of χT is typical of dominant antiferromagnetic interactions, but the thermal depopulation of the Stark sublevels of the Ln^{III} ion ground states may also be the reason. For compound **12**, at 300 K, the χT value of 3.41 cm^3 K mol^{-1} is much lower than for four non-interacting Fe^{III} ions. On lowering the temperature, the χT decreases very quickly reaching a zero value at 1.8 K. This behaviour indicates strong antiferromagnetic interactions between the linear Fe^{III}_4. Field-dependence measurements of the magnetization up to 7 T were performed at 2, 3 and 5 K for compounds **10** and **11**, and are shown in **Fig 3.35.** The lack of saturation was observed for both compounds. This behaviour is likely related to thermal and/or field-induced population of excited states, but also to the intrinsic magnetic anisotropy of the Ln^{III} ions. The spin ground state for compound **12** at low temperatures is zero, therefore the magnetization measurements were not performed.

3.2.13 Structures of $[Dy_2(HL1)(NO_3)_4]$ (13), $[Dy_2(L2)(NO_3)_4]$ (14) and $[Dy_2(HL3)_2(NO_3)_4]$ (15)

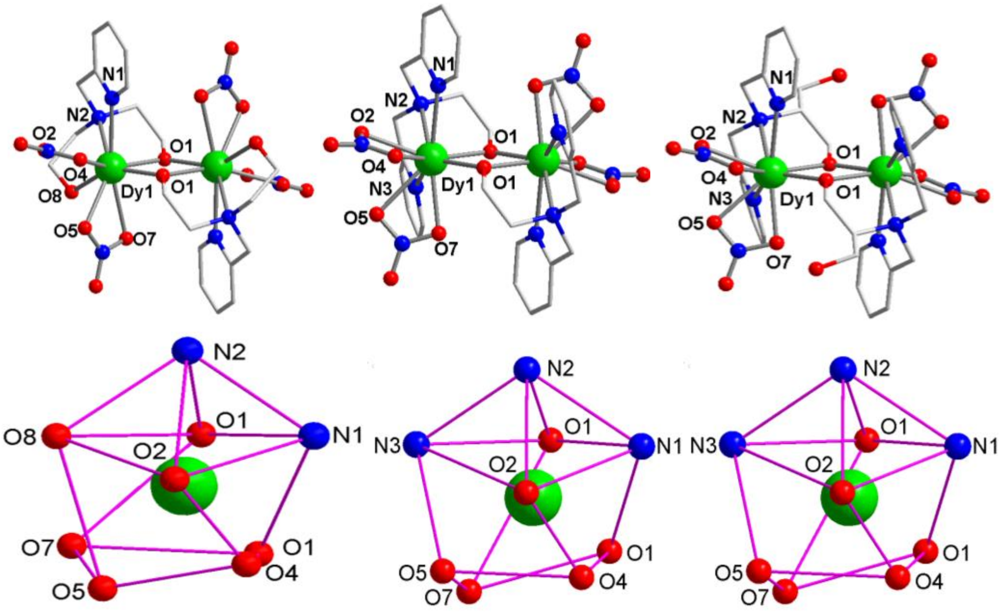

Fig 3.38 The molecular structures of compounds **13** (top left), **14** (top middle) and **15** (top right) and coordination atmosphere of compounds **13** (down left), **14** (down middle) and **15** (down right)

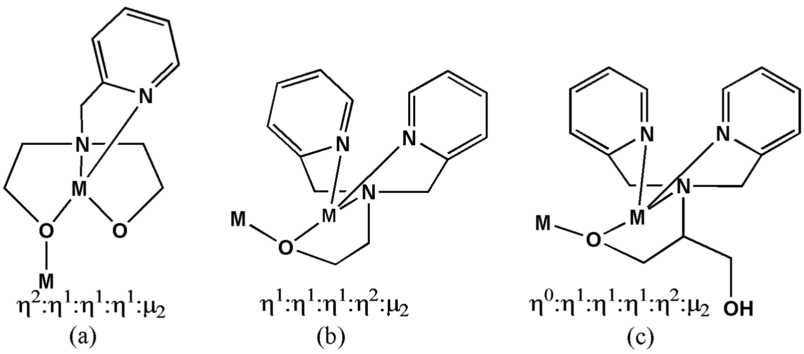

$\eta^2:\eta^1:\eta^1:\eta^1:\mu_2$
(a)

$\eta^1:\eta^1:\eta^1:\eta^2:\mu_2$
(b)

$\eta^0:\eta^1:\eta^1:\eta^1:\eta^2:\mu_2$
(c)

Scheme 3.6 The coordination modes of the H_2**L1** (a), H**L2** (b) and H_2**L3** (c) in compounds **13-15**

All compounds were structurally characterised using single crystal X-ray diffraction and checked for phase purity from powder XRD patterns (**Fig 3.39**). The single-crystal X-ray diffraction analysis revealed that compounds **13** and **14** crystallize in the monoclinic space group $P2_1/c$, while compound **15** crystallizes in the orthorhombic space group Pbca. As shown in **Fig 3.38**, all compounds consist of neutral and centrosymmetric dimers. The asymmetric unit consists of one Dy^{III} ion, one ligand and two nitrate ions. The centrosymmetric dinuclear complexes are composed of two nine-coordinated Dy^{III} ions bridged by alkoxide groups of the ligands. For the nine-coordinated Dy^{III} the geometry around the metal is best described as a distorted mono-capped square anti-prism (**Fig 3.38**). In these three related Dy^{III}_2 systems, each nitrate anion provides two donor oxygen atoms coordinating to Dy^{III} ion, the other four coordination sites of Dy^{III} are occupied by four coordinating atoms from the ligand [(N2O2 of H**L1** ($\eta^2:\eta^1:\eta^1:\eta^1:\mu_2$, **Scheme 3.6**, a) for compound **13**, N3O of **L2**$^-$ ($\eta^2:\eta^1:\eta^1:\eta^1:\mu_2$, **Scheme 3.6**, b) for compound **14** and N3O of H**L3**$^-$ ($\eta^2:\eta^1:\eta^1:\eta^1:\eta^0:\mu_2$, **Scheme 3.6**, c) for compound **15**] and the last position is occupied by a bridging alkoxide O atom from the other ligand to complete the nine-coordination environment DyO7N2 for compound **13**, and DyO6N3 for compounds **14** and **15**, respectively. In this system, the Dy-O (bridged) bonds length are 2.255(5) to 2.277(4)Å for compound **13**, 2.259(7) to 2.266(7)Å for compound **14**, 2.257(17) to 2.265(17)Å for compound **15**, respectively. The Dy···Dy distance is 3.709(7)Å, 3.706(3)Å and 3.719(3)Å for compounds **13-15**, respectively. The Dy-O-Dy angles of compounds **13-15** are 109.83(18)°, 109.71(15)° and 110.65(7)°, respectively.

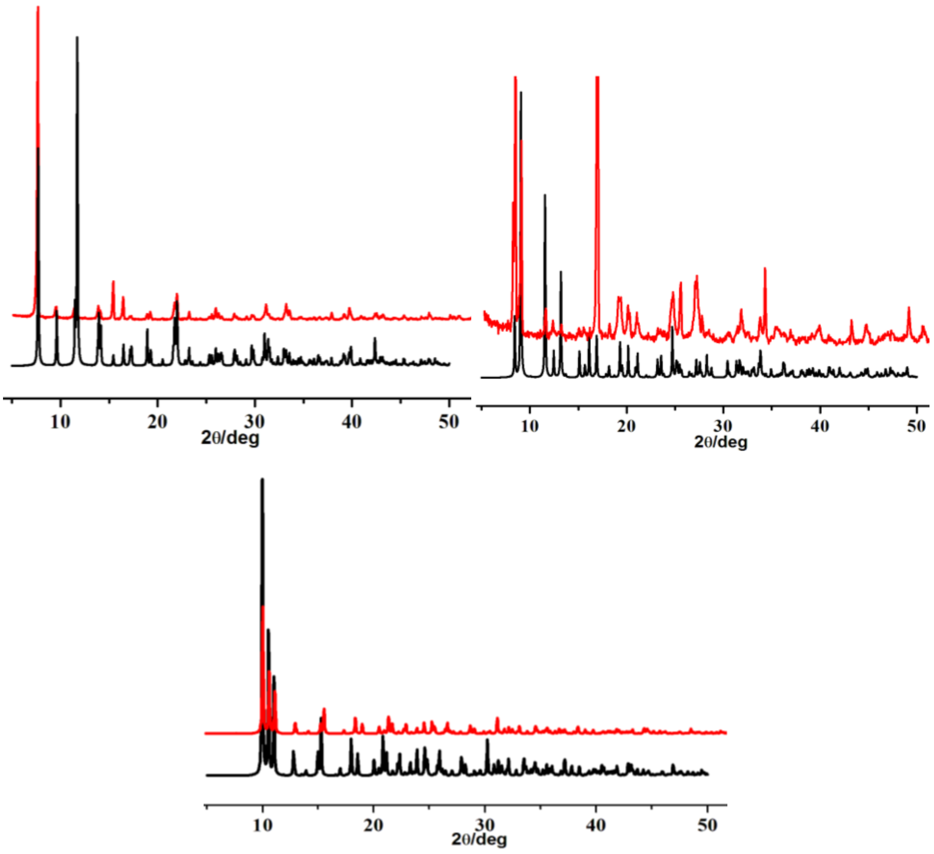

Fig 3.39 The powder XRD of compounds **13** (up left), **14** (up right) and **15** (down): simulated (Black), experimental (red)

3.2.14 Magnetic Properties of compounds 13-15

Direct-current (dc) magnetic susceptibility studies of compounds **13-15** were carried out in an applied magnetic field of 1000 Oe over the temperature range 300-1.8 K. The dc magnetic data of compounds **13-15** are summarized in **Table 3.7**. The plot of χT vs T is shown in **Fig 3.40**. At 300 K, the χT values are 26.09 $cm^3 \cdot K \cdot mol^{-1}$ for compound **13**, and 27.18 $cm^3 \cdot K \cdot mol^{-1}$ for compound **14**, which are a slightly lower than the expected value of 28.34 $cm^3 \cdot K \cdot mol^{-1}$ for two uncoupled Dy^{III} ions ($^6H_{15/2}$, g = 4/3). As the temperature is lowered, the χT values decrease gradually and more dramatically below 100 K to the minima of 14.16 $cm^3 \cdot K \cdot mol^{-1}$ and 17.57 $cm^3 \cdot K \cdot mol^{-1}$ at 1.8 K for compounds **13** and **14**, respectively. The decrease of the χT values could be ascribed to thermal depopulation of the Stark levels of the Dy^{III} ions and/or the possible antiferromagnetic interactions between the spin carriers, as observed in other dysprosium compounds.[9] Magnetization plots (M vs. H) for compounds **13** and **14** (**Fig 3.41**) at high fields (up to 7 T) show non-saturation as well as non-superposition on a single curve, indicating the presence of magnetic-anisotropy and/or low-lying excited states. In the case of compound **15**, the χ_MT value is equal to 28.80 $cm^3 \cdot K \cdot mol^{-1}$ at 300 K, which is good agreement with the expected value of 28.34 $cm^3 \cdot K \cdot mol^{-1}$ for two uncoupled Dy^{III} ions. With decreasing temperature, the χ_MT product only displays a slight decrease to 27.24 cm^3 K mol^{-1} at 18 K, which may result from the depopulation of the Stark sublevels and/or significant magnetic anisotropy present in Dy^{III} systems. Upon further decreasing temperature, the value slightly increases to 29.52 cm^3 K mol^{-1} at 1.8 K, suggesting weak intramolecular ferromagnetic interactions in compound **15**. The lack of a superposition of the M vs H data on to a single master curve and the low magnetization of 12.21 Nβ at 7.0 T suggest the presence of a significant magnetic anisotropy and/or low-lying excited states (**Fig 3.41**)

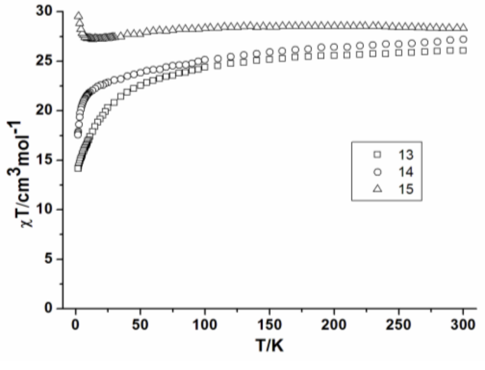

Fig 3.40 Plots of χT vs T for compounds **13-15**

Table 3.7 Magnetic data of compounds **13-15** summarized from the dc measurements

Compound	Ground state of Ln^{III} ion	χT expected for non-interacting ions per complex (cm^3 K mol^{-1})	χT measured at 300 K per complex (cm^3 K mol^{-1})	χT measured at 1.8 K per complex (cm^3 K mol^{-1})	Magnetization at 2 K and 7 T (Nβ)
Dy$^{III}_2$ (**13**)	$^6H_{15/2}$	28.28	26.08	14.15	10.96
Dy$^{III}_2$ (**14**)	$^6H_{15/2}$	28.28	27.18	17.57	9.95
Dy$_2^{III}$(**15**)	$^6H_{15/2}$	28.28	28.31	29.52	12.33

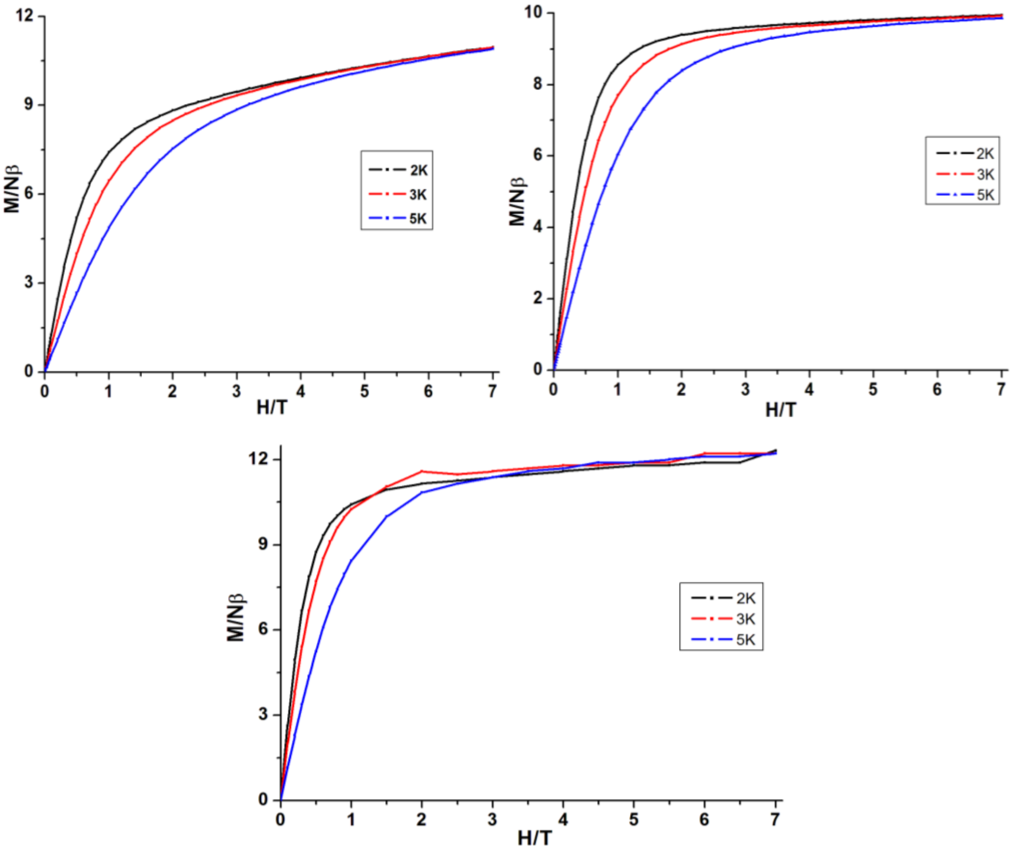

Fig 3.41 Plots of M vs H of compounds **13** (up left), **14** (up right) and **15** (down)

In order to verify their potential SMM behavior alternating current (ac) magnetic susceptibility studies were carried out on freshly filtered samples of compounds **13-15**. For compound **13**, no out-of-phase signal (χ'') was observed even on application of a static dc field (**Fig 3.42**), indicating the absence of SMM behaviour within the measurement parameters of the SQUID. This may be due to the very fast quantum tunnelling of the magnetization (QTM) commonly seen in pure lanthanide compounds. For compound **14**, an ac signal was observed in the out-of phase (χ'') vs T plot below 12 K (**Fig 3.43**). This suggests slow relaxation of the magnetization, which is generally attributed to a SMM. However, the energy barrier and characteristic relaxation time could not be obtained because the maxima of χ'' could not be detected in the available measurement window. It is possible to shortcut the QTM by applying a static dc field. Therefore, ac susceptibility measurements were performed under static dc fields (**Fig 3.42**) in the range 0-3000 Oe. The result indicates that the applied dc field indeed slows down the relaxation time by reducing or suppressing quantum tunnelling of the magnetization. The ac susceptibility measurements as a function of temperature were carried out under the optimum dc field of 1000 Oe (**Fig 3.44**). Fitting the data to an Arrhenius law, the characteristic SMM energy gap, *U*, was estimated to be 72.48 K and the pre-exponential factor $\tau_0 = 8.50 \times 10^{-8}$ s, (**Fig 3.48**). Such an observation confirms the field-induced SMM nature of compound **14**. For compound **15**, in zero dc field, the appearance of maxima for the out-of-phase (χ'') in the ac susceptibility clearly demonstrates slow relaxation of the magnetization at temperatures below 17 K **(Fig 3.45**). Plots of in-phase (χ') and out-of-phase (χ'') ac susceptibility in zero dc field as a function of frequency in the temperature range 2-12.5 K (**Fig 3.45**) and the resulting Cole-Cole plot (**Fig 3.46**) reveal shape- and frequency-dependent features typical of SMM behaviour. It is worth highlighting that a single relaxation mode with α values ranging from 0.033 to 0.173 in the frequency dependent ac susceptibility is observed, more clearly seen in the high frequency region. From these data, the temperature dependence of the relaxation time, τ_0, can be deduced. Below 6 K, the dynamics of compound **15** becomes temperature independent in a pure quantum regime with a τ value of 3.30×10^{-4} s. Above 6 K, the relaxation time becomes progressively thermally activated, and above 7.5 K the energy barrier of the thermally activated regime (U_{eff}) can be determined as roughly 27.3 K with the pre-exponential factor of the Arrhenius law $\tau_0 = 3.15 \times 10^{-6}$ s **(Fig 3.48)**. In order to probe the feasibility of lowering the relaxation probability via the quantum pathway, the ac susceptibility has been measured at 1.8 K at various applied dc fields (0-3000 Oe, **Fig 3.42**). From these data, the characteristic relaxation frequency as a function of applied dc field for the relaxation modes (i.e., thermal and quantum relaxation modes) can be extracted. The probability of magnetization relaxation via quantum tunnelling appears to be minimized at 2000 Oe. Therefore, the in-phase (χ') and out-of-phase (χ'') ac susceptibilities as a function of frequency at various temperatures has been measured under 2000 Oe dc field. The result reveals an enhancement of the peak feature as the quantum tunnelling is reduced (**Fig 3.47**). Fitting the data to an Arrhenius law, the energy gap, U_{eff}, was estimated to be 72.37 K and the pre-exponential factor $\tau_0 = 1.23 \times 10^{-7}$ s (**Fig 3.48**). The large increase of the energy barrier under an applied dc field indicates that the reversal of the spin in this compound takes a different relaxation pathway.

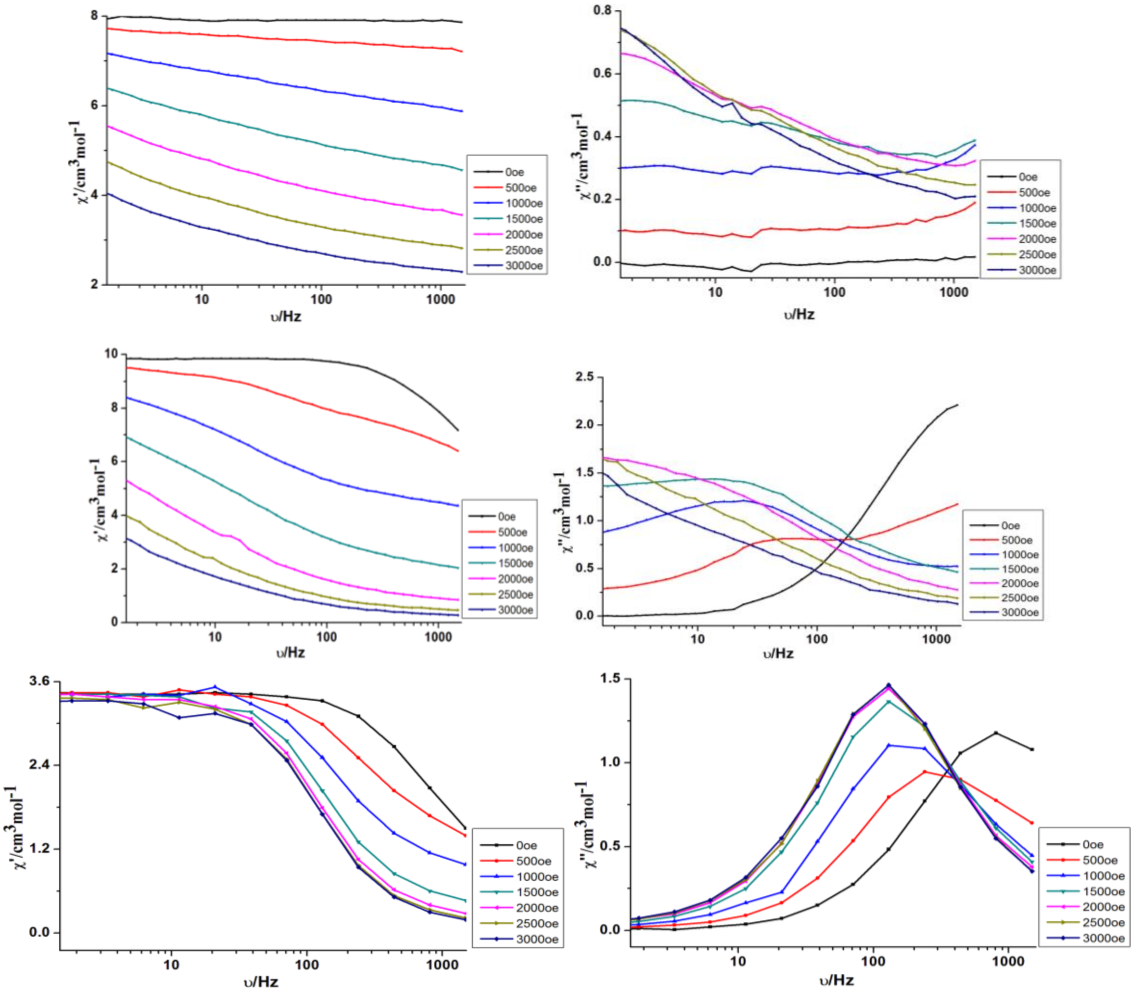

Fig 3.42 Plots of χ' (left) and χ'' (right) vs frequency under different dc magnetic fields for compounds **13** (up), **14** (middle) and **15** (down) at 1.8 K

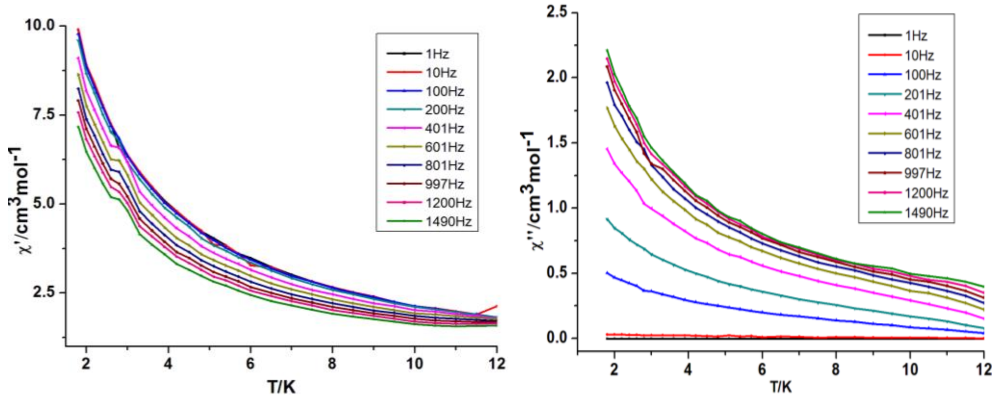

Fig 3.43 Plots of χ' (left) and χ'' (right) vs T under zero dc field for compound **14**

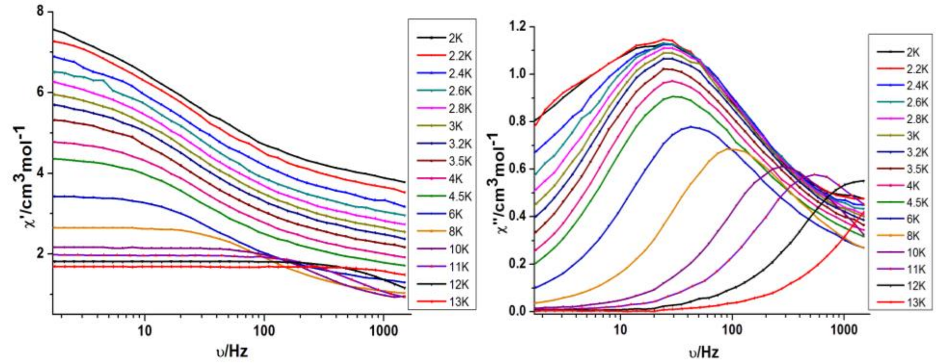

Fig 3.44 Plots of χ' (left) and χ'' (right) vs frequency under 1000 Oe dc magnetic fields for compound **14** at different temperature

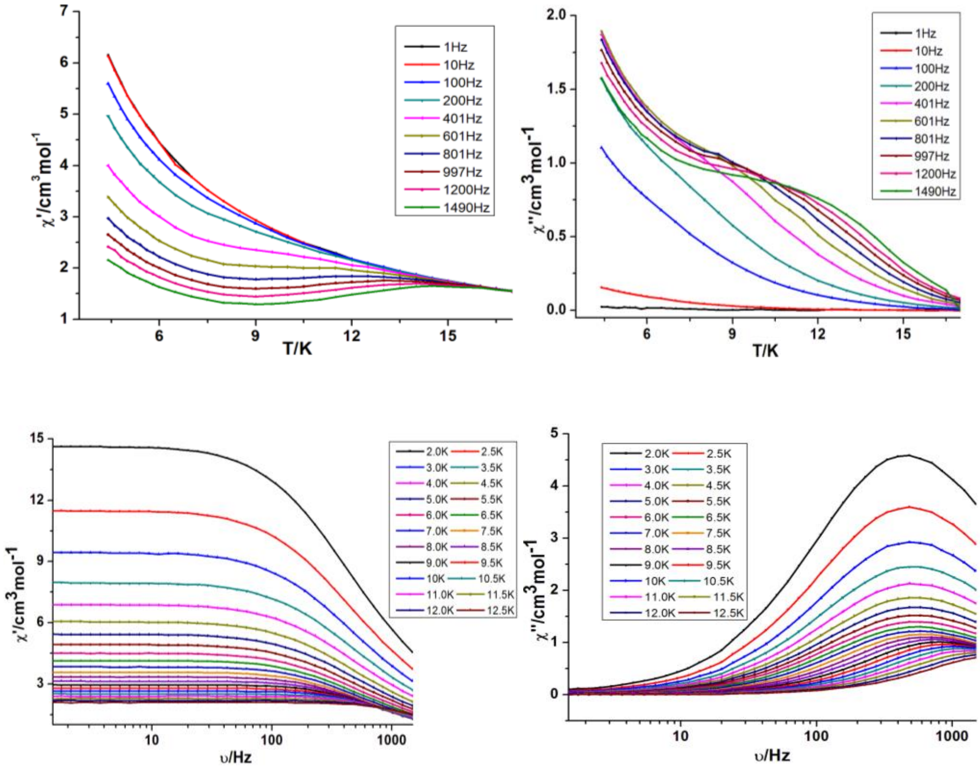

Fig 3.45 Plots of χ' (left) and χ'' (right) vs T (up) and frequency (down) under zero dc field for compound **15** at different temperature

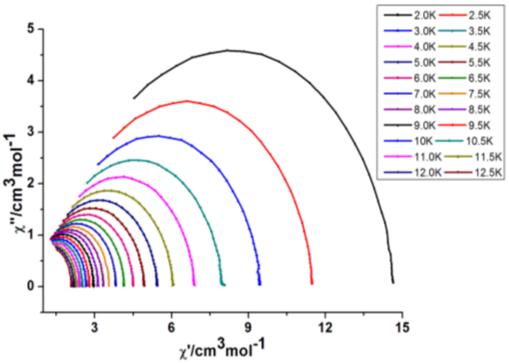

Fig 3.46 Plots of Cole-Cole for compound **15** (lines guide the eyes)

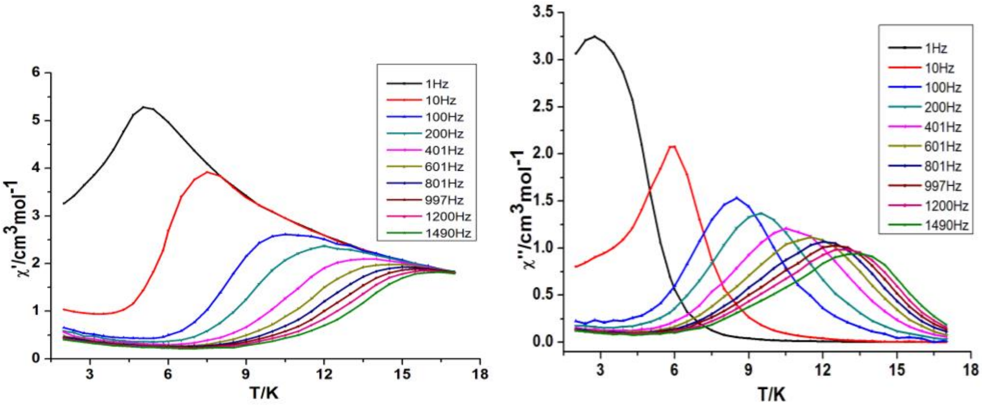

Fig 3.47 Plots of χ’ (left) and χ’’ (right) vs T under 2000 Oe dc field for compound **15** at different frequency

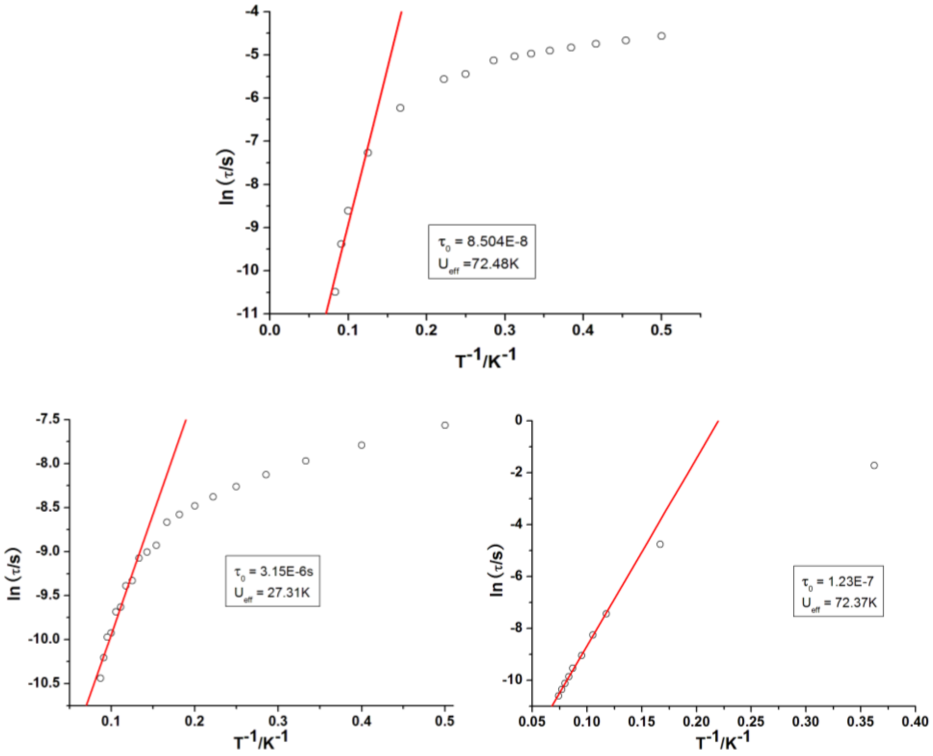

Fig 3.48 Plots of τ vs T^{-1} for copound **14** under 1000 Oe dc field (up), for compound **15** under zero field (down left) and 2000 Oe dc field (down right)

3.2.15 Structure-property relationship of compounds 13-15

Each Dy^{III} ion of compounds **13-15**, with a nine-coordinate coordination environment, is linked to the other Dy^{III} via μ_2-alkoxide bridges from two mono-deprotonated ligands. As evidenced in **Fig 3.40**, they exhibit distinct magnetic behaviour in their dc magnetic susceptibilities. Compounds **13** and **14** show antiferromagnetic interactions between the two Dy^{III} ions with N2O7 and N3O6 coordination environment, respectively, while a ferromagnetic interaction was clearly observed in compound **15**, in which the metal ions also have an N3O6 coordination environment as seen in compound **14**. It is noteworthy that the Dy-O-Dy angles of these three compounds are slightly different (109.83(18)°, 109.71(15)° and 110.65(7)°, respectively). According to the previously reported similar dinuclear compounds, the parameters for the $Dy_2(\mu_2\text{-}O)_2$ unit play an important role and influence to the magnetic properties. The Dy-O-Dy angles could influence the magnetic interactions, although such interactions are expected to be very weak.

In addition, comparison of bond distances in compounds **13**-**15** reveals that compound **15** displays the shortest Dy-O bonds in the Dy_2O_2 cores of the three compounds which should lead to the shortest Dy···Dy distance. In contrast, compound **15** has the longest Dy···Dy distance. The average Dy-O (NO_3^-) bonds length in the three compounds is similar (~2.50 Å). Although the average bonds lengths and angles of these three compounds are very close, the coordination positions are different. Comparing the clusters, the other main disparities between the cores are the ligands. For compound **13**, each Dy^{III} displays an N_2O_7 coordinate environment, while for compound **14**, each Dy^{III} displays an N_3O_6 coordinate environment where one of the alkoxide O atom is replaced by pyridine N atom. For compound **15**, it exhibits the same coordinate environment as compound **14**, but with a hydrogen atom replaced by a $-CH_2OH$ group on the ligand. These features suggest that it is the differences in the organic ligands which probably lead to the different magnetic behaviour of these three compounds. The SMM behaviour is more pronounced when the ligand is more bulky. The steric effect of the bulky ligand probably weakens the intramolecular interaction in this way quenching partially the fast zero-field tunnelling effect.

3.3 Conclusions

In this chapter fifteen new *3d-4f* and *4f* complexes (**1**-**15**) based on amino-polyalcohol ligands and showing six different nuclearities, have been discussed. The syntheses were carried out under aerobic conditions and products were crystallized either from MeOH and/or MeCN by slow evaporation in air. At the beginning, the H_2**dea** as coordination ligand was selected and the compounds $[Co^{III}_3Co^{II}_2Ln^{III}_2(OH)_2(C_6H_5COO)_6(\mathbf{dea})_4(H\mathbf{dea})(NO_3)](NO_3)\cdot 3MeOH\cdot H_2O$ [Ln = Dy (**1**) and Gd (**2**)] were obtained. Then, three related ligands were selected: H_2**L1**, H**L2** and H_2**L3** but no analogouns Co^{II}-4f coordination clusters could be obtained and only with H_2**L1**, could any Co-4f clusters be obtained, but here the Co occurs as Co^{III} ions rather than Co^{II} ions. The two related $[Co^{III}_3Dy_3(\mathbf{L1})_3(\mu_3\text{-}OH)_4(O_2CPh)_6(H_2O)_3]\cdot(O_2CPh)\cdot Cl\cdot 4MeOH\cdot 10H_2O$ (**3**) and

$[Co^{III}_3Dy_3(\mathbf{L1})_3(\mu_3\text{-}OH)_4(O_2CPh\text{-}Me)_6(H_2O)_3]\cdot 2Cl\cdot 10MeOH$ (**4**) compounds have similar structures, the small difference being in the nature of the benzoate ligands and number of free solvent molecules. It is possible to replace the diamagnetic Co^{III} ion with paramagnetic M^{III} ions (such as Fe^{III} and Cr^{III}) to give three isostructural compounds: $[Fe^{III}_2Dy^{III}_2(\mathbf{L1})_2(Me\text{-}PhCO_2)_6(OH)_2]\cdot 2MeCN\cdot MeOH\cdot 3.35H_2O$ (**5**) and $[Cr_2Ln_2(\mathbf{L1})_2(Me\text{-}PhCO_2)_6(OH)_2]\cdot 2MeCN$ [Ln = Dy (**6**) and Y (**7**)]. Using the same ligand it was also possible to obtain five Fe^{III}-4f complexes (**8-12**) of two different nuclearities: $[Fe^{III}Ln^{III}(H\mathbf{L1})_2(O_2CPh)_3(NO_3)]$ [Ln = Dy (**8**) and Y (**9**)] and $[Fe^{III}_4Ln^{III}_4(\mathbf{L1})_2(PhCO_2)_{10}(O)_3(OH)_2(MeOH)_2(MeO)_2]\cdot 3MeOH\cdot xH_2O$ [Ln = Dy (**10**), x = 0; Tb (**11**), x = 1 and Y (**12**), x = 1]. Unfortunately, with the other two ligands (H**L2** and H_2**L3**), no *3d*-4f clusters could be obtained, but they were successfully used in assembling three related Dy^{III} dimers: $[Dy_2(H\mathbf{L1})(NO_3)_4]$ (**13**), $[Dy_2(\mathbf{L2})(NO_3)_4]$ (**14**) and $[Dy_2(H\mathbf{L3})_2(NO_3)_4]$ (**15**).

All complexes (**1-15**) were magnetically investigated. The dc magnetic measurements reveal that all complexes show intramolecular antiferromagnetic interactions except **8** and **15**, which show weak intramolecular ferromagnetic interactions. For compounds **10-12**, the Fe_4 chain shows antiferromagnetic interactions. The dynamic magnetic property measurements reveal that compounds **3** and **4** exhibit slow relaxation of magnetization in zero dc field, but it was not possible to obtain the energy barrier for relaxation of magnetisation, U_{eff}. Compound **5** is a field-induced SMM with $U_{eff} = 16.2$ K while the isomorphous compound **6** does not show any ac signal even in a dc applied field. A possible explanation for this is that there is some difference in the electronic structure leading to changes in the coupling interactions between the *3d* and *4f* ions. In future it might be possible to extend this series to other *3d* or *4d* metals. The three Dy_2 compounds (**13-15**) are rare examples of alkoxide-O bridged Dy_2 compounds and display mono-capped square antiprism coordination geometry around each Dy^{III} ion. Magnetic properties reveal that compound **13** is not a SMM, but compounds **14** and **15** are QTM dominated SMMs. Within this series, changes to the ligands have been made and, in particular, the effect of introducing a neutral pyridine group in place of an alkoxide group made it possible to vary the ligand field around the Dy^{III} ion and this appears to promote the slow relaxation process. A further change of replacing one hydrogen atom by a $-CH_2OH$ group induces a typical SMM behaviour. These observations may provide a means to elucidate the influence of the ligand field around the Dy^{III} ions on magnetic properties.

Chapter 4

3d, 3d-4f and 4f Coordination Clusters with Schiff Base Ligands

4.1 Introduction

The discovery of the first 3d-4f SMM, Cu_2Tb_2,[19] has provoked even more interest in the field of molecular magnetism. The interest in molecular clusters containing lanthanide ions stems from the fact that many of the lanthanide ions provide significant spin and magnetic anisotropy to the system and both of these factors are key components for producing high energy barriers to spin reversal of the magnetisation. In particular, the magnetic anisotropy, which in favourable ligand fields can be of the easy axis or easy plane type, should be able to generate SMMs with properties significantly different from those of pure transition metal SMMs. On the other hand, the inherent anisotropy of most lanthanide ions makes the description of the magnetic properties of *3d*-4f couples very difficult. Furthermore, pure Ln systems tend to show rather low superexchange coupling, whereas relatively strong super-exchange is widely held to be a desirable feature to incorporate in SMM systems.[39] A number of research groups interested in producing new SMMs, as well as elucidating key properties which steer their magnetic behaviour, have turned their attention to mixed 3d-4f coordination clusters and their potential as SMMs. In particular, the Powell group at KIT have reported coordination clusters mixing Ln ions with 3d metals ranging across the 3d series from Cr^{III} to Cu^{II}.[25, 26c, 40] Amongst these are examples where the *3d* metal ion is Co^{II} and which show that incorporating highly anisotropic Co^{II} with a highly uniaxially anisotropic lanthanide ion such as Dy^{III} can give very interesting SMM behaviour arising from the interplay of superexchange and single ion properties.[25] For the construction of 3d-4f complexes, Schiff-base ligands have been widely employed (e.g. Cu-4f [19, 26a, 26b,31, 38, 40d, 41] and Ni-4f,[21b,40b, 42] since such ligands can provide pockets favourable for 3d ion coordination, 4f ion coordination or else a suitable combination of these.[43] So far, for Co^{II}-4f compounds only a few examples have been reported.[20-25] Thus, the synthesis of new examples of Co^{II}-4f compounds using Schiff base ligands was explored and the magnetic properties of these were studied. It was found that in some cases pure Co^{II} compounds were obtained, sometimes pure 4f compounds were obtained and finally mixed Co^{II}-4f systems could also be obtained. The replacement of Co^{II} with Fe^{II} or Zn^{II} was also explored to study the effect of 3d electron configuration. The compounds resulting from interaction of the 3d/4f reaction mixtures with the Schiff base ligands shown below are discussed in this chapter (**Scheme 4.1**).

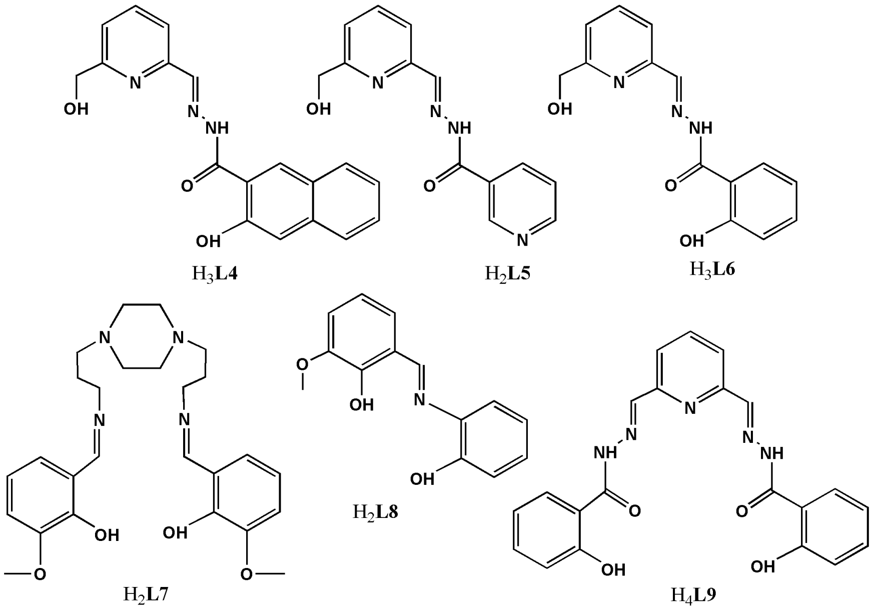

Schiff base ligands

Scheme 4.1 The selected ligands

4.2 Synthesis

As discussed above, Schiff base ligands are good candidates for assembling Co^{II}-4f clusters. A significant degree of control can be exerted over the formation of such molecular cluster-aggregates by using selected ligands and metal salts in suitable solvents as shown in **Table 4.1**.

To begin with, H_3**L4**, H_3**L5** and H_2**L6** were selected as ligands. For the compounds containing H_3**L4**, H_3**L5** and H_2**L6** these ligands resulted from the *in-situ* condensation of the components indicated in **Table 4.1**. Thus, the reactions of 6-hydroxymethyl-pyridine-2-carbaldehyde, 3-hydroxy-2-naphthoic acid hydrazide or 3-pyridinecarboxylic acid hydrazide or 2-hydroxy-benzoic acid hydrazide, $Co(NO_3)_2 \cdot 6H_2O$, $Dy(NO_3)_3 \cdot 6H_2O$ and $NaOAc \cdot 3H_2O$ with a ratio of 2:2:1:1:5 in MeOH and MeCN or CH_2Cl_2 yielded the three mononuclear Co^{II} compounds: [Co(H**L4**)$_2$]·2THF (**16**), [Co(H**L5**)$_2$] (**17**) and [Co(H_2**L6**)$_2$]·CH_2Cl_2 (**18**).

Furthermore, attempts to assemble 4f clusters were made. The reactions of

6-hydroxymethyl-pyridine-2-carbaldehyde, 3-hydroxy-2-naphthoic acid hydrazide or 3-pyridinecarboxylic acid hydrazide, $DyCl_3·6H_2O$, $NaOAc·3H_2O$ and Et_3N with a ratio of 3:3:10:10 in MeOH and $CHCl_3$ resulted in the two dinuclear Dy clusters: [Dy_2(H**L4**)$_2$(OAc)$_2$(EtOH)$_2$] (**19**) and [Dy_2(**L5**)$_2$(OAc)$_2$(H_2O)$_2$]·2MeOH (**20**). Because H_3**L4**, H_2**L5** and H_3**L6** are only suitable for coordinating Co^{II} ions as mononuclear complexes, possibly as a result of the rich N coordination sites and for steric reasons, the ligand H_2**L7** was selected. However, the reaction of H_2**L7** with $Co(NO_3)_2·6H_2O$ and $Dy(NO_3)_3·6H_2O$ in DMF in a ratio of 1:1:1 in the presence of Et_3N yielded another mononuclear Co^{II} compound, [Co(**L7**)] (**21**).

Table 4.1 The relationship of reaction conditions and final products discussed in Chapter 4

Molar ratio	Solvent	Volume (mL)	Base	Temperature	products
A:B:$Co(NO_3)_2$:$Dy(NO_3)_3$: NaAc 2:2:1:1:5	MeOH/MeCN	20		rt	Co^{II} (**16**)
A:C:$Co(NO_3)_2$:$Dy(NO_3)_3$: NaAc 2:2:1:1:5	MeOH/MeCN	20		rt	Co^{II} (**17**)
A:D:$Co(NO_3)_2$:$Dy(NO_3)_3$: NaAc 2:2:1:1:5	MeOH/CH_2Cl_2	20		rt	Co^{II} (**18**)
A:B:$DyCl_3$:NaAc 3:3:3:10	EtOH/$CHCl_3$	25	Et_3N	rt	Dy^{III}_2 (**19**)
A:C:$DyCl_3$:NaAc 3:3:3:10	MeOH/$CHCl_3$	25	Et_3N	rt	Dy^{III}_2 (**20**)
H_2**L7**:$Co(NO_3)_2$: $Dy(NO_3)_3$ 1:1:1	DMF	2	Et_3N	rt	Co^{II} (**21**)
H_2**L8**: $Co(NO_3)_2$: $Dy(NO_3)_3$:NaAc 2:1:1:5	MeOH/CH_2Cl_2	20		rt	$Co^{II}_2Dy^{III}_2$ (**22**)
22	DMF/Aceton	25		rt	$Co^{II}_2Dy^{III}_2$ (**23**)
H_2**L8**: $Zn(NO_3)_2$: $Dy(NO_3)_3$:NaAc 2:1:1:5	MeOH/CH_2Cl_2	20		rt	$Zn^{II}_2Dy^{III}_2$ (**24**)
H_2**L8**: $FeCl_2$: $Ln(NO_3)_3$:NaAc 2:1:1	MeOH	20		rt	$Fe^{III}_2Ln^{III}$ (**25** and **26**)
H_4**L9**: $Co(NO_3)_2$: $Ln(NO_3)_3$ 1:1:1	MeOH/MeCN	15	Et_3N	rt	$NaCo^{II}_2Dy^{III}$ (**27**-**30**)
H_4**L9**: $CoCl_2$:$LnCl_3$:NaAc 1:1:1:5	MeOH/MeCN	20		rt	$Co^{II}_2Dy^{III}$ (**31**-**34**)
H_4**L9**: $CoCl_2$:$LnCl_3$:NaN_3 1:1:1:5	MeOH/MeCN	20		rt	$Co^{II}_2Dy^{III}_2$ (**35**)

A = 6-hydroxymethyl-pyridine-2-carbaldehyde, B = 3-Hydroxy-2-naphthoic acid hydrazide

C = 3-pyridinecarboxylic acid hydrazide, D = 2-hydroxy-benzoic acid hydrazide

Thus, although these four Schiff-base ligands do not seem favourable for assembling Co^{II}-4f coordination clusters, they are obviously suitable for coordinating and stabilising Co^{II} ions.

Given the previous success using the ligand $H_2\mathbf{L8}$ for capturing Co-4f ions[25] this ligand as well as the more rigid $H_2\mathbf{L9}$ were selected. The reaction of $H_2\mathbf{L8}$, $Co(NO_3)_2·6H_2O$, $Dy(NO_3)_3·6H_2O$ and $NaOAc·3H_2O$ in a ratio of 2:1:1:1:5 in MeOH and CH_2Cl_2 gave crystals of $[Co^{II}_2Dy^{III}_2(\mathbf{L8})_4(NO_3)_2(MeOH)_2]·2CH_2Cl_2$ (**22**). Diffusion of C_3H_6O into the solution of **22** in DMF crystallizes $[Co^{II}_2Dy^{III}_2(\mathbf{L8})_4(NO_3)_2(DMF)_2]·2C_2H_6CO$ (**23**). As mentioned in chapter 3, replacing the 3d ions might produce interesting magnetic properties. For example, the reaction of $H_2\mathbf{L8}$, $Zn(NO_3)_2·6H_2O$ or $FeCl_2$, $Dy(NO_3)_3·6H_2O$ and $NaOAc·3H_2O$ with a ratio of 2:1:1:1:5 in MeOH and CH_2Cl_2 gave crystals of $[Zn^{II}_2Dy^{III}_2(\mathbf{L8})_4(NO_3)_2(MeOH)_2]·2CH_2Cl_2$ (**24**) and $[Fe^{III}_2Ln^{III}(\mathbf{L8})_4(MeOH)(AcO)]·4MeOH$ [Ln = Dy (**25**) and Y (**26**)]. With the $H_4\mathbf{L9}$ ligand, changing the metal salts and base, we obtained three series of Co^{II}-4f clusters (**27-35**). The reaction of $H_4\mathbf{L9}$, $Co(NO_3)_2·6H_2O$ and $Dy(NO_3)_3·6H_2O$ in MeOH with a ratio (1:2:1:1) in presence of Et_3N produces crystals of $[Co_2Ln(H_2\mathbf{L9})(NO_3)_2(MeOH)_4]·NO_3·xMeOH·yH_2O$, [Ln = Dy (**27**), x = 5, y = 5; Ln = Tb (**28**), x = 0, y= 8; Ln = Ho (**29**), x = 0, y = 10; Ln = Y (**30**), x = 0, y = 10)]. Using $CoCl_2·6H_2O$ and $DyCl_3·6H_2O$ in place of $Co(NO_3)_2·6H_2O$ and $Dy(NO_3)_3·6H_2O$ and selecting $NaOAc·3H_2O$ as base, another series of compounds was formed: $Co_2Ln(\mathbf{L9})_2(H_2O)_4]·7H_2O$ [Ln = Dy (**31**), Tb (**32**), Ho (**33**) and Y (**34**)]. With the same reaction conditions, but using NaN_3 instead of $NaOAc·3H_2O$ as base, $[Co_2Dy_2(H\mathbf{L8})_2(N_3)_2(NO_3)_2(MeOH)_4]·4MeOH$ (**35**) was obtained. In this chapter the synthesis, crystal structures and magnetic properties of compounds **16-35** will be discussed.

4.2.1 Structures of $[Co(H_2L4)_2]·2THF$ (16), $[Co(HL5)_2]$ (17) and $[Co(H_2L6)_2]·CH_2Cl_2$ (18)

The results of the structural analyses for **16-18** are presented in **Fig 4.1** and **4.2**. As can be seen they display similar coordination environments (**Scheme 4.2**). Two perpendicular mono-deprotonated ligands chelate the Co^{II} ions to form neutral $[Co(\mathbf{L})_2]$ complexes. The Co^{II} ions have a distorted six-coordinate N4O2 octahedral environment where the two hydrazones O atoms are in *cis* positions and two pyridine N atoms from the two hydrazones Schiff base ligands then define the equatorial plane while the remaining two imines N atoms occupy the axial positions with N-Co-N angles, 166.93(11)°, 167.23(16)° and 167.51(12)° for **16-18**, respectively. The $Co\text{-}O_{hydrazones}$

bond distances are shorter than the equatorial Co-$N_{pyridine}$ bond distances, which are in turn slightly larger than the axial Co-N bond distances in these three compounds, all of which are typical of high-spin Co^{II} ions. The mono-nuclear units are well isolated from each other, the shortest intermolecular Co-Co distance being 8.358(17), 7.922(8) and 6.249(13)Å for **16-18**, respectively. Additionally, there are intramolecular hydrogen bonds in compound **16**, and intermolecular hydrogen bonds in complex **17**. No other interactions were found in these two compounds, while for **18**, there are not only intramolecular and intermolecular hydrogen bonds, but also short interactions (π-π, 4.04) were found (**Fig 4.3**). The program *SHAPE*[44] was used for calculating the deviation of these structures from the idealised octahedral geometry. Thus values were calculated to be 5.537°, 5.915°, and 4.992° for compounds **16-18**, respectively.

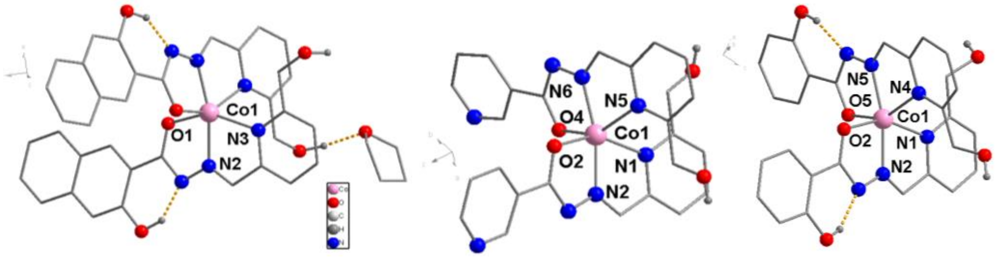

Fig 4.1 The structure of **16** (left), **17** (middle) and **18** (right)

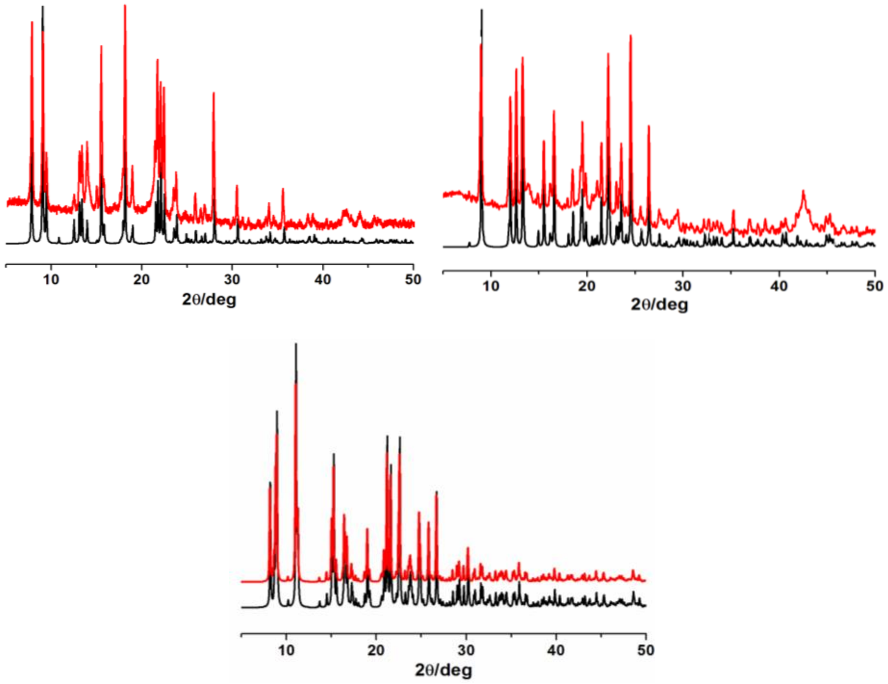

Fig 4.2 The powder XRD of **16** (up left), **17** (up right) and **18** (down): experimental (red), simulated (black)

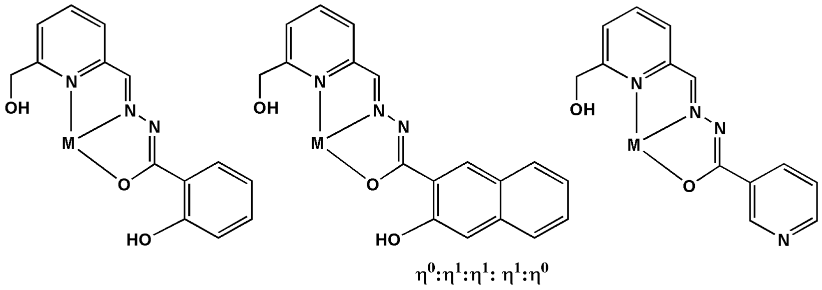

Scheme 4.2 The coordination modes of the H_3**L4** (left), H_3**L5** (middle) and H_2**L6** (right) in compounds **16-18**

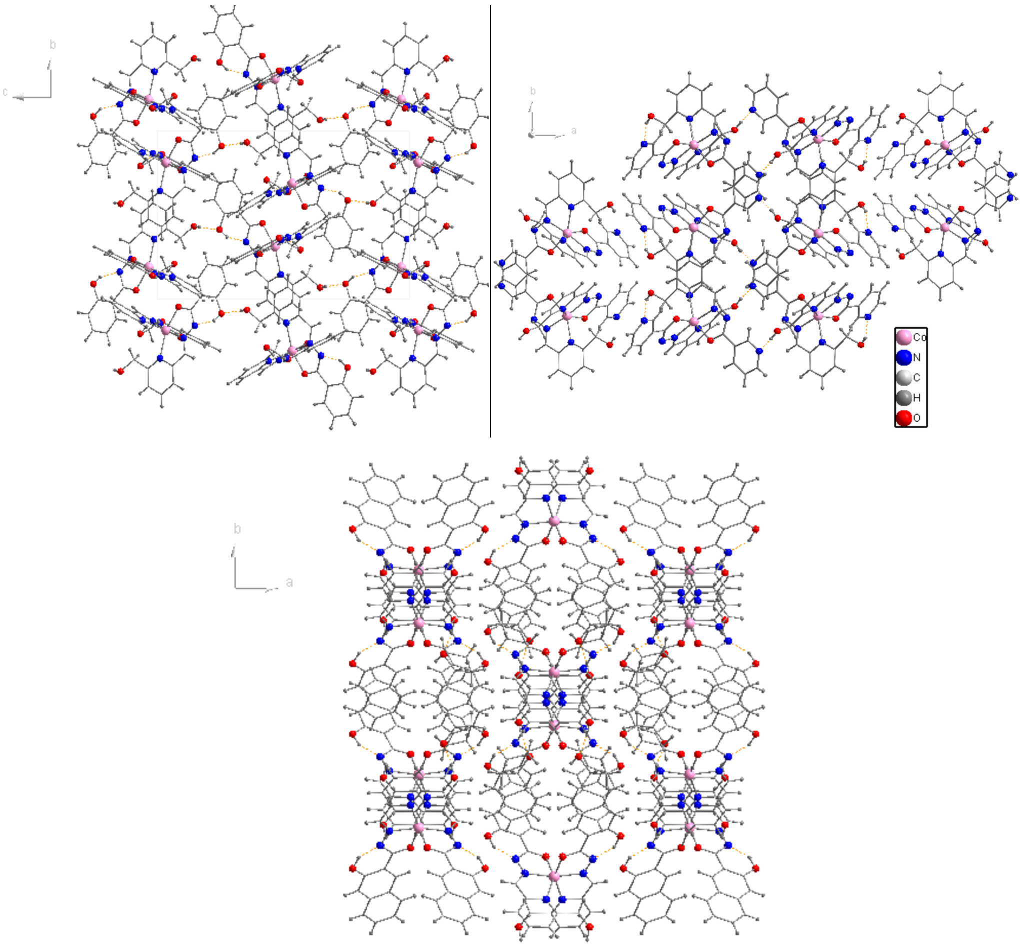

Fig 4.3 The packing of compounds **16** (up left), **17** (up right) and **18** (down)

4.2.2 Magnetic properties of 16-18

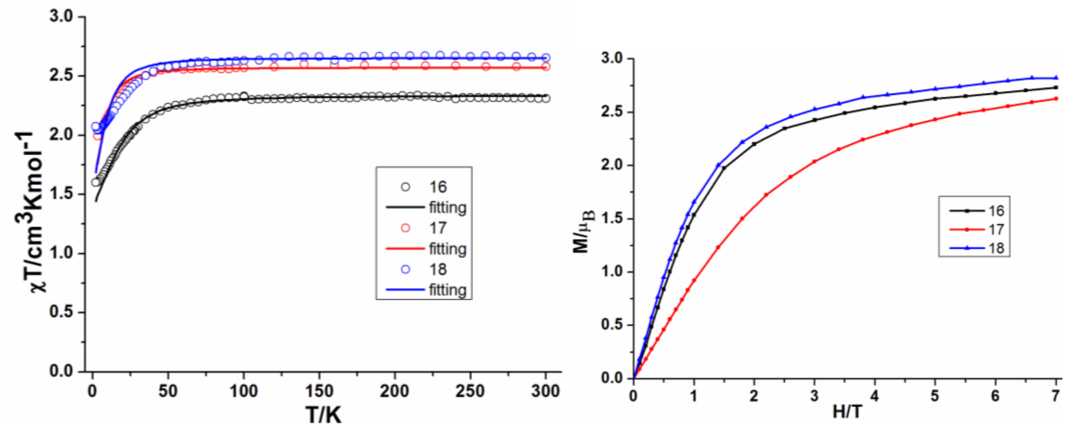

Fig 4.4 plots of the χT vs T at 1000 Oe (left) and M vs H at 2 K for **16-18**

Table 4.2 Magnetic data of compounds **16-18** summarized from the dc measurements

Compound	Ground state of Co^{II} ion	χT expected for non-interacting ions per complex (cm^3Kmol^{-1})	χT measured at 300 K per complex (cm^3Kmol^{-1})	χT measured at 1.8 K per complex (cm^3Kmol^{-1})	Magnetisation at 2 K and 7 T (Nβ)
Co^{II} (**16**)	$^2I_{9/2}$	1.875	2.31	1.60	2.73
Co^{II} (**17**)	$^2I_{9/2}$	1.875	2.58	2.00	2.62
Co^{II} (**18**)	$^2I_{9/2}$	1.875	2.65	2.08	2.82

Magnetic measurements were performed on samples of crushed single crystals at 1000 Oe over the temperature range 1.8-300 K. Dc magnetic susceptibility data (**Fig 4.4**, **Table 4.2**) revealed that the room temperature χT values for **16-18** are 2.31, 2.58 and 2.65 cm^3 K mol^{-1}, respectively, which are significantly higher than the expected value of 1.875 cm^3 K mol^{-1} for one isolated Co^{II} ion (S = 3/2) centre with g = 2, but fall well in the range of 2.1-3.4 cm^3 K mol^{-1} for experimentally observed highly anisotropic Co^{II} centres.[45] The χT values for all compounds are roughly constant in the high temperature range (50-300K), then rapidly drop to a minimum of 1.60, 2.00 and 2.08 cm^3 K mol^{-1} at 1.8 K for **16-18** respectively. The phenomenon is consistent with Curie-type behaviour of isolated Co^{II} centres. The decrease at low temperature is possibly due to intrinsic magnetic anisotropy of the Co^{II} ions. For one Co^{II} ion, the distorted octahedral ligand field plus the spin-orbit coupling lead to six Kramers doublets with energy splittings in the order of 100 K. Hence, below about 40 K, each

Co^{II} ion may be described by an effective spin S = 1/2 and a Zeeman-type Hamiltonian, $\mu_B S_i \cdot g_i \cdot B$ with typically highly anisotropic g matrices. [13a, 46] The experimental χT data were fit using the PHI program[47] using the anisotropic Hamitonian given by the following equation:

$$H = D\,(S_z^2 - S(S+1)/3) + E\,(S_x^2 + S_y^2) + g\mu_B S\cdot B$$

where μ_B is the Bohr magneton and D, E, S, B represent the axial and rhombic ZFS parameters, the spin operator, and magnetic field vectors, respectively. The best fit yields D = -27.7 cm^{-1}, E/D = 0.04 cm^{-1}, g_x = 2.112, g_y = 2.246, and g_z = 2.601 for compound **16**, D = -22.3 cm^{-1}, E/D = 0.054 cm^{-1}, g_x = 2.123, g_y = 2.303, and g_z = 2.544 for compound **17**, and D = -30.3 cm^{-1}, E/D = 0.03 cm^{-1}, g_x = 1.835, g_y = 2.575, and g_z = 2.605 for compound **18**. These data suggest that the magnetic anisotropy is of the Ising type i.e. the M_S = ±3/2 sub-levels lie lower in energy than the ±1/2 ones and there is an easy axis of magnetisation. It is not possible to obtain a fit with positive D values. The field dependence of the magnetisation for the compounds at 2 K is shown in **Fig 4.4**. The magnetisation at 7 T reaches 2.73, 2.62, and 2.82 μ_B for compounds **16-18**, respectively. The lack of saturation for the compounds also suggests the presence of magnetic anisotropy. Attempts to fit the magnetisation data were unsuccessful.

To further support the conclusions arising from the magnetic analysis, the zero-field splitting parameters were calculated using CASPT2 method. The calculated values are D = -34.3 cm^{-1}, E/D = 0.149 cm^{-1}, g_x = 2.126, g_y = 2.221, g_z = 2.598 for compound **16**, D = -27.2 cm^{-1}, E/D = 0.121 cm^{-1}, g_x = 2.135, g_y = 2.201, and g_z = 2.523 for compound **17**, and D = -40.8 cm^{-1}, E/D = 0.176 cm^{-1}, g_x = 2.102, g_y = 2.216, and g_z = 2.643 for compound **18**. The calculated large value and negative sign of D and the g factors are good agreement with the experimental data obtained from variable-temperature dc susceptibility measurements.

To probe the slow relaxation of the magnetisation and quantum tunnelling effects within these systems, ac magnetic susceptibilities of **16-18** were investigated at 2 K in the temperature range 1.8-20 K. No out-of-phase ac susceptibility (χ'') signal were observed under the zero applied dc field in compounds **16-18** (**Fig 4.5**). The absence of SMM behavior is no surprise, since each complex is closely related to previously reported six-coordinate mononuclear Co^{II} compounds. The absence of slow relaxation under zero applied dc field should is due to quantum tunnelling of the magnetisation (QTM) which can be suppressed by an applied dc field. The maximum values of the relaxation time under 1000 Oe dc field were visually observed by extracting the relaxation time from the field dependence ac susceptibility (**Fig 4.6**). Hence, additional ac measurements under 1000 Oe were investigated in the selected temperature range for compounds **16-18**. The temperature dependence of the ac susceptibility of compounds **16-18** show magnetic relaxation processes for all of them (**Fig 4.7**).

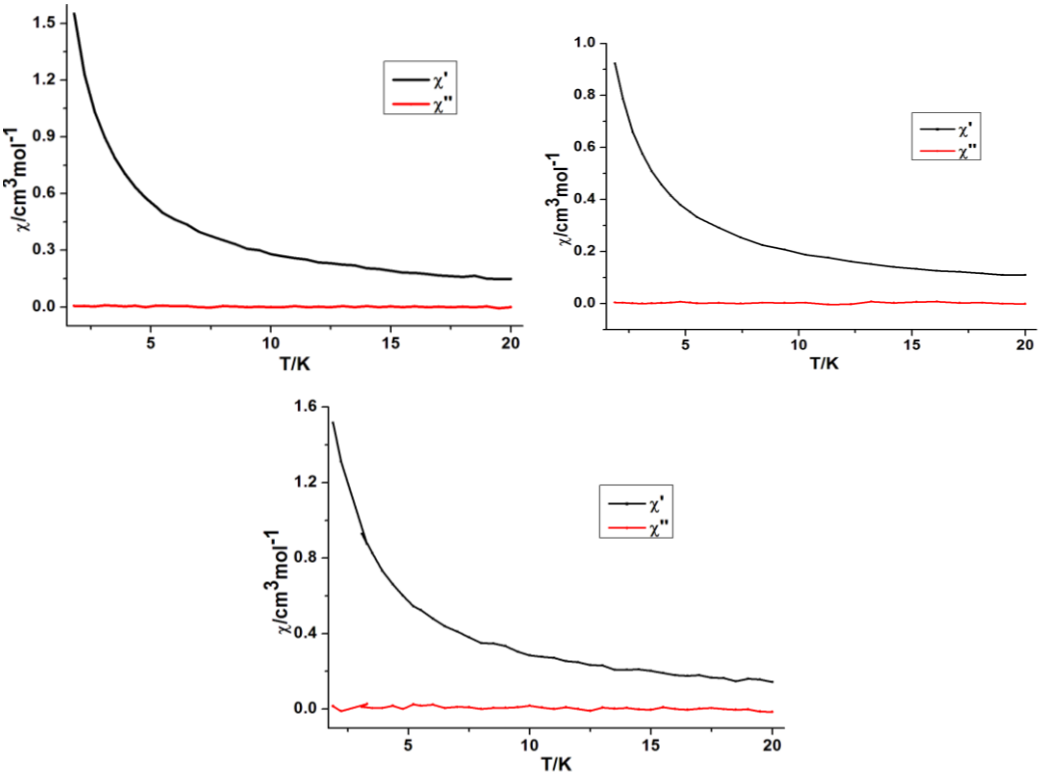

Fig 4.5 Plots of χ' and χ'' vs T under zero dc magnetic fields for **16** (up), **17** (middle) and **18** (down) at 1.8 K

The magnetisation relaxation time (τ) was derived from the frequency-dependence measurements and is plotted as a function of 1/T in **Fig 4.9**. The τ of each compound shows a strong temperature dependence and fits well with the Arrhenius equation, $\tau = \tau_0 \exp(U_{eff}/k_B T)$ characteristic of a thermally activated mechanism. There is only one relaxation process for compound **16** and **17**, and no quantum tunnelling regime was observed, implying that the applied field of 1000 Oe is appropriate to suppress any QTM effect mediated by the hyperfine and dipolar mediated relaxation process. The extracted values of the pre-exponential factor and the activation energy barrier are $\tau_0 = 8.35 \times 10^{-6}$ s, $U_{eff} = 7.30$ K for **16**, $\tau_0 = 6.13 \times 10^{-6}$ s, $U_{eff} = 10.18$ K for **17** and $\tau_0 = 1.16 \times 10^{-5}$ s, $U_{eff} = 14.10$ K for **18**. The thermally activated behaviour observed in the high-temperature range are mainly attributed to an Orbach relaxation process through the excited Ms = ± 1/2 levels. The region at low temperature is likely dominated by a Raman and/or a direct phonon-based relaxation mechanisms.[48]

To inspect the distribution of the relaxation time, the Cole-Cole plots were scrutinized for the compounds (**16-18**) **Fig 4.8**. The data can be fitted using a generalized Debye model with $\alpha < 0.08$ for **16**, $\alpha < 0.16$ for **17**, and $\alpha < 0.12$ for **18** (α indicates deviation from the pure Debye model), respectively (**Table 4.3**). These low degrees of disorder support the proposal that the present relaxation process can be considered as having a single relaxation time for each compound.

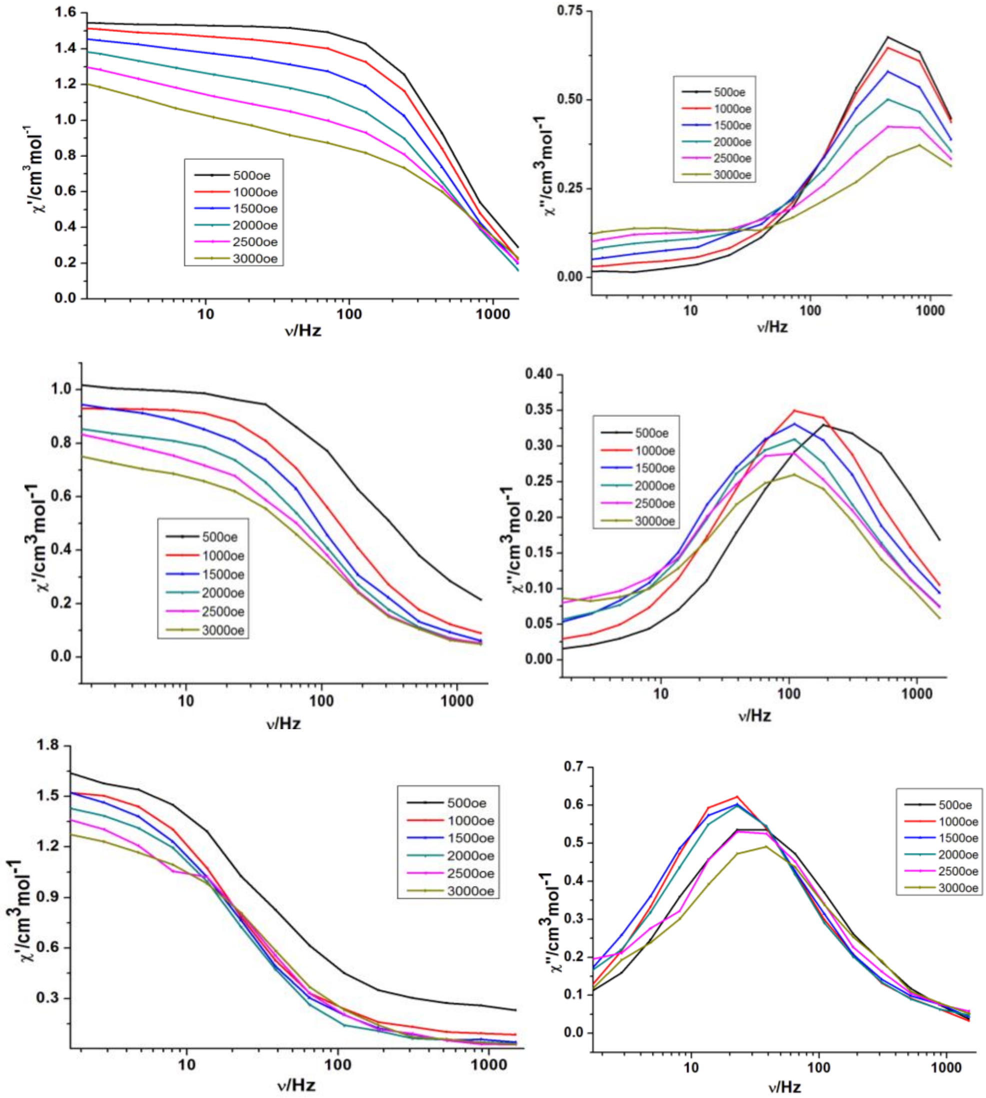

Fig 4.6 Plots of χ' (left) and χ'' (right) vs frequency under different dc magnetic fields for **16** (up), **17** (middle) and **18** (down) at 1.8 K

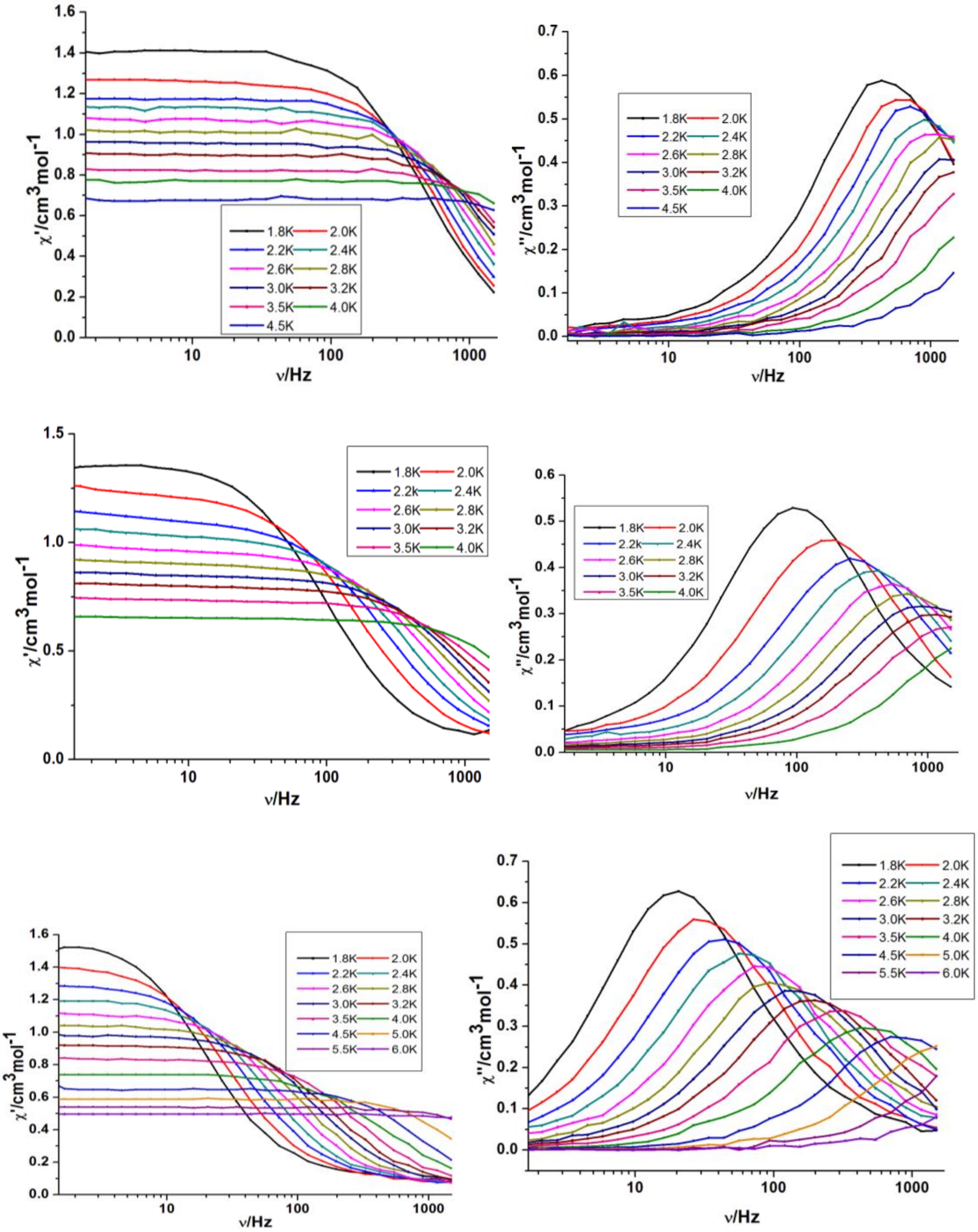

Fig 4.7 Plots of χ' (left) and χ'' (right) vs frequency under 1 KOe fields for **16** (up), **17** (middle) and **18** (down) at indicates temperatures

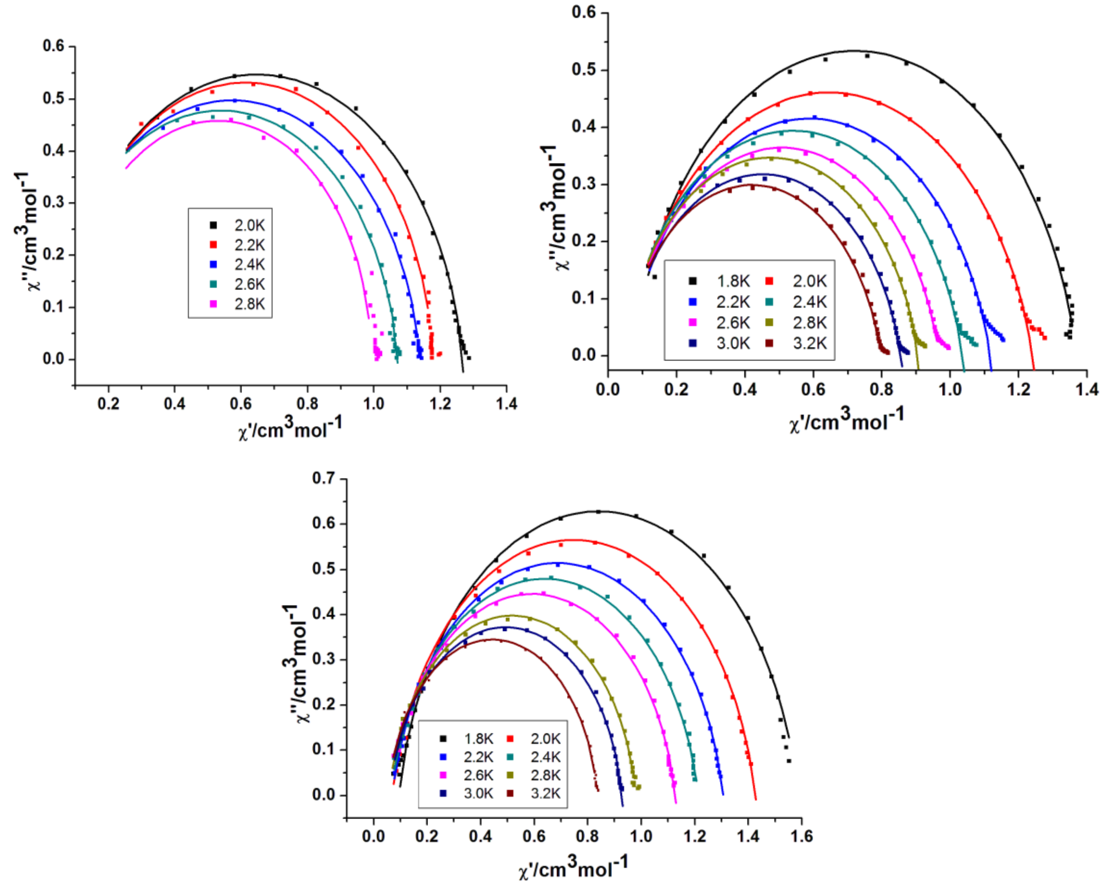

Fig 4.8 Plots of Cole-Cole for compounds **16** (up left), **17** (up right) and **18** (down), lines for fit

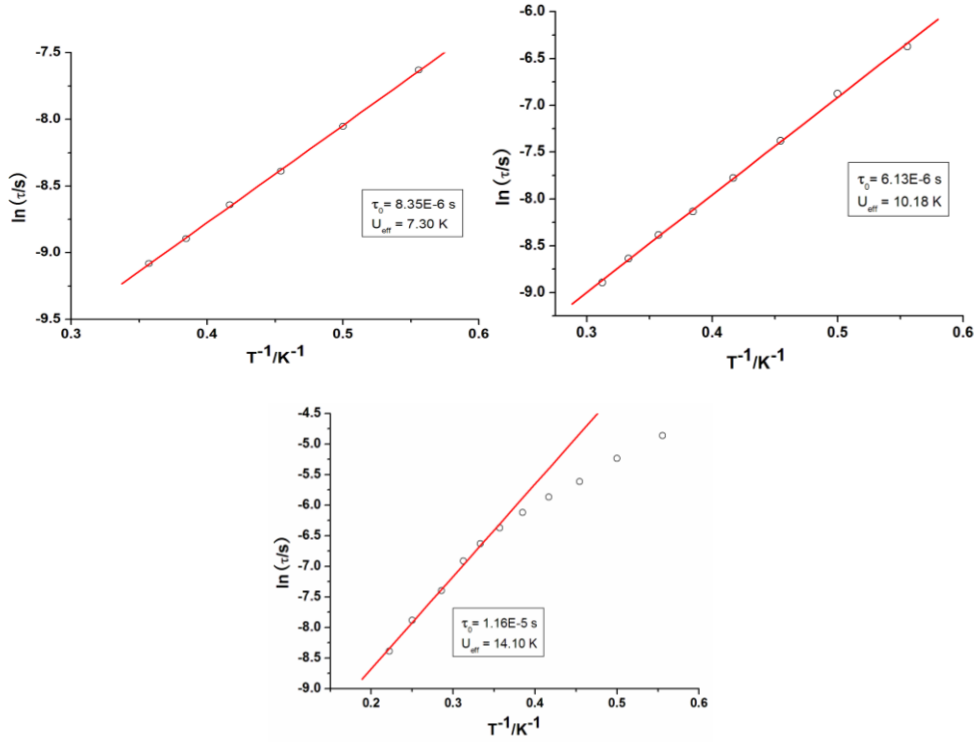

Fig 4.9 Magnetisation relaxation time (τ) versus 1/T plots for compounds **16** (up left), **17** (up right) and **18** (down)

Table 4.3 Analysis of Cole-Cole plots of complexes **16-18**

	T(K)	χ_0 (cm^3/mol)	χ_{inf} (cm^3/mol)	α	R^2
16	2.0	1.2640(1)	0.0262(3)	0.0788 (1)	0.99395
	2.2	1.1767 (9)	0.0492(6)	0.0372(1)	0.99309
	2.4	1.1359(3)	0.0050(2)	0.0784(3)	0.98819
	2.6	1.0743(5)	0.0076(2)	0.0701(3)	0.98616
	2.8	0.9955 (5)	0.06844 (7)	0.0100(2)	0.92853
17	1.8	1.3697(6)	0.0708(3)	0.1190(1)	0.98230
	2.0	1.2404 (4)	0.0503(5)	0.1599(7)	0.98236
	2.2	1.1129(4)	0.0550(7)	0.1485(5)	0.96184
	2.4	1.0356(5)	0.0427(5)	0.1390(1)	0.97693
	2.6	0.9647(8)	0.0444(9)	0.1393(6)	0.98182
	2.8	0.9050(7)	0.0423(3)	0.1401(8)	0.98290
	3.0	0.8492(7)	0.0400(6)	0.1401(7)	0.98464
	3.2	0.7980(2)	0.0399(5)	0.1400(2)	0.98312
18	1.8	1.5867(2)	0.0962(7)	0.1074(4)	0.99022
	2.0	1.4260(4)	0.0697(3)	0.1147(2)	0.99539
	2.2	1.3027(3)	0.0666(1)	0.1155(1)	0.99729
	2.4	1.2081(8)	0.0623(1)	0.1183(2)	0.99258
	2.6	1.1238(8)	0.0551(1)	0.1171(2)	0.99344
	2.8	0.9841(2)	0.0622(4)	0.1001(4)	0.99367
	3.0	0.9229(4)	0.0555(2)	0.1043(6)	0.99572
	3.2	0.8356(3)	0.05500(3)	0.0858(1)	0.99374

4.2.3 Structures of [$Dy_2(HL4)_2(OAc)_2(EtOH)_2$] (19) and [$Dy_2(L5)_2(OAc)_2(H_2O)_2$]·2MeOH (20)

Both compounds **19** and **20** crystallize in the triclinic P-1 space group. These two compounds are dinuclear Dy^{III} complexes with eight-coordinate metal centres (**Fig 4.10**). Phase purity was confirmed by powder XRD (**Fig 4.11**). The Dy^{III} ions in both compounds are ligated by an NO2 ligand set and bridged by the same μ_2-O$_{alkoxide}$ atoms of two pyridine methanol arms from two ligands which display an $\eta^2:\eta^1:\eta^1:\eta^0:\mu_2$ coordination mode (**Scheme 4.3**). The Dy-O bond lengths are 2.263(5)Å and 2.285(4)Å for **19** and 2.265(3)Å and 2.274(3)Å for **20**. The Dy···Dy distance is 3.642(4)Å for **19** and 3.631(5)Å for **20** and the Dy-O-Dy angle is 106.42(17)° for **19** and 106.23(12)° for **20**. Each Dy^{III} ion adopts a "hula hoop" coordination geometry with the cyclic ring formed by N_2O_3 from two ligands (**Fig 4.10**). In addition, one acetate anion and one EtOH are coordinated to each Dy^{III} ion and complete the coordination spheres in **19**, whereas in **20** the coordinated MeOH molecules are replaced by water ligands. Additionally, there are intra-molecule hydrogen bonds in compounds **19**, but no π-π interactions, whereas for compound **20**, there are intra- and inter-molecule hydrogen bonds and short π-π (3.7972(4)Å) interactions. Furthermore, the closest intermolecular distances between Dy^{III} ions was found to be 10.65Å in compound **19**, which is much longer than the distance found in compound **20** (7.09Å) (**Fig 4.12**).

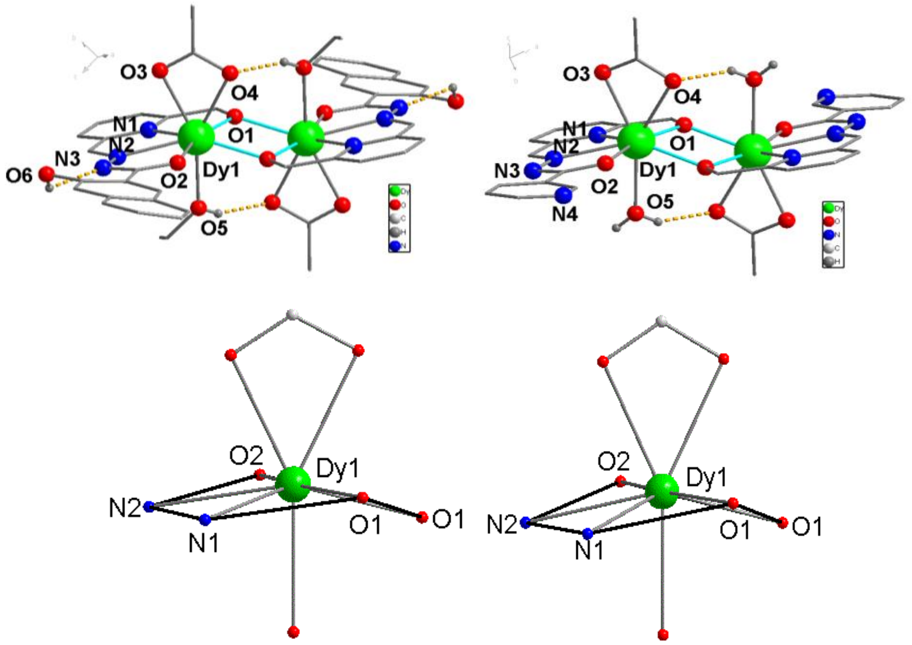

Fig 4.10 The molecules of **19** (upper left) and **20** (upper right) and coordination geometry of Dy^{III} in **19** (lower left) and **20** (lower right)

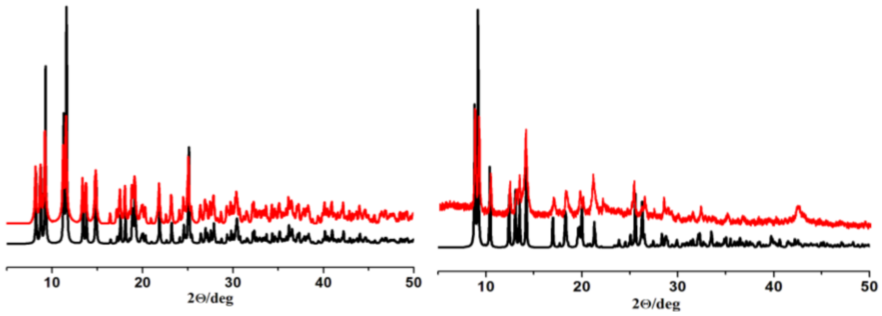

Fig 4.11 The XRD of compounds **19** (left) and **20** (right): simulated (black), experimental (red)

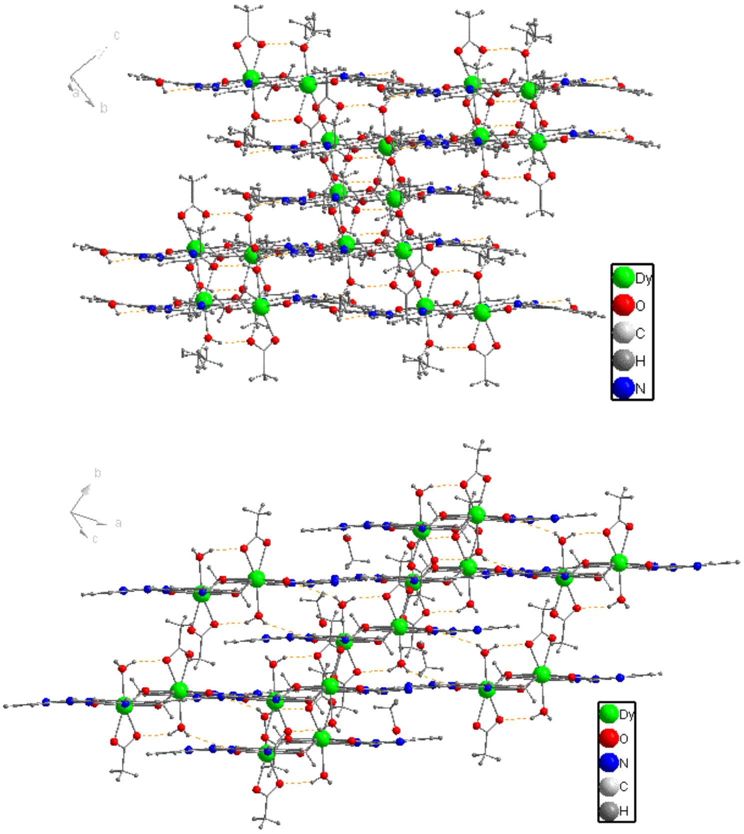

Fig 4.12 The packing of complexes **19** (upper) and **20** (lower)

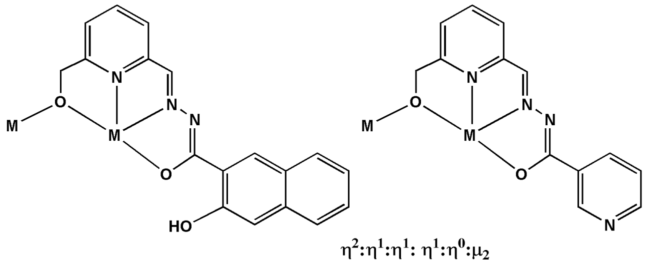

Scheme 4.3 The coordination modes of the H_3**L5** and H_2**L6** in compounds **19** and **20**

4.2.4 Magnetic properties of compounds 19 and 20

Direct-current (dc) magnetic susceptibilities of **19** and **20** have been measured in an applied magnetic field of 1000 Oe between 300 and 1.8 K (**Fig 4.13**). The data are summarized in **Table 4.4**. The observed χT value at 300 K is 28.45 cm^3 K mol^{-1} for **19** (26.46 cm^3 K mol^{-1} for **20**), which is in good agreement with the expected value of 28.36 cm^3 K mol^{-1} for two uncoupled Dy^{III} ions (S = 5/2, L = 5, $^6H_{15/2}$, g = 4/3). The χT value gradually decreases on the lowering of temperature from 300 to 50 K and then further decreases rapidly to reach 4.84 cm^3 K mol^{-1} for **19** and 7.54 cm^3 K mol^{-1} for **20** at 1.8 K. The decline of χT is likely due to a combination of the progressive depopulation of

Dy^{III} excited Stark sublevels[39a] and possible exchange interaction between the metal ions.

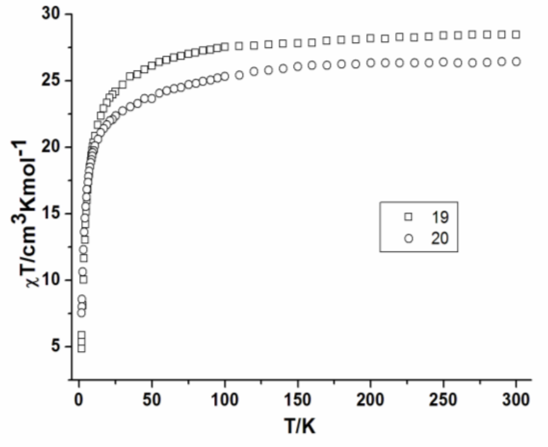

Fig 4.13 Plots χT vs T products at 1000 Oe dc field for **19** and **20**

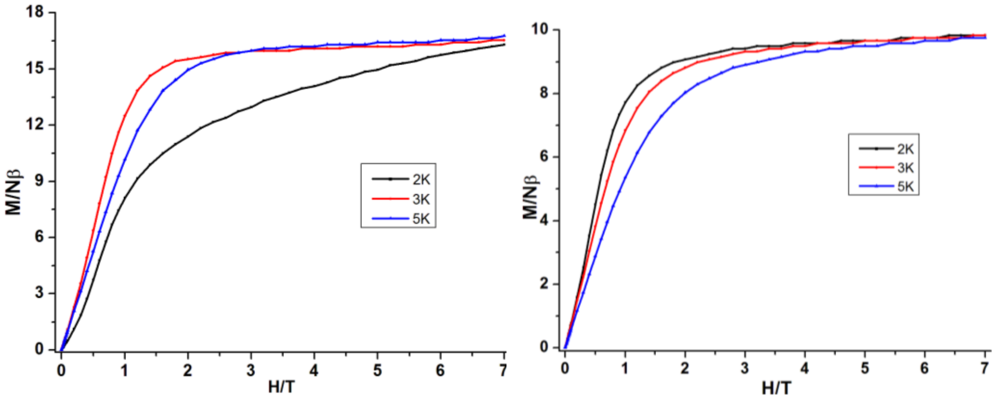

Fig 4.14 Plots of M vs H for **19** (left) and **20** (right)

Magnetisation (M) data were collected in the 0-7 T field range at different temperatures. The lack of saturation of magnetisation (**Fig 4.14**) suggests the presence of a significant magnetic anisotropy and/or low-lying excited states. The magnetisation increases rapidly at low field and eventually reaches the value of 16.76 μ_B for **19** and 9.84 μ_B for **20** at 7 T without clear saturation. These values are lower than the expected saturation value of 20 μ_B (g = 4/3) for two non-interacting Dy^{III} ions, most likely due to the crystal-field effect. From the shape of the magnetisation of compound **19** a hysteresis might be expected. However, the absence of the hysteresis loop at 2 K may be caused by the presence of a relatively fast zero-field relaxation.

Table 4.4 Magnetic data of compounds **19** and **20** summarized from the dc measurements

Compound	Ground state of Ln^{III} ion	χT expected for non-interacting ions per complex (cm^3 K mol^{-1})	χT measured at 300 K per complex (cm^3 K mol^{-1})	χT measured at 1.8 K per complex (cm^3 K mol^{-1})	Magnetisation at 2 K and 7 T (Nβ)
Dy^{III}_2 (**19**)	$^6H_{15/2}$	28.28	28.50	4.84	16.31
Dy^{III}_2 (**20**)	$^6H_{15/2}$	28.28	26.46	7.54	9.84

In order to explore potential SMM behaviour alternating current (ac) magnetic susceptibility studies were carried out on freshly filtered samples of **19** and **20**. In zero field, no out-of-phase signal (χ'') was observed in **19**, indicating the absence of SMM behaviour. Generally, this behaviour maybe due to the very fast quantum tunnelling of the magnetisation (QTM), as is commonly seen in pure lanthanide complexes. The QTM may be shortcut by applying a static dc field. Therefore, ac susceptibility measurements were obtained under a static dc field (**Fig 4.15**) (0-3000 Oe). The result indicates that the applied dc field indeed slows down the relaxation time by reducing or suppressing quantum tunnelling of the magnetisation. Therefore ac susceptibility measurements were carried out under a dc field of 2000 Oe (**Fig 4.16**). From the frequency dependencies of the ac susceptibility, it is possible to derive the magnetisation time in the form of τ plotted as a function of 1/ T between 4 and 8 K (**Fig 4.18**). At lower temperatures, the dynamics of **19** become temperature independent as expected in a pure quantum regime with a τ value of 1.22×10^{-3} s. Above 5 K, the data obey the Arrhenius law $\tau = \tau_0\exp(U_{eff}/k_BT)$ with an energy barrier of 35.36 K, and a pre-exponential factor τ_0 of 3.15×10^{-7} s. For compound **20**, in zero dc field, the ac susceptibilities measured reveal the presence of slow relaxation of the magnetisation, typical of SMM behaviour (**Fig 4.17**). The relaxation time shows two distinct regimes stemming from a temperature-independent quantum tunnelling regime at low temperatures and a temperature-dependent thermally activated regime at temperatures above 6 K. This high-temperature regime follows the Arrhenius law $\tau = \tau_0\exp(U_{eff}/k_BT)$ giving an energy barrier of 38.46 K and pre-exponential value τ_0 of 1.04×10^{-6} s (**Fig 4.18**).

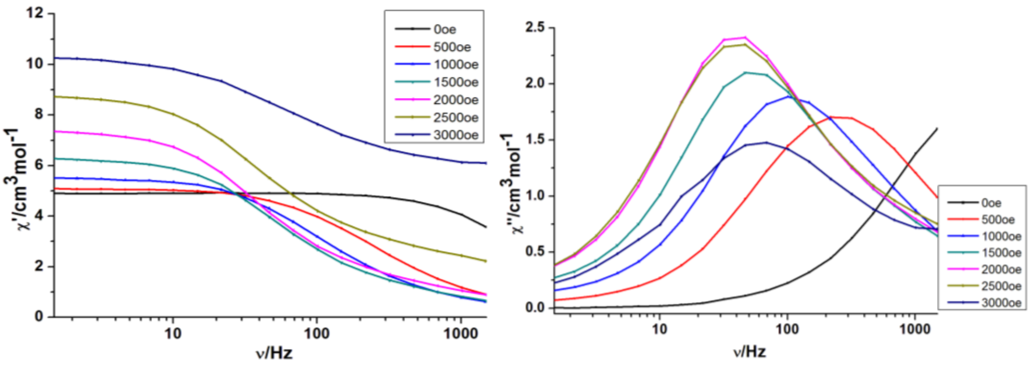

Fig 4.15 Plots of χ’ (left) and χ’’ (right) vs frequency under different dc magnetic fields for **19** at 2 K

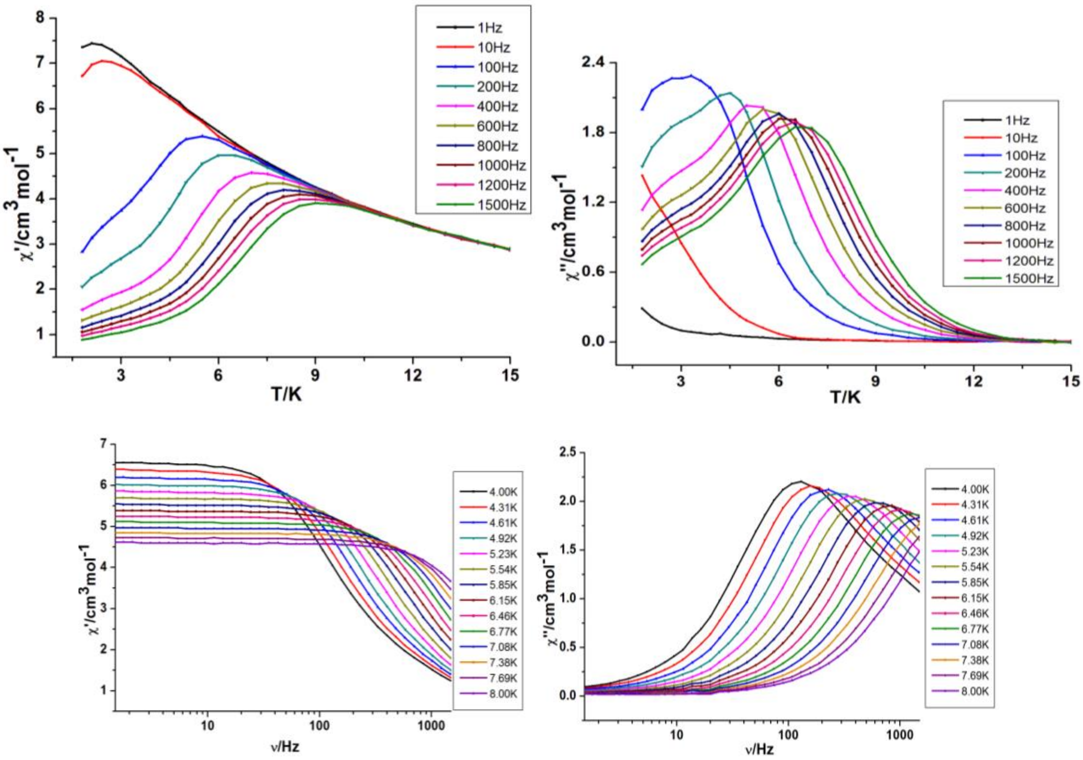

Fig 4.16 Plots of χ’ (left) and χ’’ (right) vs frequency (up) and teperature (down) for **19** under 2000 Oe dc field

The Cole-Cole diagram (χ’’ vs χ’ at different temperatures) can be used to study the distribution of the relaxation process, which is frequently characterized and discussed for SMMs or SCMs. The data of **19** and **20** plotted as Cole-Cole diagrams are shown in **Fig 4.19**, the shape of the Cole-Cole plot of **19** is relatively unsymmetrical. A good fit to the generalized Debye model could only be obtained between 5.5 and 7.3 K giving small α values (less than 0.1) (**Table 4.5**). The small α value suggests that there is only one relaxation process present in **19**. However, for **20**, a good fit was obtained according to the Debye model, the α values are less than 0.33 which indicates a relatively wide range of relaxation processes most likely due to a combination of QTM and thermally assisted relaxation pathways.[36a]

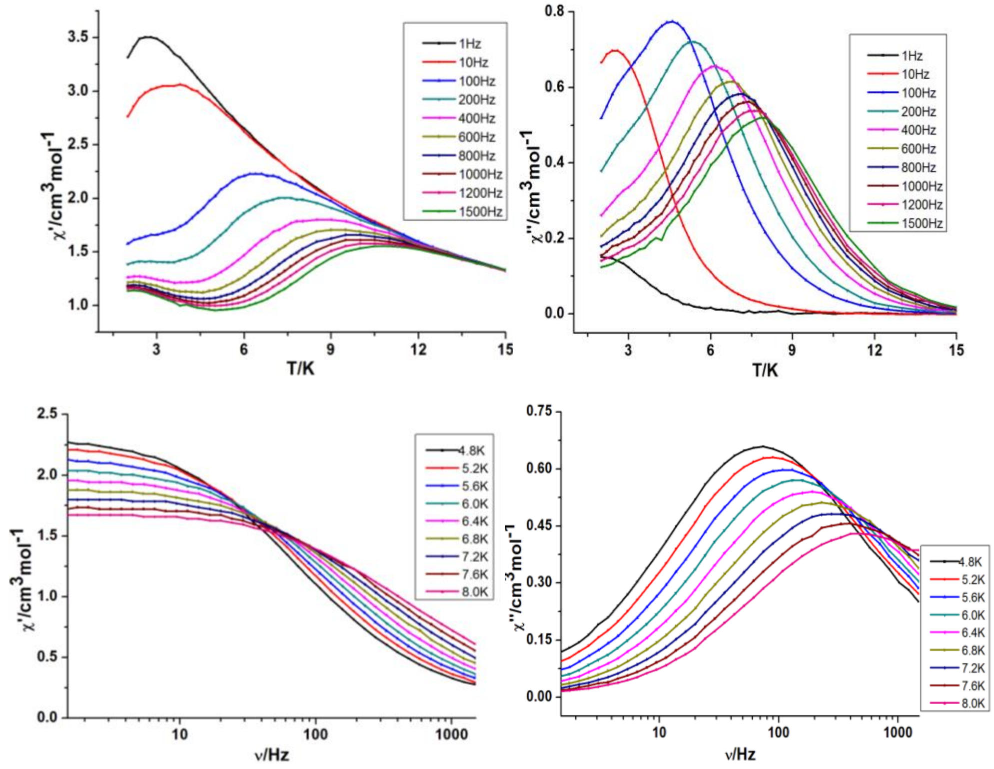

Fig 4.17 Plots of χ’ (left) and χ’’ (right) vs frequency (up) and teperature (down) for **20** under zero dc field

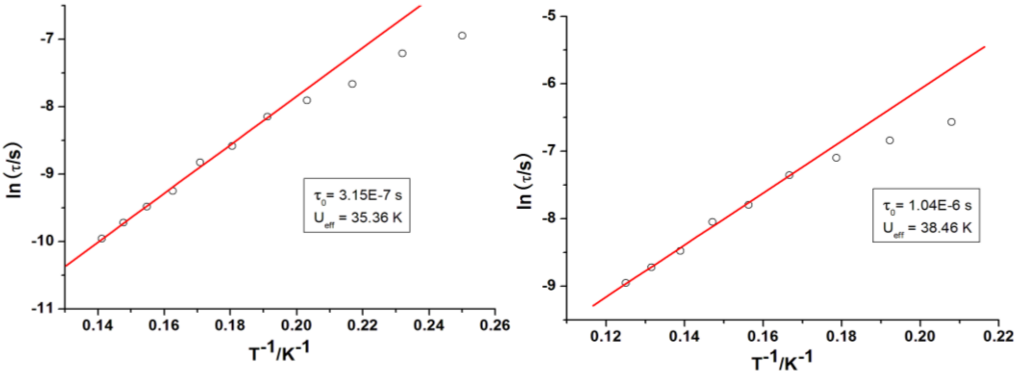

Fig 4.18 Magnetisation relaxation time (τ) versus 1/T plots for compounds **19** (left) under 2000 Oe dc field and **20** (right) under zero dc field.

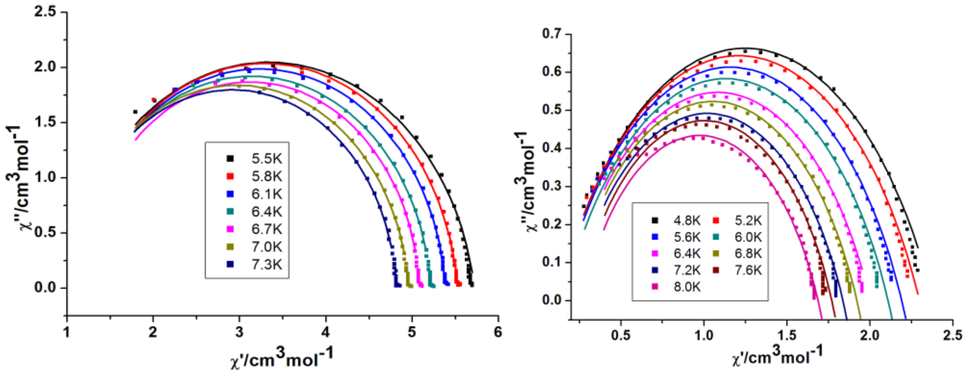

Fig 4.19 Cole-Cole plots of compounds **19** (left) and **20** (right) (solid lines for fit)

Table 4.5 Analysis of Cole-Cole plots of complexes **19** and **20**

	T(K)	χ_0 (cm^3/mol)	χ_{inf} (cm^3/mol)	α	R^2
19	5.5	5.7274(4)	0.9582(3)	0.0938(5)	0.99586
	5.8	5.5240(3)	1.07211(2)	0.0564 (2)	0.99767
	6.1	5.3759(2)	1.0672(1)	0.0534(2)	0.99837
	6.4	5.2296(1)	1.0761(4)	0.0465(8)	0.99806
	6.7	5.0843(6)	1.1682(8)	0.0288(6)	0.99758
	7.1	4.9576(8)	0.9891(1)	0.0472(2)	0.99782
	7.4	4.8305(6)	1.0288(4)	0.0379(2)	0.99588
20	4.8	2.3653(8)	0.1010(3)	0.3235(5)	0.9943
	5.0	2.2811(4)	0.1131(2)	0.3219(9)	0.99542
	5.2	2.1750(9)	0.1286(4)	0.3163(5)	0.99589
	5.4	2.0769(2)	0.1528(8)	0.3054(9)	0.99438
	5.6	1.9880(1)	0.1638(7)	0.3069(2)	0.99501
	5.8	1.9026(8)	0.1825(3)	0.3022(9)	0.99537
	6.0	1.8350(7)	0.2073(3)	0.3070(7)	0.993
	6.2	1.7586(8)	0.2367(1)	0.3020(&)	0.98917
	6.4	1.7008(3)	0.2510(4)	0.3094(8)	0.99265

4.2.5 Structure-property relationship of compounds 19, 20 and the related Dy2 dimer

To probe the structure-property relationship in mono-hydrazone Schiff-base ligand based Dy$_2$ SMM systems, some crucial parameters of the structures of **19**, **20** and **A-D**[49] have been listed in **Table 4.6**. According to the data obtained on previously synthesized Dy$_2$ systems,[39] it is clear that the mono-hydrazone Schiff-base ligand is a rigidly linear ligand that can provide different kinds of coordination modes in terms of the available multichelating sites. The tautomeric nature of the arylhydrazone ligands makes this system especially favourable for the isolation of such Dy$_2$ SMMs.[49b] There is a general route to assemble such Dy$_2$ systems with varying magnetic properties using such ligands. The "hula-hoop" geometry is a suitable and robust ligand field for slow magnetic relaxation of Dy^{III} ions. The interposition of another O atom into the coordination sphere breaks this hula-loop geometry, thus leading to a weakening or disappearance of the relaxation behaviour. In compounds **19** and **20**, each Dy^{III} ion has an eight-coordinate N2O6 coordination environment and is linked to the other Dy^{III} via μ_2-O$_{alkoxide}$ bridges. As seen in **Fig 4.20**, both compounds have similar static magnetic behaviour and are antiferromagnetically coupled, as expected from the small Dy-O-Dy angle.

The dysprosium ions in compounds **A**, **B** and **C** are bridged by hydrazone-O, in compound **19** and **20** they are bridged by alkoxides, while in compound **D** they are bridged by phenolate. They all show different magnetic behaviour and coupling. Thus it is not possible to predict the nature of the coupling between Dy ions from the Dy-O-Dy angle. Probably, the dominating factors governing the Dy-Dy coupling are a combination of Dy-O length and the local ligand field. For the dynamic magnetisation, compound **A** has the highest energy barrier, because of the high axiality and strong Ising exchange interaction, which efficiently suppresses quantum tunnelling of the magnetisation. The energy barriers of compound **19** and **20** are lower, which may be due to the coordinating anions which are different from those in **A** to **D**. A similar behaviour has been previously observed in a Dy dimer system.[36a] Also, the axial solvent molecule contributes to this effect in terms of different energy barrier heights. Last but not least, it is noticeable that, by designing the ligands, suitable modulation of inter- or intramolecular hydrogen bonds or π-π interactions may have an unexpected effect on magnetic relaxation dynamics.

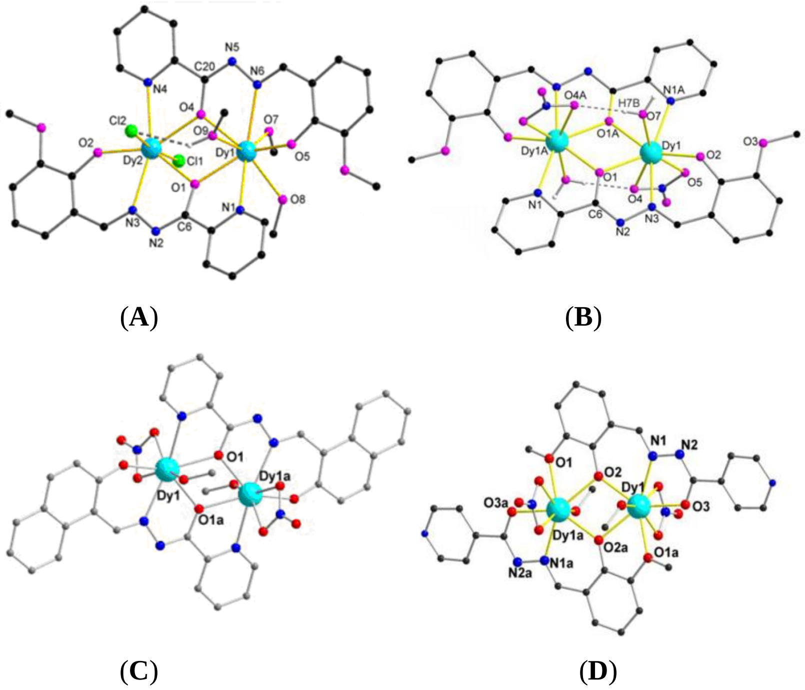

(**A**) (**B**)

(**C**) (**D**)

Fig 4.20 The reported Dy2 SMMs based on mono-hydrazone ligands

Table 4.6 Selected crucial parameters of structure of **19**, **20** and reported Dy_2 based on related ligands

compounds	**A**	**B**	**C**	**D**	**19**	**20**
Bridged atoms	Hydrazone-O	Hydrazone-O	Hydrazone-O	Phenoxide-O	Alkoxide-O	Alkoxide-O
coupling	ferro	ferro	antiferro	ferro	antiferro	antiferro
$d_{average}$	2.370	2.355	2.372	2.381	2.384	2.384
Dy-O-Dy	111.67 °	110.12 °	114.88	106.41	106.40	105.79
Dy-Dy	3.769	3.8258	3.9225	3.9553	3.643	3.631
Field (dc)	0	0	0	0	2000 Oe	0
Ueff	198K, 150 K	69 K	41.29 K	56 K	35.36 K	38.46 K

4.2.6 Structure of $[Co^{II}(L7)]$ (21)

Complex **21** crystallizes in the monoclinic space group $P2_1/n$. As show in **Fig 4.21** (a), the molecule is neutral and consists of one diprotonated Schiff-base ligand (L^{2-}) and one Co^{II} ion, The Co^{II} ion is encapsulated in a slightly distorted trigonal prismatic coordination environment. The top and bottom planes of the prism are built by one piperazine nitrogen, and one nitrogen and oxygen of the corresponding Schiff base arms in such a way, that always one oxygen and one nitrogen of the different arms are on top of each other (**Fig 4.21** b). The normals of these planes are tilted with respect to each other by 6° (**Fig 4.21** b) and twisted by 3° (**Fig 4.21** c). We assume that the tilting angle is caused by the piperazine unit. The two N of piperazine are much closer to each other (2.47Å) than the N-O pairs (2.81Å). The Co^{II}-$N_{piperazine}$ distances are longer than the Co^{II}-N_{imino} distances, and both of these two groups are longer than Co-O_{phenol} distances. The Co(II) atoms are well-separated with an interatomic separation of 7.02Å, thus excluding pertinent intermolecular magnetic interactions.

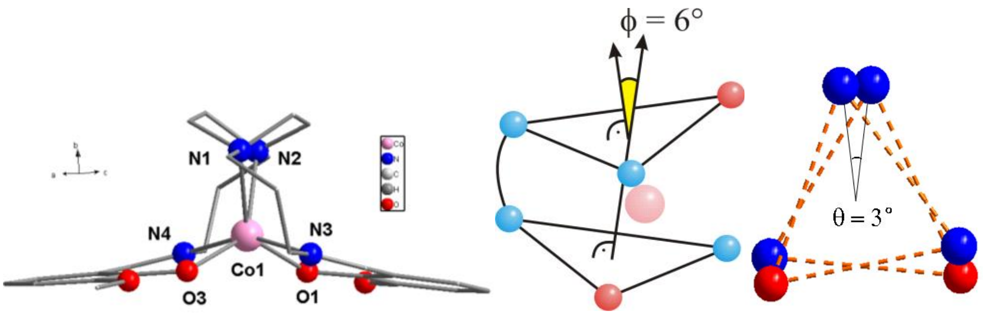

(a) (b) (c)

Fig 4.21 (a) The molecular structure of **21** (hydrogen atoms have been omitted for clarity). The theoretical calculation provides that the easy axis points out of the plane of paper; (b and c) Tilt- and twist angles of the coordination polyhedron with respect to ideal prismatic symmetry.

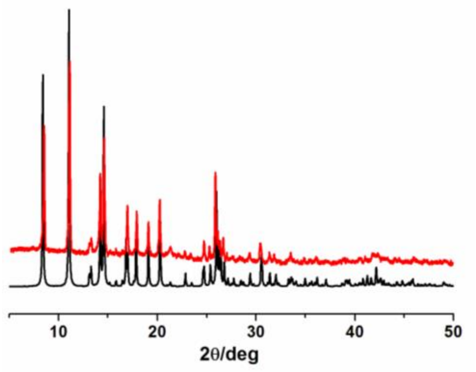

Fig 4.22 The XRD of compound **21**

4.2.7 Magnetic properties of compound 21

Magnetic measurements were carried out on polycrystalline samples. As show in **Fig 4.23** (left), the χT value at 300 K is 2.46 cm^3 K mol^{-1}, a little higher than the expected value, which is in the range of a single non-interacting high spin d^7 Co^{II} ion with a considerable contribution of the orbital angular momentum. It remains roughly constant for the high temperature range (300-50 K), then decreases quickly to 1.83 cm^3 K mol^{-1} at 2.0 K due to the zero field splitting of the Co^{II} ion. The magnetisation was measured up to 7 T dc field at 2, 3 and 5 K, respectively. The lack of saturation of the magnetisation at higher field (**Fig 4.23**) implies the presence of significant magnetic anisotropy. The magnetisation data were fitted using the *ANISOFIT 2.0* program (**Fig 4.23**),[50] which takes account of the phenomenological spin Hamiltonian. The obtained D value was -44.56 K, with the corresponding E and g being 0.0006 K and 2.47, respectively. The large negative D value indicates that compound **21** has large uniaxial anisotropy. No reasonable optimization was obtained when the initial D value is positive, indicating the correct choice of the negative sign.

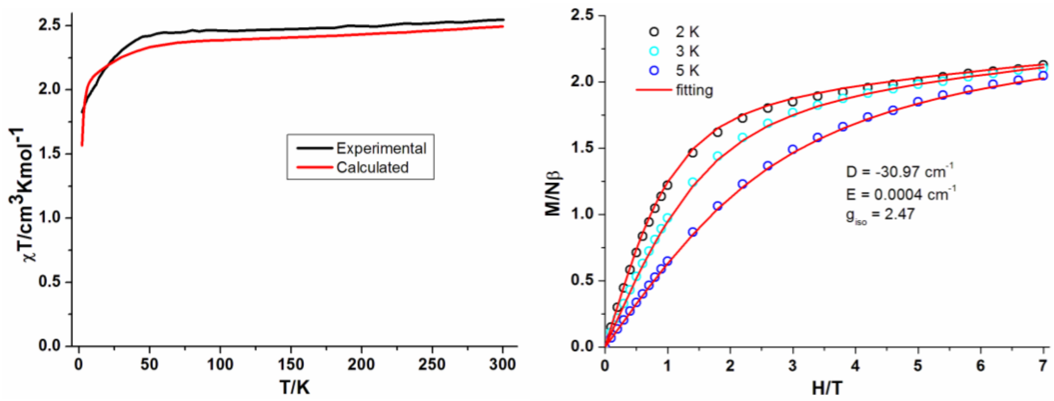

Fig 4.23 Experimental (black) and calculated (red) plots of χT vs T (left) and plots of M vs H of compound **21** (right)

In order to probe the magnetic dynamic behaviour, the ac susceptibilities of **21** were measured in the temperature range 1.8-10 K under zero dc field and 3.0 Oe ac field oscillating at frequencies between 1 and 1500 Hz. A frequency-dependent signal was observed in the χ'' versus T plot below 10 K (**Fig 4.24**). This suggests slow relaxation of the magnetisation, which is generally attributed to an SMM. However, relaxation barriers cannot be extracted from this data as a broad peak was observed at high frequencies. In mononuclear Co^{II} systems, the broad peak generally indicates the presence of QTM, which could be suppressed or quenched by applying a static dc field. Therefore, ac susceptibility measurements were obtained under a static dc field from 300 Oe to 1500 Oe. When different small dc fields are applied, the χ'' versus frequency signal at 4.3 K dramatically changes with the magnitude of the applied dc field (**Fig 4.25**). The signal observed without dc field shows a clear maximum and diminishes when the dc field is increased. With a field of 600 Oe at high frequency, the maximum disappears under our measurement conditions. On the other hand, another peak at about 10 Hz appeared with the application of the dc field up to 300 Oe, the increase of the dc field shifts the peak to lower frequencies and enhances its magnitude. The behaviour is similar to that reported for the mononuclear $[Co^{II}(P(S)\{[N(CH_3)N{=}CHC_3N_2H_3]_3)\}](NO_3)_2$,[51] which also has a trigonal prismatic coordination geometry. Due to the fact that the peak shift is negligible between 900 Oe and 1500 Oe, the variations of the χ'' versus frequency signal with temperature under 1200 Oe applied dc field were studied. At 1200 Oe, the χ'' versus frequency signal for complex **21** only showed one peak (**Fig 4.26**) which shifts to higher frequencies when the temperature is increased. This indicates a thermally activated regime and confirms the SMM behaviour. Characteristic Arrhenius linearity (**Fig 4.27**) was observed between 5.4 and 6.0 K giving a U_{eff} of 98 K and a τ_0 of

1.54×10^{-11} s.

To estimate the nature of magnetic anisotropy of the ground state, the axial zero-field-splitting parameter and g-matrix were calculated by PD Dr. Karin Fink and Dr. Tilman Bodenstein using the CASSCF/SOCI method. These *ab* initio calculations reveal a splitting of the ionic ^4F ground state of Co^{II} of the order of 14600 K due to the trigonal prismatic ligand field. The ground state is separated from the next states by about 2253 K. Due to spin-orbit interaction, the ^4A ground state splits into two Kramers doublets E_1 and E_2, with a spin-orbit splitting of 145.12 K. The next excited states follow above 2410 K.

Thus, the low-lying energy spectrum, consisting of the two Kramers partners, can be mapped onto an $S = 3/2$ spin Hamiltonian $D\ S_z^2 - 1/3\ S(S-1)$ yielding $D = -72.56$ K. The sign of D was obtained by comparing the wave functions for E_1 and E_2, namely a 78.6% S = 3/2 and 21.4% S = 1/2 mixture was found for E_1, and vice versa for E_2, respectively. The calculated large value and negative sign for D are in good agreement with the experimental data obtained from magnetisation measurements, further demonstrating the large magnetic uniaxial anisotropy of **21**. It is important to keep in mind the uncertainties in the determination of the D values for this kind of system due to the limitations of the Hamiltonian employed.[52]

For calculating g-factors, two different approaches were considered, one in which the Zeeman interaction is included into the SOCI using finite perturbation theory,[53] and another where the Zeeman splitting is accounted for by first-order degenerate perturbation theory within the ground-state Kramers doublet.[54] The calculated g-factors confirm the high uniaxial anisotropy of **21** with $g_1 = 8.12$, $g_2 = 0.59$, $g_3 = 0.11$, for method 1 and $g_1 = 8.14$, $g_2 = 0.084$ and $g_3 = 0.073$ for method 2. The obtained easy axes of these methods differ only by ~ 4°. Since the g-factors are very small in the perpendicular plane, the other two axes are not well-defined. The isotropic g-factors 2.94 and 2.74 are in reasonable agreement with the fitted values. Furthermore, the χT were simulated directly from the *ab initio* energies[53] (**Fig 4.23**).

Very recently, Ruiz and co-workers predicted the property of 3d SIMs based on the coordination numbers and electronic structures of paramagnetic centres. For a Co^{II} system, SMM behaviour could occur either via the trigonal pyramid (large positive D values) or the trigonal prism (large negative D values) coordination modes. The present compound **21** further supports the hypothesis that trigonal prismatic coordination geometry of Co^{II} can generate large uniaxial anisotropy and lead to high energy barriers.

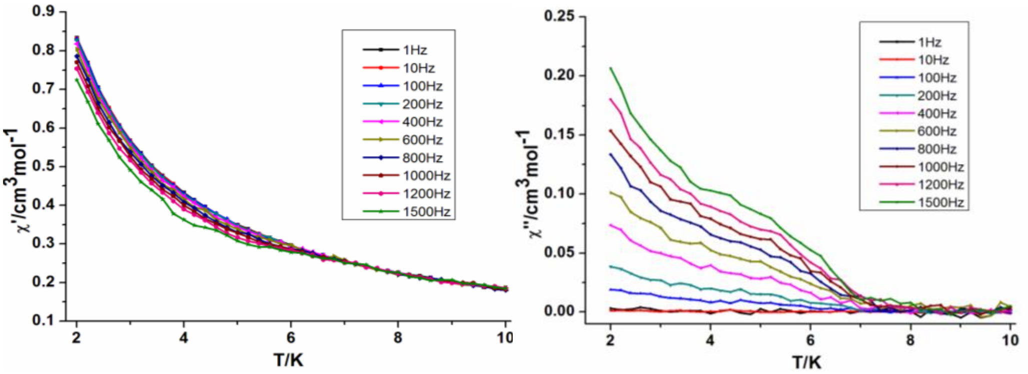

Fig 4.24 Plots of χ' (left) and χ'' (right) vs T under different frequency for **21** in zero dc field

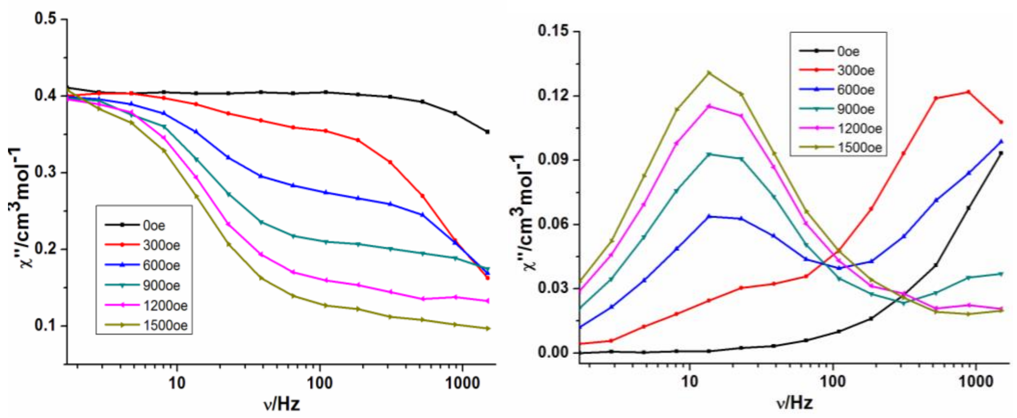

Fig 4.25 Plots of χ' (left) and χ'' (right) vs frequency under different dc magnetic fields of compound **21** at 4.3 K

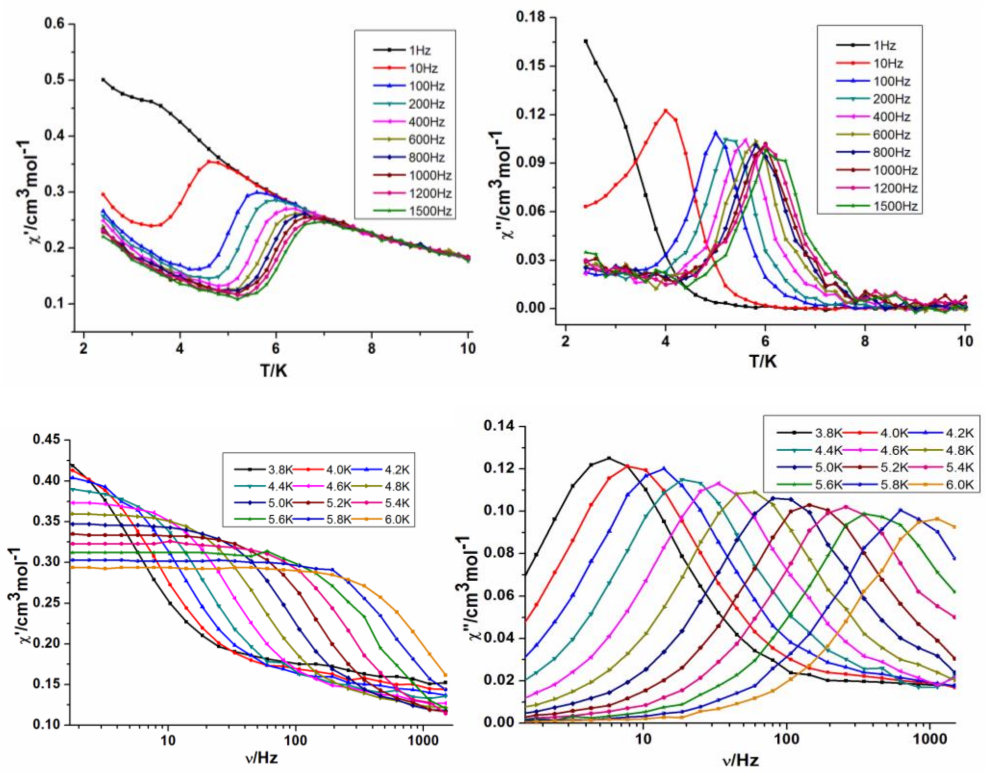

Fig 4.26 Plots of χ' (left) and χ'' (right) vs T (up) under different frequencies for **1** in 1200 Oe dc field; Plots of χ' (left) and χ'' (right) vs frequency (down) under different temperatures in 1200 Oe dc field

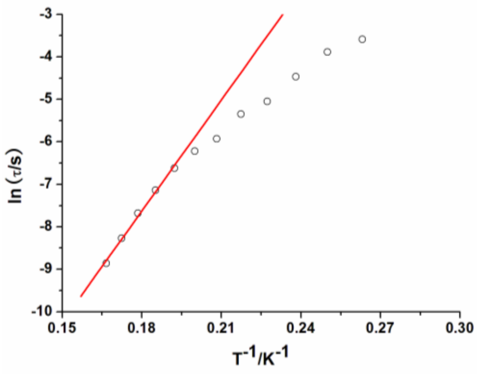

Fig 4.27 Plots of ln(τ) vs T^{-1}: The red lines represent Arrhenius fitting

4.2.8 Structures of $[Co_2Dy_2(L8)_4(NO_3)_2(MeOH)_2]\cdot 2CH_2Cl_2$ (22), $[Co_2Dy_2(L8)_4(NO_3)_2(DMF)_2]\cdot 2C_2H_6CO$ (23) and $[Zn_2Dy_2(L8)_4(NO_3)_2(MeOH)_2]\cdot 2CH_2Cl_2$ (24)

All three compounds (**22-24**) were measured by single crystal X-ray diffraction. The results indicate the three compounds crystallize in the monoclinic space group $P2_1/c$, triclinic space group P-1 and monoclinic space group $P2_1/c$ for compounds **22-24**, respectively and the phase purity of compounds **22-24** was confirmed by powder XRD (**Fig 4.29**). Compounds **22** and **24** are isomorphous, differing only in the nature of the 3d metal ion. Compound **23** is similar to compound **22**, differing only in the details of the coordinated and lattice solvent molecules. Therefore, only compound **22** will be described in detail. The asymmetric crystallographic unit contains one dipositve 3d ion (Co^{II} for **22** and **23**, Zn^{II} for **24**), one Dy^{III} ion, two dianionic ligands $(\mathbf{L4})^{2-}$, one nitrate (NO_3^-) and one coordinated solvent molecule (MeOH, **22** and **24**; DMF, **23**) (**Fig 4.28**).

The Co^{II} ion has a distorted octahedral geometry with an O5N donor set, while the Dy^{III} ion has a distorted square antiprismatic geometry with an O7N donor set. The Co^{II} ion is coordinated by ONO atoms on three equatorial positions while the fourth equatorial and the axial positions are occupied by two μ_3-phenoxide O-atoms of the amino-phenol part of the Schiff base ligands and one O- atom of the solvent (MeOH) molecule. Each Dy^{III} ion is ligated by both the NO2 group and O2 group from opposite directions, filling five coordination sites. The sixth coordination site is occupied by a μ-O-atom (phenoxide) of the amino-phenol part of the Schiff base ligand and seventh and eighth sites are taken by two O atoms of a chelating nitrate.

Both compounds have heterometallic defect-dicubane or butterfly cores (Dy_2Co_2) with two Co^{II} ions in the body positions and each Dy^{III} ion in the wing positions with all the metals in the same plane (**Fig 4.28**). Two dianionic ligands $(\mathbf{L4})^{2-}$ coordinate and bridge among the metal centres, one from above and one from below the plane of co-planar Dy_2Co_2 unit, displaying a $\eta^0:\eta^1:\eta^1:\eta^3:\mu_3$ bridging mode (**Scheme 4.4**, a). Two further ligands also bind and bridge to the Dy_2Co_2 core with a $\eta^1:\eta^2:\eta^1:\eta^2:\mu_3$ bridging mode (**Scheme 4.4**, b). Two μ_3-phenoxide O-atoms of the amino-phenol part of the Schiff base ligands bridge Co-Co-Dy ions in a triangular fashion, one from above and another from below the plane of the Dy_2Co_2 unit and the other four bridging positions are bridged by alternating μ-O-atoms of the phenoxide of the two pockets of the Schiff base ligands $(\mathbf{L4})^{2-}$. The Co-O/N and Dy-O/N bond distances vary from 2.032(17)Å to 2.296(2)Å and 2.159(4)Å to 2.515(3)Å, respectively. There are strong intra-molecular hydrogen bonds in compound **22** and **24**. There is no π-π stacking interaction between the aromatic rings within the compounds **22-24**.

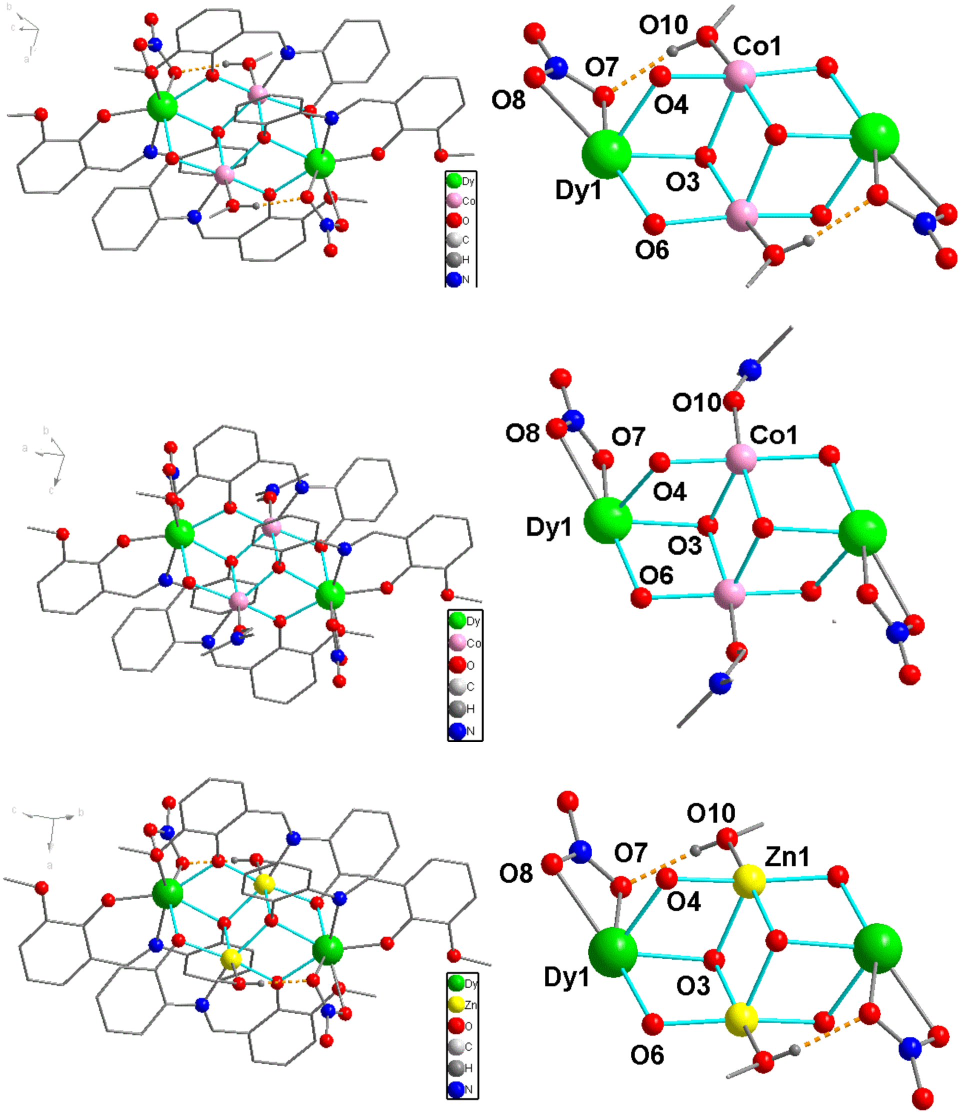

Fig 4.28 The structures and cores of compounds **22** (up), **23** (middle) and **24** (down)

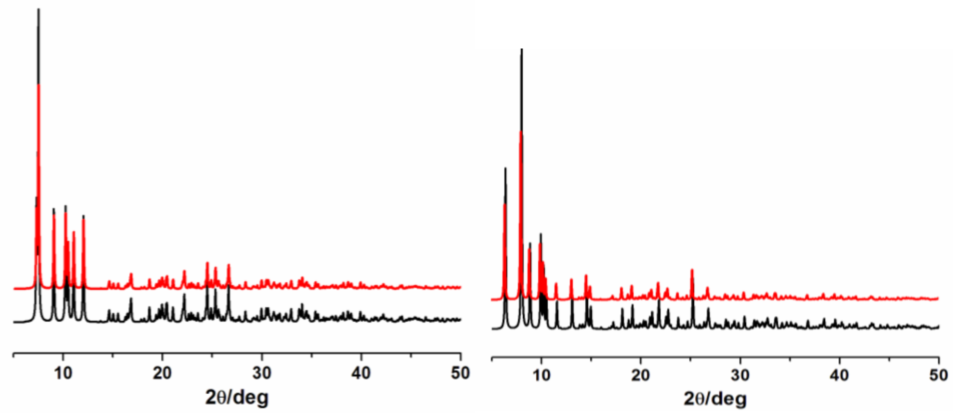

Fig 4.29 The XRD of **22** (left) and **23** (right): simulated (black), experimental (red)

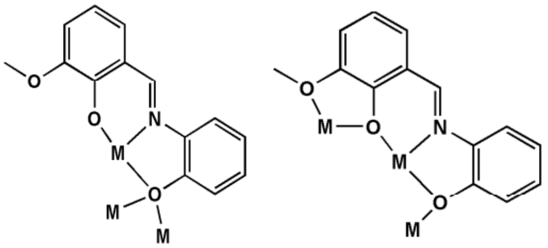

$\eta^0:\eta^1:\eta^1:\eta^3:\mu_3$ $\eta^1:\eta^2:\eta^1:\eta^2:\mu_3$

(a) (b)

Scheme 4.4 The coordination modes of the H_2**L8** in compounds **22-24**

4.2.9 Magnetic properties of compounds 22-24

The bulk magnetic properties of compounds **22-24** were probed via variable temperature, dc and ac susceptibility measurements on polycrystalline samples. Magnetic data of compounds **22-24** summarized from the dc measurements (**Table 4.7**). The dc studies (**Fig 4.30**) measured in magnetic fields of 1000 Oe reveal room temperature χT values of **22** and **23** of 30.21 and 32.29 cm^3 K mol^{-1}, respectively, in good agreement with the expected value of 32.09 cm^3 K mol^{-1} for two uncoupled Co^{II} ions (3.75 cm^3 K mol^{-1}) and two uncoupled Dy^{III} ions (28.34 cm^3 K mol^{-1}). As the temperature is lowered, the χT value increases very slowly (300-50 K) and then sharply increases (50-3.5 K), reaching maximum values of 67.95 and 68.20 cm^3 K mol^{-1} at 3.5 K for **22** and **23**, respectively. This suggests intramolecular ferromagnetic interactions dominate. Below 3.5 K, the χT products of **22** and **23** sharply decrease down to 1.8 K. The field dependence of the magnetisation of compounds **22** and **23** below 5 K abruptly increases below 0.5 T confirming the presence of ferromagnetic interactions (**Fig 4.31**). At higher field the magnetisation curve follows a linear slope and reaches 13.11 and 13.37 μ_B for compounds **22** and **23**, respectively, without saturation even up to 7 T, suggesting the presence of low-lying excited states and/or magnetic anisotropy within the compounds. For compound **24**, the room temperature χT value of 28.79 cm^3 K mol^{-1} is in good agreement with the expected value of 28.34 cm^3 K $mol^{-1}$for two non-interacting Dy^{III}. The χT product remains roughly constant until 75 K and then decreases to reach a minimum of 28.19 at 1.8 K. The decline of χT is likely due to the progressive depopulation of Dy^{III} excited Stark sublevels.[34a]

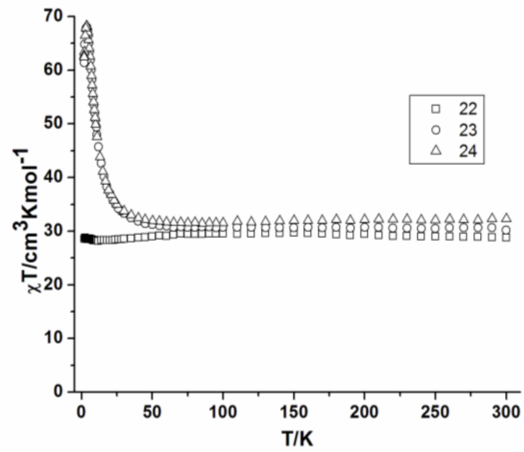

Fig 4.30 Plots of χT vs T of compounds **22-24** under indicated applied dc magnetic fields (1000Oe)

The field dependence of the magnetisation of compounds **22-24** is shown in **Fig 4.31.** At low temperatures, there is a gradual increase of the magnetisation with a lack of saturation even at 7 T. The magnetisation increases sharply below 0.5 T and increases linearly at higher fields, indicating the presence of magnetic anisotropy and/or low-lying excited states.

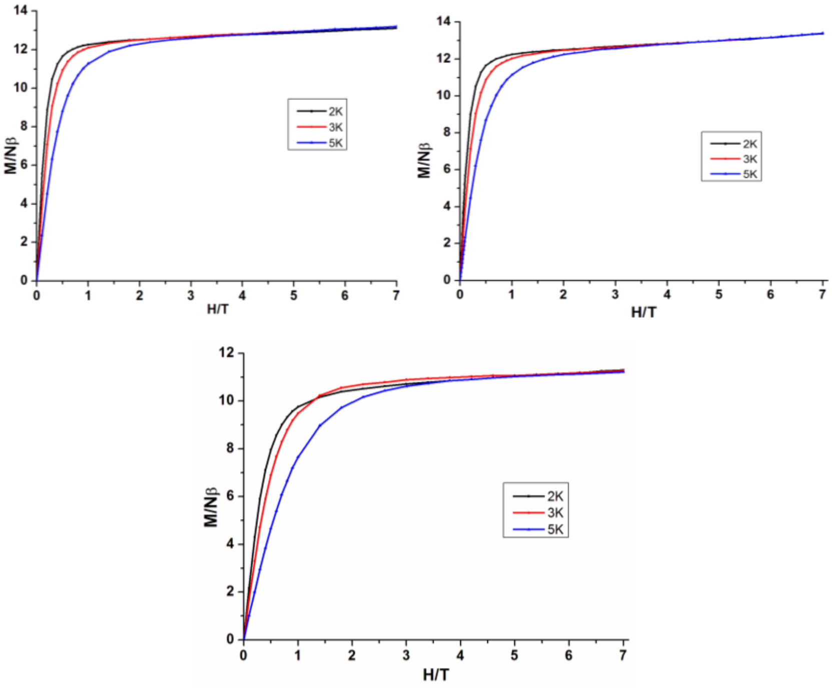

Fig 4.31 Plots of M vs H of **22** (up left), **23** (up right) and **24** (down)

Table 4.7 Magnetic data of compounds **22-24** summarized from the dc measurements

Compound	Ground state of Ln^{III} ion	χT expected for non-interacting ions per complex (cm^3 K mol^{-1})	χT measured at 300 K per complex (cm^3 K mol^{-1})	χT measured at 1.8 K per complex (cm^3 K mol^{-1})	Magnetisation at 2 K and 7 T (Nβ)
$Co^{II}_2Dy^{III}_2$ (**22**)	$^6H_{15/2}$	32.09	30.21	61.39	13.11
$Co^{II}_2Dy^{III}_2$ (**23**)	$^6H_{15/2}$	32.09	32.29	62.43	13.37
$Zn^{II}_2Dy^{III}_2$ (**23**)	$^6H_{15/2}$	28.34	28.50	28.19	11.30

To probe the slow relaxation of the magnetisation and quantum tunnelling effects within these systems, variable temperature and frequency ac magnetic measurements were performed, utilizing a 3.0 Oe oscillating field and a zero-applied dc magnetic field. Both the in-phase (χ') susceptibilities and out-of-phase (χ'') susceptibilities display a frequency and temperature dependence for **22-24** (**Fig 4.32** and **4.34**), which are characteristic for SMM behaviour. The temperature dependent ac measurements of **22** (**Fig 4.32**, top) indicate that more than one relaxation pathway is operating. Such a behaviour is similar to that observed for the compound $[Co^{II}_2Dy^{III}_2(L)_4(NO_3)_2(THF)_2]\cdot 4THF$ (L = 2-[(2-hydroxy-phenylimino)-methyl]-6-methoxy-phenol) reported by our group,[25] in which the two solvent molecules coordinated to Co^{II} centres are THF, but the Schiff base is the same as the one used here. As shown in **Fig 4.33**, for compound **23** the high temperature relaxation is slightly shifted to lower temperature. At the same time, the maximum seen at low temperature is almost unchanged. The magnetisation relaxation time (τ) is derived from the frequency-dependence measurements and is plotted as a function of T^{-1} for **22** and **23** (**Fig 4.37**). The τ of each compound shows a strong temperature dependence and fits well with the Arrhenius equation, $\tau = \tau_0 \exp(U_{eff}/k_B T)$. Complex **22** show two thermally activated regimes with U_1 = 17.85 K and $\tau_1 = 2.3 \times 10^{-4}$ s in the temperature range 2-8 K and U_2 = 104.78 K and $\tau_2 = 9.2 \times 10^{-7}$ s between 18 and 22 K. For complex **23**, there are also two thermally activated regimes with U_1 = 17.45 K and $\tau_1 = 1.45 \times 10^{-4}$ s in the temperature range 2-8 K and U_2 = 94.53 K and $\tau_2 = 1.2 \times 10^{-6}$ s between 17 and 21 K. Notably, the regime of quantum tunnelling of magnetisation is still not achieved within the investigated temperature domain. They all show nearly symmetrical Cole-Cole plot results between 5 and 21 K (**Fig 4.35**). Fitting the diagram at each temperature to the generalized Debye model leads to an α parameter of 0.036 for **22** and an α parameter of 0.053 for **23** (**Table 4.8**), respectively, over the temperature range 8-15 K (**Fig 4.36**), indicating a very narrow distribution of relaxation times for each process. For compound **24**, the ac plots indicate frequency and temperature dependence of ac susceptibilities confirming the zero- field slow magnetisation relaxation and SMM behavior of complex **24**. The presence of one relaxation process is attributed to the presence of one crystallographically independent Dy^{III} ion in the centrosymmetric complexes.[55] The thermally induced relaxation can be fit using the Arrhenius law ($\tau = \tau_0 \exp(U_{eff}/kT)$) yielding effective energy barriers of $U_{eff} = 140.4$ K $\tau_0 = 1.36 \times 10^{-7}$ s. It was not possible to fit the Cole-Cole plots, because the quantum tunnelling leads to unsymmetrical curves. As mentioned above, compounds **22** and **23** are related to the $Co^{II}_2Dy^{III}_2$ compound reported earlier by our group.[28]

The main difference consists in the nature of the coordinated solvent and lattice solvent molecules. These three compounds have similar bond length and angles and show similar static magnetic behaviour. Comparing the dynamic magnetic behaviour of these three complexes, it can be noted that the dynamic magnetisation of complex **22** is very similar to the previously reported one.[28] This again demonstrates the existence of unusual single-ion blocking of the relaxation of the magnetisation of the Dy^{III} ions at higher temperatures with a crossover to molecular exchanged-based blocking at low temperatures which was confirmed by the ab initio calculation for previously reported compound. For compound **23**, as shown in **Fig 4.32**, the high temperature single-ion blocking of the relaxation of the magnetisation of Dy^{III} has moved to lower temperatures making observation of a clear relaxation process difficult. This situation has been resolved using frequency dependent ac measurements (**Fig 4.34**) which show that two relaxation processes are present in these compounds. To further confirm the high temperature single-ion blocking of the relaxation of the magnetisation of Dy^{III}, compound **24** was synthesized and investigated, in which paramagnetic Co^{II} was replaced by diamagnetic Zn^{II} to eliminate the molecular exchanged-based blocking at low temperatures. The results indicate that the high temperature relaxation still exists and this derives from the single ion blocking of Dy^{III}. Based on these results, it can be concluded that the coordinated solvent molecules of the Co^{II} ions are responsible for the observed differences between the compounds **22**, **23** and the reported one. The ab initio calculations for compounds **22-24** are in progress and will help to further elucidate the mechanism of the relaxation processes in such Co^{II}-4f compounds.

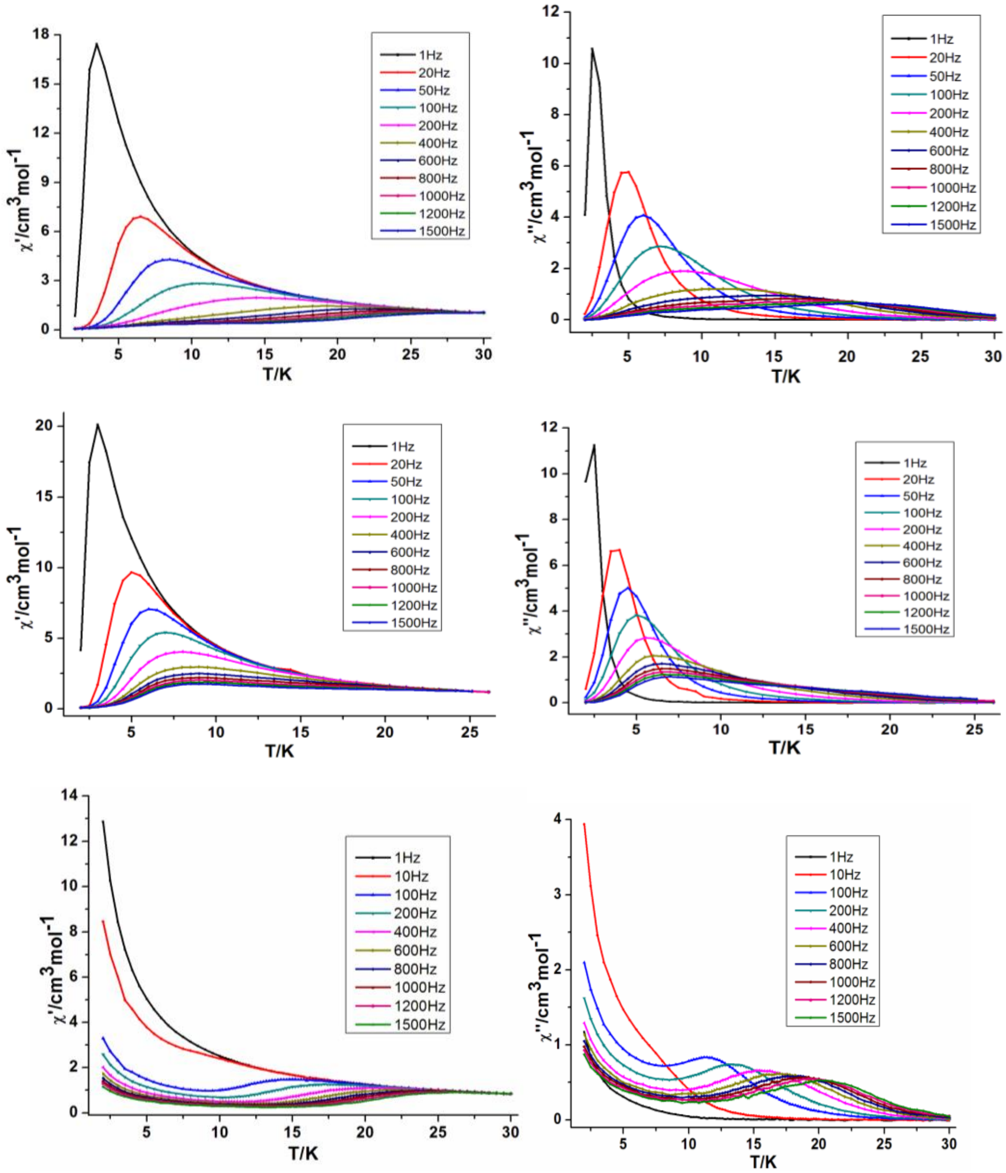

Fig 4.32 Plots of χ’ (left) and χ’’ (right) vs T of **22** (up), **23** (middle) and **24** (down) at indicated frequencies.

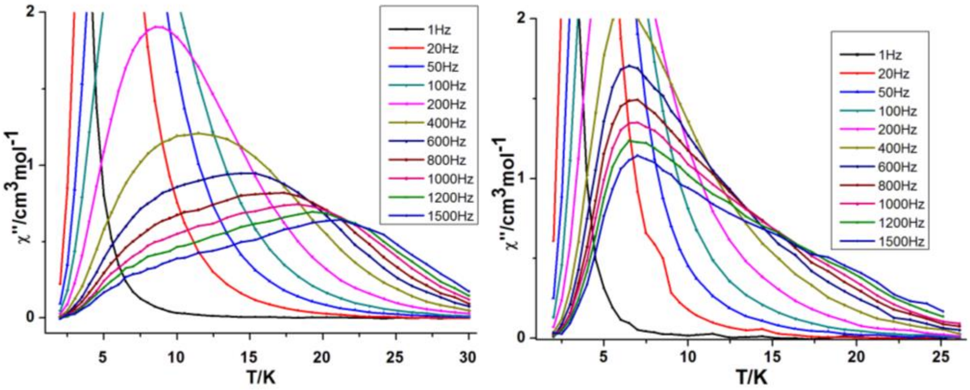

Fig 4.33 Zoom-in of plots of χ’’ vs T for **22** (left) and **23** (right)

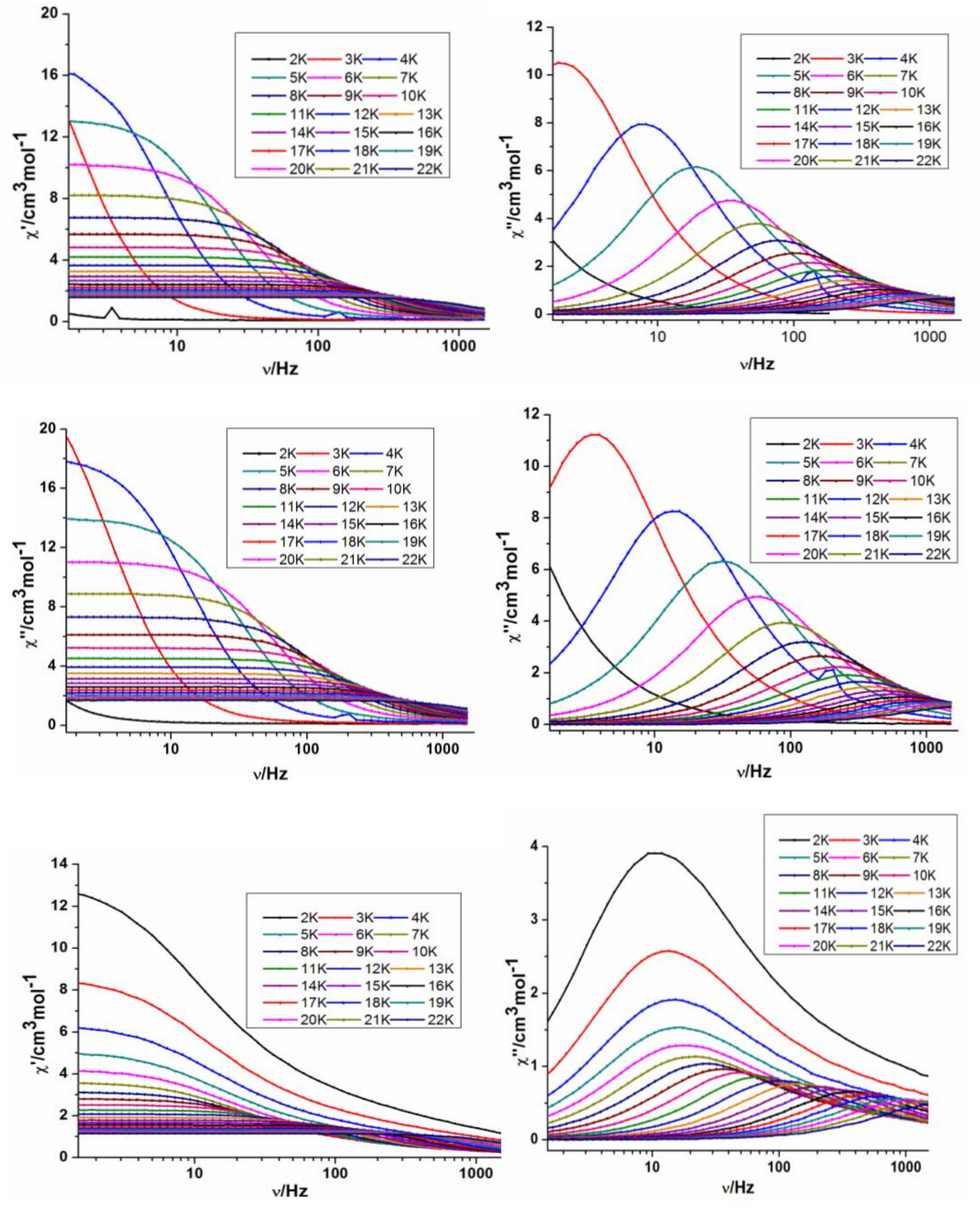

Fig 4.34 Plots of χ’ (left), χ’’ (right) vs frequency of **22** (up), **23** (middle) and **24** (down) at indicated temperatures

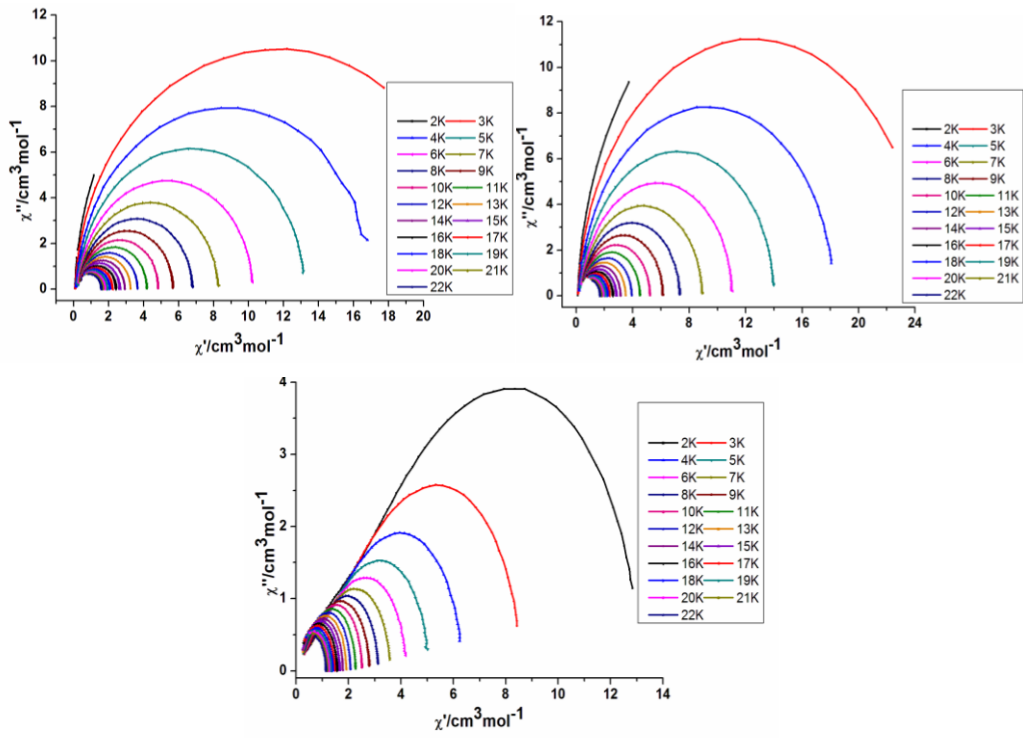

Fig 4.35 Cole-Cole plots of **22** (up left), **23** (up right) and **24** (down) from 2-22K

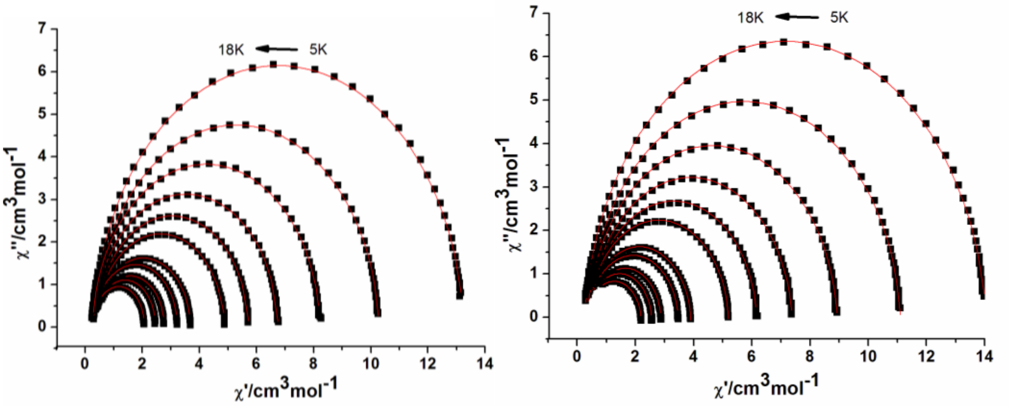

Fig 4.36 Fitted Cole-Cole plots of **22** (down left) and **23** (down right) at indicated temperatures (The same temperatures were selected)

Table 4.8 Analysis of Cole-Cole plots of complexes **22** and **23**

	T(K)	χ_0 (cm^3/mol)	χ_{inf} (cm^3/mol)	α	R^2
22	5	13.2341(4)	0.02351(4)	0.0358(1)	0.98994
	6	10.2565(1)	0.2656(6)	0.03146(2)	0.99871
	7	8.2504(8)	0.2990(9)	0.02834(2)	0.99703
	8	6.7893(9)	0.3516(9)	0.02243(3)	0.99583
	9	5.6942(1)	0.3469(1)	0.02587(4)	0.99590
	10	4.8444(5)	0.3577(8)	0.02042(4)	0.99383
	12	3.6603(3)	0.3547(1)	0.01902(1)	0.99870
	13	3.2585(1)	0.3470(4)	0.01469(2)	0.99878
	15	2.6544(5)	0.3140(6)	0.01961(2)	0.99832
	16	2.4215(5)	0.3212(9)	0.01071(1)	0.99522
	18	0.3091(2)	2.0600(3)	0.0033(4)	0.99628
23	5	14.0491(1)	0.2495(7)	0.05252(1)	0.99856
	6	11.0703(3)	0.3074(8)	0.05085(3)	0.99712
	7	8.9275(5)	0.3500(1)	0.05214 (4)	0.99478
	8	7.3391(2)	0.38473(3)	0.04808(3)	0.99697
	9	6.1290(9)	0.4199(6)	0.03563(6)	0.99035
	10	5.2294(1)	0.4172(4)	0.03948(2)	0.99824
	12	3.9351(6)	0.4160(2)	0.03177(2)	0.99807
	13	3.5021(1)	0.3942(8)	0.03298(3)	0.99815
	15	2.8438(3)	0.3869(5)	0.02356(4)	0.99743
	16	2.5902(4)	0.3756(1)	0.01681(4)	0.99657
	18	2.1979(1)	0.3433(5)	0.01696(4)	0.99667

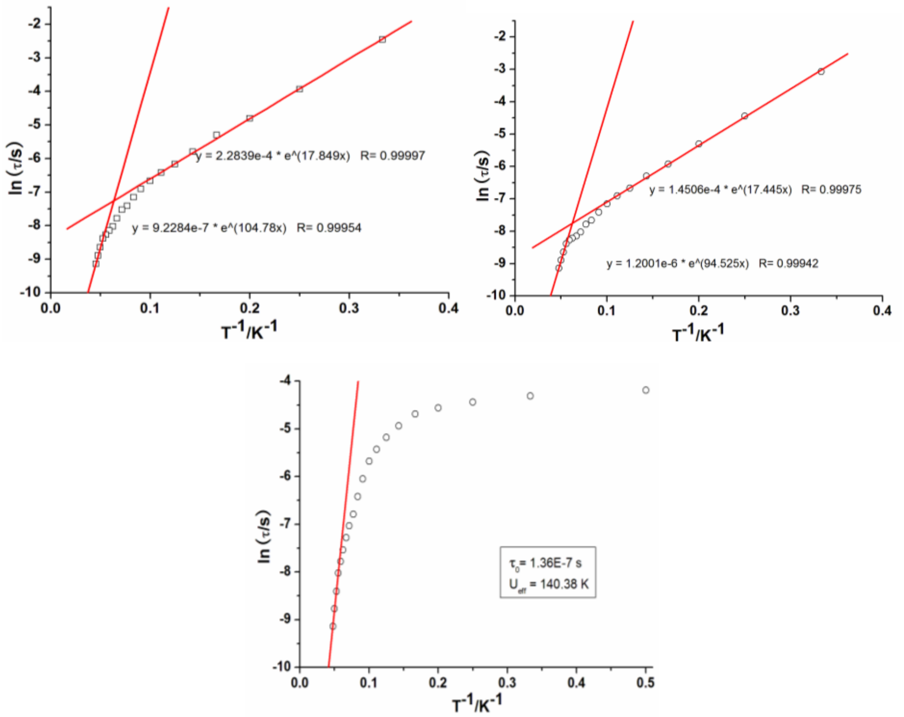

Fig 4.37 Arrhenius plots of complex **22** (up left), **23** (up right) and **24** (down)

4.2.10 Structures of $[Fe^{III}_2Ln^{III}(L8)_4(MeOH)(AcO)]\cdot 4MeOH$ [Ln = Dy (25) and Y (26)]

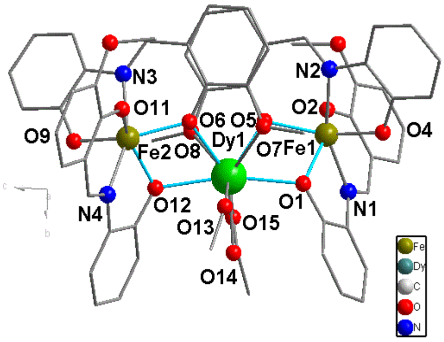

Fig 4.38 The structure of **25**

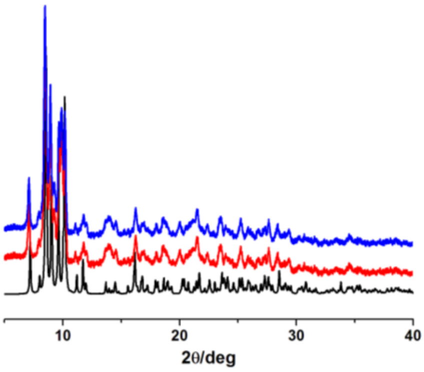

Fig 4.39 The powder XRD of **25** (red), **26** (blue), Simulated (black, based on Fe_2Dy)

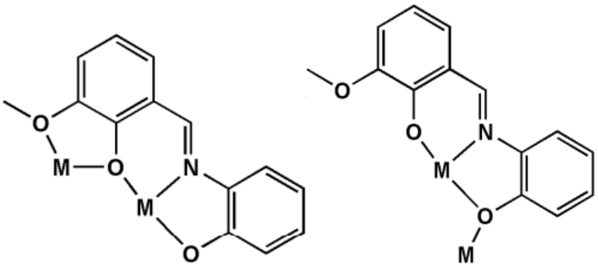

$\eta^1:\eta^2:\eta^1:\eta^1:\mu_2$ (a)

$\eta^0:\eta^1:\eta^1:\eta^2:\mu_2$ (b)

Scheme 4.5 The coordination modes of the H_2**L8** in compounds **25** and **26**

Compounds **25** and **26** are isomorphous and crystallize in the monoclinic space group $P2_1/c$, which was also confirmed from PXRD (**Fig 4.38**). A full structure determination was carried out for compound **25** and the molecular structure for this will by described in detail. The asymmetric unit contains four ligands, two Fe^{III} ions, one Dy ion, one MeOH and one acetate anion (**Fig 4.39**). Two of these four ligands display a $\eta^1:\eta^2:\eta^1:\eta^1:\mu_2$ coordination mode (**Scheme 4.5**, a) and the other two a $\eta^0:\eta^1:\eta^1:\eta^2:\mu_2$ coordination mode (**Scheme 4.5**, b). Each Fe^{III} ion displays a distorted octahedron coordination geometry, chelated by one ($\eta^1:\eta^2:\eta^1:\eta^1:\mu_2$) and one ($\eta^0:\eta^1:\eta^1:\eta^2:\mu_2$) ligand, and bridging to the central Ln by two phenol O atoms. The central nine coordinate Ln ion (six O atoms from the peripheral four ligands, two O atoms from the coordinated anions and one from the solvent molecule), displays monocapped square antiprismatic coordination geometry.

4.2.11 Magnetic properties of compounds 25 and 26

Magnetic studies were performed on compounds **25** and **26** in the temperature range 1.8-300 K under an applied dc field of 1000 Oe (**Fig 4.40**). The dc data are summarized in **Table 4.9**. The experimental χT products at room temperature are all comparable to the expected values for two Fe^{III} and one non-interacting Ln^{III} ions. As illustrated in the χT vs T plots, for compound **25**, on lowering the temperature, the χT product increases slowly until around 50 K, then increases quickly to reach a maximum value of 31.27 $cm^3 K mol^{-1}$ at 6 K, and then rapidly falls to 23.05 $cm^3 K mol^{-1}$ at 1.8 K. This type of magnetic behaviour indicates the presence of dominant ferromagnetic interactions within this compound that are strong enough not to be overwhelmed by any thermal depopulation of the Dy^{III} excited states. The final decrease of χT is likely to result from magnetic anisotropy and/or antiferromagnetic interactions. A weak antiferromagnetic interaction between the iron centres is observed for compound **26**. The field dependence of the magnetisation of the compound **25** containing the highly anisotropic Dy^{III} ion shows that the magnetisation increases smoothly with increasing applied dc field without saturation even at 7 T (**Fig 4.41**). This behaviour indicates the presence of magnetic anisotropy and/or low lying-excited states in these systems. The χT product of the Y analogue (**26**) is almost constant down to 10 K before it decreases down to 1.8 K, which suggests that the interaction between the two well-spaced Fe^{III} ions through the single Ln^{III} centre is very weak in nature. This is also supported by the field dependence of magnetisation at low temperatures, in which the magnitude of the magnetisation at 2 K under a field of 7 T is ~ 10.0 μ_B (**Fig 4.41**). This magnitude is consistent with the calculated one for a parallel alignment of two $S = 5/2$ spins when the weak interaction is overcome by the external dc field. The ac susceptibilities were checked but did not show any out-of-phase signals above 1.8 K for **25**, even under weak (0.5-3000 Oe) dc applied fields (**Fig 4.42**), suggesting that this compound does not act as an SMM.

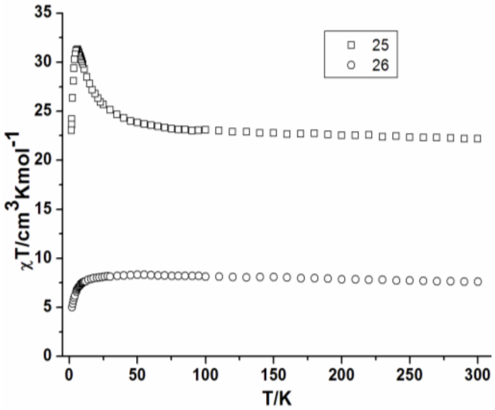

Fig 4.40 Plots of χT vs T of compounds **25** and **26** under 1000 Oe dc field

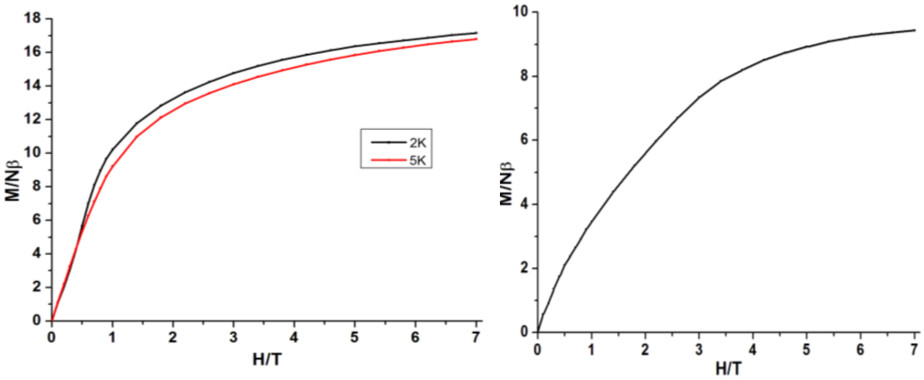

Fig 4.41 Plots of M vs H of **25** (left) and **26** (right)

Table 4.9 Magnetic data of compounds **25** and **26** summarized from the dc measurements

Compound	Ground state of Ln^{III} ion	χT expected for non-interacting ions per complex (cm^3Kmol^{-1})	χT measured at 300 K per complex (cm^3Kmol^{-1})	χT measured at 1.8 K per complex (cm^3Kmol^{-1})	Magnetisation at 2 K and 7 T (Nβ)
$Fe^{III}_2Dy^{III}$ (**25**)	$^6H_{15/2}$	22.92	22.17	23.05	15.53
$Fe^{III}_2Y^{III}$ (**26**)		8.75	7.61	5.04	9.43

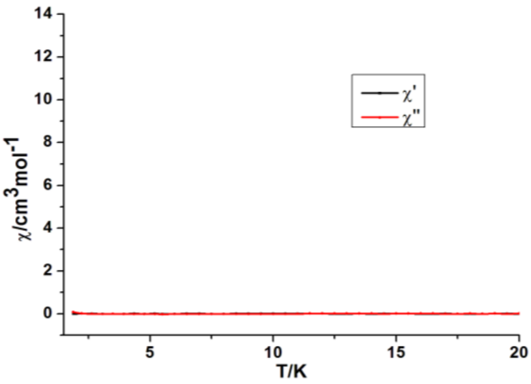

Fig 4.42 Plots of χ' and χ'' vs T of **25** (1000 Hz)

4.2.12 Structures of $[Co_2Ln(H_2L9)(NO_3)_2(MeOH)_4]\cdot NO_3\cdot xMeOH\cdot yH_2O$, [Ln = Dy (27), x = 5, y = 5; Ln = Tb (28), x = 0, y = 8; Ln = Ho (29), x = 0, y = 10; Ln = Y (30), x = 0, y = 10)]

All compounds are isomorphous and isostructural as revealed from powder X-ray diffraction. The relative amounts of methanol and water in the lattice were estimated from the microanalytical results. A full single crystal X-ray diffraction structure determination was performed on compound **27** and ther other three were confirmed by powder XRD and unit cell measurements (**Fig 4.43**). The compound crystallizes in the orthorhombic Aba2 space group, and its asymmetric unit consists of two H**L9** ligands, two Co^{II} ions, one Dy^{III} ion, two NO_3^- anions and four coordinated MeOH molecule as shown in **Fig 4.44**. Each Co^{II} ion displays pentagonal bipyramidal coordination geometry chelated by a planar N3O2 donor set of atoms from the ligand with the axial positions occupied by two MeOH molecules. The Dy^{III} displays square anti-prismatic coordination geometry with an O8 donor set, in which four O atoms are from two chelating nitrate (NO_3^-) anions and the other four from four phenol O atoms of four ligands. Each H_2**L9** ligand adopts a $\eta^1:\eta^1:\eta^1:\eta^1:\eta^1:\eta^1:\eta^1:\mu_3$ coordination mode (**Scheme 4.6**) and chelates one Co^{II} ion and bridges two Dy^{III} ions with two phenol O atoms. The observed Co-O/N, and Dy-O bond lengths are in the range 1.951(10)-2.212(7)Å, 2.238(5)-2.480(6)Å, respectively. In this 2-dimensional structure, complex **27** shows very ineresting 4×4 square channels alternately divided by the $[Co_4L_4(MeOH)_8Dy_4(NO_3)_8]$ moieties.

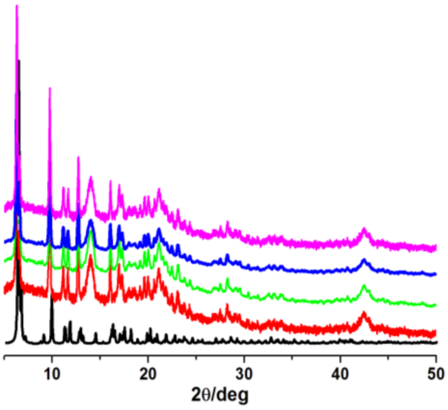

Fig 4.43 The powder XRD of **27-30**: black (simulated based Co_2Dy), **27** (red, Co_2Dy), **28** (green, Co_2Tb), **29** (blue, Co_2Ho), **30** (pink, Co_2Y)

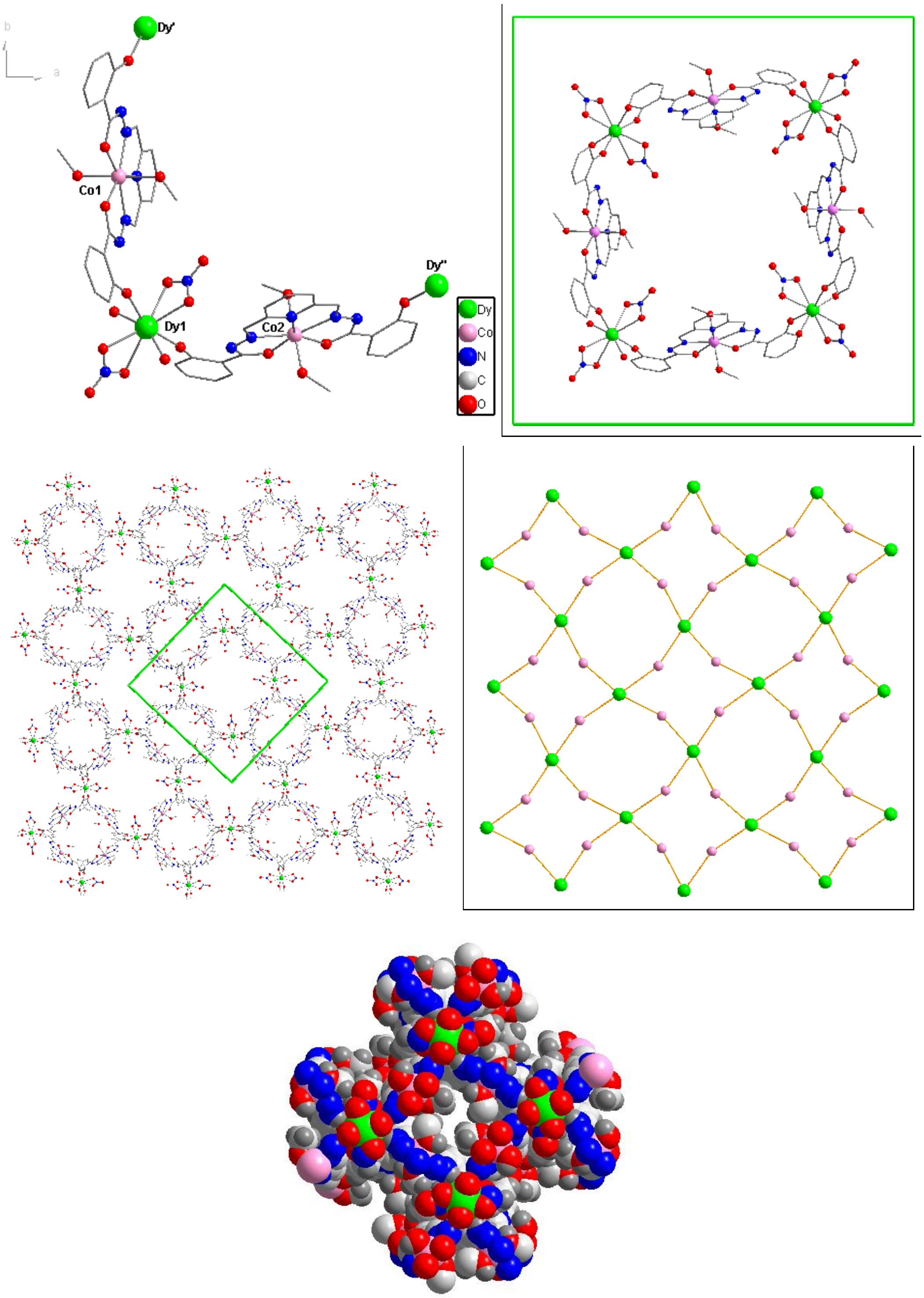

Fig 4.44 The structure of asymmetric unit of **27** (up left), the Co_4Dy_4 square (up right), 2D net (middle left), 2D metal core net (middle right) and space filling representation (down)

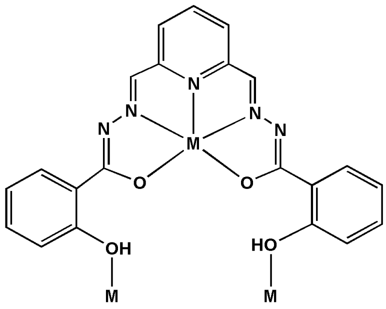

$\eta^1:\eta^1:\eta^1:\eta^1:\eta^1:\eta^1:\eta^1:\mu_3$

Scheme 4.6 The coordination mode of the H_4**L9** in compounds **27-30**

4.2.13 Magnetic properties of 27-30

The temperature dependence of the magnetic susceptibilities of complexes **27-30** were measured on powdered samples in the temperature range 1.8-300 K under an applied dc magnetic field of 1000 Oe (**Fig 4.45** and **4.46**). Selected dc magnetic data are given in **Table 4.10**. The χT values of **27-30** at room temperature are slightly higher than the theoretically expected χT values because of spin-orbit contributions of Co^{II}. For the complex Co^{II}_2Y (**30**), the χT product remains almost constant from room temperature to 100 K and then decreases to 3.08 cm^3 K mol^{-1} at 1.8 K indicating the presence of small antiferromagnetic intramolecular interactions and/or small ZFS contributions of Co^{II} ions. The decrease of the χT product of **30** below 50 K could also be due to weak antiferromagnetic intermolecular interaction. The thermal evolution of χT for the $Co^{II}_2Dy^{III}$ (**27**) and $Co^{II}_2Ho^{III}$ (**28**) compounds are similar. The χT product slowly decreases on decreasing temperature to reach a value of 18.21 (**27**) and 17.88 (**29**) cm^3 K mol^{-1} at 50 K and then decreases to 16.27 (**27**) cm^3 K mol^{-1} and 11.49 (**29**) cm^3 K mol^{-1} at 1.8 K. This type of behaviour at low temperatures suggests the presence of overall intramolecular weak antiferromagnetic coupling among the metal centres, but the decrease of the χT product in the higher temperature range (50-100 K) is likely due to the depopulation of Stark sublevels of Ln^{III} ions. In contrast to compounds **27**, **28** and **30**, the χT product of compound **28** ($Co^{II}_2Tb^{III}$) remains almost constant from room temperature to 100 K and slowly decreases with the decrease of temperature to 15.21 cm^3 K mol^{-1} at 12 K, but then rapidly increases to 16.77 cm^3 K mol^{-1} at 1.8 K. The high temperature decrease can be attributed to the depopulation the Tb^{III} ion substates, while the increase at lower temperatures suggests non-negligible weak ferromagnetic interactions present between the Tb^{III} and the Co^{II} ions.

Taking into consideration the static magnetic behaviour of this family, we conclude that within the Co^{II}_2-Dy/Ho and Co^{II}_2-Tb compounds different metal-metal interactions occur. The dipolar interactions between the anisotropic Ln^{III} ions such as Dy^{III}, Tb^{III} or Ho^{III} ions can be rather large and ferromagnetic or antiferromagnetic, depending on the orientation of the easy axes. Since the intramolecular magnetic exchange between Co^{II} and Ln ions in this family is very weak we can expect that the dipolar contribution in the case of Dy^{III} and Ho^{III} complexes is sufficient to dominate the exchange interaction, thereby leading to the observed differences within this studied Co-Ln family. A similar effect was observed in a recently reported Dy^{III}_3 complex.[56]

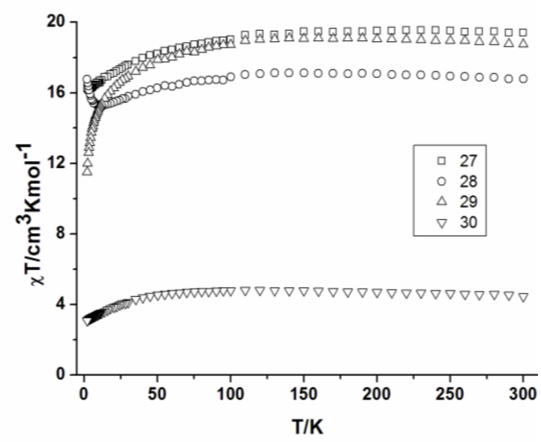

Fig 4.45 Plots of χT *vs* T of **27-30** under 1000 Oe dc field

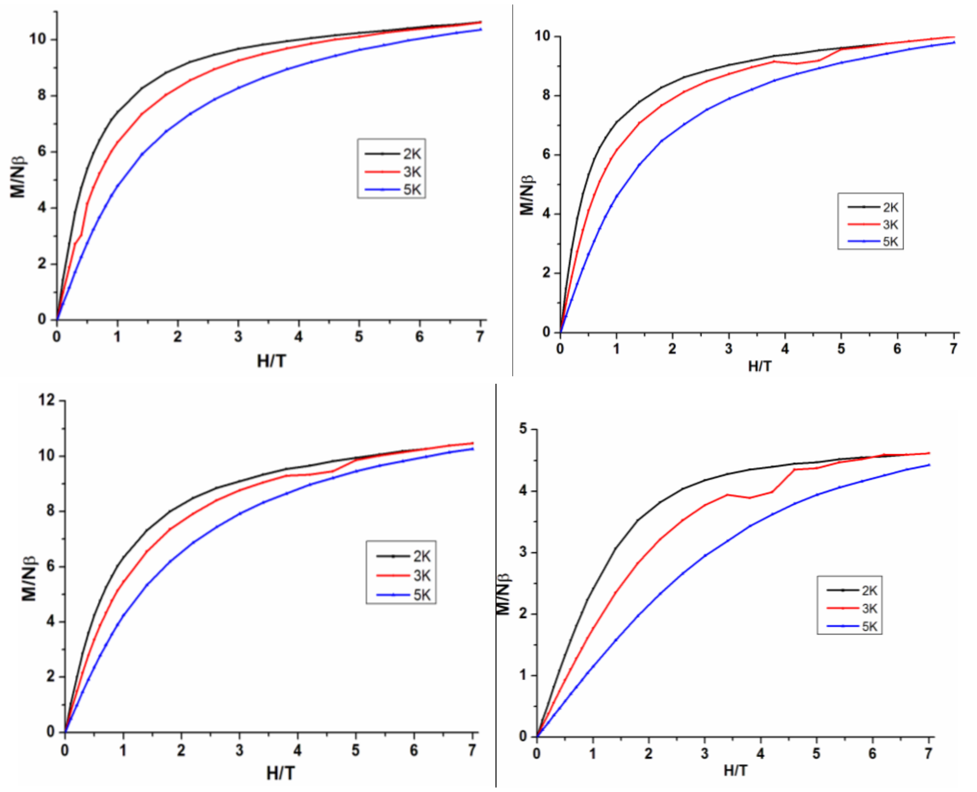

Fig 4.46 Magnetisation vs H of **27** (up left), **28** (up right), **29** (down left) and **30** (down right) at indicated temperatures.

Table 4.10 Magnetic data of compounds **27-30** summarized from the dc measurements

Compound	Ground state of Ln^{III} ion	χT expected for non-interacting ions per complex (cm^{3}Kmol^{-1})	χT measured at 300 K per complex (cm^{3}Kmol^{-1})	χT measured at 1.8 K per complex (cm^{3}Kmol^{-1})	Magnetisation at 2 K and 7 T (Nβ)
Co$^{II}_2$Dy^{III} (**19**)	$^6H_{15/2}$	17.92	19.40	16.27	10.63
Co$^{III}_2$Tb^{III} (**20**)	$^7H_6$	16.68	16.55	16.77	9.99
Co$^{II}_2$Ho^{III} (**21**)	$^5I_8$	17.28	18.75	11.49	10.46
Co$^{II}_2$Y^{III} (**22**)		3.75	4.45	3.08	4.62

The ac susceptibility measurements of **27-30** indicate that complex **27** shows slow relaxation in zero field (**Fig 4.47**), but with no maximum even under an applied dc field (**Fig 4.48** and **4.49**), while for complexes **28** and **29**, there no ac signals both in zero and non-zero dc field. Compound **30** shows slow relaxation when a dc field applied, but no maximum was observed (**Fig 4.49**). All these studies and observations indicate the absence of slow relaxation of magnetisation in this family of Co^{II}-4f compounds within our measurement parameters.

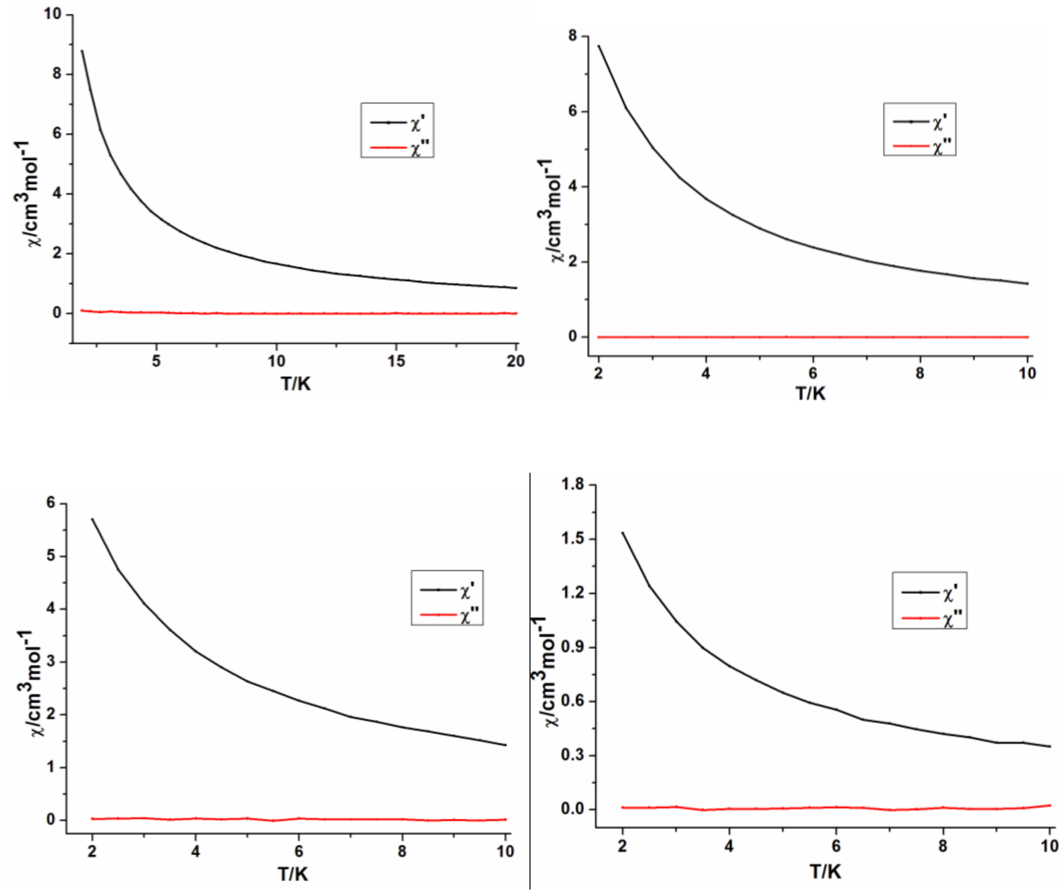

Fig 4.47 Plots of χ 'and χ'' vs T of **27** (up left), **28** (up right), **29** (down left) and **30** (down right)

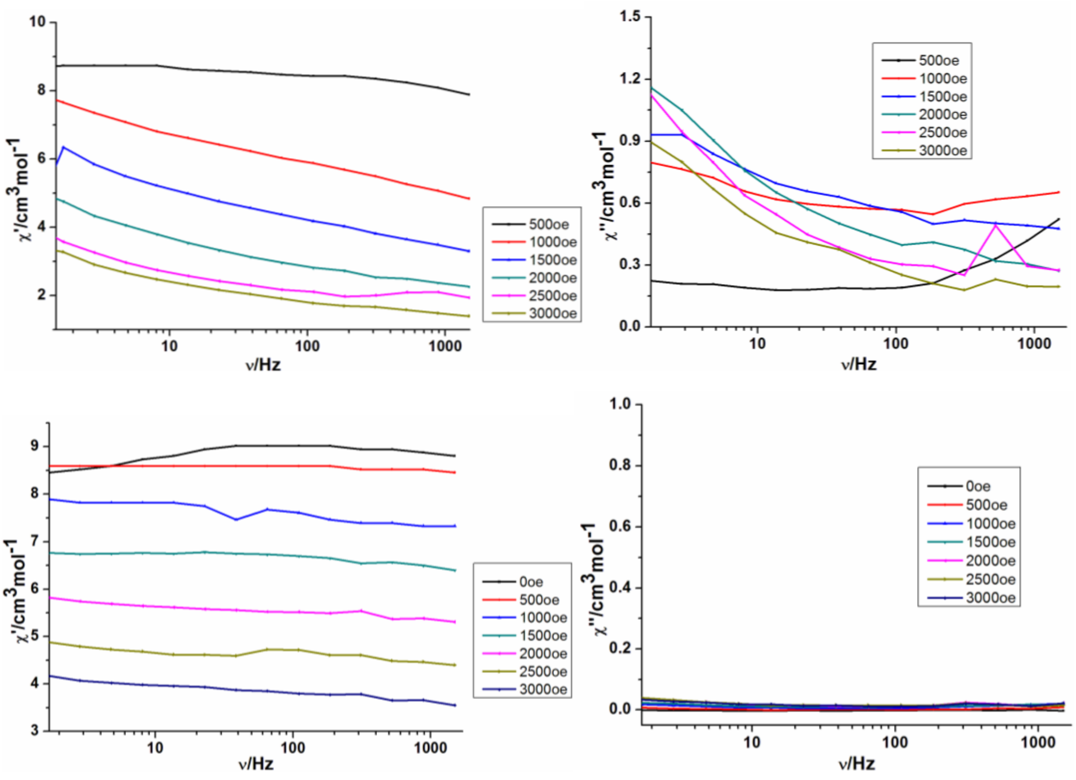

Fig 4.48 Plots of χ'(left) and χ'' (right) vs frequency of **27** (up) and **28** (down) at 1.8 K under indicated applied dc magnetic fields.

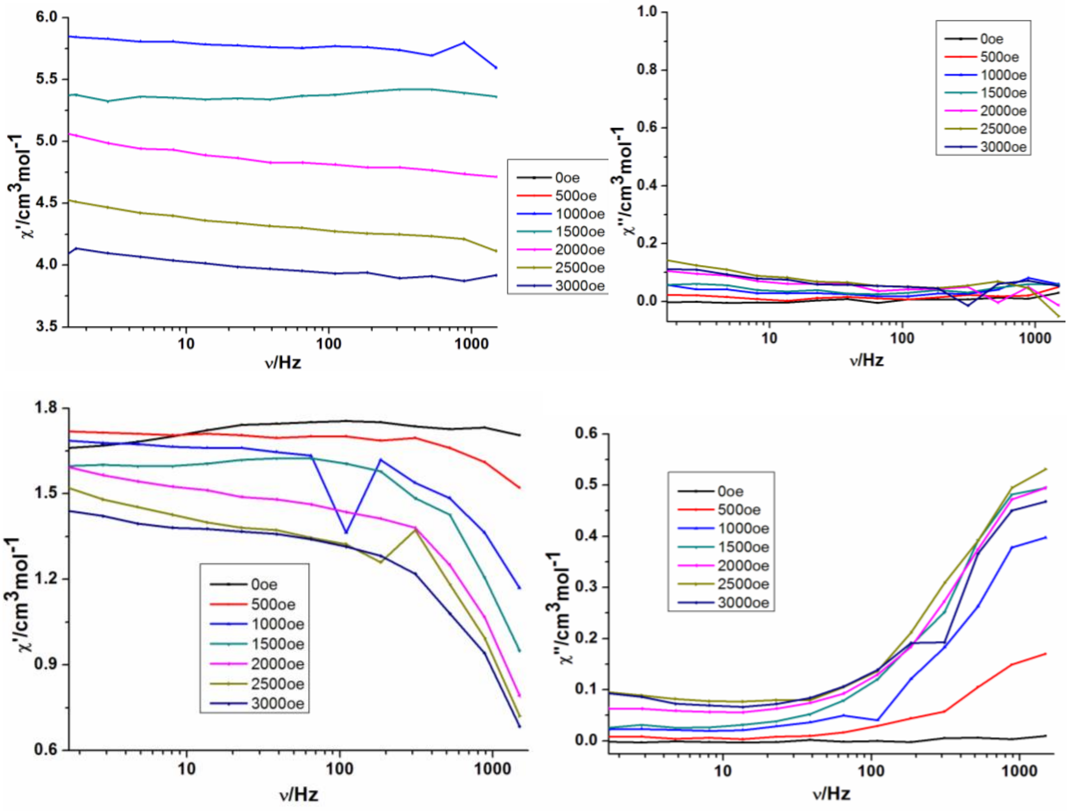

Fig 4.49 Plots of χ ' (left) and χ '' (right) vs frequency of **29** (up) and **30** (down) at 1.8 K under indicated applied dc magnetic fields.

4.2.14 Structures of $Na[Co_2Ln(L9)_2(H_2O)_4]\cdot 7H_2O$ [Ln = Dy (31), Tb (32), Ho (33) and Y (34)]

The trinuclear heterometallic compound **31** crystallizes in the tetragonal space group $I4_1/a$. Complexes **32-34** are isomorphous, confirmed by the unit cell constants and X-ray powder diffraction (**Fig 4.51**). The molecular structure of **31** contains a complex anion $\{\mathbf{L9}Co^{II}_2Dy^{III}(H_2O)_4\}^-$, one Na^+ and seven disordered lattice water molecules. The molecular structure of **31** is shown in **Fig 4.50**. It reveals that the three metal ions are held together by a concerted coordination action of two tetra-anionic ligands, $\mathbf{L9}^{4-}$ adopting the $\eta^1:\eta^2:\eta^1:\eta^1:\eta^1:\eta^2:\eta^1:\mu_2$ coordination mode (**Scheme 4.7**). The seven coordination sites of each ligand are utilized. The two terminal Co^{II} ions display a facial coordination environment (N3O4) comprising one pyridine oxygen atom, two imino nitrogen atoms, two hydrazone oxygen atoms and two water oxygen atoms, inducing distorted pentagonal bipyramidal coordination geometry around Co^{II}. An all-oxygen coordination environment is present around the central lanthanide ion, which is has a distorted square antiprismatic geometry. This coordination sphere around the lanthanide ion is achieved by utilizing four phenolate oxygen atoms and four hydrazone oxygen atoms of two ligands. Thus, every hydrazone oxygen atom acts as a μ-bridging ligand. Two such bridging ligands hold the Co^{II} and Ln^{III} ions together to form the final complex. The observed Co-O/N, and Dy-O bond lengths are in the range 2.122(8)-2.239(5)Å, 2.383(6)-2.480(5)Å, respectively.

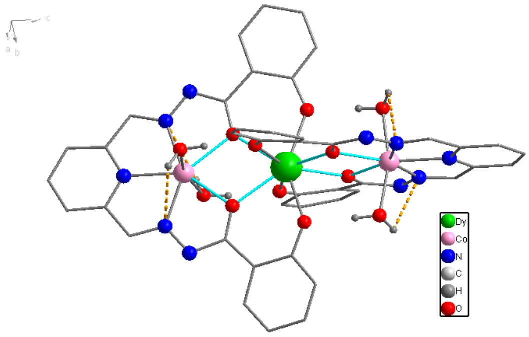

Fig 4.50 Molecular structure of **31**

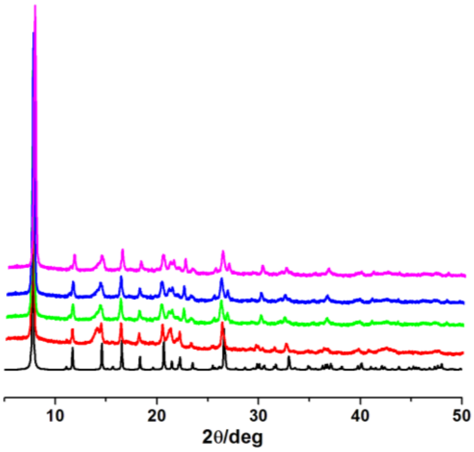

Fig 4.51 The PXRD of **31-34**: simulated (black, base Co_2Dy), **31** (red, Co_2Dy), **32** (green, Co_2Tb), **33** (blue, Co_2Ho), **34** (pink, Co_2Y)

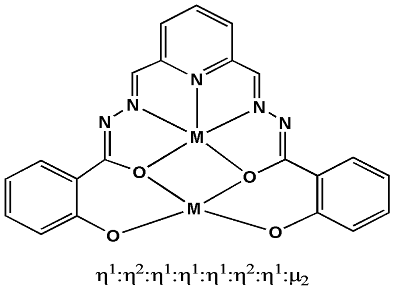

Scheme 4.7 The coordination mode of the H_4**L9** in compounds **31-34**

4.2.15 Magnetic properties of compounds 31-34

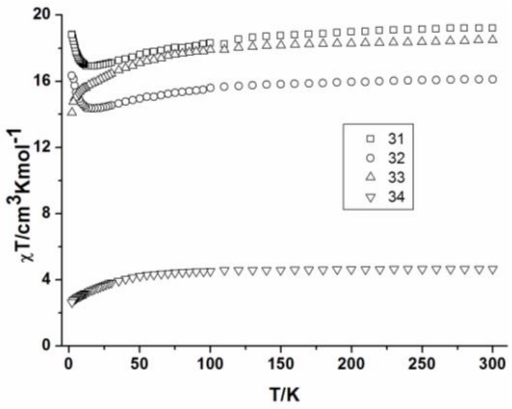

Fig 4.52 Plots of χ T vs T of compounds **31-34**

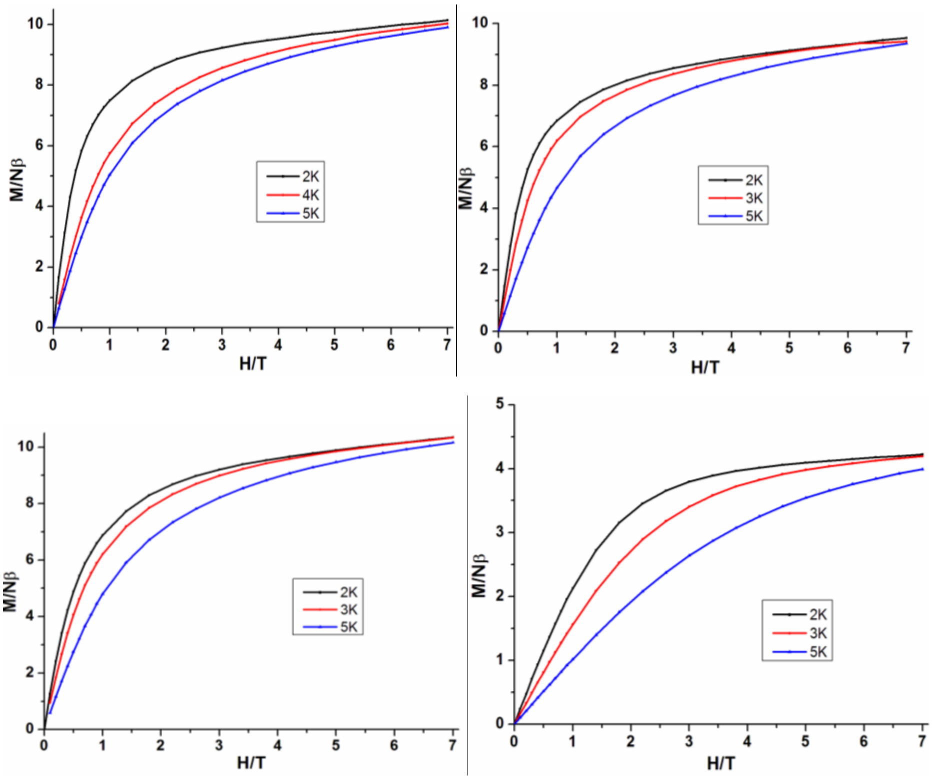

Fig 4.53 M vs H of compounds **31** (up left), **32** (up right), **33** (down left) and **34** (down right)

Magnetic susceptibility measurements were carried out on polycrystalline samples of **31**-**34** in the temperature range 1.8-300 K at 1000 Oe. The dc susceptibility (**Fig 4.52** and **4.53**) data of **31**-**34** are summarized in **Table 4.11**. The experimental χT value at 300 K is in good agreement with the theoretically expected values for $Co^{II}_{2}Tb$ (**32**). For **31**, **33** and **34**, the experimental χT values at 300 K are slightly higher than the theoretically expected values. For complex **34**, the χT product remains almost constant on decreasing the temperature from room temperature to 50 K, then, it decreases to 2.65 cm^3 K mol^{-1} at 1.8 K. The χT product of **33** slowly decreases from room temperature to 50 K, then rapidly decreases to 14.10 cm^3 K mol^{-1} at 1.8 K, possibly due to the combined effect of depopulation of Stark sub-levels and weak intramolecular antiferromagnetic interactions. In complexes **31** and **32**, a different trend was observed in the χT vs T plot. For both of them, the χT products slowly decrease on decreasing the temperature from room temperature to 12 K (16.90 cm^3 K mol^{-1}) for **31** and to 16 K (14.36 cm^3 K mol^{-1}) for **34**, respectively, and then below these temperatures the χT products increase to 18.79 cm^3 K mol^{-1} for **31** and to 16.33 cm^3 K mol^{-1} for **32** at 1.8 K. The upturn of χT at low temperature could be due to intramolecular weak ferromagnetic dipolar interactions between Co^{II}-Dy^{III} ions or Co^{II}-Tb^{III} ions in **31** and **32,** respectively.

Since Dy^{III} and Tb^{III} ions are comparatively more anisotropic than the other rare-earth analogues and the exchange interaction between these ions is usually very weak, the dipolar intramolecular ferromagnetic interactions between Dy^{III} and Co^{II} or Tb^{III} and Co^{II} ions are likely to be most important in **33** and **34**. A linear Dy_3[56] has been reported, in which the central Dy^{III} ion is doubly connected to each terminal Dy^{III} ion by three mono atomic μ-O bridges. The ab initio calculation on this molecule established that the central Dy^{III} ion is ferromagnetically coupled to other Dy^{III} ions. The striking aspect is that intramolecular Dy-Dy ferromagnetic dipolar interaction is stronger than intramolecular Dy-Dy ferromagnetic exchange coupling. The intramolecular ferromagnetic dipolar interaction is due to highly anisotropic nature of Dy^{III} ions in reported Dy_3 compound.[46]

The magnetisation values of **31-33** rapidly increase below 1 T and, then increase linearly without reaching true saturation (**Fig 4.53**). This indicates the presence of anisotropy in these systems. The maximum magnetisation values of **31-33** are 10.13, 9.53 and 10.34 μ_B, respectively, which are much lower than the sum of the expected values, ~ 16 μ_B. This indicates the presence of low lying energy states and/or anisotropy in the systems. The magnetisation at 2 K of $Co^{II}_2Y^{III}$ (**34**) slowly increases and reaches 4.22 μ_B at 7 T. This value is lower than the expected value (3 μ_B, for g = 2), which, as in case of Tb, Dy or Ho ions, indicates the presence of low lying energy states and/or anisotropy of Co^{II} ions in this system.

Table 4.11 Magnetic data of compounds **31-34** summarized from the dc measurements

Compound	Ground state of Ln^{III} ion	χT expected for non-interacting ions per complex (cm^3 K mol^{-1})	χT measured at 300 K per complex (cm^3 K mol^{-1})	χT measured at 1.8 K per complex (cm^3 K mol^{-1})	Magnetisation at 2 K and 7 T (Nβ)
$Co^{II}_2Dy^{III}$ (**31**)	$^6H_{15/2}$	17.92	19.20	18.79	10.13
$Co^{III}_2Tb^{III}$ (**32**)	$^7H_6$	16.68	16.12	16.33	9.53
$Co^{II}_2Ho^{III}$ (**33**)	$^5I_8$	17.28	18.47	14.10	10.34
$Co^{II}_2Y^{III}$ (**34**)		3.75	4.66	2.65	4.22

The ac susceptibilities were measured on polycrystalline powder samples of compounds **31-34** in the temperature range 1.8-10 K at 1000 Hz. The compound containing $Co^{II}_2Dy^{III}$ (**31**) displays a weak frequency-dependent out-of-phase (χ'') signal (**Fig 4.54**) below 3 K in zero field, indicating slow relaxation of the magnetisation in compound **31**. No maxima were observed even under applied dc field (**Fig 4.55**). For compounds **32** and **33**, very weak ac signals were only observed at applied dc fields, but without maxima indicating the absence of SMM behaviour under our measurement conditions for **32** and **33**. For compound **34**, out of phase (χ'') signals were observed under applied dc field (**Fig 4.56**). This behaviour is from the anisotropy of the single Co^{II} ion, which is expected for mononuclear Co^{II} complexes.[57]

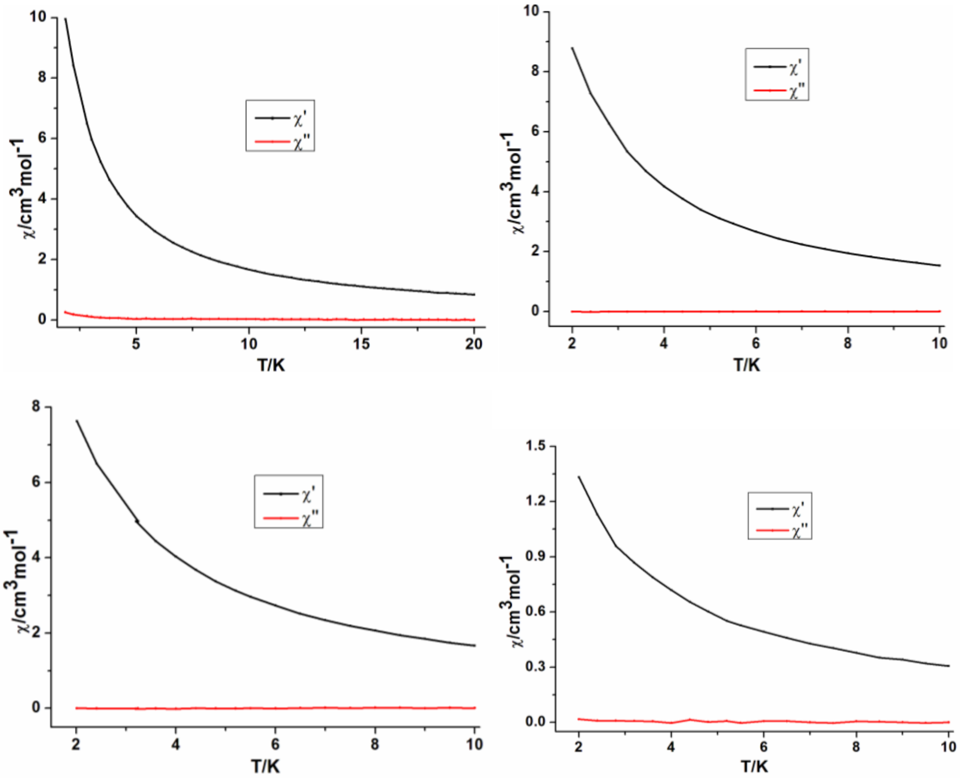

Fig 4.54 Plots of χ' and χ'' vs T of **31** (up left), **32** (up right), **33** (down left) and **34** (down right)

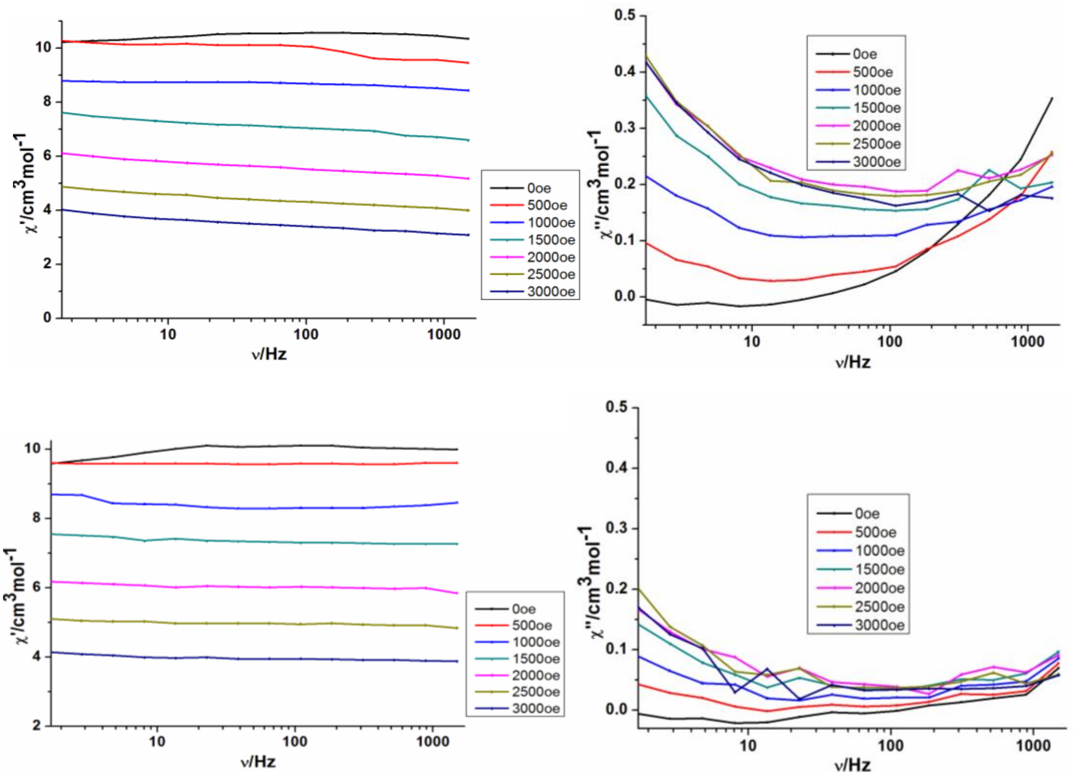

Fig 4.55 Plots of χ’ (left) and χ’’ (right) vs frequency of **31** (up) and **32** (down) at 1.8 K under indicated applied dc magnetic fields.

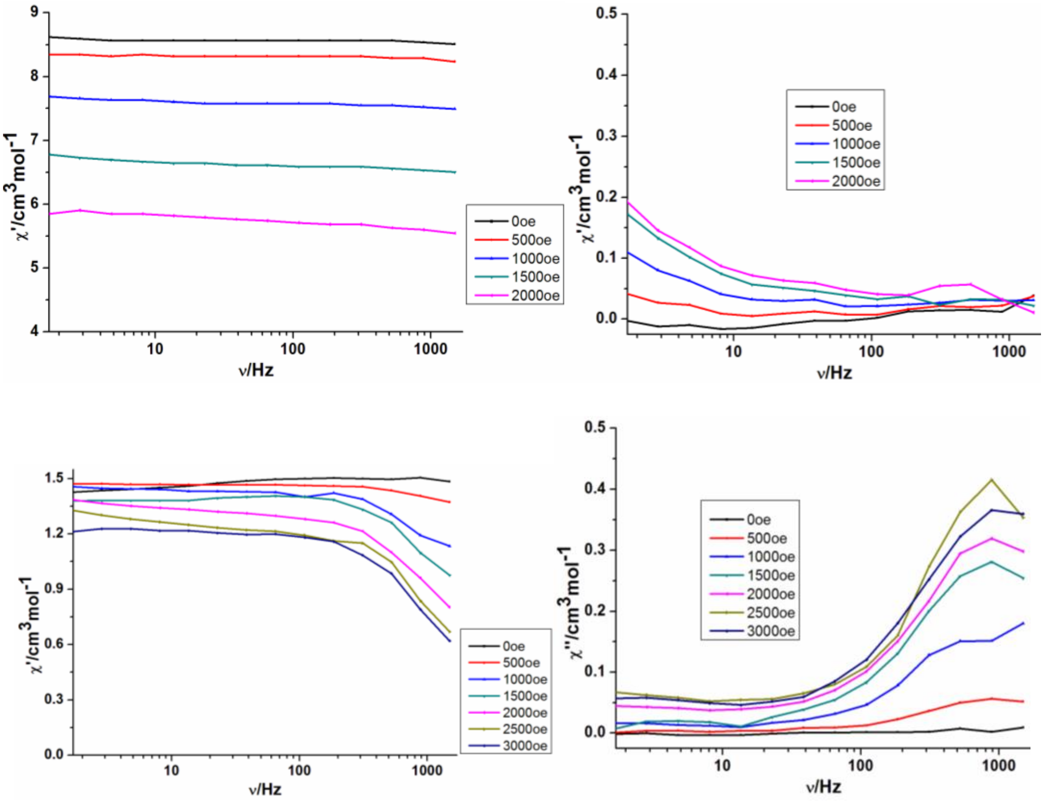

Fig 4.56 Plots of χ’ (left) and χ’’ (right) vs frequency of **33** (up) and **34** (down) at 1.8 K under indicated applied dc magnetic fields.

4.2.16 Structure of compound $[Co_2Dy_2(HL9)_2(N_3)_2(NO_3)_2(MeOH)_4]\cdot 4MeOH$ (35)

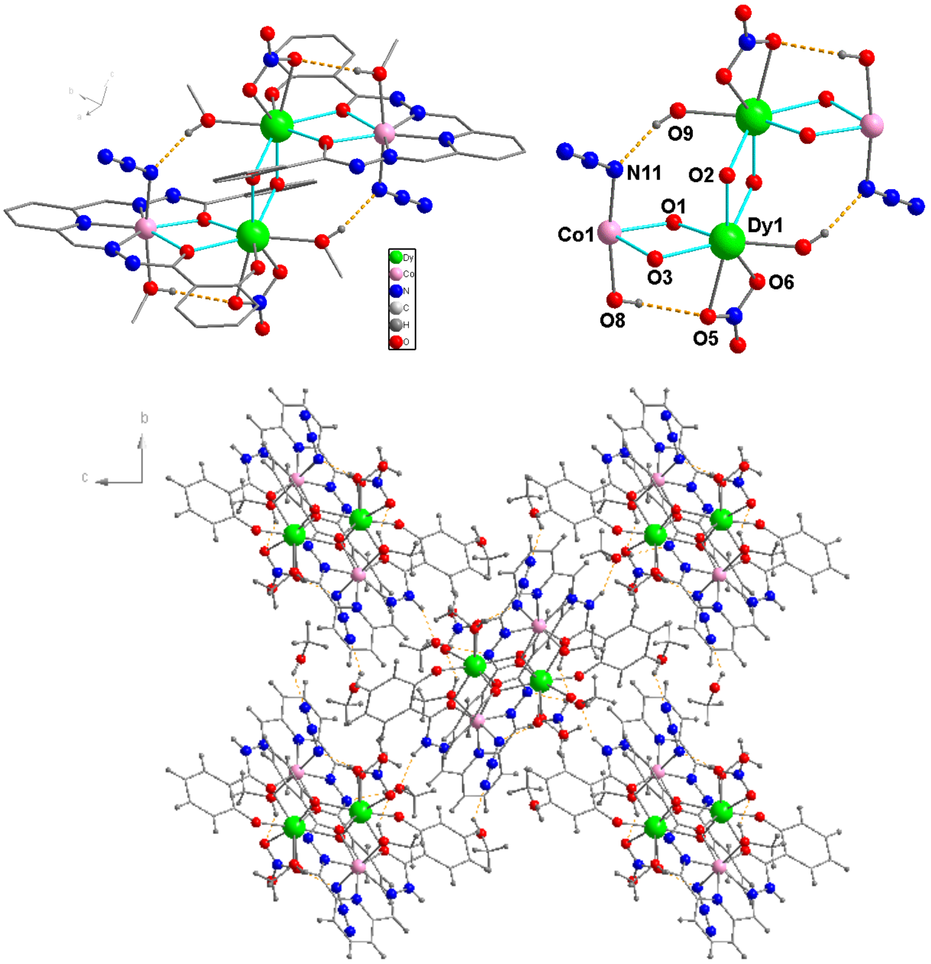

Fig 4.57 Molecular structure (upper left), core (upper right) and packing (down) of compound **35**

The tetranuclear compound **35** crystallizes in the space group $P2_1/c$. The molecules of compound **35** consist of two Dy^{III} ions, two Co^{II} ions, two N_3^-, two NO_3^-, four MeOH and two triply deprotonated ligands (H**L9**)$^{3-}$ displaying a $\eta^2:\eta^2:\eta^1:\eta^1:\eta^1:\eta^2:\eta^1:\mu_3$ coordination mode (**Scheme 4.8**). Each of the two Co^{II} ions adopts a distorted square pyramidal pentagonal bipyramidal geometry with an O3N4 donor set and each of the two Dy^{III} ions has adopted an eight coordinate distorted square anti-prism geometry with an O8 donor set. The tetranuclear structure, which has an inversion centre, can be described as two $[Co^{II}Dy^{III}]$ dinuclear units $[Co^{II}$(H**L9**)$(MeOH)(N_3)Dy^{III}(NO_3)(MeOH)]$, Co···Dy = 3.7109(2)Å) bridged by two deprotonated phenoxo groups from two ligands, where the metal···metal distances are Dy···Dy = 3.8181(5)Å and Co···Co = 8.7870(4)Å and the Dy-O-Dy angle is 110.75(12)°. The dinuclear unit consists of a di-μ-hydrazone-bridged structure of $([Co^{II}$(H**L9**)$(MeOH)(N_3)Dy^{III}(NO_3)(MeOH)]$, in which $\{Co^{II}$(H**L9**)$(MeOH)(NO_3)\}$ is acting as a ligand-complex which bridges Co^{II} and Dy^{III} ions with help of two hydrazono-oxo groups and with help of two phenoxo groups coordinating to the Dy^{III} ions of the second Co-Dy subunit to give the $(Co^{II}\text{-}Dy^{III})_2$ tetranuclear structure. Selected bond lengths and angles in the $Co^{II}O_2Dy^{III}$ dinuclear units are: Co-O1 = 2.160(3)Å, Co-O3 = 2.237(3)Å with Co-O-Dy angles of 110.68(14)° and 105.50(13)° , Dy-O1 = 2.350(3)Å, and Dy-O3 = 2.422(3)Å and Co···Dy = 3.7109(2)Å. The Dy-O (phenol) distances, Dy-O2 = 2.339(3)Å and Dy-O4 = 2.220(3)Å, are longer than those of Dy-O (hydrazone-oxo).

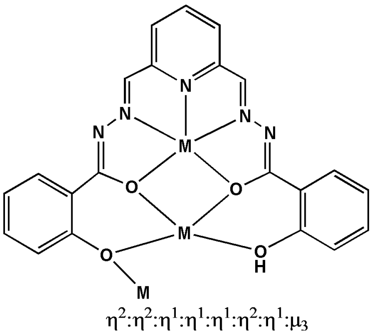

Scheme 4.8 The coordination mode of the H_4**L9** in compounds **27-30**

The high-spin Co^{II} ion has a pentagonal bipyramidal coordination environment formed by the N3O2 donor atoms of the ligand, with bond distances of Co-O1 = 2.160(3)Å, Co-O3 = 2.237(3)Å, Co-N1 = 2.151(4)Å, Co-N2 = 2.134(4)Å and Co-N4 = 2.167(4)Å in the equatorial plane and the two axial sites are occupied by an oxygen atom of the methanol ligand with a distance of Co-O8 = 2.174(4)Å and one nitrogen atom of the N_3^- ion with a distance of Co-N11 = 2.142(4)Å. The Co-N and Co-O bond distances and the coordination numbers of 7 are consistent with a high-spin state of the Co^{II} ion. The Dy^{III} ion is coordinated by the five oxygen atoms of two phenoxo and two hydrazonoxo atoms of $\{Co^{II}$(H**L9**)(MeOH)$(N_3)\}$ and one phenoxo of the other $\{Co^{II}$(H**L9**)(MeOH)$(N_3)\}$, two oxygen atoms of the NO_3^- ion acting as a chelating ligand, with Dy-O5 = 2.527(4)Å and Dy-O6 = 2.494(5)Å, one oxygen atom of a MeOH, with Dy-O6 = 2.364(4)Å; a coordination number of 8 is thus attained. The Co-N/O and Dy-O are in the range of 2.134(3)-2.174(4)Å and 2.220(3)-2.527(4)Å. There are very rich and strong intra- and intermolecular hydrogen bonds in this compound (**Fig 4.57**).

4.2.17 Magnetic properties of compound 35

Direct current (dc) magnetic susceptibility measurements were performed on polycrystalline samples in the temperature range 2-300 K, with an applied magnetic field of 1000 Oe. The χT versus T plot for **35** (**Fig 4.58**, left), reveals room temperature χT values of 34.59 cm^3 K mol^{-1}, which is higher than the value of 32.09 cm^3 K mol^{-1} expected for two Co^{II} and two Dy^{III} non-interacting ions. The small difference is due to the unquenched spin-orbital moment of Co^{II} ions. As the temperature is reduced the χT value gradually decreases, before a faster drop occurs between 75-25 K, below which an upturn is observed before decreasing again at the lowest temperatures. The high temperature decrease can be attributed to the depopulation of the excited M$_J$ states of the Dy^{III} ions, while the increase at lower temperatures suggests non-negligible and significant magnetic exchange interactions present between the Dy^{III} and the Co^{II} ions or the Dy^{III} and Dy^{III}. The magnetisation (M) measurements for **35** (**Fig 4.58**, right), plotted as a function of the magnetic field (H), display a rapid increase in magnetisation below 2 T, before following a more gradual linear-like increase, without saturating, thus signifying a significant magnetic anisotropy is presented in compound **35**.

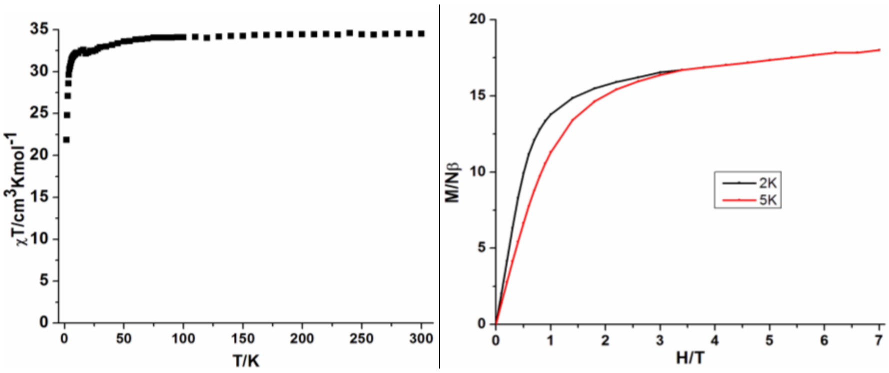

Fig 4.58 Plots of χ T vs T at 1000 Oe (left) and M vs H at indicated temperatures (right) of **35**

The ac susceptibilities indicate that compound **35** shows slow relaxation of the magnetisation in zero field, but no maximum was observed. A dc field was also applied, but it did not influence the magnetic relaxation indicating the absence of SMM behaviour in this compound (**Fig 4.59**).

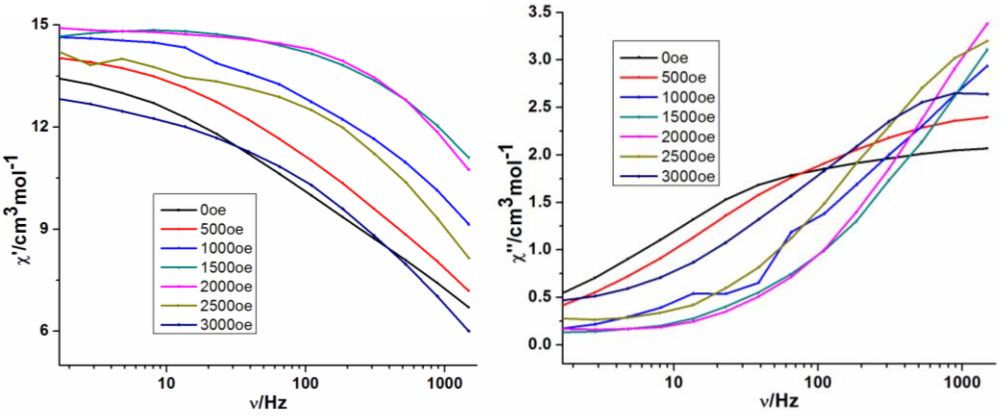

Fig 4.59 Plots of χ’ (left) and χ” (right) vs frequency of **35** at 1.8 K under indicated applied dc magnetic fields.

4.3 Conclusion

In this chapter, the synthesis, crystal structures and magnetic properties of compounds (**16**-**35**) are presented. These are based on the Schiff base ligands: H_3**L4**, giving $[Co(H_2\mathbf{L4})_2]\cdot 2THF$ (**16**) and $[Dy_2(H\mathbf{L4})_2(OAc)_2(EtOH)_2]$ (**19**); H_2**L5**, giving $[Co(H\mathbf{L5})_2]$ (**17**) and $[Dy_2(\mathbf{L5})_2(OAc)_2(H_2O)_2]\cdot 2MeOH$ (**20**); H_3**L6**, giving $[Co(H_2\mathbf{L6})_2]\cdot CH_2Cl_2$ (**18**); H_2**L7**, giving $[Co(\mathbf{L7})]$ (**21**); H_2**L8**, giving $[Co_2Dy_2(\mathbf{L8})_4(NO_3)_2(MeOH)_2]\cdot 2CH_2Cl_2$ (**22**), $[Co_2Dy_2(\mathbf{L8})_4(NO_3)_2(DMF)_2]\cdot 2C_2H_6CO$ (**23**), $[Zn_2Dy_2(\mathbf{L8})_4(NO_3)_2(MeOH)_2]\cdot 2CH_2Cl_2$ (**24**), $[Fe_2Dy(\mathbf{L8})_4(MeOH)(AcO)]\cdot 4MeOH$ (**25**) and $[Fe_2Y(\mathbf{L8})_4(MeOH)(AcO)]\cdot 4MeOH$ **(26)** and H_4**L9**, giving $[Co_2Ln(H_2\mathbf{L9})(NO_3)_2(MeOH)_4]\cdot NO_3\cdot xMeOH\cdot yH_2O$, [Ln = Dy (**27**), x = 5, y = 5; Ln = Tb (**28**), x = 0, y = 8; Ln = Ho (**29**), x = 0, y =10; Ln = Y (**30**), x = 0, y = 10)], $Na\cdot[Co_2Ln(\mathbf{L9})_2(H_2O)_4]\cdot 7H_2O$ [Ln = Dy (**31**), Tb (**32**), Ho (**33**) and Y (**34**)] and $[Co_2Dy_2(H\mathbf{L9})_2(N_3)_2(NO_3)_2(MeOH)_4]\cdot 4MeOH$ (**35**). It is worth to mention that the family of $[Co_2Ln(H_2\mathbf{L9})(NO_3)_2(MeOH)_4]\cdot NO_3\cdot xMeOH\cdot yH_2O$ (**27-30**) is two dismensional and displays a very interesting square channel structure.

All the complexes (**16-35**) were magnetically investigated. The mononuclear Co^{II} systems (**16-18** and **21**) exhibit significant uniaxial anisotropy and slow relaxation of the magnetisation has been observed under an applied dc field. The subtle difference in their octahedral geometry leads to variations in their magnetic anisotropy and energy barrier. The barriers of complexes **16-18** are 7.30 K, 10.18 K and 14.10 K, respectively. For compound **21**, the trigonal prismatic coordination geometry of Co^{II} leads to enhanced SIM behaviour with a high energy barrier of 98 K.

The dc magnetic measurements of the Dy_2 compounds (**19** and **20**) indicate they show antiferromagnetic behaviour. Remarkably, different dynamic magnetisation behaviour was observed. Compound **19** shows slow magnetic relaxation with an energy barrier of 35.36 K under 2000 Oe dc field, while compound **20** shows slow magnetic relaxation with an energy barrier of 38.46 K under zero dc field. These results provide important evidence that the dynamic behaviour of Dy containing complexes can be modulated by careful tuning of the structural environments.

Compounds **22**, **23** and **25** which are based on the H_2**L8** ligand and compounds **28**, **31** and **32** based on H_4**L9** ligand show ferromagnetic interactions between the 3d-4f ions. On the other hand, compounds **27**, **29**, **33** and **35** show weak antiferromagnetic interactions. The dynamic magnetic property measurements reveal that compounds **22** and **23** exhibit two slow relaxation of the magnetisation processes with energy barriers U_1 = 17.85 K and U_2 = 104.78 K for **22**, U_1 = 17.45 K and U_2 = 94.53 K for **23**, whereas compound **24** has a single process with a barrier U_1 = 140 K. Through varying the coordinated solvent on the Co^{II} ions, it was possible to affect the high temperature single-ion relaxation of Dy^{III} ions. For the other compounds **25-35**, no ac signals were observed even in applied dc field, which indicates that these compounds are not SMMs.

Chapter 5 Summary

This research has produced compounds exhibiting a wide range of structural motifs and interesting magnetic properties. The results are divided into two chapters according to ligand type.

In chapter 3, fifteen heterometallic 3d-4f and homometallic 4f coordination compounds (**1-15**) have been successfully synthesized using the amino polyalcohol ligands H_2**dea**, H_3**L1,** H_2**L2** and H_3**L3**. Variation of the reaction conditions led to seven distinct structure types. All compounds were crystallographically characterised and magnetically studied. Compounds **1** and **2** were made with H_2**dea** as ligand and have the same core structure $\{Co^{III}_3Co^{II}_2Ln^{III}_2\}$. A further five series were produced with the related ligand H_2**L1**: $Co^{III}_3Dy^{III}_3$ (**3** and **4**), $Fe^{III}_2Dy^{III}_2$ (**5**), $Cr^{III}_2Ln^{III}_2$ [Ln = Dy (**6**) and Y (**7**)], $Fe^{III}Ln^{III}$ [Ln = Dy (**8**) and Y (**9**)], $Fe^{III}_4Ln^{III}_4$ [Ln = Dy (**10**), Tb (**11**) and Y (**12**)]. The last series of Dy_2 (**28-30**) dimers is based on the related amino polyalcohol ligands [H_2**L1** (**13**), H**L2** (**14**) and H_2**L3** (**15**)]

From the magnetic point of view, all compounds exhibit antiferromagnetic interactions except $Fe^{III}Dy^{III}$ (**8**) and Dy_2 (**15**). The field dependence at low temperature for all compounds indicates the presence of magnetic anisotropy and or the lack of a well defined ground state suggesting the presence of low-lying excited states that might be populated when a field is applied. In contrast, compounds **8** and **15** display weak ferromagnetic interactions. The ac measurements show that compounds **3**, **4**, **5**, **10**, **11**, **14** and **15** display slow relaxation in zero dc field, but only compound **15** shows maxima with U_{eff} = 27.3 K. On application of a dc field, compounds **5** and **14** show typical SMM behaviour with energy barriers of 16.13 K and 72.48 K, respectively. Compounds **5** and **6** are isostructural only differing in the 3d ions (Fe^{III}, **5** and Cr^{III}, **6**). Compound **5** is a field-induced SMM, while for complex **6** no ac signal even under dc applied field could be observed, suggesting that the different electronic structure of the 3d metal ion must be responsible for the differences in behaviour. For the related Dy_2 (**13-15**) family, control of the ligand field can slow down the relaxation of the magnetisation of Dy^{III}.

In chapter 4, twenty Co^{II}, 3d-4f and 4f coordination compounds (**16-35**) are described. These have been successfully synthesized based on the Schiff base ligands H_3**L4**, H_2**L5**, H_3**L6**, H_2**L7**, H_2**L8** and H_4**L9**. A Co^{II} mononuclear system (**17-18** and **21**) was formed with the H_3**L4**, (**16**), H_2**L5**, (**17**), H_3**L6**, (**18**); H_2**L7**, (**21**) ligands. A Dy^{III}_2 system was formed with H_3**L4**, (**19**) and H_2**L5**, (**20**).

$[Co^{II}_2Dy^{III}_2]$ (**22** and **23**), $[Zn^{II}_2Dy^{III}_2]$ (**24**), and $[Fe^{III}_2Ln^{III}]$, (Ln = Dy (**25**) and Y (**26**)) were formed with H_2**L8**. A 2D coordination polymer $Co^{II}_2Ln^{III}$ (Ln = Dy (**27)**, Tb (**28)**, Ho (**29)** and Y, (**30**)), a linear $Co^{II}_2Ln^{III}$ (Ln = Dy (**31)**, Tb (**32)**, Ho (**33)** and Y, (**34**)) motif and a linear $[Co^{II}_2Dy^{III}_2]$ (**35**) compound were formed with H_2**L9**. All compounds were crystallographically characterised and magnetically studied.

From the magnetic point of view, the mononuclear Co^{II} compounds (**16-18** and **21**) exhibit significant uniaxial anisotropy. For compounds **16-18**, slow relaxation of magnetisation has been observed under an applied 1000 Oe dc field, which means they are field induced SIMs. For compound **21**, slow relaxation of magnetisation has been observed without applied dc field. The results indicate if the coordination geometry of the Co^{II} is changed from octahedral to trigonal prismatic, enhanced SIM properties with an energy barrier of 98 K were observed. The results on the mononuclear Co^{II} compounds suggest that subtle variation of the ligand field via small modifications to the ligand can influence the relaxation behaviour. The tunnelling speed clearly depends on the environment of the Co^{II}.

In the two similar Dy_2 compounds (**19** and **20**) the metal centres are antiferromagnetically coupled. Distinct ac susceptibility behaviour was observed but while compound **19** only shows slow relaxation of magnetisation under application of a 2000 Oe dc field, compound **20** shows slow magnetic relaxation under zero dc field. Thus through changing the details of the coordination environment in complexes **19** and **20** and in the mononuclear Co^{II} systems, it is possible to significantly change energy barriers and relaxation times.

These results further confirm that the ligand field is one of the most important keys for designing 3d or 4f SMMs. The dc measurements of compounds **22-24**, reveal that compounds **22** and **23** have dominant ferromagnetic interactions between the 3d-4f ions and the ac susceptibility measurements reveal that compounds **22**, **23** and **24** exhibit interesting slow relaxation of the magnetisation.

For example, for the first time it was possible to observe that the anisotropy of a single Dy^{III} can be steered through changes in the coordination geometry of the Co^{II} ions in the $Co^{II}_2Ln^{III}_2$ compounds. Furthermore, this provides experimental proof of the suggestion from the *ab initio* calculation results on the $Co^{II}_2Dy^{III}_2$ compound previously reported by our group that two or more relaxation pathways can be important in determining the overall magnetic behaviour of Co^{II}-4f systems.

The dc susceptibility measurements on compounds **25-35** indicate that compounds **25**, **28**, **31** and **32** show weak ferromagnetic interactions, while the other compounds (**27**, **29**, **33** and **35**) show weak antiferromagnetic inteactions. In the ac susceptibilitiy measurements no maxima were observed even under applied dc field, which indicates that these compounds do not show SMM behaviour under these conditions.

Chapter 6 Experimental Sections

6.1 General procedures

Most of the chemicals and all of the solvents were obtained from commercial sources and were used without further purification. The starting materials of 6-hydroxymethyl-pyridine-2-carbaldehyde and pyridine-2,6-dicarbaldehyde[58] and the ligands of H_2**L1**,[59] H**L2**,[60] H_2**L3**,[60] H_2**L7**, H_2**L8**[61] and H_4**L9** were prepared according to literature procedures.

6.2 Preparation of organic ligands

6.2.1 Synthesis of 2-(bis-pyridin-2-ylmethyl-amino)-propane-1, 3-diol (H_2L_3)

A mixture of 2-amino-1,3-propanediol (2.73 g, 30 mmol) and 2-picolyl chloride hydrochloride (9.84 g, 60 mmol) in MeCN (100 ml) was refluxed under a nitrogen gas atmosphere for 48 h in the presence of K_2CO_3 (16.66 g, 120 mmol) and KI (1.66 g, 10 mmol). The resulting orange solution was filtered, and the solvent was removed under reduced pressure. The obtained pale yellow oil was purified by chromatography using MeOH/ethyl acetate (v/v = 1/3) as eluant. H_2**L**3 was obtained as a pale yellow oil (6.20 g, 76.5%). ^{1}H-NMR (300 MHz, $CDCl_3$): δ(ppm) = 3.32-3.46 (m, 1 H, N-C*H*), 3.56 (d, 4 H, ^3J = 7 Hz, CH_2OH), 4.02 (s, 4 H, NCH_2), 6.94-7.00 (m, 2 H, H_{Ar}), 7.19 (m, 2 H, H_{Ar}), 7.59 (td, 2 H, ^3J = 7.7 Hz, 1.8 Hz, H_{Ar}) 8.54-8.62 (m, 2 H, H_{Ar}). Anal. Calcd (Found) % for $C_{16}H_{21}N_3O_3$: C, 65.91 (65.67); H, 7.01 (7.22); N, 15.37 (15.55).

6.2.2 Synthesis of 6,6'-((1Z)-((piperazine-1,4-diylbis(propane-3,1-diyl))bis(azanylylidene))bis(methanylylidene)) bis(2-methoxyphenol) (H_2L7)

A mixture of *o*-vanillin (3.04 g, 20 mmol) and 1,4-bis (3-aminopropyl) piperazine (2.0 g, 10 mmol) was refluxed for 4 h in EtOH (50 mL). The resultant yellow precipitate was filtered and washed well with cold EtOH followed by ether and dried in air. Yield is 90% (4.23 g). Anal Calc. (found)% for $C_{26}H_{36}N_4O_4$: C, 66.64 (66.55); N, 11.96 (11.80); H, 7.74 (7.82).

6.2.3 Synthesis of (N',N'''E,N',N'''E)-N',N'''-(pyridine-2,6-diylbis(methanylylidene))bis(2-hydroxybenzohydrazide) (H_4L9)

A mixture of pyridine-2,6-dicarbaldehyde (1.35 g, 10 mmol) and 2-hydroxy-benzoic acid hydrazide (3.04 g, 20 mmol) was refluxed for 4 h in EtOH (30 mL). The resultant yellow precipitate was filtered and washed well with cold EtOH followed by ether and dried in air. Yield is 93%. Anal. Calc (found)% for $C_{22}H_{21}N_5O_4$: C, 63.00 (62.85); N, 16.70 (16.80); H, 5.05 (5.17).

6.3 Preparation of coordination clusters

6.3.1 Synthesis of $[Co^{III}_3Co^{II}_2Ln^{III}_2(OH)_2(PhCO_2)_6(dea)_4(Hdea)(NO_3)](NO_3)\cdot 3MeOH\cdot H_2O$ (1 and 2)

$[Co^{III}_3Co^{II}_2Dy^{III}_2(OH)_2(PhCO_2)_6(dea)_4(Hdea)(NO_3)](NO_3)\cdot 3MeOH\cdot H_2O$ (1)

The complexes **1** and **2** were prepared according to the same experimental process, therefore only the dysprosium synthesis will be described. Solid $DyCl_3\cdot 6H_2O$ (94 mg, 0.25 mmol) or $GdCl_3\cdot 6H_2O$ (94 mg, 0.25 mmol) was added to a solution of H_2**dea** (109 mg, 1 mmol), $Co(NO_3)_2\cdot 6H_2O$ (290 mg, 1 mmol), sodium benzoate (144 mg, 1 mmol), and Et_3N (0.25 ml) in MeOH (12 mL). The mixture stirred for 10 min. The rose solution was then left and undisturbed. After one week well formed purple-pink crystals were collected. Yield is 23% (based on Dy). Anal. Calc (Found)% for $C_{65}H_{90}Co_5Dy_2N_7O_{36}$: C, 36.06 (35.94); H, 4.19 (4.25); N, 4.53 (4.20). Selected IR data (KBr, cm^{-1}): 3404 (br), 2923(w) 1596 (s), 1558 (s), 1474 (s), 1389 (s), 1294 (m), 1176 (w), 1157 (w), 1084 (w), 1068 (w), 1022 (w), 1008 (w), 941 (w), 912 (w), 845 (w), 829 (w), 815 (w), 760 (w), 738 (w), 714 (w), 687 (w).

$[Co^{III}_3Co^{II}_2Gd^{III}_2(OH)_2(PhCO_2)_6(dea)_4(Hdea)(NO_3)](NO_3)\cdot 3MeOH\cdot H_2O$ (2)

Yield: 30%. Anal.Calc (Found)% for $C_{65}H_{90}Co_5Gd_2N_7O_{36}$: C, 36.26 (35.24); H, 4.21 (4.39); N, 4.55

(4.40). Selected IR data (KBr, cm^{-1}): 3404 (br), 2923 (w), 1596 (s), 1558 (s), 1474 (s), 1389 (s), 1294 (m), 1176 (w), 1157 (w), 1084 (w), 1068 (w), 1022 (w), 1008 (w), 941 (w), 912 (w), 845 (w), 829 (w), 815 (w), 760 (w), 738 (w), 714 (w), 687 (w)

6.3.2 Synthesis of $[Co^{III}_3Dy_3(L1)_3(\mu_3\text{-}OH)_4(O_2CPh)_6(H_2O)_3]\cdot(O_2CPh)\cdot Cl\cdot 4MeOH\cdot 10H_2O$ (3)

A solution of $CoCl_2\cdot 6H_2O$ (0.06 g, 0.25 mmol) and $DyCl_3\cdot 6H_2O$ (0.094g, 0.25 mmol) in MeOH (5 mL) was added to H_2**L1** (0. 10 g, 0.50 mmol) and $PhCO_2H$ (0.122 g, 1 mmol) in MeCN (20 ml). The mixture was stirred for 10 min, then, triethylamine (0.14 ml, 0.1 mmol) was added. The final solution was stirred for 20 min before filtering. Big crystals were obtained after 1 week from the filtrate. Yield is 84.2% (based on Co). Anal. Calc (Found)% for $[Co^{III}_3Dy_3(\mathbf{L1})_3(\mu_3\text{-}OH)_4(O_2CPh)_6(H_2O)_3]\cdot(O_2CPh)\cdot Cl\cdot MeCN\cdot 15H_2O$: C, 38.10 (38.11); H, 4.34 (4.49); N, 3.84 (4.03). Selected IR data (KBr, cm^{-1}): 3415 (br), 2955 (w), 2882 (w), 1603 (s), 1564 (s), 1550 (s), 1469(m), 1404 (s), 1384 (s), 1352 (w), 1110 (m), 1071 (m), 1024 (w), 923 (w), 832 (w), 722 (s), 680 (m), 615 (w), 480 (w).

6.3.3 Synthesis of $[Co^{III}_3Dy_3(L1)_3(\mu_3\text{-}OH)_4(O_2CPh\text{-}\mathit{Me})_6(H_2O)_3]\cdot 2Cl\cdot 10MeOH$ (4)

Using para-*Me*-$PhCO_2H$ in place of $PhCO_2H$, resulted in compound **4**. Yield is 66%. $[Co^{III}_3Dy_3(\mathbf{L1})_3(\mu_3\text{-}OH)_4(O_2CPh\text{-}\mathit{Me})_6(H_2O)_3]\cdot 2Cl\cdot 2MeOH\cdot 4H_2O$: C, 38.10 (38.11); H, 4.34 (4.49); N, 3.84 (4.03) Selected IR data (KBr, cm^{-1}): 3415 (br), 2956 (w), 2884(w), 1613 (s), 1565 (s), 1551 (s), 1467(m), 1414 (s), 1381 (s), 1351 (w), 1110 (m), 1078 (m), 1026 (w), 925 (w), 833 (w), 726 (s), 681 (m), 614 (w), 482 (w).

6.3.4 Synthesis of $[Fe_2Dy_2(L1)_2(O_2CPh\text{-}\mathit{Me})_6(OH)_2]\cdot 2MeCN\cdot MeOH\cdot 3.35H_2O$ (5)

H_2**L1** (100 mg, 0.5 mmol) in MeOH (5 ml) was added to a solution of $FeCl_3\cdot 3H_2O$ (50.5 mg, 0.25 mmol), $DyCl_3\cdot 6H_2O$ (94 mg, 0.25 mmol) and 4-methylbenzoic acid (136 mg, 1 mmol) in MeCN and MeOH (25 ml, v/v = 4:1). After 10 min of stirring, Et_3N (0.42 ml, 3 mmol) was added, leaving the solution stirring for a further 0.5 h. The final solution was filtered and left undisturbed. Pale yellow crystals suitable for X-ray analysis formed overnight and were collected and air dried. Yield: 61% (187.5 mg, based on 4-methylbenzoic acid). Anal. Calcd (Found)% for

$Fe_2Dy_2C_{68}H_{72}N_4O_{18}\cdot 2MeCN\cdot MeOH\cdot 3.35H_2O$: C, 47.53 (47.29); H, 4.85 (4.51); N, 4.56 (4.51). Selected IR data (KBr, cm^{-1}): 3503 (br), 3058 (w), 2975 (w), 2854 (m), 1593 (s), 1541 (s), 1099 (s), 906 (s), 722 (s), 672 (s), 593 (s).

6.3.5 Synthesis of $[Cr_2Ln_2(L1)_2(O_2CPh\text{-}Me)_6(OH)_2]\cdot 2MeCN$ (6 and 7)

$[Cr_2Dy_2(L1)_2(O_2CPh\text{-}Me)_6(OH)_2]\cdot 2MeCN$ (6)

H_2**L1** (100 mg, 0.5 mmol) in MeOH (5 ml) was added to a solution of $CrCl_3\cdot 6H_2O$ (66 mg, 0.25 mmol), $DyCl_3\cdot 6H_2O$ (94 mg, 0.25 mmol) and 4-methylbenzoic acid (136 mg, 1 mmol) in a mixture of MeCN (20 ml) and MeOH (5 ml). After 10 min of stirring, Et_3N (0.42 ml, 3 mmol) was added, leaving the solution stirring for a further 30 min. The final solution was filtered and left undisturbed. After three days pale green crystals suitable for X-ray analysis were collected and air dried. Yield: 50% (145. 4 mg, based on 4-methylbenzoic acid). Anal. Calcd (found)% for $Cr_2Dy_2C_{68}H_{72}N_4O_{18}\cdot 2MeCN$: C, 49.57 (49.44); H, 4.51 (4.37); N, 4.82 (5.02). Selected IR data (KBr, cm^{-1}): 3493 (br), 3062 (w), 2978 (w), 2856 (m), 1595 (s), 1542 (s), 1097 (s), 908 (s), 719 (s), 673 (s), 593 (s).

$[Cr_2Y_2(L1)_2(O_2CPh\text{-}Me)_6(OH)_2]\cdot 2MeCN$ (7)

Yield: 56% (based on 4-methylbenzoic acid). Anal. Calcd (found)% for $Cr_2Y_2C_{68}H_{72}N_4O_{18}\cdot 2MeCN$: C, 54.14 (54.03); H, 4.92 (4.93); N, 5.26 (5.38). Selected IR data (KBr, cm^{-1}): 3500 (br), 3063 (w), 2977 (w), 2854 (m), 1592 (s), 1540 (s), 1099 (s), 909 (s), 718 (s), 674 (s), 592 (s).

6.3.6 Synthesis of $[FeLn(HL1)_2(O_2CPh)_3(NO_3)]$ (8 and 9)

$[FeDy(HL1)_2(O_2CPh)_3(NO_3)]$ (8)

A solution of $[Fe_3O(O_2CPh)_6(H_2O)_3](O_2CPh)$ (0.125 g, 0.125 mmol) in MeCN (10 mL), was added to a solution of H_2**L1** (0.20 g, 1.0 mmol) and $Dy(NO_3)_3\cdot 6H_2O$ (0.056 g, 0.125 mmol) in MeCN (15 mL) under stirring. The mixture was stirred for another 30 min at room temperature, and filtered.

The pale yellow solution was then left undisturbed and opened to the air. After 2 weeks pale-yellow crystals were obtained. Yield was 55% (based on Dy). Anal. Calc (Found)% for $C_{41}H_{45}N_5O_{13}FeDy$: C, 47.62 (47.60); H, 4.39 (4.42); N, 6.77 (6.75). Selected IR data (KBr, cm^{-1}): 3652 (s), 3235 (br), 2873 (m), 1598 (s), 1558 (s), 1538 (m), 1493 (m), 1467 (w), 1543 (m), 1442 (m), 1384 (s), 1367 (s), 1307 (w), 1092 (s), 1070 (s), 1024 (m), 922 (s), 902 (s), 720 (s), 688 (m), 671 (s), 636 (w), 601 (s), 430 (w), 407 (w).

$[FeY(HL1)_2(O_2CPh)_3(NO_3)]$ (9)

Yield: 60% (based on Y). Anal.Calc (Found)% for $C_{41}H_{45}N_5O_{13}FeY$: C, 51.27 (51.08); H, 4.72 (4.73); N, 7.29 (7.16). The IR is similar with complex **8**.

6.3.7 Synthesis of $[Fe_4Ln_4(L1)_2(O_2CPh)_{10}(O)_3(OH)_2(MeOH)_2(MeO)_2]\cdot 3MeOH\cdot xH_2O$ (10-12)

$[Fe_4Dy_4(L1)_2(O_2CPh)_{10}(O)_3(OH)_2(MeOH)_2(MeO)_2]\cdot 3MeOH$ (10)

A solution of $FeCl_2\cdot 6H_2O$ (0.068 g, 0.25 mmol), $Dy(NO_3)_3\cdot 6H_2O$ (0.113 g, 0.25 mmol), H_2**L1** (0.1g, 0.5 mmol) and $PhCO_2Na$ (0.118 g, 2 mmol) in MeOH (20 mL) was stirred for 10 min at room temperature, followed by addition of Et_3N (0.14 ml, 1 mmol). The mixture was stirred for another 20 min and filtered. The filtrate was left undisturbed, pale yellow crystals were obtained after 4 days. Yield is 57% (based on Dy). Anal.Calc (Found)% for $C_{94}H_{102}Dy_4Fe_4N_4O_{37}$: C, 41.01 (40.73); H, 3.73 (3.39); N, 2.03 (2.11) Selected IR data (KBr, cm^{-1}): 3404 (br), 2857 (m), 1608 (s), 1567 (s), 1537 (s), 1493 (m), 1422 (vs), 1175 (m), 1082 (s), 1071 (s), 1026 (s),1000 (s), 900 (m), 856 (m), 763 (w), 719 (s), 688 (m), 673 (m), 610 (s), 569 (m).

$[Fe_4Tb_4(L1)_2(O_2CPh)_{10}(O)_3(OH)_2(MeOH)_2(MeO)_2]\cdot 3MeOH\cdot H_2O$ (11)

Yield: 66%. Anal. Calc (Found)% for $C_{94}H_{106}Tb_4Fe_4N_4O_{39}$: C, 40.69 (40.36); H, 3.85 (3.52); N, 2.02 (2.11). Selected IR data (KBr, cm^{-1}): 3409 (br), 2856 (m), 1603 (s), 1568 (s), 1531 (s), 1493 (m), 1423 (vs), 1175 (m), 1079 (s), 1071 (s), 1026 (s),1003 (s), 905 (m), 856 (m), 763 (w), 719 (s), 688 (m), 678 (m), 612 (s), 568 (m).

$[Fe_4Y_4(L1)_2(O_2CPh)_{10}(O)_3(OH)_2(MeOH)_2(MeO)_2]\cdot3MeOH\cdot H_2O$ (12)

Yield: 63%. Anal.Calc (Found)% for $C_{94}H_{106}Y_4Fe_4N_4O_{39}$: C, 45.25 (45.03); H, 4.28 (3.99); N, 2.25 (2.34). Selected IR data (KBr, cm^{-1}): 3404 (br), 2853 (m), 1610 (s), 1566 (s), 1536 (s), 1492 (m), 1421 (vs), 1172 (m), 1085 (s), 1075 (s), 1022 (s), 997 (s), 903 (m), 854 (m), 761 (w), 718 (s), 685 (m), 672 (m), 611 (s), 571 (m).

6.3.8 Synthesis of [$Dy_2(HL1)(NO_3)_4$] (13)

A solution of $Dy(NO_3)_3\cdot6H_2O$ (223 g, 0.50 mmol) in MeOH (5 mL) was added to a stirring solution of H_2**L1** (66 mg, 0.33 mmol) and Et_3N (0.07 ml, 0.50 mmol) in MeCN (40 mL). The solution was stirred for 5 min and filtered. The filtrate was left undisturbed, colourless single crystals suitable for X-ray diffraction analysis was obtained overnight (144 mg, 87%, based on ligand). Anal. Calcd (Found)% for $C_{20}H_{30}Dy_2N_8O_{16}$: C, 24.93 (24.85); H, 3.14 (3.27); N, 11.63 (11.68). Selected IR data (KBr, cm^{-1}): 3217.5 (s), 2996.5 (w), 2958.5 (m) 2905.5(m), 2858.5 (m), 1636.5 (m), 1607.5(s), 1575 (m), 1516 (vs), 1484.5 (vs), 1466.5 (vs), 1444 (s), 1385 (s), 1304.5 (s), 1158.5 (m), 1149 (m), 1072.5 (s), 1033 (s), 1025 (m), 1009.5 (s), 920.5 (m), 906 (w), 888 (m), 874 (m), 836.5 (w), 812.5 (m), 789.5 (m), 769.5 (m), 739.5 (m), 732 (w), 636.5 (vw), 587 (m) 555.5 (m), 499 (ms), 467.5 (w)

6.3.9 Synthesis of $[Dy_2(L2)(NO_3)_4]$ (14) and $[Dy_2(HL3)_2(NO_3)_4]$ (15)

The complexes **14** and **15** were prepared according to the same experimental process, but using H_2**L3** in place of H**L2**, so that only the method for complex **14** will be described. A suspension of $Dy(NO_3)_3\cdot6H_2O$ (0.5 mmol, 223 mg) and H_1**L2** (0.33 mmol, 81 mg) or H_2**L3** (0.33, 91 mg) in MeOH and MeCN (45 mL, v/v:1/8) was treated with Et_3N (0.035 ml, 0.25 mmol). The resulting colorless solution was stirred for 5 min and subsequently filtered. The filtrate was left undisturbed to allow the slow evaporation of the solvent. White single crystals of $[Dy_2($**L2**$)_2(NO_3)_4]$ (**14**) or $[Dy_2(H$**L3**$)_2(NO_3)_4]$ (**15**) were formed after 2 days. The yield is 85% (151 mg, based on ligand) for (**14**), and 90% (166 mg, based on ligand) for (**15**), respectively. Anal. Calcd (Found)% for $C_{28}H_{32}Dy_2N_{10}O_{14}$（14）: C, 31.80 (32.4); H, 3.05 (3.07); N, 13.24 (13.13). Selected IR data (KBr, cm^{-1}) (**14**): 3414.5 (s), 3102 (w), 2977.5 (w), 2957.5 (w), 2921.5 (w), 2898.5 (m), 2872 (m), 1642 (m), 1607 (s), 1574 (m), 1498.5 (vs), 1468 (vs), 1444 (s), 1385 (s), 1294 (vs), 1159 (m), 1105 (m), 1067.5 (s), 1036.5 (s), 1016 (s), 1005.5 (s), 878.5 (m), 818.5 (m), 801.5 (m), 762.5 (m), 741 (m), 661.5 (w), 638 (m), 628.5 (w), 573.5 (m), 511.5 (m), 497.5 (ms), 473.5 (m), 458.5 (m), 418 (m). Anal. Calcd (found)% for $C_{30}H_{36}Dy_2N_{10}O_{16}$ (**15**): 32.24 (32.34); H, 3.25 (3.41); N, 12.53 (12.46). Selected IR data (KBr, cm^{-1}) (**15**): 2947.5 (w), 2911(w), 2852(w), 2427.5 (w), 1605.5 (m), 1574.5 (w), 1499.5 (m), 1482 (m), 1448 (m), 1385 (vs), 1298.5 (m), 1239 (w), 1156 (w), 1075 (m), 1046.5 (m), 1016 (m), 995.5 (m), 798 (m), 758 (m), 638 (m), 576.5 (m), 554 (w), 499 (m), 438 (m).

6.3.10 Synthesis of $[Co(HL4)_2]\cdot 2THF$ (16)

A solution of 6-hydroxymethyl-pyridine-2-carbaldehyde (27.4 mg, 0.2 mmol) and 3-hydroxy-naphthalene-2-carboxylic acid hydrazide (40.4 mg, 0.2 mmol) in 5 mL MeOH and 10 mL MeCN was stirred for 10 minutes at room temperature, then $Co(NO_3)_2\cdot 6H_2O$ (29 mg, 0.1 mmol) was added under stirring. The resulting mixture was stirred for an additional 5 min before $NaOAc\cdot 3H_2O$ (68 mg, 0.5 mmol) in MeOH (5 ml) was added. The resulting mixture was filtered. The pale red colour solution was left undisturbed and after one week microcrystalline material had precipitated out which was dissolved in 15 mL THF/MeOH (v/v:2/1). Slow evaporation from air produced red colour needle shaped crystals of **16** in yield of 90% (388 mg, base on Co). Anal. Calcd (found)% for $CoC_{36}H_{28}N_6O_6\cdot 2THF\cdot MeOH$: C, 61.71 (61.99); H, 5.52 (5.28); N, 9.60 (9.86). Selected IR data (KBr, cm^{-1}): 3380 (br), 3053 (w), 1621 (s), 1562 (m), 1537 (s), 1508 (m), 1477 (s), 1455 (s), 1441 (m), 1425 (m), 1384 (m), 1341 (s), 1192 (m), 1150 (m), 1095 (w), 1052 (w), 1011 (w), 927 (w), 802 (w), 751 (m), 652 (w), 574 (w), 481 (w).

6.3.11 Synthesis of $[Co(HL5)_2]$ (17)

A solution of 6-hydroxymethyl-pyridine-2-carbaldehyde (27.4 mg, 0.2 mmol) and 3-pyridinecarboxylic acid hydrazide (27.4 mg, 0.2 mmol) in 5 mL MeOH and 10 mL MeCN was stirred for 10 minutes at room temperature, then $Co(NO_3)_2\cdot 6H_2O$ (29 mg, 0.1 mmol) was added under stirring. The resulting mixture was stirred for an additional 5 min before $NaOAc\cdot 3H_2O$ (68 mg, 0.5 mmol) in MeOH (5 ml) was added. The resulting mixture was filtered. The pale red filtrate was left undisturbed to allow for the slow evaporation of the solvent. Red prismatic single crystals, suitable for X-ray diffraction analysis, were formed after one week in 87% (293 mg, base on Co) yield for **17**. Anal. Cal (Found)% for $CoC_{28}H_{22}N_8O_4 \cdot 2MeCN \cdot 0.5H_2O$: C, 54.55 (54.55) ; H, 4.43 (4.39); N, 21.20 (21.50). Selected IR data (KBr, cm^{-1}): 3450 (br), 2926 (w), 1632 (s), 1572 (s), 1543 (w), 1484 (s), 1461 (s), 1427 (s), 1383 (s), 1352 (s), 1288 (s), 1242 (s), 1220 (s), 1171 (w), 1155 (w), 1128 (s), 1081 (s), 1003 (w), 975 (s), 890 (w), 850 (w), 771 (s), 740 (s), 645 (s), 627 (w), 420 (s).

6.3.12 Synthesis of $[Co(H_2L6)_2] \cdot CH_2Cl_2$ (18)

A solution of 6-hydroxymethyl-pyridine-2-carbaldehyde (27.4 mg, 0.2 mmol) and 2-hydroxy-benzoic acid hydrazide (30.4 mg, 0.2 mmol) in 5 mL MeOH and 10 mL CH_2Cl_2 was stirred for 10 min at room temperature, then $Co(NO_3)_2 \cdot 6H_2O$ (29 mg, 0.1 mmol) was added under stirring. The resulting mixture was stirred for an additional 5 min before $NaOAc \cdot 3H_2O$ (68mg, 0.5 mmol) in MeOH (5 ml) was added. The resulting mixture was filtered. The pale red filtrate was left undisturbed to allow for the slow evaporation of the solvent. Red prismatic single crystals, suitable for X-ray diffraction analysis, were formed after one week in 93% (307.5 mg, base on Co) yield for **18**. Anal. Calcd (found)% for $CoC_{28}H_{24}N_6O_6 \cdot 0.85CH_2Cl_2$: C, 51.59 (51.56); H, 3.86 (3.98); N, 12.51 (12.51). Selected IR data (KBr, cm^{-1}): 3420 (br), 2927 (w), 1622 (s), 1577 (s), 1546 (w), 1485 (s), 1461 (s), 1427 (s), 1383 (s), 1351 (s), 1285 (s), 1243 (s), 1222 (s), 1171 (w), 1155 (w), 1128 (s), 1081 (s), 1005 (w), 975 (s), 890 (w), 850 (w), 771 (s), 740 (s), 646 (s), 629 (w), 422 (s).

6.3.13 Synthesis of $[Dy_2(HL4)_2(OAc)_2(EtOH)_2]$ (19) and $[Dy_2(L5)_2(OAc)_2(H_2O)_2] \cdot 2MeOH$ (20)

A solution of 6-hydroxymethyl-pyridine-2-carbaldehyde (21 mg, 0.15 mmol) and 3-hydroxy-2-naphthoic acid hydrazide (26.50 mg, 0.15 mmol) or 3-pyridinecarboxylic acid hydrazide (20 mg, 0.15 mmol) in 5 mL MeOH/EtOH and 10 mL $CHCl_3$ was stirred for 30 min at room temperature, then $DyCl_3 \cdot 6H_2O$ (56.50mg, 0.15 mmol) was added under stirring. The resulting mixture was stirred for an additional 30 min after which $NaOAc \cdot 3H_2O$ (68 mg, 0.50 mmol) and triethylamine (0.5 mmol) were added. The solution was filtered and the yellow filtrate was left undisturbed to allow for the slow evaporation of the solvent. Yellow needle single crystals, suitable for X-ray diffraction analysis, were formed after one week in 55% yield (based on Dy) for **19** **[**Dy_2(H**L6**)$_2(OAc)_2(EtOH)_2$] and 65% yield (based on Dy) for **20** [Dy_2(**L7**)$_2(OAc)_2(H_2O)_2] \cdot 2MeOH$. Anal. Calcd (Found)% for $C_{42}H_{40}Dy_2N_6O_{12}$ **19**: C, 44.03 (44.01); H, 3.52 (3.69); N, 7.33 (7.25). Selected IR data (KBr, cm^{-1}) for **19**: 3380 (w), 3053 (w), 1601 (s), 1562 (m), 1537 (s), 1508 (m), 1477 (s), 1455 (s), 1441 (m), 1425 (m), 1384 (m), 1341 (s), 1192 (m), 1150 (m), 1095 (w), 1052 (w), 1011 (w), 927(w), 802 (w), 751 (m), 652 (w), 574 (w), 481(w). Anal. Calcd (Found)% for $C_{30}H_{30}Dy_2N_8O_{10}$ (lost solvent molecules) **20**: C, 36.48 (36.33); H, 3.06 (3.15); N, 11.35 (11.49). Selected IR data (KBr, cm^{-1}) for **20**: 3402 (w), 3070 (w), 1637 (m), 1569 (m), 1537 (s), 1505 (m), 1477 (s), 1455 (s), 1441 (m), 1425 (m), 1372 (m), 1341 (s), 1194 (m), 1160 (s), 1095 (m), 1052 (w), 1011 (w), 927 (w), 802 (w), 769 (s), 652 (w), 576 (w), 481 (w).

6.3.14 Synthesis of [Co^{II}(L7)] (21)

A mixture of H_2**L7** (46.8 mg, 0.1 mmol), $Co(NO_3)_2{\cdot}6H_2O$ (29 mg, 0.1 mmol) $Dy(NO_3)_3{\cdot}6H_2O$ in 2 mL DMF was stirred for 10 min, then, Et_3N (50 mg, 0.5 mmol) was added to the mixture under stirring. After 1 min stirring, the solution was filtered and left undisturbed. Red-brown block-shaped crystals formed overnight in 50% yield. Anal Calc. (found)% for $C_{26}H_{34}CoN_4O_4$: C, 59.42 (59.45); N, 10.66 (10.55); H, 6.52 (6.50).

6.3.15 Synthesis of [$Co_2Dy_2(L8)_4(NO_3)_2(MeOH)_2]{\cdot}2CH_2Cl_2$ (22)

A mixture of $Dy(NO_3)_3{\cdot}6H_2O$ (0.1 mmol, 45 mg), $Co(NO_3)_2{\cdot}6H_2O$ (0.1 mmol, 29 mg) and H_2**L8** (0.2 mmol, 48.6 mg) was stirred in 15 mL of MeOH and CH_2Cl_2 (v/v:1/2) for 10 min. Then $NaOAc{\cdot}3H_2O$ (0.5 mmol, 68 mg) in 5 ml MeOH was poured into the solution. The resulting red coloured solution was filtered after 1 min stirring. The filtrate was left undisturbed and after 30 min crystalline material had precipitated out, suitable for measurement. The yield is 81% (based on Co). Anal. Calcd (Found)% for $C_{58}H_{56}Co_2Dy_2N_6O_{22}$ corresponding to replacement of two CH_2Cl_2 molecules by two H_2O molecules leading to $[Co_2Dy_2($**L8**$)_4(NO_3)_2(MeOH)_2]{\cdot}2H_2O$; C, 42.69 (42.61); H, 3.46 (3.29); N, 5.15 (5.06). Selected IR data (KBr, cm^{-1}): 3414 (br), 3056 (w), 2941 (w), 2834 (w), 1606 (s), 1586 (s), 1546 (m), 1517 (s), 1481 (s), 1459 (s), 1438 (s), 1386 (s), 1331 (m), 1288 (m), 1254 (m), 1225 (s), 1182 (w), 1108 (w), 1075 (w), 1019 (w), 966 (m), 822 (w), 737 (s), 642 (w), 589 (w), 521 (w).

6.3.16 Synthesis of [$Co_2Dy_2(L8)_4(NO_3)_2(DMF)_2]{\cdot}2C_2H_6CO$ (23)

Compound **23** (45 mg, 0.025 mmol) was dissolved in 1.5 mL DMF. Red color block crystals of **22** could be isolated from diffusion of acetone into the DMF, and in approximate yield of 63% (based on Co). Anal. Calcd (Found)% for $C_{65}H_{64}Co_2Dy_2N_8O_{21}$ corresponding to lost one C_3H_6O molecules leading to $[Co_2Dy_2(\mathbf{L8})_4(NO_3)_2(DMF)_2]\cdot C_2H_6CO$: C, 44.97 (45.13); H, 3.72 (3.58); N, 6.45 (6.37). Selected IR data (KBr, cm^{-1}): 3545 (m), 3477 (s), 3413 (s), 3233 (w), 2925 (w), 1661 (s), 1604 (s), 1583 (m), 1546 (m), 1474 (s), 1455 (s), 1383 (s), 1398 (m), 1385 (m), 1298 (m), 1228 (s), 1180 (s), 1107 (w), 1032 (w), 958 (w), 870 (w), 818 (m), 745 (m), 729 (m), 687 (w), 639 (w), 584 (w), 518 (w).

6.3.17 Synthesis of $[Zn_2Dy_2(L8)_4(NO_3)_2(MeOH)_2]\cdot 2CH_2Cl_2$ (24)

In place of $Co(NO_3)_2\cdot 6H_2O$, $Zn(NO_3)_2\cdot 6H_2O$ was used with the same procedure as above and compound **24** was obtained: $[Zn_2Dy_2(L\mathbf{8})_4(NO_3)_2(MeOH)_2]\cdot 2CH_2Cl_2$. Anal. Calcd (Found)% for $C_{58}H_{56}Zn_2Dy_2N_6O_{22}$ corresponding to replacement of two CH_2Cl_2 molecules by two H_2O molecules led to $[Co_2Dy_2(\mathbf{L8})_4(NO_3)_2(MeOH)_2]\cdot 2H_2O$; C, 42.35 (42.41); H, 3.43 (3.27); N, 5.11 (5.00). The IR is similar with compound **22**.

6.3.18 Synthesis of $[Fe_2Ln(L8)_4(MeOH)(AcO)]\cdot 4MeOH$ (25 and 26)

$[Fe_2Dy(L4)_4(MeOH)(AcO)]\cdot 4MeOH$ (25)

The same procedure was employed to prepare complexes **25** and **26** hence only the synthesis of **25** will be described here in detail. A mixture of $Dy(NO_3)_3\cdot 6H_2O$ (45 mg, 0.1 mmol), $FeCl_2\cdot 6H_2O$ (20 mg, 0.1 mmol), $H_2\mathbf{L8}$ (48.6 mg, 0.2 mmol) was dissolved in 15 mL of MeOH. After 10 minutes stirring, a solution of $NaOAc\cdot 3H_2O$ in MeOH (5 mL) was added under stirring. The final solution was stirred for 30 minutes and filtered. After one week black block shaped crystals of **25** suitable for X-ray crystallography were isolated in 85% yield. Anal. Calc (found)% for $Fe_2DyC_{63}H_{66}N_4O_{19}$: C, 51.92 (51.76); H, 4.56 (4.59); N, 3.84 (3.91). Selected IR data (KBr, cm^{-1}): 3440 (b), 3062 (w), 2923 (w), 2851 (w), 1687 (m), 1635 (s), 1615 (s), 1587 (m), 1566 (w), 1485 (m), 1463 (m), 1383 (s), 1305 (w), 1232 (m), 1183 (m), 1115 (w), 1092 (w), 1071 (w), 966 (w), 822 (w), 733 (w), 622 (w), 480 (w).

$Fe_2Y(L4)_4(MeOH)(AcO)]\cdot 4MeOH$ (26)

The procedure which gave **25** was followed for the preparation of **26**, using $Y(NO_3)_3\cdot 6H_2O$ in place of $Dy(NO_3)_3\cdot 6H_2O$. Yield is 77%. Anal. Calc. (found)% for $Fe_2YC_{63}H_{66}N_4O_{19}$: C, 54.68 (54.71); H, 4.81 (4.75); N, 4.05 (4.22). Selected IR data (KBr, cm^{-1}): 3441 (br), 3062 (w), 2924 (w), 2850 (w), 1686 (m), 1634 (s), 1615 (s), 1582 (m), 1567 (w), 1484 (m), 1466 (m), 1384 (s), 1303 (w), 1232 (m), 1183 (m), 1115 (w), 1092 (w), 1071 (w), 966 (w), 822 (w), 734 (w), 622 (w), 481 (w).

6.3.19 Synthesis of $[Co_2Ln(H_2L9)(NO_3)_2(MeOH)_4]\cdot NO_3\cdot xMeOH\cdot yH_2O$ (27-30)

$[Co_2Dy(H_2L9)_2(NO_3)_2(MeOH)_4]\cdot NO_3\cdot 5MeOH\cdot 5H_2O$ (27)

$Co(NO_3)_3\cdot 6H_2O$ (58 mg, 0.2 mmol) was added to a suspension of H_4**L9** in MeOH and MeCN (v/v:2/1) under stirring. $Dy(NO)_3\cdot 6H_2O$ (90 mg, 0.2 mmol) was added to the solution after 10 min stirring. The solution was stirred for 10 min before adding Et_3N (20 μl). The final solution was stirred for 10 min and then filtered. The filtrate was left undisturbed, after one week, pale yellow crystals had formed. Yield is 53%. Anal. Calc (found)% for $[Co_2Dy(H_2\mathbf{L9})(NO_3)_2(MeOH)_4]\cdot NO_3\cdot 5MeOH\cdot 5H_2O$: C, 37.18 (36.92); 4.65 (4.43); 11.05 (11.02). Seleted IR data (KBr, cm^{-1}): 3350 (br), 1612(s), 1589 (s), 1560 (s), 1469 (vs), 1382 (vs), 1297 (s), 975 (m), 740 (m).

$[Co_2Tb(H_2L9)(NO_3)_2(MeOH)_4]\cdot NO_3\cdot 8H_2O$ (28)

Yield: 66%. Anal. Calc (found)% for $[Co_2Tb(H_2\mathbf{L9})(NO_3)_2(MeOH)_4]\cdot NO_3\cdot 8H_2O$: C, 35.93 (35.92); 4.06 (4.33); 11.84 (11.52) Seleted IR data (KBr, cm^{-1}): 3348 (br), 1615(s), 1588 (s), 1560 (s), 1468 (vs), 1385 (vs), 1299 (s), 976(m), 742 (m).

$[Co_2Ho(H_2L9)(NO_3)_2(MeOH)_4]\cdot NO_3\cdot 10H_2O$ (29)

Yield: 58%. Anal. Calc (found)% for $[Co_2Ho(H_2\mathbf{L9})(NO_3)_2(MeOH)_4]\cdot NO_3\cdot 10H_2O$: C, 34.97 (34.62); 4.21 (4.23); 11.53 (11.42). Seleted IR data (KBr, cm^{-1}): 3353 (br), 1612(s), 1586 (s), 1562 (s), 1463 (vs), 1388 (vs), 1292 (s), 977 (m), 745 (m).

$[Co_2Y(H_2L9)(NO_3)_2(MeOH)_4]\cdot NO_3\cdot 10H_2O$ (30)

Yield: 48%. Anal. Calc (found) % for $[Co_2Y(H_2$**L9**$)(NO_3)_2(MeOH)_4]\cdot NO_3\cdot 10H_2O$: C, 36.74 (36.62); 4.42 (4.23); 12.11 (12.02). Seleted IR data (KBr, cm^{-1}): 3350 (br), 1617(s), 1583 (s), 1564 (s), 1465 (vs), 1389 (vs), 1291 (s), 974 (m), 741 (m).

6.3.20 Synthesis of $Na\cdot[Co_2Ln(L9)_2(H_2O)_4]\cdot 7H_2O$ (31-34)

$Na\cdot[Co_2Dy(L9)_2(H_2O)_4]\cdot 7H_2O$ (31)

The same procedure was employed to prepare all complexes (**31-34**) and hence only the synthesis of complex **31** will be described here in detail. $DyCl_3\cdot 6H_2O$ (37.5 mg, 0.1 mmol) was added to a suspension of H_4**L9** in MeOH and MeCN (v/v:2/1) under stirring, $CoCl_2\cdot 6H_2O$ was added to this solution until the solution is clear. After 5 minutes stirring, $NaOAc\cdot 3H_2O$ (68 mg, 0.5 mmol) in MeOH (5 ml) was added. The mixture was stirred for another 2 minutes and then filtered. The filtrate was left undisturbed, red single crystals suitable for X-ray diffraction analysis were obtained after three days. Yield: 58%. Anal. Calcd (Found)% for $NaCo_2DyC_{42}H_{46}N_{10}O_{18}$: C, 39.34 (39.38); H, 3.62 (3.58); N, 10.92 (10.86). Seleted IR data (KBr, cm^{-1}): 3340 (br), 1622 (s), 1591 (s), 1561 (s), 1469 (vs), 1388 (vs), 1295 (s), 972 (m), 741 (m).

$Na\cdot[Co_2Tb(L9)_2(H_2O)_4]\cdot 7H_2O$ (32)

Yield is 63% for **32**. Anal. Calcd (Found)% for $NaCo_2TbC_{42}H_{46}N_{10}O_{18}$: C, 39.45 (39.46); H, 3.63 (3.59); N, 10.95 (10.95). Seleted IR data (KBr, cm^{-1}): 3343 (br), 1625 (s), 1593 (s), 1561 (s), 1469 (vs), 1388 (vs), 1295 (s), 971 (m), 744 (m).

$Na\cdot[Co_2Ho(L9)_2(H_2O)_4]\cdot 7H_2O$ (33)

Yield is 59% for **33**. Anal. Calcd (Found)% for $NaCo_2HoC_{42}H_{46}N_{10}O_{18}$: C, 39.27 (39.43); H, 3.61

(3.48); N, 10.90 (10.97). Seleted IR data (KBr, cm^{-1}): 3342 (br), 1622 (s), 1590 (s), 1565 (s), 1467 (vs), 1389 (vs), 1297 (s), 971 (m), 740 (m).

$Na[Co_2Y(L9)_2(H_2O)_4]\cdot 7H_2O$ (34)

Yield is 45% for **34**. Anal. Calcd (Found)% for $NaCo_2YC_{42}H_{46}N_{10}O_{18}$: C, 41.74 (41.68); H, 3.84 (3.88); N, 11.59 (11.57). Seleted IR data (KBr, cm^{-1}): 3344 (br), 1627 (s), 1592 (s), 1563 (s), 1468 (vs), 1389 (vs), 1295 (s), 975 (m), 741 (m).

6.3.21 Synthesis of $[Co_2Dy_2(HL9)_2(N_3)_2(NO_3)_2(MeOH)_4]\cdot 4MeOH$ (35)

$DyCl_3\cdot 6H_2O$ (37.5 mg, 0.1 mmol) was added to a suspension of H_4**L9** in MeOH and MeCN (v/v:2/1) under stirring, $CoCl_2\cdot 6H_2O$ was added to this solution until the solution is clear. After 5 min stirring, NaN_3 (32.5 mg, 0.5 mmol) in MeOH (5 ml) was added to the solution. The mixture was stirred for another 2 min and then filtered. The filtrate was left undisturbed, red single crystals suitable for X-ray diffraction analysis were obtained after three days. Yield is 76%. Anal. Calcd (Found)% for $Co_2Dy_2C_{48}H_{47}N_{19}O_{18}$ (four MeOH replaced by one MeCN: 35.57, (35.61); 2.92 (3.15); 16.42 (16.57). Seleted IR data (KBr, cm^{-1}): 3440 (br), 2200 (m), 1629 (s), 1590 (s), 1564 (s), 1465 (vs), 1388 (vs), 1293 (s), 974 (m), 744 (m).

6.4 Characterisation techniques

6.4.1 Elemental analyses

Elemental analyses for C, H, N were performed using an Elementar Vario EL analyzer and carried out at the Institute of Inorganic Chemistry, Karlsruhe Institute of Technology.

6.4.2 Infrared spectroscopy

Infra-red spectroscopy is a useful technique for identifying organic ligands and thus helps to verify the presence of organic ligands in the metal-ligand complexes. In addition, it provides a unique fingerprint of the molecule and enables identification of similar structures involving the same ligand. A small amount of the sample to be measured was ground into a fine powder together with absolutely dry KBr. This was then pressed into a transparent disk while under vaccum using a force of 10 N. Fourier Transform IR measurements was carried out on a Perkin-Elmer Spectrum instrument.

6.4.3 X-ray powder diffraction

The X-ray powder diffraction patterns were measured at room temperature using a Stoe STADI-P diffractometer with a Cu-Kα radiation at the Institute of Inorganic Chemistry, Karlsruhe Institute of Technology.

6.4.4 X-ray crystallography

X-ray crystallographic data were collected either on a Bruker SMART Apex CCD diffractometer or on a Stoe IPDS II area detector diffractometer using graphite-monochromated Mo-Kα radiation. Semi-empirical absorption corrections were applied using XPREP in SHELXTL.[62] The structures were solved using direct methods, followed by a full-matrix least-squares refinement against F^2 (all data) using SHELXTL.[62] Anisotropic refinement was used for all ordered non-hydrogen atoms; organic hydrogen atoms were placed in calculated positions, while coordinates of hydroxo hydrogen and amine hydrogen atoms were either placed in calculated positions or located from the difference Fourier map and then constrained to ride on their parent atom with Uiso = 1.5Ueq (parent atom). The crystallographic and structure refinement data are given in Chapter 7. When the solvent molecules could not be modelled, a SQUEEZE command was applied to remove those solvents.[63] The merging error R_{int} are defined as:

$$R_{\mathrm{int}} = \frac{\sum \left\| F_0 \right| - \left| F_c \right\|}{\sum \left| F_0 \right|}$$

Where F_o is the observed structure factor. The high value of the merging error can result from the incorrect Laue group, bad or missing absorption correction, crystal decomposition, twinning or problems of goniometer.[64] And the residual factors $R1$ and $wR2$ are defined as:

$$R_1 = \frac{\sum \left\| F_o \right| - \left| F_c \right\|}{\sum \left| F_o \right|}$$

$$wR_2 = \sqrt{\frac{\sum w\left(F_o^2 - F_c^2\right)^2}{\sum w\left(F_o^2\right)^2}}$$

Where F_c is the calculated structure factor and w is a weighting factor.[64] Another value describing the quality of the model is the Goodness of Fit, *GooF* or *S*, which is defined as:

$$GooF = S = \sqrt{\frac{\sum w\left(F_o^2 - F_c^2\right)^2}{N_{ref.} - N_{par.}}}$$

Herein $N_{ref.}$ and $N_{par.}$ are the number of independent reflections or parameters, respectively.[64]

6.4.5 *Ab initio* calculations

CASSCF/SOCI calculations were performed on the crystal structure of compounds **18-19** and **21**. Co, O, and N were equipped with a def2-TZVP basis for C and H, a def2-SVP basis was used.[65] All calculations were done with the bochum suite of ab inito programs.[53, 66]

The active space was spanned by the five 3d orbitals of Co. In the SOCI calculations, the scaled-nuclear spin-orbit Hamiltonian[67] (ξ = 0.61) was constructed and diagonalised within the active space.

Chapter 7 **Crystallographic Data**

Compound	**1**	**2**
Formula	$C_{65}H_{92}Co_5Dy_2N_7O_{34}$	Co_5Gd_2
Mr [g mol^{-1}]	2135.12	
Colour	red	red
Crystal System	Monoclinic	Monoclinic
Space Group	$P2_1/c$	$P2_1/c$
T [K]	150	150
a [Å]	23.903(2)	23.873
b [Å]	13.985(9)	13.9476
c [Å]	25.440(2)	25.478
[°]	90	90
[°]	113.688(10)	113.799
[°]	90	90
V [Å]	7787.6(11)	7762.8
Z	4	4
$D_{x\ calc}$ [g·cm^{-3}]	1.816	
μ(Mo-Ka) [mm^{-1}]	3.05	
F(000)	4265	
Reflns collected	47826	
Unique data	15341	
Rint	0.077	
Data with $I > 2\sigma(I)$	9379	
parameters/restraints	1032/19	
S on F^2	0.98	
R_1 [$I > 2\sigma(I)$]	0.0418	
wR_2 (all data)	0.075	
Largest diff. peak/hole [e Å^{-3}]	0.87/-0.97	

Compound	**3**	**4**
Formula	$Co_3Dy_3C_{83}H_{127}N_6O_{43}Cl$	$Co_3Dy_3C_{89}H_{146}N_6O_{35}Cl_2$
Mr [g mol^{-1}]	2560.61	2585.22
Colour	red	red
Crystal System	Triclinic	Monoclinic
Space Group	P-1	$P2_1/n$
T [K]	180	293
a [Å]	14.9592(5)	17.4590(17)
b [Å]	17.6034(7)	19.1907(14)
c [Å]	22.3297(8)	33.452(3)
[°]	67.637(3)	90
[°]	84.626(3)	92.077(12)
[°]	71.806(3)	90
V [Å]	5163.9(4)	11200.9(18)
Z	2	4
$D_{x\ calc}$ [g·cm^{-3}]	1.674	1.533
µ(Mo-Ka) [mm^{-1}]	2.73	2.53
F(000)	2574	5220
Reflns collected	35922	88853
Unique data	18228	22120
Rint	0.035	0.088
Data with $I > 2\sigma(I)$	13766	13824
parameters/restraints	1203/10	1077/8
S on F^2	0.95	0.90
R_1 [$I > 2\sigma(I)$]	0.034	0.043
wR_2 (all data)	0.086	0.101
Largest diff. peak/hole [e Å^{-3}]	1.67/-1.56	+0.63/-1.83

Compound	**5**	**6**	**7**
Formula	$Fe_2Dy_2C_{72}H_{90.7}N_5O_{25\cdot35}$	$Cr_2Dy_2C_{72}H_{78}N_6O_{18}$	Cr_2Y_2
Mr [g mol^{-1}]	1835.48	1744.40	
Colour	yellow	green	green
Crystal System	Monoclinic	Monoclinic	Monoclnic
Space Group	$P2_1/n$	C2/c	C2/c
T [K]	220	150(2)	293
a [Å]	10.9064(13)	28.044(3)	28.86
b [Å]	51.166(8)	10.4184(9)	10.44
c [Å]	14.2640(3)	24.335(3)	25.85
[°]	90	90	90
[°]	99.246(15)	94.793(9)	102.05
[°]	90	90	90
V [Å]	7856.4(19)	7085.3(13)	7012.4
Z	4	4	
$D_{x\ calc}$ [g·cm^{-3}]	1.552	1.635	
μ(Mo-Ka) [mm^{-1}]	2.32	2.458	
F(000)	3710	3504	
Reflns collected	57468	28433	
Unique data	14987	6736	
Rint	0.099	0.0912	
Data with $I > 2\sigma(I)$	10874	4031	
parameters/restraints	954/5	459/1	
S on F^2	0.99	0.875	
R_1 [$I > 2\sigma(I)$]	0.049	0.0432	
wR_2 (all data)	0.118	0.0886	
Largest diff. peak/hole [e Å^{-3}]	+0.91/-1.36	+0.59/-0.93	

Compound	**8**	**9**
Formula	$C_{41}H_{45}FeN_5O_{13}Dy$	$C_{41}H_{45}FeN_5O_{13}Y$
Mr [g mol^{-1}]	1034.18	961.58
Colour	pale yellow	pale yellow
Crystal System	Monoclinic	Monoclinic
Space Group	$P2_1/c$	$P2_1/c$
T [K]	180	293
a [Å]	8.8951	8.955(2)
b [Å]	18.795	18.927(4)
c [Å]	24.477	24.679(5)
[°]	90	90
[°]	95.57	95.29(3)
[°]	90	90
V [Å]	4072.7	4165.2(15)
Z	1	1
$D_{x\ calc}$ [g·cm^{-3}]		1.532
μ(Mo-Ka) [mm^{-1}]		1.82
F(000)		1970.4
Reflns collected		44532
Unique data		8503
Rint		0.124
Data with $I > 2\sigma(I)$		5133
parameters/restraints		553/3
S on F^2		0.82
R_1 [$I > 2\sigma(I)$]		0.052
wR_2 (all data)		0.130
Largest diff. peak/hole [e Å^{-3}]		+0.60/-1.37

Compound	**10**	**11**	**12**
Formula	$Fe_4Dy_4C_{97}H_{106}N_4O_{36}$	Fe_4Tb_4	Fe_4Tb_4
Mr [g mol^{-1}]	602.85		
Colour	yellow	yellow	yellow
Crystal System	Monoclinic	Monoclinic	Monoclinic
Space Group	$P2_1/n$	$P2_1/n$	$P2_1/n$
T [K]	150	293	293
a [Å]	13.6729(15)	13.5884	137772
b [Å]	29.220(3)	29.2250	29.333
c [Å]	26.626(3)	26.600	26.642
[°]	90	90	90
[°]	102.736(3)	102.533	101.942
[°]	90	90	90
V [Å]	10376.2(19)	10352.1	10447.5
Z	4	4	4
$D_{x\ calc}$ [g·cm^{-3}]	1.778		
μ(Mo-Ka) [mm^{-1}]	4.77		
F(000)	5488		
Reflns collected	67039		
Unique data	21595		
Rint	0.051		
Data with $I > 2\sigma(I)$	15937		
parameters/restraints	1314/38		
S on F^2	1.47		
R_1 [$I > 2\sigma(I)$]	0.071		
wR_2 (all data)	0.225		
Largest diff. peak/hole [e Å^{-3}]	+2.70/-2.08		

Compound	**13**	**14**	**15**
Formula	$C_{20}H_{30}Dy_{2}N_{8}O_{16}$	$C_{28}H_{32}Dy_{2}N_{10}O_{14}$	$C_{3}0H_{36}Dy_{2}N_{10}O_{16}$
Mr [g mol^{-1}]	963.50	1057.64	1117.69
Colour	colorless	colorless	colorless
Crystal System	Monoclinic	Monoclinic	orthorhombic
Space Group	$P2_1/c$	$P2_1/c$	Pbca
T [K]	150	150	180
a [Å]	11.4774(16)	9.993(10)	16.0416(6)
b [Å]	15.404 (2)	20.97(2)	13.7439(6)
c [Å]	8.6564(11)	8.424(8)	16.7924(8)
[°]	90	90	90
[°]	90.972(12)	102.566(14)	90
[°]	90	90	90
V [Å]	1530.2(4)	1723(3)	3702.3(3)
Z	2	2	4
$D_{x\ calc}$ [g·cm^{-3}]	2.091	2.038	2.05
μ(Mo-Ka) [mm^{-1}]	4.93	4.39	4.09
F(000)	932	1027	2184
Reflns collected	10007	18845	20862
Unique data	2775	3001	3488
Rint	0.054	0.092	0.039
Data with $I > 2\sigma(I)$	2366	2560	2996
parameters/restraints	208/0	243/1	262/0
S on F^2	0.99	1.08	1.01
R_1 [$I > 2\sigma(I)$]	0.039	0.071	0.02
wR_2 (all data)	0.099	0.126	0.051
Largest diff. peak/hole [e Å^{-3}]	+0.86/-0.68	1.89/-1.70	0.74/-1.15

Compound	**16**	**17**	**18**
Formula	$C_{44}H_{44}CoN_6O_8$	$C_{26}H_{22}CoN_8O_4$	$C_{29}H_{26}CoN_6O_6$
Mr [g mol^{-1}]	843.78	569.44	684.39
Colour	red	red	red
Crystal System	Monoclinic	Monoclinic	Monoclinic
Space Group	C2/c	$P2_1/c$	$P2_1/n$
T [K]	150	150	218
a [Å]	19.473 (3)	20.027 (3)	11.7543(12)
b [Å]	14.0263 (14)	14.0260 (18)	12.8415(9)
c [Å]	15.034 (2)	8.9926 (16)	19.736 (2)
[°]	90	90	90
[°]	107.686(11)	100.235(14)	91.266(12)
[°]	90	90	90
V [Å]	3912.2(9)	2485.8(7)	2978.3(5)
Z	4	4	4
$D_{x\ calc}$ [g·cm^{-3}]	1.433	1.522	1.526
µ(Mo-Ka) [mm^{-1}]	0.50	0.742	0.81
F(000)	1764	1172	1404
Reflns collected	17279	15181	22668
Unique data	4317	3038	5683
Rint	0.054	0.089	0.075
Data with $I > 2\sigma(I)$	3105	1797	3822
parameters/restraints	273/0	354/0	427/29
S on F^2	0.96	0.85	1.00
R_1 [$I > 2\sigma(I)$]	0.047	0.0406	0.055
wR_2 (all data)	0.109	0.0771	0.154
Largest diff. peak/hole [e Å^{-3}]	+0.55/-0.67	0.25/-0.39	1.06/-0.70

Compound	**19**	**20**	**21**
Formula	$C_{43}H_{42}Dy_2N_6O_{12}$	$C_{32}H_{38}Dy_2N_8O_{12}$	$C_{26}H_{34}CoN_4O_4$
Mr [g mol^{-1}]	1159.83	1051.70	525.50
Colour	Yellow	Yellow	red
Crystal System	Triclinic	Triclinic	monoclinic
Space Group	P-1	P-1	P21/n
T [K]	293	150(2)	150
a [Å]	9.8233(9)	9.8189(12)	16.1119(11)
b [Å]	10.2588(10)	10.0060(11)	7.0151(6)
c [Å]	10.9391(11)	10.5795(12)	21.1805(14)
[°]	92.521(8)	85.777(9)	90
[°]	99.381(8)	65.913(9)	96.396(13)
[°]	99.221(8)	86.200(9)	90
V [Å]	1070.81(18)	945.6 (2)	2379.1(3)
Z	1	1	2
$D_{x\ calc}$ [g·cm^{-3}]	1.799	1.847	1.467
μ(Mo-Ka) [mm^{-1}]	3.533	3.991	0.763
F(000)	570	514	1108
Reflns collected	10674	9105	16727
Unique data	3787	4316	4819
Rint	0.115	0.0424	0.0322
Data with $I > 2\sigma(I)$	3362	3987	3898
parameters/restraints	289/1	255 / 6	316 / 0
S on F^2	1.02	1.058	0.989
R_1 [$I > 2\sigma(I)$]	0.048	0.0348	0.0326
wR_2 (all data)	0.125	0.092	0.0867
Largest diff. peak/hole [e Å^{-3}]	+1.69/-1.23	+1.40/-2.95	+0.24/-0.66

Compound	**22**	**23**	**24**
Formula	$C_{60}H_{56}Cl_4Co_2Dy_2N_6O_{20}$	$C_{68}H_{68}Co_2Dy_2N_8O_{22}$	$C_{60}H_{56}Cl_4Zn_2Dy_2N_6O_{20}$
Mr [g mol^{-1}]	1765.76	1794.18	1778.64
Colour	Red	Red	Pale-yellow
Crystal System	Monoclinic	Monoclinic	Triclinic
Space Group	$P2_1/c$	$P2_1/c$	P-1
T [K]	100K	100K	100K
a [Å]	12.237(9)	13.955(8)	10.597(3)
b [Å]	24.202(18)	14.408(7)	11.182(3)
c [Å]	11.090(8)	17.393(9)	13.685(4)
[°]	□□□□90.00	90.00	100.366(2)
[°]	105.717(2)	95.11(4)	91.738(2)
[°]	□□□□90.00	90.00	97.091(2)
V [Å]	3161.6(4)	3483.1(3)	1580.59(8)
Z	2	2	1
$D_{x\ calc}$ [g·cm^{-3}]	1.855	1.711	1.869
μ(Mo-Ka) [mm^{-1}]	3.101	2.671	3.34
F(000)	1744	1792	878
Reflns collected	21072	24484	29062
Unique data	6971	7974	7554
Rint	0.0442	0.0261	0.032
Data with I > 2σ(I)	6385	6757	7014
parameters/restraints	433/17	466/0	429/1
S on F^2	1.075	0.0951	1.05
R_1 [I > 2σ(I)]	0.0533	0.0285	0.026
wR_2 (all data)	0.1424	0.0716	0.055
Largest diff. peak/hole [e Å^{-3}]	+5.10/-2.53	+0.38/-1.69	+0.88/-0.73

Compound	**25**	**26**
Formula	$C_{63}H_{67}DyFe_2N_4O_{19}$	Fe_2Y
Mr [g mol^{-1}]	1458.40	
Colour	black	black
Crystal System	Triclinic	Triclinic
Space Group	P-1	P-1
T [K]	180	220
a [Å]	11.0560 (11)	10.8809
b [Å]	11.8361(11)	11.9642
c [Å]	24.710(2)	24.8464
[°]	92.811(8)	94.520
[°]	94.134(8)	93.726
[°]	110.582(7)	113.857
V [Å]	3009.6(5)	2932.4
Z	2	
$D_{x\ calc}$ [g·cm^{-3}]	1.609	
μ(Mo-Ka) [mm^{-1}]	1.78	
F(000)	1486	
Reflns collected	23026	
Unique data	11760	
Rint	0.075	
Data with I > 2σ(I)	6593	
parameters/restraints	816 / 3	
S on F^2	0.82	
R_1 [I > 2σ(I)]	0.0326	
wR_2 (all data)	0.114	
Largest diff. peak/hole [e Å^{-3}]	+1.09/-1.44	

Compound	**27**	**28**
Formula	$Co_2DyC_{52.5}H_{72}N_{13}O_{27.5}$	Co_2Tb
Mr [g mol^{-1}]	1605.59	
Colour	Red	Red
Crystal system	Orthogonal	Orthogonal
Space Group	Aba2	Aba2
T [K]	150	293
a [Å]	27.5720(15)	27.572
b [Å]	27.888(2)	27.886
c [Å]	17.945(2)	17.844
[°]	90	90
[°]	90	90
[°]	90	90
V [Å]	13776(2)	13633
Z	8	
$D_{x\ calc}$ [g·cm^{-3}]	1.548	
µ(Mo-Ka) [mm^{-1}]	1.639	
F(000)	6544	
Reflns collected	66957	
Unique data	15717	
Rint	0.0420	
Data with I > 2σ(I)	13271	
parameters/restraints	713/44	
S on F^2	1.036	
R_1 [I > 2σ(I)]	0.0444	
wR_2 (all data)	0.1190	
Largest diff. peak/hole [e Å^{-3}]	+3.39/-1.32	

Compound	**29**	**30**
Formula	Co_2Ho	Co_2Y
Mr [g mol^{-1}]		
Colour	Red	Red
Crystal system	Orthogonal	Orthogonal
Space Group	Aba2	Aba2
T [K]	293	293
a [Å]	27.4721	27.3651
b [Å]	27.682	27.565
c [Å]	17.843	17.740
[°]	90	90
[°]	90	90
[°]	90	90
V [Å]	13685	13859
Z	8	8
$D_{x\ calc}$ [g·cm^{-3}]		
μ(Mo-Ka) [mm^{-1}]		
F(000)		
Reflns collected		
Unique data		
Rint		
Data with $I > 2\sigma(I)$		
parameters/restraints		
S on F^2		
R_1 [$I > 2\sigma(I)$]		
wR_2 (all data)		
Largest diff. peak/hole [e Å^{-3}]		

Compound	**31**	**32**
Formula	$NaCo_2DyC_{42}H_{48}N_{10}O_{19}$	Co_2Tb
Mr [g mol^{-1}]	1300.25	
Colour	red	red
Crystal system	Tetragonal	Tetragonal
Space Group	$I4_1/a$	$I4_1/a$
T [K]	150	213
a [Å]	12.1334(17)	12.2793
b [Å]	12.1334(17)	12.2793
c [Å]	31.921(6)	31.5318
[°]	90	90
[°]	90	90
[°]	90	90
V [Å]	4699.4(16)	4762.8
Z	4	4
$D_{x\ calc}$ [g·cm^{-3}]	1.838	
μ(Mo-Ka) [mm^{-1}]	2.37	
F(000)	2612	
Reflns collected	13519	
Unique data	2405	
Rint	0.121	
Data with $I > 2\sigma(I)$	1251	
parameters/restraints	159/2	
S on F^2	0.82	
R_1 [$I > 2\sigma(I)$]	0.055	
wR_2 (all data)	0,140	
Largest diff. peak/hole [e Å^{-3}]	0.46/-2.29	

Compound	**33**	**34**	**35**
Formula	Co_2Ho	Co_2Y	$Co_2Dy_2C_{50}H_{60}N_{18}O_{22}$
Mr [g mol^{-1}]			1708.02
Colour	red	red	red
Crystal System	Tetragonal	Tetragonal	Monoclinic
Space Group	$I4_1/a$	$I4_1/a$	$P2_1/n$
T [K]	213		218
a [Å]	12.2688	12.1442	11.9296(7)
b [Å]	12.2688	12.1442	14.5623(11)
c [Å]	31.6479	31.2326	18.3672(11)
[°]	90	90	90
[°]	90	90	102.359(4)
[°]	90	90	90
V [Å]	4763.5	4655.4	3116.8(4)
Z	4	4	2
$D_{x\ calc}$ [g·cm^{-3}]			1.820
μ(Mo-Ka) [mm^{-1}]			2.984
F(000)			1696
Reflns collected			24854
Unique data			6189
Rint			0.0480
Data with $I > 2\sigma(I)$			5596
parameters/restraints			441/0
S on F^2			0.982
R_1 [$I > 2\sigma(I)$]			0.0404
wR_2 (all data)			0.0997
Largest diff. peak/hole [e Å^{-3}]			+0.94/-2.34

Chapter 8

Bibliography

[1] G. L. Verschuur, Hidden attraction, The Mystery and History of Magnetism, Oxford University Press, Oxford, **1993**

[2] A. Kloss, Geschichte des Magnetismus, VDE Verlag, Berlin, **1994**

[3] J. S. Miller; D. Gatteschi; *Chem. Soc. Rev.*, **2011**, 40, 3065

[4] J. S. Miller; J. C. Calabrese; H. Rommelmann; S. R. Chittipeddi; J. H. Zhang; W. M. Reiff; A. J. Epstein, *J. Am. Chem. Soc.,* **1987**, 109, 769.

[5] a) V. I. Ovcharenko; R. Z. Sagdeev, *Russ. Chem. Rev.,* **1999**, 68, 345; b) D. Gatteschi, *Adv. Mater.,* **1994**, 6, 635.

[6] R. Sessoli; D. Gatteschi; C. A. aneschi; M. A. Novak, *Nature.*, **1993**, 365, 141

[7] J. R. Long, In Chemistry of Nanostructured Materials; P. Yan, Ed.; World Scientific Publishing: Hong Kong, **2003**

[8] K. C. Mondal, *Synthesis, Structures and Properties of f- and d-f Complexes using O-vanillin-derived Schiff base Ligands*, **2011**, KIT-Bibliothek, Karlsruhe.

[9] a) R. Sessoli; H. L. Tsai; A. R. Schake; S. Wang; J. B. Vincent; K. Folting; D. Gatteschi; G. Christou; D. N. Hendrickson, *J. Am. Chem. Soc.,* **1993**, 115, 1804-1816.

[10] M. Kurmoo, *Chem. Soc. Rev.,* **2009**, 38, 1353

[11] S. Ostrovsky; Z. Tomkowicz; W. Haase, *Coord. Chem. Rev.,* **2009**, 253, 2363

[12] a) M. Murrie, Chem. Soc. Rev., 2010, 39, 1986; b) P. Wix; G. E. Kostakis; V. A. Blatov; D. M. Proserpio; S. P. Perlepes; A. K. Powell, *Euro. J. Inorg. Chem*., **2013**, 4, 520

[13] a) O. Kahn, Molecular Magnetism, VCH Publishers, New York, **1993**; b) E. A. Boudreaux; L.N. Mulay, Theory and Applications of Molecular Paramagnetism, John Willey & Sons, New York, **1976**; c) R. Bŏca, Theoretical Foundation of Molecular Magnetism, Elsevier, Amsterdam, **1999**.

[14] S. Karasawa; D. Yoshihara; N. W atanabe; M. Nakano; N. Koga, *Dalton Trans.,* **2008**, 1418

[15] N. Ishikawa; M, Sugita; T. Ishikawa; S. Koshihara, Y. Kaizu, *J. Am. Chem. Soc.,* **2003**, 125, 8694

[16] J. K. Tang; I. Hewitt; N. T. Madhu; G. Chastanet; W. Wernsdorfer; C. E. Anson; C. Benelli; R.

Sessoli; A. K. Powell, *Angew. Chem., Int. Ed.*, **2006**, 45, 1729

[17] J. D. Rinehart; J. R. Long, *Chem. Sci.*, **2011**, 2, 2078

[18] A. Baniodeh, *Cooperative Effects in Non-cyclic and Cyclic Fe^{III}/4f Coordination Clusters*, **2012**, KIT-Bibliothek, Karlsruhe

[19] S. Osa; T. Kido; N. Matsumoto; N. Re; A. Pochaba; J. Mrozinski, *J. Am. Chem. Soc.*, **2004**, 126, 420

[20] E. Colacio; J. Ruiz; E. Ruiz; E. Cremades; J. Krzystek; S. Carretta; J. Cano; T, Guidi; W. Wernsdorfer; E. K. Brechin, *Angew. Chem., Int. Ed.*, **2013**, 52, 9130

[21] a) V. Chandrasekhar; B. M. Pandian; J. J. Vittal; R. Clérac, *Inorg. Chem.*, **2007**, 46, 5140, *Inorg. Chem.*, **2009**, 48, 1148; b) T. Yamaguchi; J. P. Costes; Y. Kishima; M. Kojima; Y. Sunatsuki; N. Brefuél; J. P. Tuchagues; L. Vendier; W. Wernsdorfer, *Inorg. Chem.*, **2010**, 49, 9125

[22] P. Wang; S. Shannigrahi; N. L. Yakovlev; T. S. A. Hor, *Inorg. Chem.*, **2012**, 51, 12059

[23] Y. Liu; Z. Chen; J. Ren; X. Q. Zhao; P. Cheng; B. Zhao, *Inorg. Chem.*, **2012**, 51, 7433

[24] L. F. Zou; L. Zhao; Y. N. Guo; G. M. Yu; Y. Guo; J. k. Tang; Y. H. Li, *Chem. Commun.*, **2011**, 47, 8659

[25] K. C. Mondal; A. Sundt; Y. h. Lan; G. E. Kostakis; O. Waldmann; L. Ungur; L. F. Chibotaru; C. E. Anson; A. K. Powell, *Angew. Chem., Int. Ed.*, **2012**, 124, 7668

[26] a) F. Mori, T. Nyui; T. Ishida; T. Nogami; K. Y. Choi; H. Nojiri, *J. Am. Chem. Soc.*, **2006**, 128, 1440; b) C. Aronica; G.. Pilet; G. Chastanet; W. Wernsdorfer; J. F. Jacquot; D. Luneau, *Angew. Chem., Int. Ed.*, **2006**, 45, 4659; c) V. Mereacre; A. M. Ako; R. Clérac; W. Wernsdorfer; G. Filoti; J. Bartolome; C. E. Anson; A. K. Powell, *J. Am. Chem. Soc.*, **2007**, 129, 9248; d) T. C. Stamatatos; S. J. Teat; W. Wernsdorfer; G. Christou, *Angew. Chem., Int. Ed.*, **2009**, 48, 521.

[27] a) L. Thomas; F. Lionti; R. Ballou; D. Gatteschi; R. Sessoli; B. Barbara, *Nature.*, **1996**, 383, 145; b) J. R. Friedman; M. P. Sarachik; J. Tejada; R. Ziolo, *Phys. Rev. Lett.*, **1996**, 76, 3830.

[28] a) M. Evangelisti; A. Candini; A. Ghirri; M. Affronte; E. K. Brechin; E. J. L. McInnes, *Appl. Phys. Lett.* **2005**, 87; b) G. Karotsis; S. Kennedy; S. J. Teat; C. M. Beavers; D. A. Fowler; J. J. Morales; M. Evangelisti; S. J. Dalgarno; E. K. Brechin, *J. Am. Chem. Soc.*, **2010**, 132, 12983

[29] M. N. Leuenberger; D. Loss, *Nature.*, **2001**, 410, 789

[30] Y. Wang; W. Li; S. Zhou; D. Kong; H. Yang; L. Wu, *Chem. Commun.*, **2011**, 47, 3541

[31] C. Beneli; D. Gatteschi, *Chem. Rev.*, **2002**, 102, 2369 and references in it

[32] a) Y. Bi; Y. N. Guo; L. Zhao; Y. Guo; S. Y. Lin; S. D. Jiang; J. K. Tang; B. W. Wang; S. Gao, *Chem. Eur. J.,* **2011**, 17, 1247; A. Yamashita; b) A. Watanabe; S. Akine; T. Nabeshima; M. Nakano; T. Yamamura; T. Kajiwara, *Chem. Eur. J.,* **2011**, 17, 4362.

[33] a) S. D. Jiang; B. W. Wang; H. L. Sun; Z. M. Wang; S. Gao, *J. Am. Chem. Soc.*, **2011**, 133, 4730; b) S. D. Jiang; B. W. Wang; G. Su; Z. M. Wang; S. Gao, *Angew. Chem., Int. Ed.*, **2010**, 49, 7448. c) P. H. Lin; W. B. Sun; M. F. Yu; G. M. Li; P. F. Yan; M. Murugesu, *Chem. Commun.,* **2011**, 47, 10993

[34] a) M. L. Kahn; J. P. Sutter; S.Golhen; P. Guionneau; L. Ouahab; O. Kahn; D. Chasseau, *J. Am. Chem. Soc.,* **2000**, 122, 3413; b) M. L. Kahn; R. Ballou; P. Porcher; O. Kahn; J. P. Sutter, *Chem. Eur. J.*, **2002**, 8, 525

[35] A. Baniodeh; V. Mereacre; N. Magnani; Y. Lan; J. A. Wolny; V. Schünemann; C. E. Anson; A. K. Powell, *Chem. Commun*., **2013**, 49, 9666

[36] a) F. Habib; G. Brunet; V. Vieru; I. Korobkov; L. F. Chibotaru; M. Murugesu, *J. Am. Chem. Soc*., **2013**, 135, 13242; b) V. E. Campbell; H. Bolvin; E. Rivière; R. Guillot; W. Wernsdorfer; T. Mallah; *Inorg. Chem*., **2014**, 53, 2598

[37] V. Mereacre; A. Baniodeh; C. E. Anson; A. K. Powell, *J. Am. Chem. Soc.,* **2011**, 133, 15335

[38] S. Sanz; K. Ferreira; R. D. McIntosh; S. J. Dalgarno; E. K. Brechin, *Chem. Commun.,* **2011**, 47, 9042

[39] P. Zhang; Y. N. Guo; J. Tang, *Coord. Chem. Rev.,* **2013**, 257, 1728; b) D. N. Woodruff; R. E. P. Winpenny; R. A. Layfield, *Chem. Rev.,* **2013**, 113, 5110; c) F. Habib; M. Murugesu, *Chem. Soc. Rev.,* **2013**, 42, 3278

[40] a) J. Rinck; G. Novitchi; W. Van den Heuvel; L. Ungur; Y. H. Lan; W. Wernsdorfer; C. E. Anson; L. F. Chibotaru; A. K. Powell, *Angew. Chem. Int. Ed.,* **2009**, 49, 7583; b) K. C. Mondal; G. E. Kostakis; Y. H. Lan; W. Wernsdorfer; C. E. Anson; A. K. Powell, *Inorg. Chem.,* **2011**, 50, 11604; c) D. Schray; G. Abbas; Y. H. Lan; V. Mereacre; A. Sundt; J. Dreiser; O. Waldmann; G. E. Kostakis; C. E. Anson; A. K. Powell, *Angew. Chem. Int. Ed.,* **2010**, 49, 5185; d) G. Novitchi; W. Wernsdorfer; L. F. Chibotaru; J. P. Costes; C. E. Anson; A. K. Powell, *Angew. Chem. Int. Ed.,* **2009**, 48, 1614

[41] a) J. P. Costes; W. Wernsdorfer, *Inorg. Chem.,* **2006**, 45, 5; b) J. P. Costes; F. Dahan; M. Auchel; F. Dahan; V. Peyrou; S. Shova; W. Wernsdorfer, *Inorg. Chem.,* **2006**, 45, 1924; (c) T. Hamamatsu; T. Kido; K. Yabe; M. Towatari; S. Osa; N. Matsumoto; N. Re; A. Pochaba; J. Mrozinski; J. L. Gallani;

A. Barla; P. Imperia; C. Paulsen; J. P. Kappler, *Inorg. Chem.,* **2007**, 46, 4458; d) T. Hamamatsu; K. Yabe; M. Towatari; N. Matsumoto; N. Re; A. Pochaba; J. Mrozinski, *Bull. Chem. Soc. Jpn.,* **2007**, 80, 523; e) T. Kajiwara; M. Nakano; S. Takaishi; M. Yamashita, *Inorg. Chem.,* **2008**, 47, 8604; f) T. Kajiwara; K. Takahashi; T. Hiraizumi; S. Takaishi; M. Yamashita; *CrystEngComm.,* **2009**, 11, 2110

[42] a) E. Pointillart; K. Bernot; R. Sessoli; D. Gatteschi; *Chem. Eur. J.,* **2007**, 13, 1602; b) V. Chandrasekhar; B. M. Pandian; R. Boomishankar; A. Steiner; J. J. Vittal; A. Houri; R. Clérac, *Inorg. Chem.*, **2008**, 47, 4918; c) J. P. Sutter; S. Dhers; R. Rajamani; S. Ramasesha; J. P. Costes; C. Duhayon; L. Vendier, *Inorg. Chem.*, **2009**, 48, 5820; d) C. G. Efthymiou; T. C. Stamatatos; C. Papatriantafyllopoulou; A. J. Tasiopoulos; W. Wernsdorfer; S. P. Perlepes; G. Christou, *Inorg. Chem.,* **2009**, 48, 9737; e) T. D. Pasatoiu; M. Etienne; A. M. Madalan; M. Andruh; R. Sessoli, *Dalton Trans.,* **2010**, 39, 4802

[43] G. E. Kostakis; I. J. Hewitt; A. M. Ako; V. Mereacre; A. K. Powell, *Phil. Trans. R. Soc. A.*, 2010, 368, 1509

[44] (a) M. Pinsky; D. Avnir, *Inorg. Chem.*, 1**998**, 37, 5575; (b) S. Alvarez; D. Avnir; M. Llunell; M. Pinsky, *New J. Chem.,* **2002**, 26, 996

[45] F. E. Mabbs; D. J. Machin, Magnetism and Transition Metal Complexes, Dover Publications, **2008**

[46] a) A. Abragam; B. Bleaney; Electron Paramagnetic Resonance of Transition Ions, Clarendon Press, Oxford, **1970**; b) A. Abragam; M. H. L. *Pryce, Proc. R. Soc. London Ser. A.,* **1950**, 206, 173

[47] N. F. Chilton; R. P. Anderson; L. D. Turner; ASoncini; K. S. Murray, *J. Comput. Chem.,* **2013**, 34, 1164

[48] a) J. M. Zadrozny; M. Atanasov; A. M. Bryan; C. Y. Lin; B. D. Rekken; P. P. Power; F. Neese; J. R. Long, *Chem. Sci.,* **2013**, 4, 125; b) D. E. Freedman; W. H. Harman; T. D. Harris; G. J. Long; C. J. Chang; J. R. Long, *J. Am. Chem. Soc.*, **2010**, 132, 1224; c) V. Chandrasekhar; A. Dey; A. J. Mota; E. Colacio, *Inorg. Chem.,* **2013**, 52, 4554

[49] a)Y. N. Guo; G. F. Xu; W. Wernsdorfer; L. Ungur; Y. Guo; J. Tang; H. J. Zhang; L. F. Chibotaru; A. K. Powell, *J. Am. Chem. Soc.,* **2011**, 133, 11948; b) Y.-N. Guo; X. H. Chen; S. Xue; J. Tang, *Inorg. Chem.*, **2011**, 50, 9705; c) L. Zou; L. Zhao; P. Chen; Y. N. Guo; Y. Guo; Y. H. Li; J. Tang, *Dalton Trans.*, **2012**, 41, 2966; d) P. H. Lin; T. J. Burchell; R. Clérac; M. Murugesu, *Angew. Chem., Int. Ed.*, **2008**, 47, 8848

[50] M. P. Shores; J. J. Sokol; J. R. Long, *J. Am. Chem. Soc.*, **2002**, 124, 2279

[51] S. Gomez-Coca; E. Cremades; N, Aliaga-Alcalde; E. Ruiz, *J. Am. Chem. Soc.*, **2013**, 135, 7010

[52] A. V. Palii; J. M. Clemente-Juan; E. Coronado; S. I. Klokishner; S. M. Ostrovsky; O. S. Reu, *Inorg. Chem.*, **2010**, 49, 8073

[53] K. Fink; C. Wang; V. Staemmler, *Inorg. Chem.*, **1999**, 38, 3847

[54] H. Bolvin, *Chem. Phys. Chem.*, **2006**, 7, 1575

[55] a) J. Long; F. Habib; P. H. Lin; I. Korobkov; G. Enright; L. Ungur; W. Wernsdorfer; L. F. Chibotaru; M. Murugesu, *J. Am. Chem. Soc.*, **2011**, 133, 5319; b) Y. N. Guo; G. F. Xu; P. Gamez; L. Zhao; S. Y. Lin; R. Deng; J. Tang; H. J. Zhang, *J. Am. Chem. Soc.*, **2010**, 132, 8538

[56] I. Hewitt; Y. H. Lan; C. E. Anson; J. Luzon; R. Sessoli; A. K. Powell, *Chem. Commun.*, **2009**, 6765

[57] G. A. Craig; M. Murrie, *Chem. Soc. Rev.*, **2015**, 44, 2135

[58] Y. Peng; Z. M. Li; Y. B. Zeng; X, Xie; H. D. Wang; L. Li; X. M. Liu, *Microchim. Acta.*, **2010**, 170, 17

[59] K. Sundaravel; M. Sankaralingam; E. Suresh; M. Palaniandavar; *Dalton Trans.*, **2011**, 40, 8444

[60] Y. Peng; C. B. Tian; Y. H. Lan; N. Magnani; Q. P. Li; H. B. Zhang; Annie K. Powell; S. W. Du, *Eur. J. Inorg. Chem.*, **2013,** 5534

[61] N. Pooransingh; E. Pomerantseva; M. Ebel; S. Jantzen; D. Rehder; T. Polenova, *Inorg. Chem.*, **2003**, 42, 1256

[62] G. M. Sheldrick, *Acta Crystallogr., Sect. A.*, **2008**, 64, 112

[63] A. L. Spek, *J. Appl. Cryst.*, **2003**, 36, 7

[64] C. Campana, Advanced Crystallography Publication of Crystal Structures, Bruker AXS

[65] F. Weigend; R. Ahlrichs, *Phys. Chem. Chem. Phys.*, **2005**, 7, 2397

[66] (a) V. Staemmler, *Thor. Chim. Acta.*, **1977**, 45, 89; (b) U. Meier; V. Staemmler, *Theor. Chim. Acta.*, **1989**, 76, 95; (c) J. Wasilewski, *Int. J. Quantum Chem.*, **1989**, 36, 504

[67] F. Neese, *J. Chem. Phys.*, **2005**, 122, 034107

Appendix

Appendix A: List of compounds

1 $[Co^{III}{}_3Co^{II}{}_2Dy^{III}{}_2(OH)_2(PhCO_2)_6(\mathbf{dea})_4(H\mathbf{dea})(NO_3)](NO_3)\cdot 3MeOH\cdot H_2O$

2 $[Co^{III}{}_3Co^{II}{}_2Gd^{III}{}_2(OH)_2(PhCO_2)_6(\mathbf{dea})_4(H\mathbf{dea})(NO_3)](NO_3)\cdot 3MeOH\cdot H_2O$

3 $[Co^{III}{}_3Dy_3(\mathbf{L1})_3(\mu_3\text{-}OH)_4(O_2CPh)_6(H_2O)_3]\cdot(O_2CPh)\cdot Cl\cdot 4MeOH\cdot 10H_2O$

4 $[Co^{III}{}_3Dy_3(\mathbf{L1})_3(\mu_3\text{-}OH)_4(O_2CPh\text{-}\mathit{Me})_6(H_2O)_3]\cdot 2Cl\cdot 10MeOH$

5 $[Fe_2Dy_2(\mathbf{L1})_2(\mathit{Me}\text{-} PhCO_2)_6(OH)_2]\cdot 2MeCN\cdot MeOH\cdot 3.35H_2O$

6 $[Cr_2Dy_2(\mathbf{L1})_2(\mathit{Me}\text{-} PhCO_2)_6(OH)_2]\cdot 2MeCN$

7 $[Cr_2Y_2(\mathbf{L1})_2(\mathit{Me}\text{-} PhCO_2)_6(OH)_2]\cdot 2MeCN$

8 $[FeDy(H\mathbf{L1})_2(O_2CPh)_3(NO_3)]$

9 $[FeY(H\mathbf{L1})_2(O_2CPh)_3(NO_3)]$

10 $[Fe_4Dy_4(\mathbf{L1})_2(PhCO_2)_{10}(\mu_4\text{-}O)_3(\mu_3\text{-}OH)_2(MeOH)_2(MeO)_2]\cdot 3MeOH$

11 $[Fe_4Tb_4(\mathbf{L1})_2(PhCO_2)_{10}(\mu_4\text{-}O)_3(\mu_3\text{-}OH)_2(MeOH)_2(MeO)_2]\cdot 3MeOH\cdot H_2O$

12 $[Fe_4Y_4(\mathbf{L1})_2(PhCO_2)_{10}(\mu_4\text{-}O)_3(\mu_3\text{-}OH)_2(MeOH)_2(MeO)_2]\cdot 3MeOH\cdot H_2O$

13 $[Dy_2(H\mathbf{L1})(NO_3)_4]$

14 $[Dy_2(\mathbf{L2})(NO_3)_4]$

15 $[Dy_2(H\mathbf{L3})_2(NO_3)_4]$

16 $[Co(H_2\mathbf{L4})_2]\cdot 2THF$

17 $[Co(H\mathbf{L5})_2]$

18 $[Co(H_2\mathbf{L6})_2]\cdot CH_2Cl_2$

19 $[Dy_2(H\mathbf{L4})_2(OAc)_2(EtOH)_2]$

20 $[Dy_2(\mathbf{L5})_2(OAc)_2(H_2O)_2]\cdot 2MeOH$

21 $[Co(\mathbf{L7})]$

22 $[Co_2Dy_2(\mathbf{L8})_4(NO_3)_2(MeOH)_2]\cdot 2CH_2Cl_2$

23 $[Co_2Dy_2(\mathbf{L8})_4(NO_3)_2(DMF)_2]\cdot 2C_2H_6CO$

24 $[Zn_2Dy_2(\mathbf{L8})_4(NO_3)_2(MeOH)_2]\cdot 2CH_2Cl_2$

25 $[Fe_2Dy(\mathbf{L8})_4(MeOH)(AcO)]\cdot 4MeOH$

26 $[Fe_2Y(\mathbf{L8})_4(MeOH)(AcO)]\cdot 4MeOH$

27 $[Co_2Dy(H_2\mathbf{L9})_2(NO_3)_2(MeOH)_4]\cdot NO_3\cdot 5MeOH\cdot 5H_2O$

28 $[Co_2Tb(H_2\mathbf{L9})(NO_3)_2(MeOH)_4]\cdot NO_3\cdot 8H_2O$

29 $[Co_2Ho(H_2\mathbf{L9})(NO_3)_2(MeOH)_4]\cdot NO_3\cdot 10H_2O$

30 $[Co_2Y(H_2\mathbf{L9})(NO_3)_2(MeOH)_4]\cdot NO_3\cdot 10H_2O$

31 $Na\cdot[Co_2Dy(\mathbf{L9})_2(H_2O)_4]\cdot 7H_2O$

32 $Na\cdot[Co_2Tb(\mathbf{L9})_2(H_2O)_4]\cdot 7H_2O$

33 $Na\cdot[Co_2Ho(\mathbf{L9})_2(H_2O)_4]\cdot 7H_2O$

34 $Na\cdot[Co_2Y(\mathbf{L9})_2(H_2O)_4]\cdot 7H_2O$

35 $[Co_2Dy_2(H\mathbf{L9})_2(N_3)_2(NO_3)_2(MeOH)_4]\cdot 4MeOH$

Appendix B: List of organic ligands

H_2**dea** Diethanolamine

H_2**L1** 2-[(2-hydroxy-ethyl)-pyridin-2-ylmethyl-amino]-ethanol

H_1**L2** 2-(bis-pyridin-2-ylmethyl-amino)-ethanol

H_2**L3** 2-(bis-pyridin-2-ylmethyl-amino)-propane-1,3-diol

H_3**L4** 3-hydroxy-naphthalene-2-carboxylic acid (6-hydroxymethyl-pyridin-2-ylmethylene)-hydrazide

H_2**L5** nicotinic acid (6-hydroxymethyl-pyridin-2-ylmethylene)-hydrazide

H_3**L6** 2-hydroxy-benzoic acid (6-hydroxymethyl-pyridin-2-ylmethylene)-hydrazide

H_2**L7** 6,6'-((1Z)-((piperazine-1,4-diylbis(propane-3,1-diyl)) bis(azanylylidene))bis(methanylylidene))bis(2-methoxyphenol)

H_2**L8** 2-[(2-hydroxy-phenylimino)-methyl]-6-methoxy-phenol

H_4**L9** (N',N'''E,N',N'''E)-N',N'''-(pyridine-2,6-diylbis(methanylylidene)) bis(2-hydroxybenzohydrazide)

Appendix C: List of abbreviations

H_3tea	triethanolanmine
TCNE	tetracyanoethylene
Ln	lanthanide

EtOH	ethanol
Fig	Figure
Me	methyl
Py	pyridine
Ph	phenyl
MeOH	methanol
MeCN	acetonitrile
DMF	dimethylformamide
THF	tetrahydrofurane
mg	milligram
mL	millilitre
mmol	millimole
IR	infrared
NMR	nuclear magnetic resonance
XRD	powder X-ray diffraction
SQUID	super-conducting quantum interference device
ac	alternating current
dc	direct current
D	zero-field splitting parameter
K	Kelvin
Oe	Oersted
H	field
Hz	Hertz
M	magnetisation
T	temperature
T	Tesla
T_b	blocking temperature
H	hour
χ	molar magnetic susceptibility
χ’	in-phase magnetic susceptibility

χ''	out-of-phase magnetic susceptibility
μ_B	bohr magneton
$N\beta$	bohr magneton
U_{eff}	effective energy barrier
cm^3	cubic centimetres
br	broad
d	doublet
t	triplet
s	singlet (NMR), strong (IR)
m	multiplet (NMR), medium (IR)
w	weak
SMM	single molecule magnet
SIM	single ion magnet
ZFS	zero field splitting
M_S	spin projection quantum number
D	uniaxial anisotropy
τ	rate of the magnetic relaxation
τ_0	relaxation time
g	g factor
k_B	Boltzmann constant
Ac	acetyl

Acknowledgements

Finally I want to say some words from my heart. This thesis is the summary of my results obtained during the last three years.

I would like to acknowledge here my gratitude for many people who contributed either directly or indirectly to this work.

I am sincerely grateful to my direct supervisor Professor Annie K. Powell. From her, I gained a great deal of experience in the field of molecular magnetism throughout the years. With her, I have learned not only how to be an independent researcher, but also how to cooperate with her and other collaborators. I am deeply grateful for all the time that she has dedicated to me and for her patience, support, and friendship.

A deep sense of gratitude and indefinable thanks are owed to Dr. Valeriu Mereacre, not only for measuring, analyzing and explaining the magnetic properties, but also for the valuable discussion and brilliant advices for my work. He teaches me to develop my skills and knowledge about science.

I would like to thank Dr. Chris Anson and George E. Kostakis for collecting the crystallographic data, refining the structures.

I’m grateful to Dr. Amer Baniodeh and Dr. Denis Prodius for their help and support, as well as the numerous helpful suggestions they gave.

I wish to thank Dr. Yanhua Lan and Dr. Abishake Mondal for performing the magnetic measurements.

I would like to thank PD. Dr. Karin Fink, Dr. Yiquan Zhang and Tilmann Bodenstein for the *ab initio* calculation.

I would like to thank Sabine Lude and Nicole Klaassen for the elemental analyses and Lena Friedrich for IR measurements. Thanks to Gabi Leichle, Kalam Munshi, Rolf Lehmann and Tobias Lampert for their help in chemical stores or with technical problems.

I want to thank Getraud Amschlinger, Katja Haberer, Hartmut Speck and Monika Kayas for their help in official works.

I was very lucky to work in the wonderful place that is KIT during my graduate career. It was especially a great experience to witness the friendly relations made between the graduate students and the professors and be a part of this. I’m thankful for Sebastian Schmidt for his help in many aspects. Thanks to Sihuai Chen, Guo Peng, Zhaosha Meng, Irina Kühne, Nadine Zill, Martin Schlageter, Thomas Kriese, Masooma Ibrahim, Nicolas Leblanc and Thomas Biet and everyone else in the group for their kindness and support.

Special thanks to my family for their continual encouragement and support. Last not the least, I would like to thank the unique one. I will always be very grateful to her for her endless support, understanding, and confidence in me. She put my success before her and accompanied me in my PhD journey in Germany. Without her love and support this thesis could not exist.